Deeply Virtual Compton Scattering off an Unpolarised Hydrogen Target at HERMES

Jonathan R.T. Burns

A Thesis presented for the degree of
Doctor of Philosophy

Nuclear Physics Experimental Research Group
Department of Physics and Astronomy
University of Glasgow
Scotland

June 2010

Deeply Virtual Compton Scattering off an Unpolarised Hydrogen Target at HERMES

Jonathan R.T. Burns

Submitted for the degree of Doctor of Philosophy
June 2010

Abstract

Deeply Virtual Compton Scattering (DVCS) i.e. $ep \rightarrow ep\gamma$ is the simplest interaction that allows access to Generalised Parton Distributions (GPDs), a theoretical framework describing nucleon structure. The strong interest in GPDs results from the fact that they can be used to determine the total angular momentum of quarks inside the nucleon and provide a 3-dimensional picture of nucleon structure. The measurement of the DVCS process is facilitated by the interference with a competing interaction known as the Bethe-Heitler process which has the same final state. DVCS information is obtained from the asymmetrical in distribution of the real photon around the azimuthal angle ϕ at HERMES. Beam charge and beam helicity asymmetries, extracted from DVCS events with an unpolarised hydrogen target recorded during the 2006-2007 and 1996-2007 data taking periods, are presented in this thesis. The asymmetry amplitudes are presented over the range of HERMES kinematic acceptance, with their dependence on kinematic variables t , x_B and Q^2 also shown and compared to a phenomenological model.

Declaration

The work in this thesis is based on research carried out at the Nuclear Physics Experimental Group, Department of Physics and Astronomy, University of Glasgow, Scotland. No part of this thesis has been submitted elsewhere for any other degree or qualification and is all my own work unless referenced to the contrary in the text.

Acknowledgements

I would like to thank a number of people who have contributed to the success of my PhD. I shall start by thanking my supervisors Prof. Ralf Kaiser and Dr Bjoern Seitz for their wisdom, advice, guidance and encouragement throughout the last four years. In addition to my supervisors, I would like to thank Prof. Guenther Rosner, the head of the NPE group for offering me a PhD position that has allowed me to undertake some fascinating research, travel to many interesting locations and build up a considerable amount of knowledge along the way. On a day to day to basis I would like to thank Dr Gordan Hill, Dr Inti Lehmann and Dr Morgan Murray for advising me on the writing of tracking software, the undertaking of a DVCS analysis and for all the other advice and explanations they have offered me. During my visits to Hamburg I was more often than not accompanied by Gordan, Morgan, David Mahon and laterally by Jennifer Bowles. Although they all the trips more enjoyable, David in particular with his constant reminder of the number of days we had left in Hamburg and his generally sunny deposition made the whole experience most pleasant. At HERMES I worked with a number of people supported my work, to highlight a few Andreas Mussgiller, Caroline Riedl and Sergey Yaschenko all offered advice on the successful completion of both my tracking studies and DVCS analysis. The cross check of my results were undertaken by Dietmar Zeiler and he has my gratitude for the discussions we had concerning this analysis. Throughout my time with the NPE group I have been based in room 407 with a number of people who have greatly encouraged they are Gordan, Elilidh McNicol, Seian Al Jebali, David Howdle, Jennifer, and Rachel Montgomery, my thanks to you all! My gratitude also to all those with whom I regularly enjoyed a beverage in one of the many coffee shops on Byres Road. Thanks also to the proof readers of this thesis

Ralf, Bjoern, Gordan, Morgan, Inti and David, it was really good form from you all. Finally and most importantly my thanks to my family, my brothers Martyn and Derek for their consistent support, especially Martyn who has always been a steady rock when life can be a bit stormy and my parents Hazel and Robert for all the encouragement, support, advice and lodgings they have afforded me over the years. May God bless each one of you.

August 6, 2010

Contents

Chapter 1

Introduction

The atom consists of a dense central nucleus of positive electric charge and a cloud of negatively charged electrons. The two baryons that comprise the nucleus, collectively known as nucleons, are positively charged protons and electrically neutral neutrons. The constituent particles of the nucleon are partons: quarks and gluons [1]. The presence of partons within the nucleon has been postulated and experimentally confirmed over the last half century [2].

The intrinsic angular momentum, known as the spin, is one of the fundamental properties of a particle. If the particle has spin, then the total angular momentum **J** is the sum of the orbital and spin angular momentum

$$\mathbf{J} = \mathbf{L} + \mathbf{S}. \tag{1.1}$$

It follows from the general theory of angular momentum that no meaning can be ascribed to the spin vector **S** having a particular direction. The average spin direction, however, can be considered and the average value of S_Z, expressed in units of $\hbar$, has been measured to be $\frac{1}{2}$ [3], while S_X and $S_Y = 0$. The z-component of the nucleon spin s_z can be written as [4]

$$S_Z = \frac{1}{2} = J_Q + J_G = \frac{1}{2}\Delta\Sigma + L_Q + \Delta G + L_G \tag{1.2}$$

where J_Q (L_Q) and J_G (L_G) are the total (orbital) angular momentum of quarks (gluons), $\Delta\Sigma$ is the fraction of the spin carried by the constituent quarks, ΔG the fraction of the spin carried by the gluons.

It was originally believed that the total spin of the nucleon was carried by the quarks, as predicted by the quark-parton model. The European Muon Collaboration (EMC) at CERN [5, 6] published a result showing that the fraction of the overall spin contributed by the spin of the quarks was $14 \pm 9 \pm 21\%$, potentially consistent with zero [7].

The result of the quarks not carrying the entire nucleon spin prompted a large amount of discussion and research interest around the globe. Two of the facilities at the forefront of this research were the Spin Muon Collaboration at CERN and the Stanford Linear Collider Center (SLAC) [8]. Both of these experiments worked on the principle of detecting a lepton that scattered off a quark. Results produced at these experiments indicated that the contribution of the quarks to nucleon spin to be closer to 30%. Determining the contributions of L_Q, ΔG and L_G to the nucleon spin is known as the "spin puzzle", illustrated in Fig 1.1. Providing answers to this "puzzle" is the reason that the HERMES experiment was constructed.

HERMES (HERa MEasurement of Spin) is one of the experiments on the HERA (Hadron Electron Ring Accelerator) at the DESY (Deutsches Electron SYnchrotron) laboratory in Hamburg, Germany [9]. It was a fixed target experiment that was initially designed to study the spin structure of the nucleon through polarised DIS (Deep Inelastic Scattering) in which longitudinally polarised electrons or positrons scatter off a polarised gas target. The experiment took data from 1995 until 2007. The most precise measurement of the quark contribution to the overall nucleon spin was published by the HERMES collaboration and was found to be $\Delta\Sigma \approx 0.33 \pm 0.011(\text{theo.}) \pm 0.025(\text{exp.}) \pm 0.028(\text{evo.})$ [10].

Recently this understanding of nucleon structure has manifested itself in the form of Generalised Parton Distributions (GPDs). GPDs are a phenomenological parametrisation of Form Factors and regular Parton Distributions. Strong interest in the formalism of GPDs emerged after it was found that GPDs give access to the total (including orbital) angular momentum carried by the quarks in the nucleon [4]. More recent focus has been on the potential of GPDs as three dimensional representations of hadrons at the partonic level [12], correlating traditional longitudinal momentum fraction to transverse spatial coordinates. Driven by the interest in GPDs HERMES

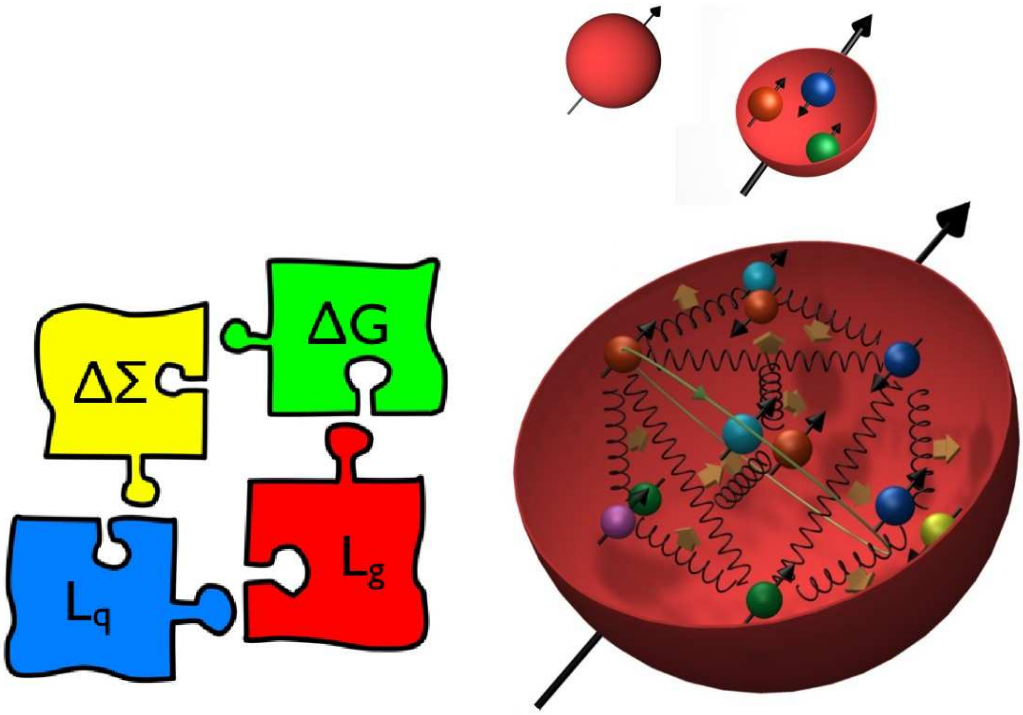

(a) Pieces of the spin puzzle. (b) Nucleon structure at different scales.

Figure 1.1: Left: The contribution of the various components of nucleon spin [11]. Right: The development of the structure of the nucleon from the individual nucleon, to the nucleon comprising of three constituent quarks and to the nucleon comprising of quarks and gluons with respective spin and angular momentum .

and other particle accelerator experiments such as CLAS and Hall A at Jefferson Lab or H1 and ZEUS at DESY all contribute to the study of GPDs as part of their physics program.

The experimentally most direct way of accessing GPDs is through DVCS (Deeply Virtual Compton Scattering) interactions i.e. the hard exclusive leptoproduction of high energy photons, denoted by $ep \rightarrow ep\gamma$ [13, 14, 15, 16, 17, 18]. Competing Bethe-Heitler interactions have the same initial and final state as DVCS interactions and are, experimentally indistinguishable. DVCS information is, therefore, accessed from the interference of the scattering amplitudes of these two processes. This information is determined from the asymmetrical distribution of the real photon around the azimuthal angle ϕ, the angle between the lepton-nucleon scattering plane and the real photon production plane. HERMES has published a number of DVCS azimuthal asymmetries using various gas targets and different beam polarisation and charge states [19, 20]. During an access period in 2005 a rather unique Recoil Detector was installed around the HERMES gas target cell to allow an exclusive measurement of the DVCS interaction [21]. Data taking resumed with the Recoil Detector present until the experiment shut down in July 2007.

The work presented in this thesis involved developing track reconstruction software for the Recoil Detector and the analysis of DVCS on an unpolarised hydrogen target. The theoretical framework of GPDs is introduced in chapter 2 of this thesis. This chapter also outlines the DVCS interaction and the azimuthal asymmetries that can be extracted from unpolarised hydrogen data. The HERMES experimental apparatus is detailed in chapter 3 and includes a description of the Recoil Detector. A track reconstruction software algorithm for the Silicon Strip Detector, the inner most detector of the Recoil Detector, is discussed in chapter 4. Chapter 5 introduces the selection process used to isolate the analysable events from the HERMES experimental data. The predicted DVCS asymmetries, used to estimate the systematic errors, extracted from Monte Carlo simulations of the HERMES experiment and produced by theoretical models are also detailed in this chapter. The final DVCS results of the Beam Helicity and Beam Charge asymmetry analysed in this thesis are presented in chapter 6. This is the DVCS result with the largest number of

analysable DVCS events at HERMES.

Chapter 2

Generalised Parton Distributions and Deeply Virtual Compton Scattering

2.1 Introduction

Generalised Parton Distributions (GPDs), are a theoretical framework that can be used to describe nucleon structure [16, 14]. GPDs embody regular Parton Distribution Functions (PDFs) and Form Factors (FFs) as limiting cases and moments, respectively. PDFs describe the longitudinal momentum and helicity distributions of partons as limiting cases and FFs describe the transverse number and current density of partons. GPDs expand significantly on the information that can be obtained from these two quantities alone providing correlated information on transverse positional and longitudinal momentum distributions of partons [22]. Strong experimental interest in GPDs developed after it was shown that the moments of certain GPDs contained information on the total angular momentum carried by partons in the nucleon [18, 4]. A number of theoretical models have been developed to describe GPDs leading to an approach [23] based on Double Distributions [24], this model was later improved upon by [25]. The four nucleon GPDs thought to be most accessible from HERMES proton data to leading order are H, $\widetilde{H}$, E and $\widetilde{E}$.

Deeply Virtual Compton Scattering (DVCS) is one the simplest interactions al-

lowing access to GPDs. DVCS on the proton ($lp \rightarrow l\gamma p$) is an incoming lepton interacting with a quark in the proton via a virtual photon. The scattered lepton then leaves the interaction along with a real photon and the recoiling proton. In addition to the DVCS process there is the competing Bethe-Heitler process, which has the same initial and final state as DVCS [26]. These two processes are experimentally indistinguishable so their scattering amplitudes interfere. DVCS information can be accessed using this interference term. DVCS results from HERMES are obtained from the asymmetrical distribution of the real photon around the azimuthal angle ϕ, which is defined as the angle between the lepton-nucleon scattering plane and the real photon production plane. DVCS results can be accessed directly from the cross section at some experiments, however, this is not the case at HERMES due to the fact that precise measurements of the luminosity were not available. Using asymmetry measurements also allows systematic effects such as acceptance to be removed as the ratio of the cross sections approximately cancel these effects.

The two asymmetries analysed in this thesis are the Beam Charge Asymmetry (BCA) and the Beam Helicity Asymmetry (BHA). The BCA and BHA are the asymmetries of DVCS events with different charge and helicity states respectively. These asymmetries are extracted using two different methods. The Beam Charge Asymmetry (BCA) is extracted simultaneously with the Beam Helicity Asymmetry (BHA) from DVCS event data and the single charge BHA is also extracted separately. The Fourier coefficients of the BHA and BCA amplitudes relate to Compton Form Factors (CFFs), convolutions of GPDs with hard scattering kernels. The leading terms of the BCA and BHA relate to the real and imaginary parts of CFF $\mathcal{H}$ respectively allowing access to GPD H.

2.2 Generalised Parton Distributions

This section describes the kinematic variables used to describe GPDs and introduces models developed to parametrise GPDs. The observables in the analysis presented in this thesis allow access to GPD H. This GPD, therefore, is the main focus of this section.

2.2.1 Kinematic Variables Associated with GPDs

Exclusive electroproduction of photons off an unpolarised nucleon target can be described as

$$l(\mathbf{k}) + N(\mathbf{P}) \rightarrow l(\mathbf{k'}) + N(\mathbf{P'}) + \gamma(\mathbf{q'}) \tag{2.1}$$

where **k (k')** and **P (P')** denote the four momenta of the incoming (outgoing) lepton and the initial (final) proton. The four momenta of the virtual photon is denoted **q'** and the quantity Q^2 can be written as

$$\mathbf{q}^2 = -Q^2 \equiv (\mathbf{k} - \mathbf{k'})^2 < 0. \tag{2.2}$$

The energy loss ν of the scattered lepton is expressed as

$$\nu \equiv \frac{\mathbf{P} \cdot \mathbf{q}}{M} \tag{2.3}$$

where M is the rest mass of the nucleon target. The $\mathbf{q}^2$ and ν terms are Lorentz invariant. For a fixed target experiment such as HERMES in which the nucleon target is at rest and the electron beam is considered to have negligible mass, these quantities can be written in the laboratory reference frame as

$$Q^2 \cong 4EE' sin^2\left(\frac{\theta_e}{2}\right) \tag{2.4}$$

and

$$\nu \cong E - E' \tag{2.5}$$

where E (E') are the energies of the incoming (outgoing) lepton respectively, θ_e is the polar angle of the lepton with respect to the beam direction. Two other quantities that are introduced to describe the process are expressed

$$x_B \equiv \frac{Q^2}{2\mathbf{P} \cdot \mathbf{q}} \cong \frac{Q^2}{2M\nu}, \tag{2.6}$$

and

$$y \equiv \frac{\mathbf{P} \cdot \mathbf{q}}{\mathbf{P} \cdot \mathbf{k}} \cong \frac{\nu}{E}. \tag{2.7}$$

In the DIS case x_B can be interpreted as the four momentum fraction of the nucleon that is carried by the struck quark. The same x_B variable is used to describe GPDs. The variable y is the fraction of the energy lost by the lepton in the interaction. The

variables Q^2, ν, x_B and y are purely inclusive in the fact that they are determined by the the initial particles. For the DVCS process, two other quantities that are also important for describing GPDs are introduced

$$\xi \equiv \frac{-q^2}{\mathbf{q} \cdot (\frac{\mathbf{P}+\mathbf{P'}}{2})} \approx \frac{x_B}{2 - x_B} \tag{2.8}$$

and

$$t = (\mathbf{P} - \mathbf{P}')^2. \tag{2.9}$$

The skewness variable ξ is related to the Bjorken scaling variable x_B in the HERMES kinematic region . The skewness variable can also be interpreted as the momentum imparted to a quark during the DVCS interaction. The quark leaves the nucleon with momenta $x + \xi$ and returns to the nucleon with momenta $x - \xi$, where x refers to the longitudinal momentum of the struck quark and the overall momentum transferred is 2ξ. The Mandelstam variable t is the squared momentum transferred during the interaction process to the target nucleon.

2.2.2 Properties of Generalised Parton Distributions

There are four GPDs at twist-2 level accessible from a spin-$\frac{1}{2}$ proton in the HERMES measurement range H, $\widetilde{H}$, E and $\widetilde{E}$. The twist referred to when discussing GPDs is defined as the dimension of the hadronic tensor minus the spin of the nucleon [27]. For the analysis presented in this thesis it is sufficient to describe the twist term as a suppression by powers of $\frac{1}{Q}$. The smallest possible twist is twist-2 which has no suppression by $(\frac{1}{Q})$, followed by twist-3 which has suppression of $(\frac{1}{Q})$ and twist-4 objects that have suppression of $(\frac{1}{Q})^2$. The GPDs discussed in this thesis are assumed to be at leading twist (twist-2) unless stated to the contrary. The properties of these GPDs are summarised in Table 2.1. GPDs H and E describe nucleon helicity conservation and inversion respectively. The distributions H and E are referred to as unpolarised and $\widetilde{H}$ and $\widetilde{E}$ polarised because H and E correspond to the sum over parton helicities and $\widetilde{H}$ and $\widetilde{E}$ to the difference. The GPDs are valid for each quark flavour q and there exists an equivalent set of GPDs for gluons. There is also an expanded set of GPDs that describe the spin-1 nucleus [28].

	Nucleon Helicity Conserving	Nucleon Helicity Inverting
Unpolarised GPDs	H	E
Polarised GPDs	$\widetilde{H}$	$\widetilde{E}$

Table 2.1: Review of different GPDs at leading twist.

Generalised Parton Distributions (GPDs) reduce to regular PDFs in the forward limit of t $\rightarrow 0$ and $\xi \rightarrow 0$ [14, 18, 29],

$$\begin{aligned} H^q(x,0,0) &= q(x), \\ \widetilde{H}^q(x,0,0) &= \Delta q(x), \end{aligned} \tag{2.10}$$

where $q(x)$ is the quark density distributions and $\Delta q(x)$ is the quark helicity distribution for quark flavour q.

The GPDs E and $\widetilde{E}$ are inaccessible in the forward limit as they do not conserve nucleon helicity and cannot be related to regular PDFs. The gluon GPDs are analogous to their quark counterparts in terms of being observable in the forward limit: $H^g(x,\xi,t)$ and $\widetilde{H}^g(x,\xi,t)$ reduce to the unpolarised and polarised gluon distributions $G(x)$ and $\Delta G(x)$ and E^g and $\widetilde{E}^g$ are, again, inaccessible in this forward limit as are the gluon helicity flip GPDs [30]. The gluons and spin-1 GPDs are beyond the scope of the work presented and are not further detailed.

The first x moments of the GPDs reduce to the elastic form factors of the nucleon

$$\int_{-1}^{1} H^q(x,\xi,t)dx = F_1^q(t), \tag{2.11}$$

$$\int_{-1}^{1} E^q(x,\xi,t)dx = F_2^q(t), \tag{2.12}$$

$$\int_{-1}^{1} \widetilde{H}^q(x,\xi,t)dx = G_A^q(t), \tag{2.13}$$

$$\int_{-1}^{1} \widetilde{E}^q(x,\xi,t)dx = G_P^q(t) \tag{2.14}$$

where $F_1^q(t)$ and $F_2^q(t)$ are the elastic Dirac and Pauli form factors respectively and $G_A^q(t)$, $G_P^q(t)$ are the axial-vector and pseudo-scalar form factors for the quark flavour q in the nucleon.

The principle aim of the HERMES experiment is the investigation of the spin of the nucleon. GPDs can access the total angular momentum of quarks in the nucleon via the Ji relation [4]

$$J^q = \lim_{t\to 0} \frac{1}{2} \int_{-1}^{1} x(H^q(x,\xi,t) + E^q(x,\xi,t))dx \tag{2.15}$$

where J^q is the total angular momentum sum of all quark flavours q and $H^q(x,\xi,t)$ and $E^q(x,\xi,t)$ are GPDs in the limit $t \to 0$. The Ji relation holds for gluons equating the total angular momentum J^g of the gluon's to the gluon GPDs.

In the Ji decomposition [4, 27] the total angular momentum can be written in terms of the contributions of the quark spin of the nucleon $\frac{1}{2}\Delta\Sigma$ and the orbital angular momentum contribution L^q

$$J^q = \frac{1}{2}\Delta\Sigma + L^q. \tag{2.16}$$

The total angular momentum of the gluons can be expressed in a similar manner

$$J^g = \Delta G + L^g, \tag{2.17}$$

where ΔG is the gluon spin of the nucleon and L^g the gluon orbital angular momentum contribution. The most precise measurement of $\Delta\Sigma \approx 0.33$ has been determined from inclusive and semi-inclusive polarised DIS measurements at HERMES [10]. The angular momentum contribution L^q can, therefore, be determined from J^q and $\Delta\Sigma$. At present this method is the only method known to determine the value L^q and this is one of the important areas of research in the developing field of GPDs. The spin of the nucleon can be expressed as the sum of the quarks and gluon contributions

$$\frac{1}{2} = J^q + J^g. \tag{2.18}$$

The determination of the value of J^q also gives the total angular momentum of the gluon's J^g within the nucleon.

GPD Models

A non-trivial property of GPDs is the polynomiality of their Mellin moments that follows from Lorentz invariance. This invariance dictates that the Mellin moments of GPDs should be maximally of order $N+1$ [31]:

$$\int_{-1}^{1} dx x^N H^q(x,\xi) = h_0^{q(N)} + h_2^{q(N)}\xi^2 + ... + h_{N+1}^{q(N)}\xi^{N+1} \tag{2.19}$$

$$\int_{-1}^{1} dx x^N E^q(x,\xi) = e_0^{q(N)} + e_2^{q(N)}\xi^2 + ... + e_{N+1}^{q(N)}\xi^{N+1}. \tag{2.20}$$

Due to the time reversal invariance the polynomials contain only the even powers of ξ. As $N+1$ is odd this implies that the highest power of ξ for even N remains N [32]. This allows for the coefficients of ξ to be related to each other in a non-trivial way [25]

$$e_{N+1}^{q(N)} = -h_{N+1}^{q(N)}. \tag{2.21}$$

One method of parametrising GPDs while satisfying the polynomiality conditions is to use the Double Distribution formalism. The t-independent part can be written as [14, 29],

$$H^q_{DD} = \int_1^1 d\beta \int_{-1+|\beta|}^{1-|\beta|} d\alpha \delta(x-\beta-\alpha\xi) F^q(\beta,\alpha) \tag{2.22}$$

$$E^q_{DD} = \int_1^1 d\beta \int_{-1+|\beta|}^{1-|\beta|}, d\alpha \delta(x-\beta-\alpha\xi) K^q(\beta,\alpha) \tag{2.23}$$

where $F^q(\beta,\alpha)$ and $K^q(\beta,\alpha)$ are the double distributions. The terms β and α are the equivalent of x and ξ respectively in the Double Distribution notation. The x and ξ parameters of GPDs are disentangled using the δ functions. The GPDs obtained from double distributions satisfy the polynomiality conditions but always lead to $e_{N+1}^{q(N)} = h_{N+1}^{q(N)} = 0$ i.e. the highest power for ξ is absent for odd N. The parametrisation was completed by adding the "D-term" as proposed in [33]:

$$H^q(x,\xi) = \int_{-1}^{1} d\beta \int_{-1+|\beta|}^{1-|\beta|} d\alpha \delta(x-\beta-\alpha\xi) F^q(\beta,\alpha) + \theta\Big[1 - \frac{x^2}{\xi^2} D^q(\frac{x}{\xi})\Big] \tag{2.24}$$

$$E^q(x,\xi) = \int_{-1}^{1} d\beta \int_{-1+|\beta|}^{1-|\beta|} d\alpha \delta(x-\beta-\alpha\xi) K^q(\beta,\alpha) + \theta\Big[1 - \frac{x^2}{\xi^2} D^q(\frac{x}{\xi})\Big] \tag{2.25}$$

where $D^q(z)$ is an odd function. The D-term generates the highest power of ξ

$$-e^{q(N)}_{N+1} = h^{q(N)}_{N+1} = \int_{-1}^{1} dz z^N D^q(z). \tag{2.26}$$

The polarised GPDs $\widetilde{H}^q(x,\xi)$ and $\widetilde{E}^q(x,\xi)$ have similar polynomiality conditions to the unpolarised GPDs. The difference between $\widetilde{H}^q(x,\xi)$ and $\widetilde{E}^q(x,\xi)$ is that for polarised GPDs the highest power of the polynomial in ξ for odd (even) N is $N-1$ (N). The D-term is not included in case of polarised GPDs as it drops out of the Ji relation due to the fact that for polarised GPDs $\widetilde{H}^q$ and $\widetilde{E}^q$ are of the same magnitude and opposite sign. This is valid for leading twist-2 quark GPDs. There also exists a number of higher twist quark GPDs that can be expressed in terms of the leading twist GPDs in the Wandzura-Wilzeck approximation [34, 35]. All of these are required for a full description of the DVCS process.

2.2.3 The VGG Interpretation of a Double Distribution Model of GPDs

Several theoretical models have been proposed to describe GPDs with a phenomenological ansatz in the past decade. The result of these efforts have lead to the development of two models based on Double Distributions known as the "VGG model" [23, 25], proposed by Vanderhaeghen, Guichon and Guidal and the Dual Parametrisation, proposed by Guzey in [36]. The Dual Parametrisation was not used in this analysis as one of the parameters used in the model calculations were found to be significantly wrong [37]. The corrected version of this model produced theory bands that do not describe the experimental result. The theory curves in this analysis were, therefore, generated using the VGG model and compared to the experimental results. Only the parametrisation of GPD $H(x,\xi,t)$ is described as this is the dominant contribution to the observables presented in this analysis, detailed in Section 2.6.1.

The t-independent part of GPD $H(x,\xi,t)$ can be parametrised using the Double Distribution and is completed using the D-term. The Double Distribution model proposed by Radyushkin [24], is

$$F^q(\beta,\alpha) = h(\beta,\alpha)q(\beta) \tag{2.27}$$

where $q(\beta)$ is the forward quark distribution for quark flavour q and $h(\beta,\alpha)$ is the profile function. The profile function is parametrised using a one-parameter ansatz

$$h(\beta,\alpha) = \frac{\Gamma(2b+2)}{2^{2b+1}\Gamma^2(b-1)} \frac{[(1-|\beta|)^2-\alpha^2]^b}{(1-|\beta|)^{2b+1}}. \tag{2.28}$$

The parameter b characterises the strength of the GPD on skewness ξ. As the value of b increases the skewness of the model decreases. This parameter is applied to both valence (b_{val}) and sea quarks (b_{sea}) and is a free parameter chosen in a reasonable range [1,∞) (but in practice [1,9]).

The simplest parametrisation of the t dependence of GPD H^q in the small t region that satisfies the sum rules of Eq 2.11, consists of the factorised ansatz for the t-dependence

$$H^u(x,\xi,t) = H^u(x,\xi)F_1^u(t)/2 \tag{2.29}$$

$$H^d(x,\xi,t) = H^d(x,\xi)F_1^d(t) \tag{2.30}$$

$$H^s(x,\xi,t) = 0 \tag{2.31}$$

where $F_1^u(t)$ and $F_1^d(t)$ are determined using the parametrisations of the proton and neutron Pauli and Dirac form factors. The calculations of GPDs using the quark soliton model [38] show a dependence that is not described well by this factorised ansatz. The results from this model can be described using a simple Regge motivated ansatz for $H^q(x,\xi=0,t)$

$$H^q(x,\xi=0,t) = \frac{1}{x^{\alpha' t}} q(x) \tag{2.32}$$

where α' can be interpreted as the slope of a Regge trajectory. If this ansatz is used then the nucleon form factors follow from the sum rule of Eq 2.11

$$F_1^q(t) = \int_0^1 dx \frac{1}{x^{\alpha' t}} q_{val}(x).t \tag{2.33}$$

This gives a satisfactory description of the proton Dirac form factor over the range $0 < -t < 1$ GeV^2 with $\alpha' = 0.8$ GeV^{-2}. There is a more recent ansatz for the t-dependence which is not presented in this work [39]. The ξ-dependence of the Regge

type ansatz can be restored by modifying the model for the double distribution introduced in Eq 2.22

$$F^q(\beta,\alpha,t) = h(\beta,\alpha)q(\beta)\frac{1}{|\beta|^{\alpha' t}}. \tag{2.34}$$

2.2.4 Parametrisation of the D-term

To complete the parametrisation of GPD H^q the D-term has to be specified. The estimates of the D-term in the chiral quark-soliton model [38] show that $D^u(z) \approx D^d(z)$. The calculations assume that

$$D^q(z) = \frac{1}{N_f}D(z) \tag{2.35}$$

where N_f is the number of active flavours and $D(z) = \sum_q D^q(z)$ is the flavour singlet term. The D-term can be expanded using a sum of odd Gegenbauer polynomials

$$D(z) = (1-z^2)[d_1 C_1^{3/2} + d_3 C_3^{3/2}(z) + d_5 C_5^{3/2}(z) + ...]. \tag{2.36}$$

In principle the D-term also has a scale dependence but this is neglected in this case as the uncertainties in the modelling of the D-term are larger than the logarithmic scale dependence. The negative sign of the Gegenbauer coefficients for the D-term gives a contribution relative to the Double Distribution part to the GPD H^q.

A model of the x and ξ dependence of the parametrisation of GPD $H^u(x,\xi,t=0)$ including the double distribution and the D-term is shown in Fig 2.1. Moving along the lines of constant x illustrates the sensitivity of the GPD to the D-term (increases relative to the double distribution part with increasing skewness ξ). In the limit at $\xi = 1$, the D-term contribution dominates GPD H^q. The D-term as previously stated drops out of the sum rule of Eq 2.11, hence the t-dependence of the D-term is not constrained. Due to the lack of further information this t-dependence is factorised and a dipole is used.

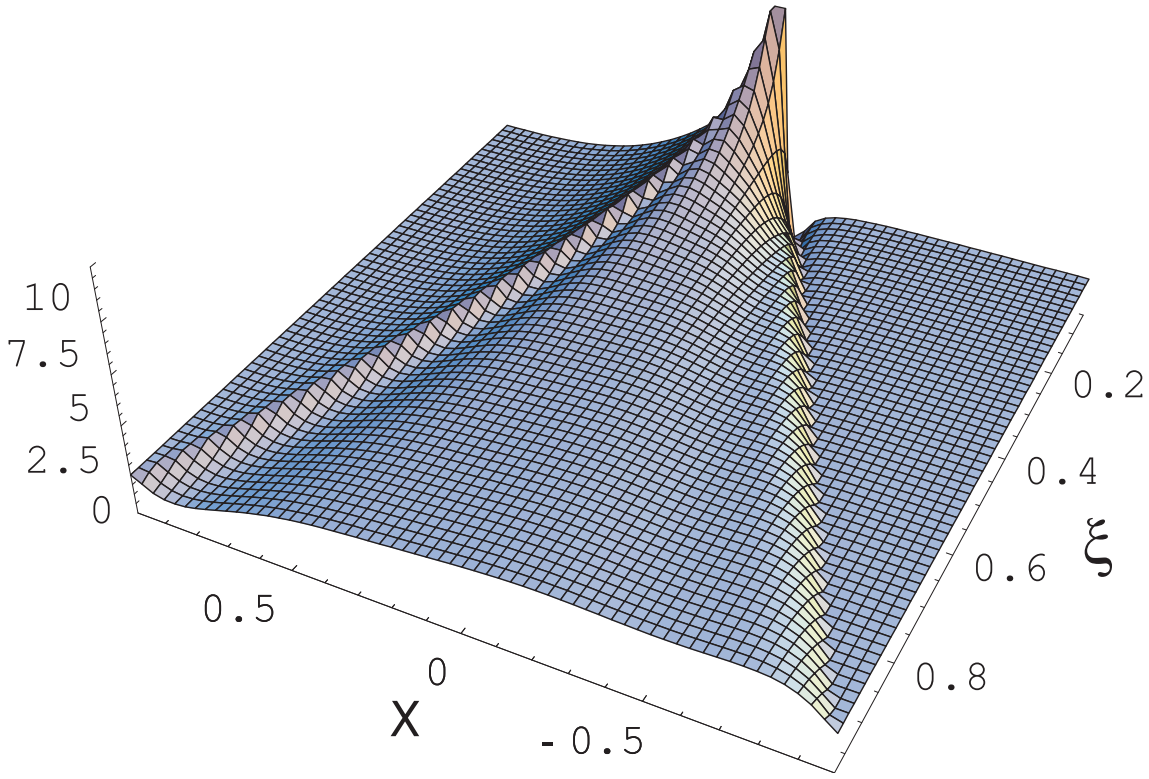

Figure 2.1: The x and ξ dependence of GPD $H^u(x, \xi, t = 0)$ for the u quark distribution including the Double Distribution part for $b_{val} = b_{sea} = 1$ and the D-term for the VGG model [25].

2.3 Using DVCS to access GPDs

Deeply Virtual Compton Scattering (DVCS) is experimentally the most simple means by which to access GPDs [40]. A variation of this process called time like Compton Scattering and Meson production [41] are also used to access GPDs. Hard exclusive leptoproduction of π^+ mesons off a nucleon target can be used to investigate helicity flip GPDs. These processes are beyond the scope of this work and as such are not discussed further. The DVCS interaction is related to Deep Inelastic Scattering (DIS) in that it involves the exchange of a virtual photon. In the DVCS process a virtual photon strikes a quark in the nucleon. The quark leaves

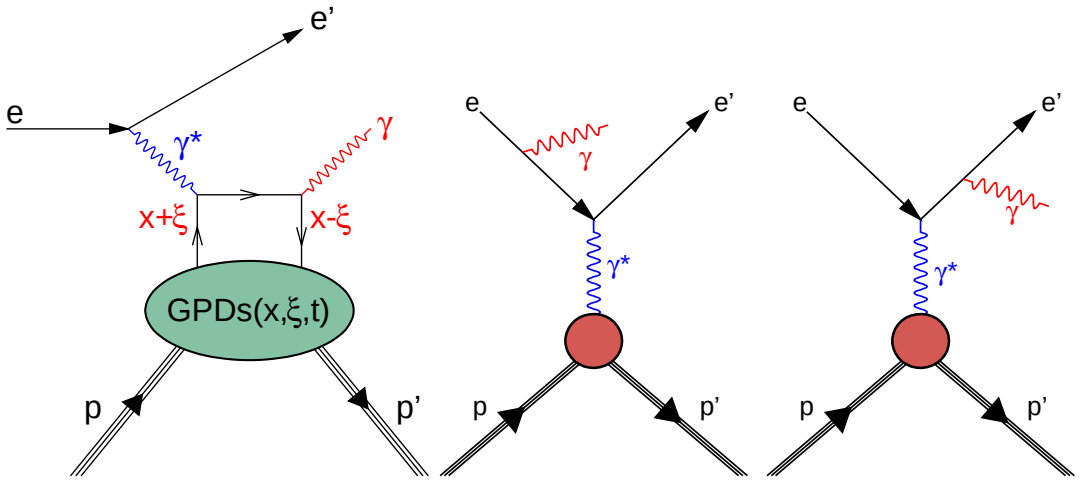

(a) DVCS (b) Bethe Heitler

Figure 2.2: Left: The DVCS interaction in which an electron/positron interacts with a quark in the nucleon via a virtual photon. The quark leaves the nucleon with momentum $x + \xi$ before emitting a real photon and returning to the nucleon with longitudinal momentum fraction $x - \xi$. Right: The Bethe-Heitler interaction which is a competing process to DVCS with the same initial and final reaction products.

the nucleon with longitudinal momentum fraction $x + \xi$ emits a real photon and returns to the nucleon with a momentum $x - \xi$ resulting in a longitudinal momentum fraction change of 2ξ. There is a competing reaction to DVCS called Bethe-Heitler (BH), an interaction in which the virtual photon interacts with the nucleon and the real photon comes from the lepton. Both DVCS and BH have the same initial and final reaction products and the two processes cannot be experimentally distinguished, and hence they interfere. The BH terms dominate at HERMES and although these terms, calculable in QED, can be subtracted at the cross section level from the DVCS cross section the errors involved are large and the result obtained is worthless. The interference between the scattering amplitudes of the BH and DVCS process facilitates access to GPDs at HERMES.

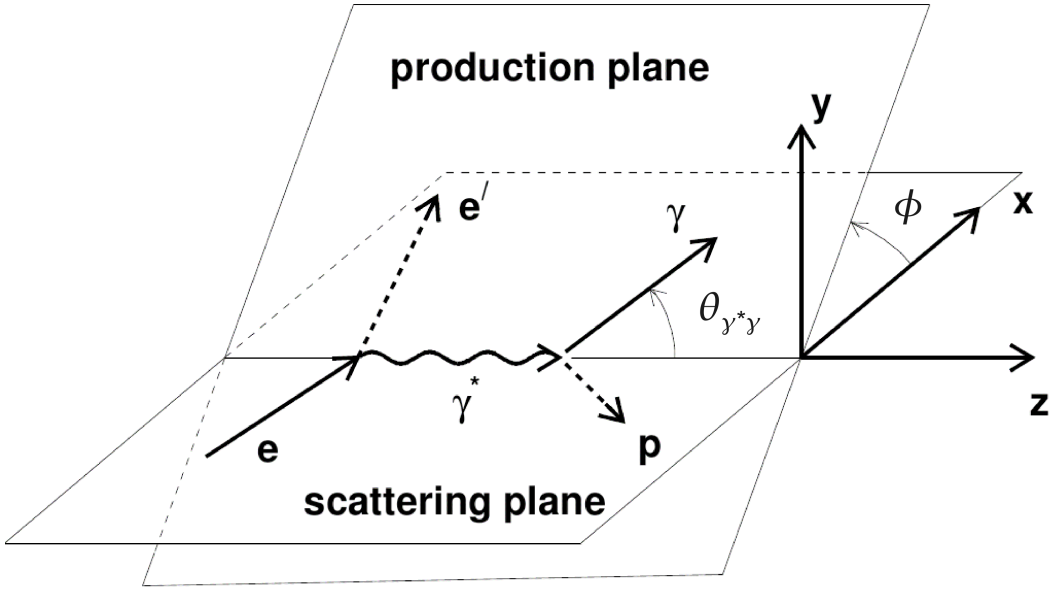

Figure 2.3: The production and scattering planes of the DVCS interaction [42]. The azimuthal angle ϕ is defined as the angle between the production and scattering plane of the real and virtual photons respectively. Also shown is the polar angle $\theta_{\gamma^*\gamma}$ between the two photons.

2.4 Kinematic Variables of DVCS Events

The DVCS interaction is shown in Fig 2.3, in which an incoming lepton interacts via a virtual photon with a quark inside the target proton at rest in the lab frame. The reaction products of this interaction are a scattered lepton, a scattered recoil proton and a real photon. The interaction is written

$$e^{\pm}(\mathbf{k}) + P(\mathbf{P}) \rightarrow e(\mathbf{k'}) + P(\mathbf{P'}) + \gamma(\mathbf{q'}) \tag{2.37}$$

where e is the lepton, P the target proton, γ the produced real photon, $\mathbf{k}$ ($\mathbf{k'}$) is the four momentum of incoming (scattered) lepton, $\mathbf{P}$ ($\mathbf{P'}$) is the four momentum of the target (recoiling) proton and $\mathbf{q'}$ is the four momentum of the real photon.

The angle ϕ shown in Fig 2.3 is defined as the azimuthal angle between the lepton scattering and photon production planes of the virtual and real photons respectively. The polar angle $\theta_{\gamma^*\gamma}$ is determined from the angle between the two photons.

2.4.1 Cross Section

In terms of the variables defined in the previous sections, the four fold cross section for $ep \rightarrow ep\gamma$ is

$$\frac{d\sigma}{dx_B dy d|t| d\phi} = \frac{\alpha^3 x_B y}{8\pi Q^2 \sqrt{1+\epsilon^2}} \frac{\tau}{e^3}^2 \tag{2.38}$$

in which α is the fine structure constant, e is the elementary charge, τ is the scattering amplitude and

$$\epsilon = 2x_B \frac{M_P}{Q} \tag{2.39}$$

where M_P is the proton mass [40, 43]. The amplitude τ^2 is given by

$$\tau^2 = |\tau_{BH}|^2 + |\tau_{DVCS}|^2 + I \tag{2.40}$$

where τ_{DVCS} is the DVCS amplitude, τ_{BH} is the Beth-Heitler amplitude and the interference term I is expressed as

$$I = \tau_{DVCS}\tau^*_{BH} + \tau^*_{DVCS}\tau_{BH}. \tag{2.41}$$

The contributions $|\tau_{BH}|^2$, $|\tau_{DVCS}|^2$ and the interference term I for an unpolarised target can be Fourier expanded in ϕ to twist-3 approximation [40]

$$|\tau_{BH}|^2 = \frac{e^6}{x_B^2 y^2 (1+\epsilon^2)^2 t P_1(\phi) P_2(\phi)} \Big(c_0^{BH} + \sum_{n=1}^{2} c_n^{BH} cos(n\phi) \Big), \tag{2.42}$$

$$|\tau_{DVCS}|^2 = \frac{e^6}{y^2Q^2}\Big(c_0^{DVCS} + \sum_{n=1}^{2} c_n^{DVCS} cos(n\phi) + \lambda s_1^{DVCS} sin(1\phi)\Big), \tag{2.43}$$

$$I = \frac{\eta e^6}{x_B y^2 t P_1(\phi) P_2(\phi)}\Big(c_0^I + \sum_{n=1}^{3} c_n^I cos(n\phi) + \lambda \sum_{n=1}^{2} s_n^I sin(n\phi)\Big) \tag{2.44}$$

where η denotes the charge of the incoming lepton in the DVCS/BH interaction, $\pm\lambda$ denotes the polarisation of the beam, c_n^{BH}, c_n^{DVCS}, s_1^{DVCS}, c_n^I and s_n^I are Fourier coefficients detailed in Section 2.6 and $P_{1,2}(\phi)$ are the lepton propagators

$$Q^2 P_1 \equiv (k - q')^2 \tag{2.45}$$

and

$$Q^2 P_2 \equiv [k - (p' - p))]^2. \tag{2.46}$$

The coefficients c_1^I, s_1^I and c_0^{DVCS} arise at the twist-2 level and are dependent on GPDs.

2.5 Asymmetry Measurements of DVCS

In order to measure the absolute DVCS cross section precise knowledge of the luminosity of the experiment is required. It is, therefore, experimentally simpler to analyse asymmetries, the ratio of different cross sections, when exact measurements of the luminosity are not available. By using the ratio of different cross sections the acceptance effects approximately cancel. At HERMES kinematics the Bethe-Heitler interaction dominates the DVCS process.

A number of asymmetry measurements have been published by the HERMES collaboration that make use of the different polarisation states of the beam and target, the positron and electron beam particles and different target gases. HERMES has produced asymmetry results of the Beam Helicity Asymmetry, A_{LU}, using the positive and negative beam polarisation states and an unpolarised target [19], the Beam Charge Asymmetry, A_C, using electrons and positrons and an unpolarised target, [44], the Transverse Target Spin Asymmetry, A_{UT}, using an unpolarised beam and a transversely polarised target [45], the Longitudinal Target Spin Asymmetry,

A_{UL}, using an unpolarised beam and a longitudinally polarised target and the Longitudinal Double Spin Asymmetry A_{LL} using both a longitudinally polarised beam and target [46]. A_{LU}, A_C , A_{UL} and A_{LL} results have been published by the HERMES using a hydrogen and in the case of A_{LU} and A_C using a deuterium target [47]. HERMES has also investigated the dependence of A_{LU} on the nuclear mass of the target [20]. The work presented in this thesis details the combined extraction of A_{LU} and A_C from data taken at HERMES during 2006-2007 period with an unpolarised hydrogen target. The asymmetries presented in this thesis are extracted from the largest DVCS event sample that is available at HERMES.

2.5.1 Single Charge Beam Helicity Asymmetry

Two different extraction techniques were used in this analysis. The first extracts only the Beam Helicity Asymmetry (BHA) from proton data with a single charge and two beam polarisation states. The second is a combined extraction of BHA and Beam Charge Asymmetry (BCA) using data with both two beam polarisation states and with positively and negatively charged leptons. The cross section which is independent of beam helicity, having an unpolarised beam (U), and an unpolarised target (U) with a constant charge can be expressed as [40]

$$\begin{aligned}\sigma_{UU} = &\frac{\alpha^3}{8\pi Q^2 x_B y(1-\epsilon^2)^{5/2} t P_1(\phi) P_2(\phi)} \left[c_0^{BH} + \sum_{n=1}^{2} c_n^{BH} cos(n\phi) \right] \\ &+ \frac{\alpha^3 x_B}{8\pi y Q^4 \sqrt{1+\epsilon^2}} \left[c_0^{DVCS} + \sum_{n=1}^{2} c_n^{DVCS} cos(n\phi) \right] \\ &- \eta \frac{\alpha^3}{8\pi Q^2 \sqrt{1+\epsilon^2} y^2 t P_1(\phi) P_2(\phi)} \left[c_0^{I} + \sum_{n=1}^{3} c_n^{I} cos(n\phi) \right]. \end{aligned} \tag{2.47}$$

The cross section dependent on the longitudinally polarised beam (L) and the unpolarised target (U) can be expressed as

$$\begin{aligned}\sigma_{LU} = &\frac{\alpha^3}{8\pi Q^2 x_B y(1-\epsilon^2)^{5/2} t P_1(\phi) P_2(\phi)} \left[c_0^{BH} + \sum_{n=1}^{2} c_n^{BH} cos(n\phi) \right] \\ &+ \frac{\alpha^3 x_B}{8\pi y Q^4 \sqrt{1+\epsilon^2}} \left[c_0^{DVCS} + \sum_{n=1}^{2} c_n^{DVCS} cos(n\phi) - \lambda s_1^{DVCS} sin(\phi) \right] \\ &- \eta \frac{\alpha^3}{8\pi Q^2 \sqrt{1+\epsilon^2} y^2 t P_1(\phi) P_2(\phi)} \left[c_0^{I} + \sum_{n=1}^{3} c_n^{I} cos(n\phi) + \lambda \sum_{n=1}^{2} s_n^{I} sin(n\phi) \right]. \end{aligned} \tag{2.48}$$

The cross section σ_{LU} can, therefore be expressed as

$$\sigma_{LU} = \sigma_{UU}\left[1 + \lambda\left(K_1\frac{s_1^{DVCS}sin(\phi)}{\sigma_{UU}} - \eta K_2\frac{\sum_{n=1}^{2} s_n^I sin(n\phi)}{\sigma_{UU}}\right)\right] \tag{2.49}$$

where λ and η represent the polarisation and charge state respectively and K_1 and K_2 are kinematic factors expressed in equation 2.49. The beam helicity asymmetry is defined as

$$A_{LU}^{\eta}(\phi) = \frac{d\sigma(\overrightarrow{e},\phi) - d\sigma(\overleftarrow{e},\phi)}{d\sigma(\overrightarrow{e},\phi) + d\sigma(\overleftarrow{e},\phi)} \tag{2.50}$$

where $\overrightarrow{e}$ and $\overleftarrow{e}$ are the positive and negative beam helicity states respectively. The beam helicity asymmetry for a constant beam charge η using the cross section, σ_{LU} can be written as

$$A_{LU}^{\eta} = \frac{s_1^{DVCS}sin(\phi) - \eta\frac{1}{Z}\frac{x_B}{y}s_1^I sin(\phi) + s_2^I sin(2\phi)}{\frac{1}{Z}\frac{c_0^{BH} + \sum_{n=1}^{2} c_n cos(n\phi)}{t(1+\epsilon^2)^2} + c_0^{DVCS} + \sum_{n=1}^{2} c_n^{DVCS}cos(n\phi) - \eta\frac{1}{Z}c_0^I + \sum_{n=1}^{3} c_n^I cos(n\phi)} \tag{2.51}$$

where

$$Z = \frac{x_B^2 P_1(\phi)P_2(\phi)}{Q^2}. \tag{2.52}$$

Analysis of the above equation for A_{LU} reveals that the asymmetry contains both beam charge dependent interference terms and DVCS terms which are independent of beam charge. BH is the dominant factor in the denominator of A_{LU}^{η} with c_0^{BH} being the leading term [26]. The prevalent term in the numerator is the interference term with the s_1^I leading twist term dominating over the twist-3 s_2^I term suppressed by a factor of $\sim \frac{1}{Q}$. The asymmetry value can therefore be approximated as

$$A_{LU}^{\eta} \approx \eta\frac{x_B}{y}\frac{s_1^I}{c_0^{BH}}sin(\phi). \tag{2.53}$$

Using both equation 2.51 for A_{LU} and the helicity dependent cross section σ_{LU} can be expressed as

$$\sigma_{LU} \cong \sigma_{UU}[1 + \lambda A_{LU}^{\eta}]. \tag{2.54}$$

2.5.2 Beam Helicity Asymmetry Arising From Both the Interference Term and DVCS Squared Term of the Overall Cross Section

The previous section detailed the calculation of the Beam Helicity Asymmetry (BHA) which was independent of polarisation and dependent on a single beam charge only. The charge independent BHA and the Beam Charge Asymmetry are simultaneously extracted. The BHA is induced by the beam helicity dependence of the pure DVCS cross section and the Interference term. The BHA arising from both of these terms are accessible using the simultaneous extraction method. The charge independent BHA A_{LU}^{I} and A_{LU}^{DVCS}, for a longitudinally polarised beam (L) and an unpolarised target (U), are defined as:

$$A_{LU}(\phi) = \frac{d\sigma(\overrightarrow{e^+},\phi) - d\sigma(\overleftarrow{e^+},\phi) - d\sigma(\overrightarrow{e^-},\phi) + d\sigma(\overleftarrow{e^-},\phi)}{d\sigma(\overrightarrow{e^+},\phi) - d\sigma(\overleftarrow{e^+},\phi) - d\sigma(\overrightarrow{e^-},\phi) + d\sigma(\overleftarrow{e^-},\phi)}, \tag{2.55}$$

where $\overrightarrow{e}$ ($\overleftarrow{e}$) refer to the positive (negative) beam helicity states and $\pm$ to the beam charge.

The BHA is calculated using the cross section σ_{LU} defined in 2.49.Using this information the BHA induced by the interference terms and DVCS squared term can be expressed as [40]

$$A_{LU}^{I} = \frac{\frac{x_B}{y}\sum_{n=1}^{2} s_n^I sin(n\phi)}{\frac{\sum_{n=1}^{2} c_n^{BH} cos(n\phi)}{(1+\epsilon^2)^2} + Z\sum_{n=1}^{2} c_n^{DVCS} cos(n\phi)}, \tag{2.56}$$

$$A_{LU}^{DVCS} = \frac{Z s_1^{DVCS} sin(\phi)}{\frac{\sum_{n=1}^{2} c_n^{BH} cos(n\phi)}{(1+\epsilon^2)^2} + Z\sum_{n=1}^{2} c_n^{DVCS} cos(n\phi).} \tag{2.57}$$

As discussed in the previous section the term c_0^{BH} dominates in the denominator of the asymmetries. In the numerator the s_1^I term dominates over s_2^I. The two asymmetries can be approximated as

$$A_{LU}^{I} \approx -\frac{x_B}{y}\frac{s_1^I}{c_0^{BH}} sin(\phi). \tag{2.58}$$

$$A_{LU}^{DVCS} \approx \frac{x_B^2 t P_1(\phi) P_2(\phi)}{Q^2} \frac{s_1^{DVCS}}{c_0^{BH}} sin(\phi), \tag{2.59}$$

Comparing the BHA that is dependent on a specific beam charge η in Eq 2.53 and that arising from the interference term assuming that $A_{LU}^{I} >> A_{LU}^{DVCS}$

$$A_{LU}^{\eta} \approx \eta A_{LU}^{I} \tag{2.60}$$

where $\eta = \pm 1$

2.5.3 Beam Charge Asymmetry

The BCA is induced by the beam charge dependence of the DVCS/BH Interference and is calculated using the difference between this cross section using both charge states and is defined as

$$A_C(\phi) = \frac{d\sigma(e^+, \phi) - d\sigma(e^-, \phi)}{d\sigma(e^+, \phi) - d\sigma(e^-, \phi)} \tag{2.61}$$

where e^+ and e^- are the positive and negative charged beam respectively. Using the cross section σ_{LU}, A_C can be defined as

$$A_C = \frac{\frac{x_B}{y} \sum_{n=1}^{3} c_n^I cos(n\phi)}{\frac{\sum_{n=1}^{2} c_n^{BH} cos(n\phi)}{(1+\epsilon^2)^2} + Z \sum_{n=1}^{2} c_n^{DVCS} cos(n\phi)}, \tag{2.62}$$

As in the previous section describing the BHA, the c_0^{BH} term dominates in the denominator and the c_1^I term dominates over $c_{0,2,3}^I$ in the numerator. The $c_{2,3}^I$ terms are of higher twist and the c_0^I term is smaller and has the opposite sign of the c_1^I term. The BCA can be expressed as

$$A_C \approx -\frac{x_B}{y} \frac{c_1^I}{c_0^{BH}} cos(\phi), \tag{2.63}$$

having a cosine dependence.

The cross section which is independent of both the beam helicity and charge is defined

$$\sigma_{UU} = \frac{\alpha^3}{8\pi Q^2 x_B y(1+\epsilon^2)^{5/2} t P_1(\phi) P_2(\phi)} \left[c_0^{BH} + \sum_{n=1}^{2} c_n^{BH} cos(n\phi) \right] + \frac{\alpha^3 x_B}{8\pi Q^4 \sqrt{1+\epsilon^2}} \left[c_0^{DVCS} + \sum_{n=1}^{2} c_n^{DVCS} cos(n\phi) \right]. \quad (2.64)$$

Using the above equation for σ_{UU} the cross section σ_{LU} can be expressed as

$$\sigma_{LU} = \sigma_{UU} \left[1 + \lambda K_1 \frac{s_1^{DVCS} sin(\phi)}{\sigma_{UU}} - \eta K_2 \frac{c_0^I cos(\phi) + \sum_{n=1}^{3} c_n^I cos(n\phi)}{\sigma_{UU}} - \eta\lambda K_2 \frac{\sum_{n=1}^{2} s_n^I sin(n\phi)}{\sigma_{UU}} \right]. \quad (2.65)$$

This can be further simplified using the the asymmetries A_C, A_{LU}^{DVCS} and A_{LU}^I to

$$\sigma_{LU} \cong \sigma_{UU}[1 + \lambda A_{LU}^{DVCS} + \eta A_C + \eta\lambda A_{LU}^I]. \quad (2.66)$$

2.6 Compton Form Factors, Fourier Coefficients and GPDs

2.6.1 Relation of Fourier Coefficients to GPDs

The Fourier coefficients c_n and s_n from the DVCS squared and interference term have a bilinear and linear dependence on the Compton Form Factors (CFFs) respectively. The CFFs are convolutions of GPDs with hard scattering kernels $C^{\pm}$ that can be expressed as

$$\begin{pmatrix} \mathcal{H} \\ \mathcal{E} \end{pmatrix}(\xi, t) = \int_{-1}^{1} C^{-}(x,\xi) dx \begin{pmatrix} H \\ E \end{pmatrix}(x,\xi,t) \quad (2.67)$$

$$\begin{pmatrix} \widetilde{\mathcal{H}} \\ \widetilde{\mathcal{E}} \end{pmatrix}(\xi, t) = \int_{-1}^{1} C^{+}(x,\xi) dx \begin{pmatrix} \widetilde{H} \\ \widetilde{E} \end{pmatrix}(x,\xi,t) \quad (2.68)$$

where the right hand side of each equation expands to

$$C^{\pm}F = \sum_{q=u,d,s} C^{\pm} e_q^2 F_q, \quad (2.69)$$

for each GPD F and quark flavour q. The scattering kernels $C^{\pm}$ can be expressed as

$$C^{\pm} = \frac{1}{x - \xi - i\epsilon} \pm \frac{1}{1 + \xi - i\epsilon} + O(\alpha) \quad (2.70)$$

where ϵ is a non-zero mathematical term that allows $C^{\pm}$ to exist when the values of $x = \xi$. The imaginary terms i allow the CFF itself to be split into its real and imaginary parts

$$\Re(F) = P\int_{-1}^{1} dx \left(\frac{F}{x-\xi} \pm \frac{F}{x+\xi}\right),$$

$$\Im(F) = F(x,\xi) \pm F(x,-\xi) \tag{2.71}$$

where P denotes Cauchy's principle value and terms of $O(x)$ are ignored.

The DVCS observables at HERMES can be written in terms of the real and imaginary parts of the CFFs. The observable relating to the real part of the CFF can access only an integral value of the GPDs at a given ξ. An observable relating to the imaginary part of a CFF can access only the GPD along the line $x = \pm\xi$, as shown in Fig 2.1.

The leading twist (twist-2) amplitude for the interference term which dominates at the HERMES kinematics on an unpolarised proton target can be written as [40]

$$C^I_{unp} = F_1\mathcal{H} + \frac{x_B}{2-x_B}(F_1+F_2)\widetilde{\mathcal{H}} - \frac{\Delta^2}{4M^2}F_2\mathcal{E}. \tag{2.72}$$

where F_1 and F_2 are the Dirac and Pauli form factors of the nucleon. C^I_{unp} is dependent on the Compton Form Factors $\mathcal{H}$, $\widetilde{\mathcal{H}}$ and $\mathcal{E}$. These relate to the three GPDs that can be accessed from a hydrogen target H, $\widetilde{H}$ and E At HERMES kinematics (x_B and $|t|$ of order 0.1) the contributions of the CFFs $\widetilde{\mathcal{H}}$ and $\widetilde{\mathcal{E}}$ can be neglected with respect to the CFF $\mathcal{H}$ [19]. Hence, to first approximation C^I_{unp} is dependent only on CFF $\mathcal{H}$ and, therefore, GPD H.

2.6.2 Amplitudes that Comprise the Beam Helicity and Beam Charge Asymmetries

The Fourier coefficients of the BHA and BCA can be related to the asymmetry amplitudes. The Fourier coefficients of the BHA can be related to the interference term [40]

$$s^I_{1,unp} = 8K\lambda y(2-y)\mathfrak{Im}\mathcal{C}^I_{unp}(\mathcal{F}), \tag{2.73}$$

$$s^{I}_{2,unp} = \frac{16K^2}{2-x_B}(\lambda y)\mathfrak{Im}\mathcal{C}^{I}_{unp}(\mathcal{F}^{eff}), \tag{2.74}$$

and the squared DVCS term

$$c^{DVCS}_{1,unp} = \frac{8K}{2-x_B}(2-y)\mathfrak{Re}\mathcal{C}^{DVCS}_{unp}(\mathcal{F}^{eff},\mathcal{F}), \tag{2.75}$$

$$s^{DVCS}_{1,unp} = \frac{8K}{2-x_B}(-\lambda y)\mathfrak{Im}\mathcal{C}^{DVCS}_{unp}(\mathcal{F}^{eff},\mathcal{F}), \tag{2.76}$$

$$c^{DVCS}_{2,unp} = -\frac{4\mathcal{Q}^2K^2}{M^2(2-x_B)}\mathfrak{Re}\mathcal{C}^{DVCS}_{T,unp}(\mathcal{F}_T,\mathcal{F}*), \tag{2.77}$$

$$c_{0,unp} = 2(2-2y+y^2)\mathcal{C}^{DVCS}_{unp}(\mathcal{F},\mathcal{F}*). \tag{2.78}$$

In a similar manner the Fourier coefficients of the BCA can be related to amplitudes

$$c^{I}_{0,unp} = -8(2-y)\mathfrak{Re}\{\frac{(2-y)^2}{1-y}K^2\mathcal{C}^{I}_{unp}(\mathcal{F}) + \frac{\Delta^2}{\mathcal{Q}^2}(1-y)(2-x_B)(\mathcal{C}^{I}_{unp}+\Delta\mathcal{C}^{I}_{unp})(\mathcal{F})\}, \tag{2.79}$$

$$c^{I}_{1,unp} = -8K(-2+2y+y^2)\mathfrak{Re}\mathcal{C}^{I}_{unp}(\mathcal{F}), \tag{2.80}$$

$$c^{I}_{2,unp} = -\frac{16K^2}{2-x_B}(2-y)\mathfrak{Re}\mathcal{C}^{I}_{unp}(\mathcal{F}^{eff}), \tag{2.81}$$

$$c^{I}_{3,unp} = -\frac{8\mathcal{Q}^2K^3}{M^2(2-x_B)^2}\mathfrak{Re}\mathcal{C}^{I}_{T,unp}(\mathcal{F}_T), \tag{2.82}$$

where λ is the beam polarisation state. $s^{DVCS}_{1,unp}$, $s^{I}_{1,unp}$ and $s^{I}_{2,unp}$ are polarisation dependent. The asymmetry amplitudes that can be extracted from an unpolarised proton target and the related Fourier coefficient, twist-level and Compton Form Factors are summarised in Table 2.2. Twist-2 terms have the least amount of suppression. The amplitudes shown contain GPD information accessible from the CFF terms, additional amplitudes are extracted from the data as a consistency check but these are not related to GPDs and as such should have a zero amplitude. The asymmetry amplitudes from the squared DVCS term that give information on the

imaginary part of $\mathcal{F}$ and $\mathcal{F}*$, the complex conjugate of $\mathcal{F}$ are suppressed as are the $s^I_{2,unp}$, $c^I_{0,unp}$, $c^I_{2,unp}$ and $c^I_{3,unp}$ amplitudes from the interference term. The $c^I_{3,unp}$ asymmetry amplitude relates to $\mathcal{C}^I_{T,unp}$ and involves gluon transversity. The significant, leading twist, amplitudes are $c^I_{1,unp}$ and $s^I_{1,unp}$ that both give information on CFF $\mathcal{H}$ at HERMES kinematics. Using C^I_{unp} the $s^I_{1,unp}$ and $c^I_{1,unp}$ amplitudes can access information on the real and imaginary parts of the CFF $\mathcal{H}$.

Asymmetry Amplitude	Fourier Coefficient	CFF Dependence	Twist Level
$A^{sin(\phi)}_{LU,DVCS}$	$s^{DVCS}_{1,unp}$	$\mathfrak{Im}\mathcal{C}^{DVCS}_{unp}$	3
$A^{sin(\phi)}_{LU,I}$	$s^I_{1,unp}$	$\mathfrak{Im}\mathcal{C}^I_{unp}$	2
$A^{sin(2\phi)}_{LU,I}$	$s^I_{2,unp}$	$\mathfrak{Im}\mathcal{C}^I_{unp}$	3
$A^{cos(0\phi)}_{C}$	$c^I_{0,unp}$	$\mathfrak{Re}\mathcal{C}^I_{unp}$	2
$A^{cos(\phi)}_{C}$	$c^I_{1,unp}$	$\mathfrak{Re}\mathcal{C}^I_{unp}$	2
$A^{cos(2\phi)}_{C}$	$c^I_{2,unp}$	$\mathfrak{Re}\mathcal{C}^I_{unp}$	3
$A^{cos(3\phi)}_{C}$	$c^I_{3,unp}$	$\mathfrak{Re}\mathcal{C}^I_{T,unp}$	4

Table 2.2: Table showing each asymmetry amplitude that can be extracted from the available data set, the related Fourier coefficient, twist level and the Compton Form Factor Dependence (CFF).

The analysis of DVCS on an unpolarised hydrogen target at HERMES is presented in this thesis. The method used to extract the asymmetry measurements from experimental data is outlined in Chapter 5. The results of the BHA and BCA extracted separately from data taken during 2006-2007 and 1996-2007, the entire HERMES data set, are detailed in Chapter 6. The sin$n\phi$ and cos$n\phi$ amplitudes extracted will be compared to the theoretical predictions described in this chapter. The asymmetry results will be related to CFFs and GPDs.

Chapter 3

HERMES Experiment

The HERMES experiment was situated in the East section of the HERA storage ring at the Deutsche Elektronen Synchrotron in Hamburg, Germany. It was proposed during the construction of the HERA ring to investigate nucleon spin. Construction of HERMES began in 1993 and data taking commenced in 1995 [48]. During the lifetime of the experiment several upgrades were made. The luminosity upgrade took place during the shut-down period in 2001 and in 2005 the experiment was upgraded with a new detector designed to measure scattered protons from the DVCS reaction [21]. These upgrades were implemented due to the expanding physics program at HERMES which reflected developments in the understanding of DIS interactions and nucleon structure. The data presented in this thesis was taken using a hydrogen gas target which was available in every data taking year during the lifetime of HERMES with the exception of 1999. The final data taken with the HERMES experiment was in 2007 which coincided with the shut-down of the HERA storage ring.

The HERA storage ring consists of two concentric beams with a circumference of 6.3 km with four experimental halls having access to the ring. HERMES was constructed in the East Hall of the HERA ring. The H1, HERA-B and ZEUS experiments were situated in the North, West and South Halls respectively. took data during the entire lifetime of the HERA ring from 1992 until 2007 while HERA-B took data for three years commencing in 2000 and ending in 2003. The HERA ring has two beams; a proton beam of 920 GeV energy and an electron / positron beam of 27.6 GeV. ZEUS and H1 were collider experiments that used both of these beams

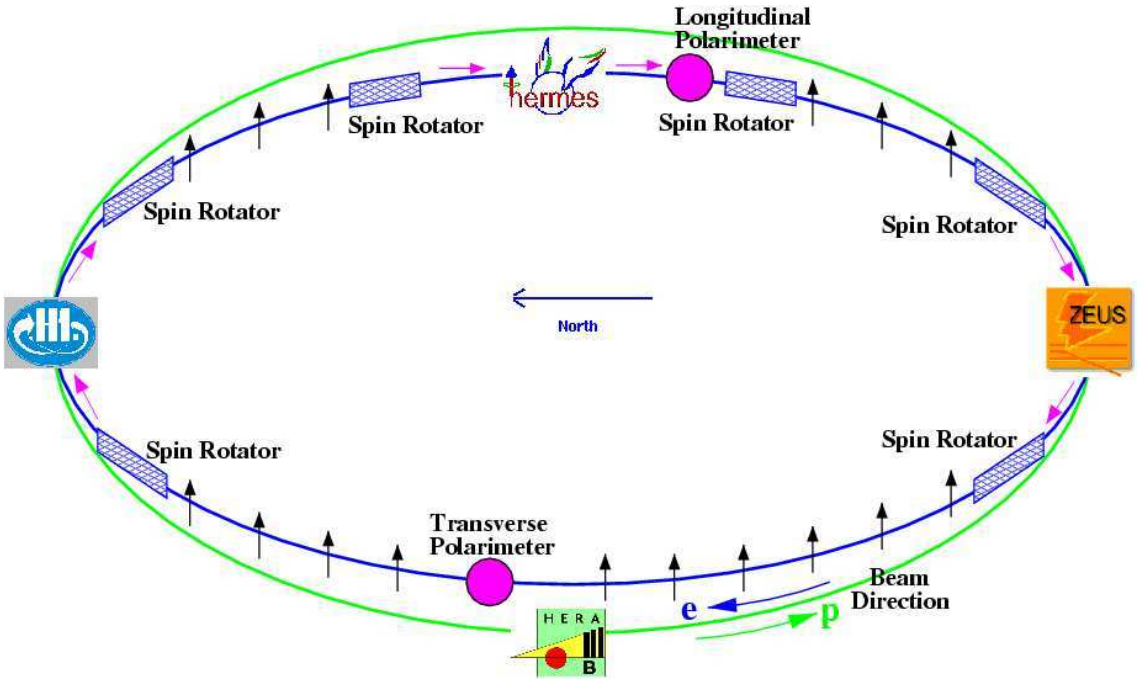

Figure 3.1: Diagram of the proton and lepton beams as they interact with the HERMES, H1, HERA-B and ZEUS experiments on the HERA ring [49]. Also shown are the polarimeters and beam spin rotators

while HERMES and HERA-B were fixed target experiments that used only one of the beams, the proton in the case of HERA-B and the lepton beam in HERMES. HERMES utilised both the electron and positron beams allowing a number of DVCS asymmetry measurements to be made. The majority of the data taken is with the positron beam and includes data taking years 1995, 1996, 1997, 2000, 2002, 2003, 2004, 2006 and 2007. Electron beam data was taken in 1998, 2005 and 2006.

The electron/positron beam was first accelerated at DESY by the Linac II linear accelerator to 450 MeV. The beam is further accelerated to 7.5 GeV in the DESY-II storage ring. The final pre-acceleration stage occurs in the PETRA storage ring, to 12 GeV. The beam is then provided to HERA and accelerated to the final operation energy of 27.56 GeV.

The HERA beam was initially unpolarised. Due to the magnetic dipole fields in the arcs of the high energy storage rings the helicity of leptons can flip by the emission of synchrotron radiation described by the Sokolov-Ternov effect [50]. This results in a transversely polarised beam which is polarised parallel $\uparrow$ and antiparallel $\downarrow$ for positrons and electrons with respect to the direction of the magnetic field of the HERA spectrometer magnets, as shown in Fig 3.1.

Longitudinal beam polarisation is necessary for high energy polarised electron scattering experiments due to the fact that in scattering with a transversely polarised beam, all spin effects are suppressed by m_e/E, where m_e is the electron mass and E is the electron energy. The beam polarisation is obtained by a pair of spin rotators [51] located up- and downstream of the HERMES experiment in the HERA East straight section, consisting of interleaved horizontal and vertical bending magnets. The first spin rotator rotates the spins into the beam direction and the second one turns them back into the vertical direction for transit before the beam enters the next section. These beam spin rotators were installed at the H1 and ZEUS experiments also in 2001 during the high luminosity upgrade. By moving the magnets of the spin rotators it is possible to reverse the spin of the beam polarisation after every fill in principle. In practice, this was not the case and the polarisation direction was typically altered every few months.

The beam polarisation is defined as:

$$P = \frac{N \uparrow - N \downarrow}{N \uparrow + N \downarrow} \tag{3.1}$$

where $N \uparrow$ ($N \downarrow$) denotes the number of electrons/positrons with polarisation $\uparrow$ ($\downarrow$). The polarisation increases with time (t) with the dependence given by:

$$P = P_{ST} \cdot \left(1 - exp\{-\frac{t}{\tau_{ST}}\}\right) \tag{3.2}$$

where P_{ST} is the theoretical maximum polarisation and τ_{ST} the characteristic rise time of $\sim$40 minutes and depends on P_{ST}, the beam energy and the bending radius in the magnetic field. The theoretical maximum of 92% polarisation cannot be reached at HERMES. This is due to a number of limiting factors; the misalignment of the magnetic field which guides the bending of the beam in the ring, interactions between the lepton and proton beams in the storage ring, proton-lepton interactions that occur in collisions at the ZEUS and H1 experiments, the lepton beam interacting with the HERMES target gas and energy loss from the emission of synchrotron radiation as the beam travels around the ring. The maximum polarisation at HERMES of 60% was achieved during the first data taking period after a rise time of 45 minutes. During a shut-down period in 2001 HERA was upgraded to include other rotator magnets which provided a longitudinally polarised beam to the two collider experiments, in addition to the existing longitudinal beam at HERMES. This resulted in a decrease in the amount of time the beam is in the transverse as opposed to the longitudinally polarised state. Therefore, the rise time decreased slightly and the average polarisation was considerably lower at 35% and decreased still further in 2005 when the electron beam was used to 25%. The polarisation values increased during the data taking years 2006 and 2007 to 40%. Precise alignment of the machine quadrupoles and fine tuning of the orbit parameters are mandatory to achieve high polarisation. As this is difficult to control, continuous monitoring of the beam polarisation was required.

3.1 HERA Polarimeters

The polarisation of the electron/positron beam at HERMES was measured simultaneously by a transverse and a longitudinal polarimeter. The transverse polarimeter was isolated in the HERA West section and the longitudinal polarimeter was located in the HERA East section downstream of the HERMES experiment. Both of these polarimeters utilise the spin dependent cross section for Compton scattering of circularly polarised laser photons on polarised electrons.

3.1.1 The Transverse Polarimeter

Transverse beam polarisation leads to a small up-down spatial asymmetry of the back-scattered photons with respect to the orbital plane of the electrons for the two helicity states of the laser beam. The Transverse Polarimeter (TPOL) [52] used the interaction of circularly polarised photons on the y-polarised electron/positron beam, the transverse direction of the polarised beam. Back scattered photons were detected in the calorimeter. The polarisation of the incident photons was flipped at ∼83 Hz, creating an asymmetry in the y-distribution of the detected photons. This asymmetrical distribution is given by

$$\Delta y\left(E_\gamma\right) = \frac{1}{2}\left(\langle y\left(E_\gamma\right)\rangle^{+}\right) = \Delta S_3 \ \cdot P_y \cdot \Pi_y\left(E_y\right) \tag{3.3}$$

and is dependent upon the energy of the photons E_γ, the y polarisation (P_γ) of the electron/positron beam and the mean magnitude of the circular polarisation ΔS_3. The relationship to E_γ is given by a second function Π_y, the analysing power of the polarimeter. A measurement of the beam polarisation to an absolute statistical accuracy of less than 1% requires typically one minute, the fractional systematic uncertainty of the TPOL is 3.4%.

3.1.2 The Longitudinal Polarimeter

Longitudinal polarisation modifies the energy dependence of the cross section. The Longitudinal Polarimeter (LPOL) [53] uses circularly polarised photons, similarly to the TPOL. The longitudinal polarimeter measures an energy asymmetry by mea-

suring the energy deposition of the photons in the laser produced photons. The LPOL operated in multi photon mode measuring the total energy lost by around 1000 backscattered photons per laser pulse allowing the individual measurement of a particular pulse. It measures an asymmetry

$$A\left(\Delta S_3, P_Z\right) = \Delta S_3 \cdot P_Z \cdot \Pi \tag{3.4}$$

where the analysing power Π is a function which relates the longitudinal polarisation P_Z to the polar scattering angle of the photon detected in the calorimeter and ΔS_3 is again the mean magnitude of the circular polarisation of the incident photon. The fractional uncertainty of the LPOL is 1.6%.

3.2 The HERMES Gas Target

The unique part of the HERMES experimental set up was the polarised gas target [54]. The gas was stored in a custom designed storage cell which was filled with a number of target gases including hydrogen and deuterium as well as heavier gaseous targets like Xenon. For the purposes of the analysis presented in this thesis a hydrogen target was used, therefore the hydrogen gas target will be referred to as the target unless stated to the contrary.

HERMES was part of a storage ring and, therefore it was necessary that the HERMES target could be used without negatively impacting upon the other experiments H1 and ZEUS by degrading the beam significantly. The usage of a gas target instead of a liquid or a solid also removes impurities that would be present in these materials and, therefore, reduces the background signal from unpolarised nucleons in the target. The density could be altered during the operation of the experiment and was increased to allow high density data taking as the beam current decayed over the period of a fill, increasing the reaction rate. Throughout the 06/07 data taking period this technique was used to substantially increase the number of interactions.

3.2.1 Unpolarised Gas Feed System

There were two systems used to inject the gas into the target cell at HERMES. These were the Atomic Beam Source (ABS) [55] and the Unpolarised Gas Feed System (UGFS) [56], which were used to provide a polarised and unpolarised gas target respectively. The analysis presented in this thesis used a polarised and unpolarised hydrogen target.

The UGFS allowed the selection of the target gas type and density as required. Throughout the lifetime of the experiment unpolarised hydrogen, deuterium, nitrogen, neon, krypton and xenon were used. The density of the target was limited by the lifetime of the electron/positron beam, which under normal operating conditions was more than 10 hours. The total lifetime τ can be expressed as

$$\frac{1}{\tau} = \frac{1}{\tau_{HERMES}} + \frac{1}{\tau_{HERA}}. \tag{3.5}$$

During normal operation τ_{HERMES} had to be less than 45 hours, with a corresponding areal target density of 0.162×10^{15} nucleons/cm^2. At the time of injection the electron beam current was typically around 35 mA and this decreased during the data taking period, known as a "fill". After the beam current had fallen to 13 mA the density of the target was increased to 0.313×10^{16} nucleons/cm^2, allowing a period of high density data towards the end of a fill, resulting in a HERMES lifetime of 2 hours. A large quantity of high quality data was taken during this period due to the increase in luminosity and the decrease in the background contaminants. The DAQ system had a maximum trigger rate of 500 Hz as increasing the target density to achieve a higher frequency of data taking would have caused a reduction in the beam lifetime. Another consequence of increasing the target density would be an increase in the number of background Mϕller electrons that would have led to an increase of the DAQ dead time.

3.2.2 The Target Cell

The target cell was designed to allow the greatest number of interactions possible between the circulating electron/positron beam and the gas target [57]. The target atoms interacted with the side walls of the cell before escaping the cell through the

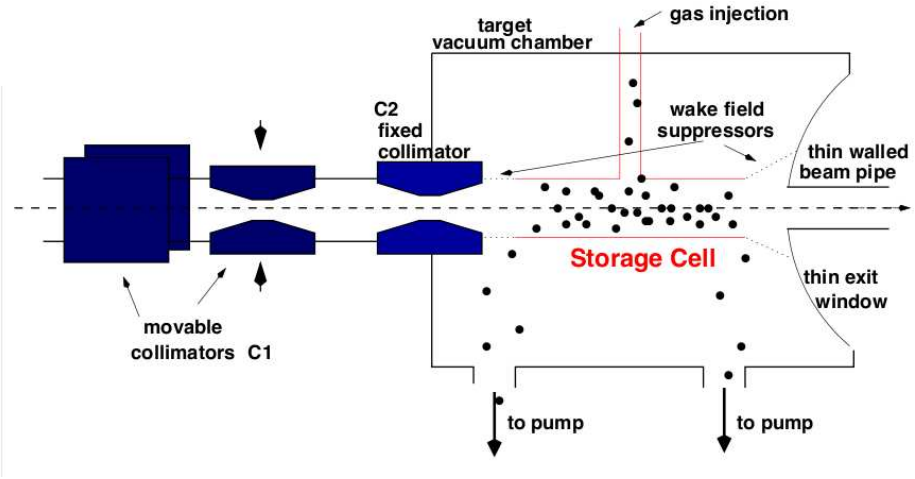

Figure 3.2: Diagram of the HERMES gas target storage cell [58]. The target gas is injected into the target cell. The target gas escapes through the ends of the cell before being removed by the pump system.

end points, thus increasing the chance of an interaction with the beam. The gas atoms were injected into the cell and eventually diffused into the storage ring where they were removed by a high powered pumping system, to ensure the high vacuum of the beam pipe was maintained.

The target cell was constructed using 75 μm thick aluminium of 99.5% purity. The walls were as thin as possible to reduce bremsstrahlung, multiple scattering and energy straggling of particles passing through them. The cell used for the longitudinally polarised target at HERMES from 1995-2002 was 400 mm in length, with an elliptical cross section to match the HERA electron beam shape, 29.0 mm wide and 9.8 mm high. For data taking with a transversely polarised beam between 2002 and 2005 these dimensions were reduced to 21.0 mm and 9.1 mm respectively to increase the target density. The final target cell used from 2006-2007 had the same width and height as the previous version but the length had to be reduced to 150 mm to accommodate the Recoil Detector.

A system of collimators in front of the target shielded the cell from synchrotron production from the electron/positron beam. The cell was connected to the beam pipe to minimise radio frequency excitations induced by the bunch structure of the beam at discontinuities of the beam pipe. Sharp steps in the beam line profile were

also minimised by the introduction of a metal mesh, mounted both upstream and downstream of the target providing a smooth transition from the elliptical cell cross section to the circular beam pipe.

3.3 The HERMES Spectrometer

The HERMES spectrometer [59] is shown in Fig 3.3. It was a forward spectrometer with a dipole magnet above and below the electron/positron and proton beam pipes, providing an integrated field of 1.5 T. The magnet was divided into two identical sections by a horizontal septum plate that shielded the electron/positron and proton beams from the spectrometer's magnetic field. The spectrometer was constructed as two identical halves mounted above and below the beam pipes. Scattered electrons/positrons and hadrons produced in the inelastic reactions were identified within an angular acceptance $\pm$ 170 mrad horizontally and 40 - 140 mrad vertically. The spectrometer provided Particle Identification (PID) and track reconstruction capability for particles from interactions of the electron/positron beam and the target.

For tracking in each spectrometer half several tracking chambers (microstrip-gas counters, multiwire proportional chambers and drift chambers) situated in front of, inside and behind the magnet were used. The scattered lepton of the physics process of interest must have been detected in both the front and rear regions of the spectrometer if it was to be used in the data to be analysed. The region before the magnet contained the Drift Vertex Chamber (DVC) and the Front Chambers (FCs), the region behind contained the Back Chambers (BCs). The Multi-Wire Proportional Chambers were inside the magnet.

3.3.1 Drift Chambers

The Drift Chambers were used to measure where a charged particle crossed a virtual plane [61]. For this purpose thin wires were fixed in a volume filled with gas in a way that the wires form cells.

Inside these cells a charged particle traversed the volume ionising the gas. Due

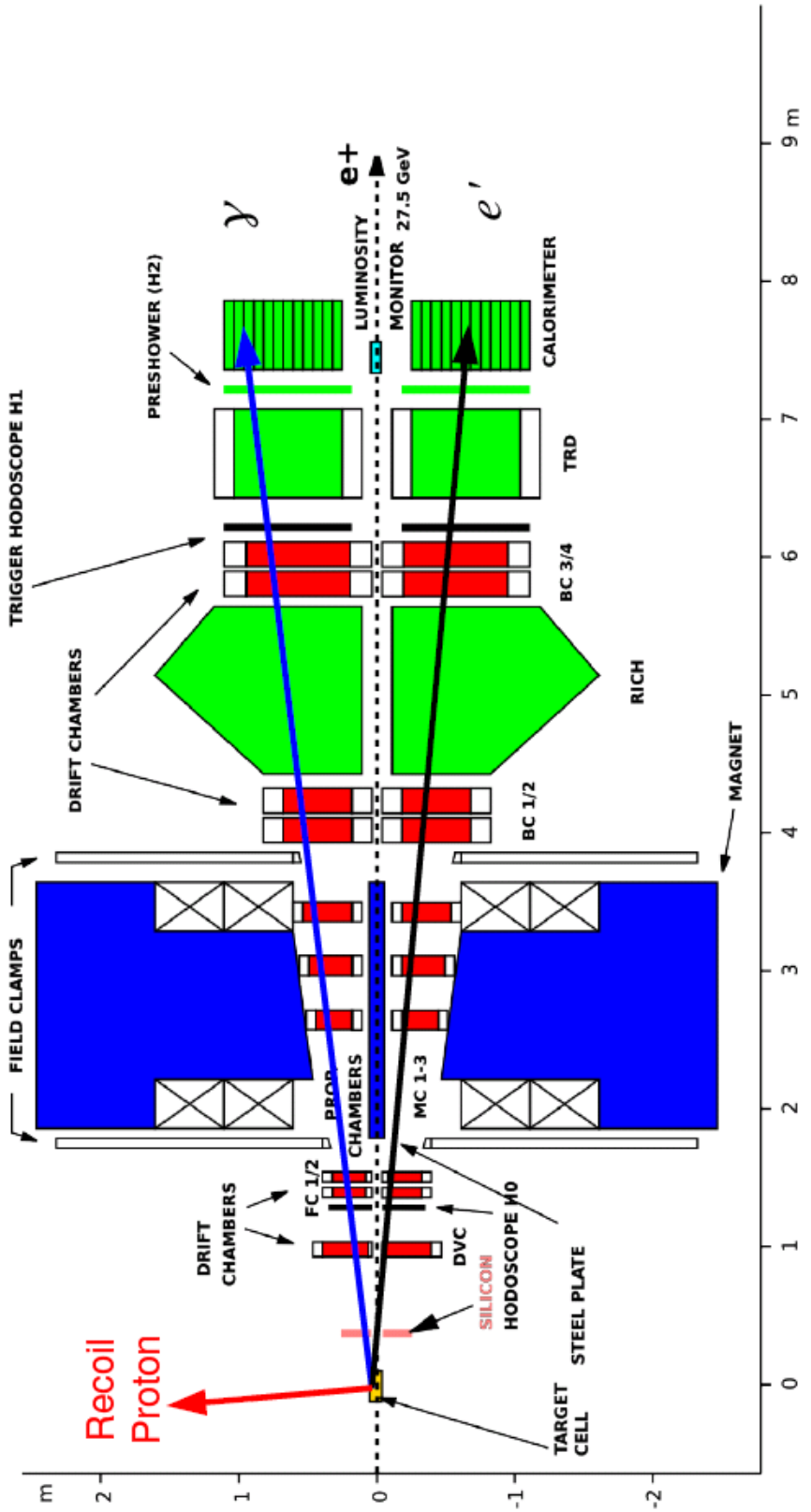

Figure 3.3: A schematic diagram of the HERMES spectrometer showing the products of the DVCS interaction as they pass through the experiment. The Magnets are shown in blue, the PID detectors in green and the tracking detectors in red. This is the spectrometer used for data taking until 2005, before the Recoil Detector was installed. Adapted from [60]

to the electrical potentials applied to the wires the electrons drifted to the sense wires, the connected electronics measured the charge of the signal when it arrived. The difference between this time and the time when the particle traversed the cell (measured by other detectors) was used to reconstruct the impact point of the particle in the chambers mid plane.

All drift chambers were operated with an Ar(90%)/CO_2 (5%)/CF_4 (5%) gas mixture which facilitated a high drift velocity and was non-flammable. The readout of the drift chambers was accomplished by Amplifier-Shaper-Discriminator (ASD) cards connected to FastBus Multihit Time to Digital Converters (TDC) with a time resolution of 0.5 ns. The spatial resolution per plane was in the order of 200 - 300 μm.

3.3.2 Multi-Wire Proportional Chambers

The HERMES Multi-Wire Proportional Chambers (MWPC) were constructed with alternating planes of high voltage wires and sense wires, which were at ground. All the wires were placed in a special gas environment. When a charged particle passed through the gas in the chamber, it ionised the gas molecules [62]. The freed electrons were accelerated towards the sense wire by the electric field, ionising more of the gas. In this way a cascade of charge, known as a Townsend Avalanche, developed and was deposited on the sense wires. The signal from the avalanche was read out using the LeCroy PCOS IV system. The drift chamber gas mixture was optimised for MWPC operation containing Ar(65%)/CO_2 (30%)/CF_4 (5%). The MCs provide a spatial resolution of about 700 μm.

3.4 Track Reconstruction

An efficient reconstruction code (HRC) using a tree-search algorithm [63] was employed to allow a determination of particle tracks from a given set of detector hits, which was possible due to the similar layout of each drift chamber. Afterwards each track was reconstructed under the assumption that front- and back- partial tracks had to form a continuous curve (forced-bridging). Every possible partial track was

reconstructed until a unique track is found that bridged the magnet gap. The DVCS analysis detailed later relies on tracks found in this manner, although HRC can provided measurements of partial tracks in the spectrometer. The momentum of a particle was then calculated from its deflection in the magnetic field, which also provided the particle charge, determined by HRC using a look up table. For electrons/positrons with momenta between 3.5 and 27 GeV/c, the average angular resolution is 0.6 - 0.3 mrad and the average momentum resolution $\Delta p/p$ was 0.7 - 1.3 % excluding bremsstrahlung tails. The resolution deteriorated when the gas threshold Cerenkov counter was replaced by a Ring Image Cerenkov Counter (RICH) which introduced more material into the particle's path. HRC was expanded as new detectors were added to the spectrometer over the lifetime of the experiment. Extensions to the reconstruction software are found in the external software package eXternal Tracking Code (XTC). A reconstruction algorithm for the Recoil Detector is investigated in Chapter 4.

In this chapter and throughout this thesis a number of references are made to the HERMES coordinate system shown in Fig 3.4. This is a right handed coordinate system in which the z-axis lies along the beam line of the experiment through the HERMES spectrometer. Also frequently refered to are the polar θ and azimuthal ϕ describing the angle between the y-z plane and the x-y plane respectively.

3.4.1 Photon Reconstruction

The above reconstruction method did not apply to uncharged particles, the paths of which were not bent by the spectrometer magnetic field. In this case photons were only detected by the calorimeter, and all information on these particles must come from this source. This caused the energy resolution of untracked particles to be poorer than that of tracked particles, and consequently in the analysis presented in this thesis, detailed in chapter 5, a missing mass assumption is made so that a minimal amount of information about the photon from the calorimeter is used.

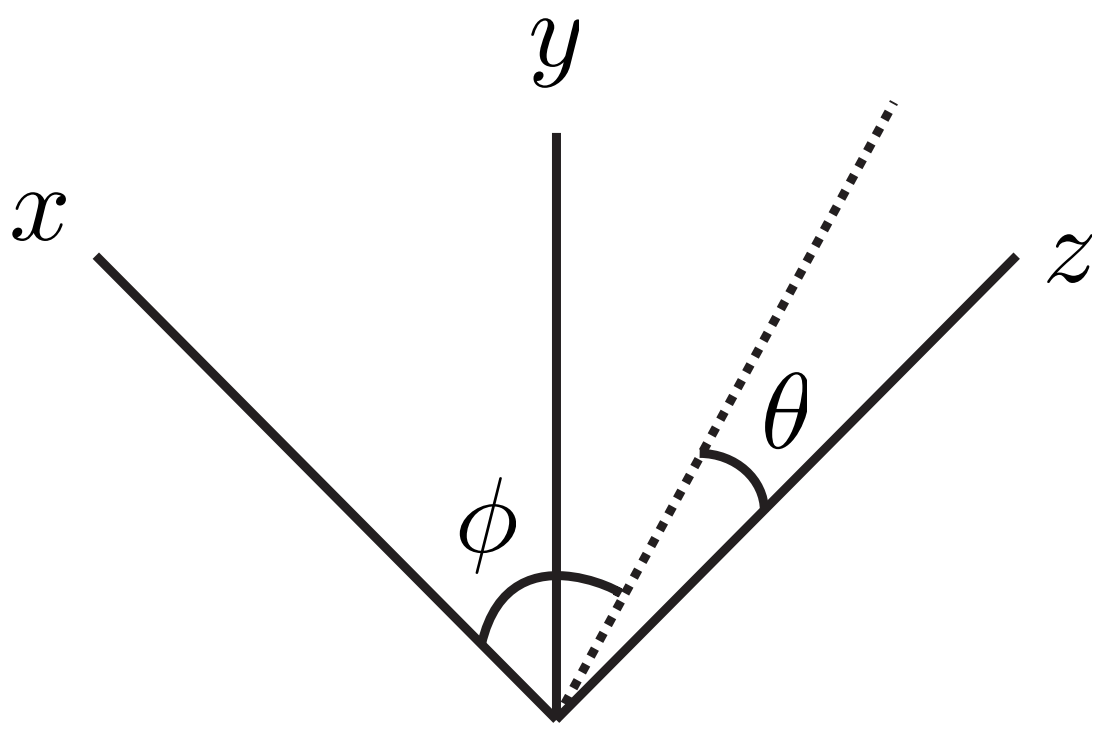

Figure 3.4: Illustration of the HERMES coordinate system [64]. The z axis is in the same direction as the beam line. The polar θ angle and azimuthal ϕ are defined in the y-z and x-y planes respectively.

3.4.2 Particle Identification Detectors

Particle Identification (PID) at HERMES was implemented using four detectors, a Transition Radiation Detector (TRD), a Pre Shower detector in front of the Calorimeter, the Calorimeter and a Cerenkov detector. The first HERMES data taken from 1995 to 1997 was taken using a Threshold Cherenkov detector, later replaced by a dual-radiator Ring Image Cerenkov counter (RICH) [65]. For the DVCS analysis presented in this thesis the Cerenkov detector was not used, therefore it will not be further detailed. PID at HERMES is performed using a likelihood technique that discriminates between leptons and hadrons with a hadron contamination of the sample in the order of 1 %.

3.4.3 Transition Radiation Detector

The Transition Radiation Detector consisted of 6 modules each containing a radiator with plastic fibres of about 20 μm diameter as radiator material and a Xe/CH_4 (90:10) filled proportional chamber with vertical wires separated by 1.27 cm. Both electrons/positrons and hadrons deposited energy in the detector due to the ionisation of the chamber gas, but only electrons/positrons produced transition radiation in the HERMES energy range. Combining the information from several modules and using the truncated mean method an average pion rejection factor greater than 1400 was obtained, for a lepton efficiency of about 90 %.

3.4.4 Calorimeter

The Electromagnetic Calorimeter [66] served many different functions in the HERMES experiment. As well as providing PID for hadrons and electrons/positrons, it provided energy measurements of photons for processes such as DVCS/BH, energy measurements of electro-produced π^0, η and other radiative decays and was used as part of the DIS event trigger. The calorimeter did not provide high energy measurements of photons, so for DVCS analysis steps are taken to avoid dependence on these measurements. The calorimeter also provided the only position measurement of the photon, which otherwise went through the detector untracked.

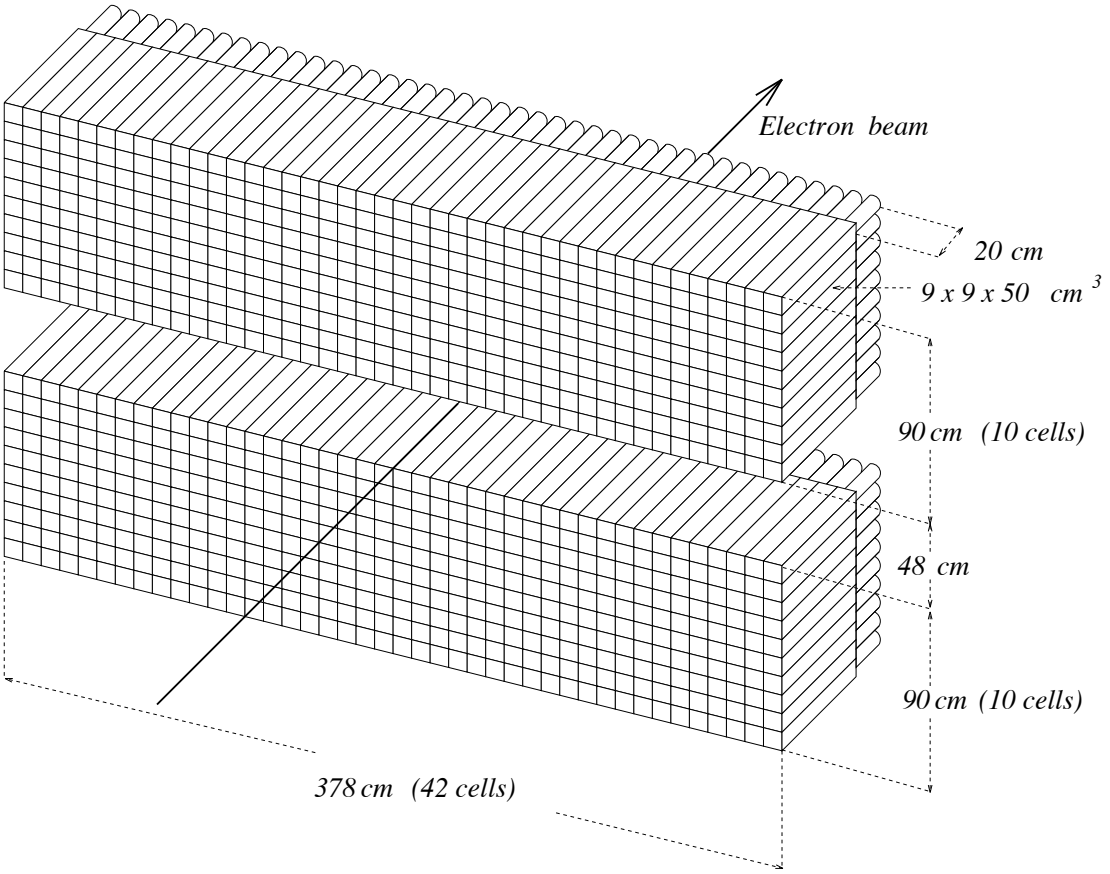

Figure 3.5: A diagram of the calorimeter [66]. A particle track passed through one of the calorimeter blocks, causing a shower in neighbouring blocks.

The calorimeter was constructed from radiation resistant F101 lead glass blocks with a front area of 9 x 9 cm^2, and a length of 50 cm (about 18 radiation lengths). These are stacked in two 42 x 10 arrays each above and below the beam as shown in Fig 3.5. As the electromagnetic showers of electrons or positrons passed through the detector they radiated Cerenkov light. As an incident particle emitted Cerenkov light it loses energy until the lepton deposits all its energy in the calorimeter block. By selecting calorimeter blocks of the correct length an electromagnetic shower can be contained inside the block. At HERMES energies this lead to a ratio of $E_{calo}/p \simeq 1$, where E_{calo} is the energy deposition in the calorimeter and p is the momentum of the electron/positron measured by the tracking detectors. Photomultiplier tubes (PMTs) were used to detect the Cerenkov light. Hadrons interacted differently with the calorimeter: energy was lost through ionising atomic collisions and nuclear interactions only. However, particles could still be produced through these collisions, including photons and neutral pions. These could create e^+e^- pairs, leading to an electromagnetic shower. The process of particle production from hadrons, known as a hadronic shower, did not begin immediately in the calorimeter and was also not contained within the length of the calorimeter. These properties, combined with the loss of neutrons and nuclear binding energy, lead to a ratio of $E_{calo}/p < 1$ for hadrons, allowing separation of hadrons and electrons/positrons for PID.

3.4.5 Hodoscopes

The scintillator hodoscopes H1 and H2 provided a fast signal that was combined with the calorimeter to form a trigger. Both counters were composed of 42 vertical scintillators with a width of 9.3 cm to match the size of the calorimeter. In addition H2, which had a passive radiator of two radiation wavelengths of lead in front of it and acted as a pre-shower counter, provided discrimination between electrons and hadrons. Hadrons did not produce an electromagnetic shower when passing through the lead layer, thus they produced an amount of light in the H2 hodoscope different to that of an incident lepton. Part of the light production distribution of the hadrons and lepton overlapped, shown in Fig 3.6, however, the calorimeter worked by a similar principle and had better separation in this area.

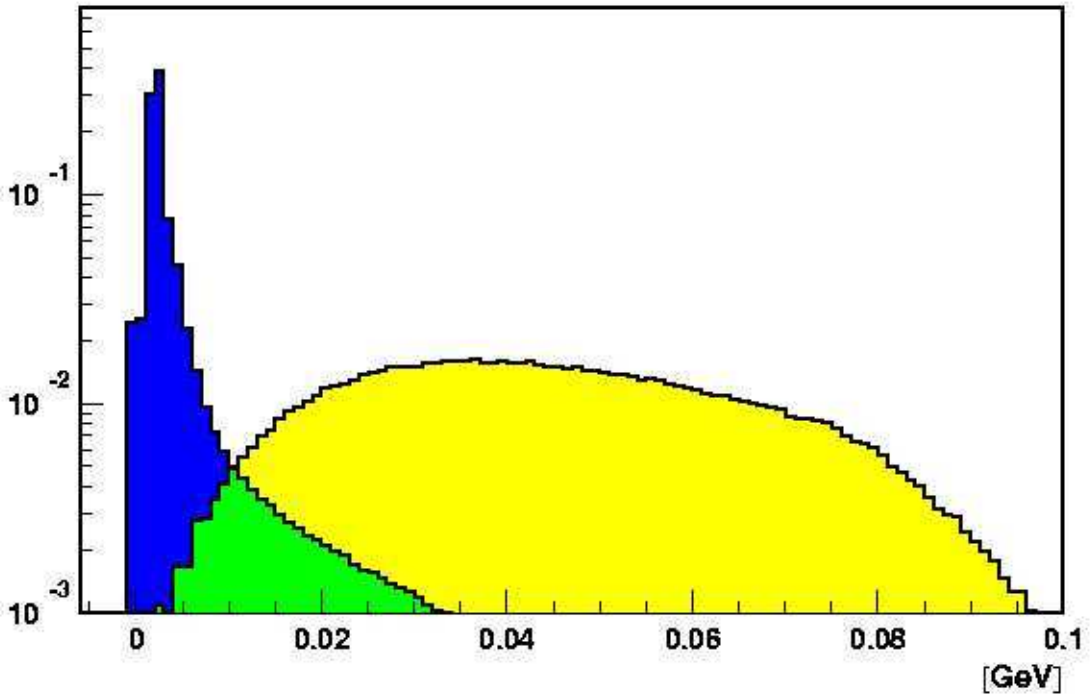

Figure 3.6: The distribution of the energy deposited in the preshower detector [58]. The hadron energy is shown in blue and the lepton in yellow. The overlap region is shown in green.

3.4.6 Luminosity Monitor

The luminosity of the experiment was measured by detecting elastic scattering of the beam leptons from electrons of target atoms [67]. The scattered and ejected electrons are detected on either side of the beamline, 7.2 m downstream of the centre of the target cell. The calorimeter consisted of $NaBi(WO_4)_2$ crystals with a very high radiation tolerance. Due to the proximity of the detector to the beam pipe it experienced a high radiation background. To suppress the detection of the background events, coincident signals above a threshold of 4.5 GeV were required for both detectors.

3.5 Recoil Detector

The HERMES Recoil Detector [21] was proposed as a final upgrade to the HERMES experiment in order to obtain a more precise measurement of DVCS asymmetries. This unique detector permitted the measurement of the recoiling target nucleon allowing for a truly exclusive measurement to be made for the first time at HERMES. The position of the Recoil Detector within the HERMES spectrometer is shown in Fig 3.7. For analysing events without using the Recoil Detector the proton was identified by calculating the missing mass of the desired interaction. For this reason, analyses that were dependent on the HERMES spectrometer only maintained exclusivity on the data sample by using a defined missing mass range. The main aim of the Recoil Detector is to improve this overall measurement by establishing exclusivity at the event level eliminating background events that were included using the missing mass technique.

Exclusive measurements will greatly improve and enhance the study of DVCS at HERMES in two ways. The design of the Recoil Detector allowed measurements of DVCS at low t, increasing the resolution of the experiment and allowing measurements of the t dependence of DVCS asymmetry amplitudes. The Recoil Detector also allowed for the separation of events where a Δ^+ resonance was produced instead of a proton. The Δ decays into a nucleon and a pion, emitted back to back in the rest frame of the Δ. These decay products will usually possess a transverse

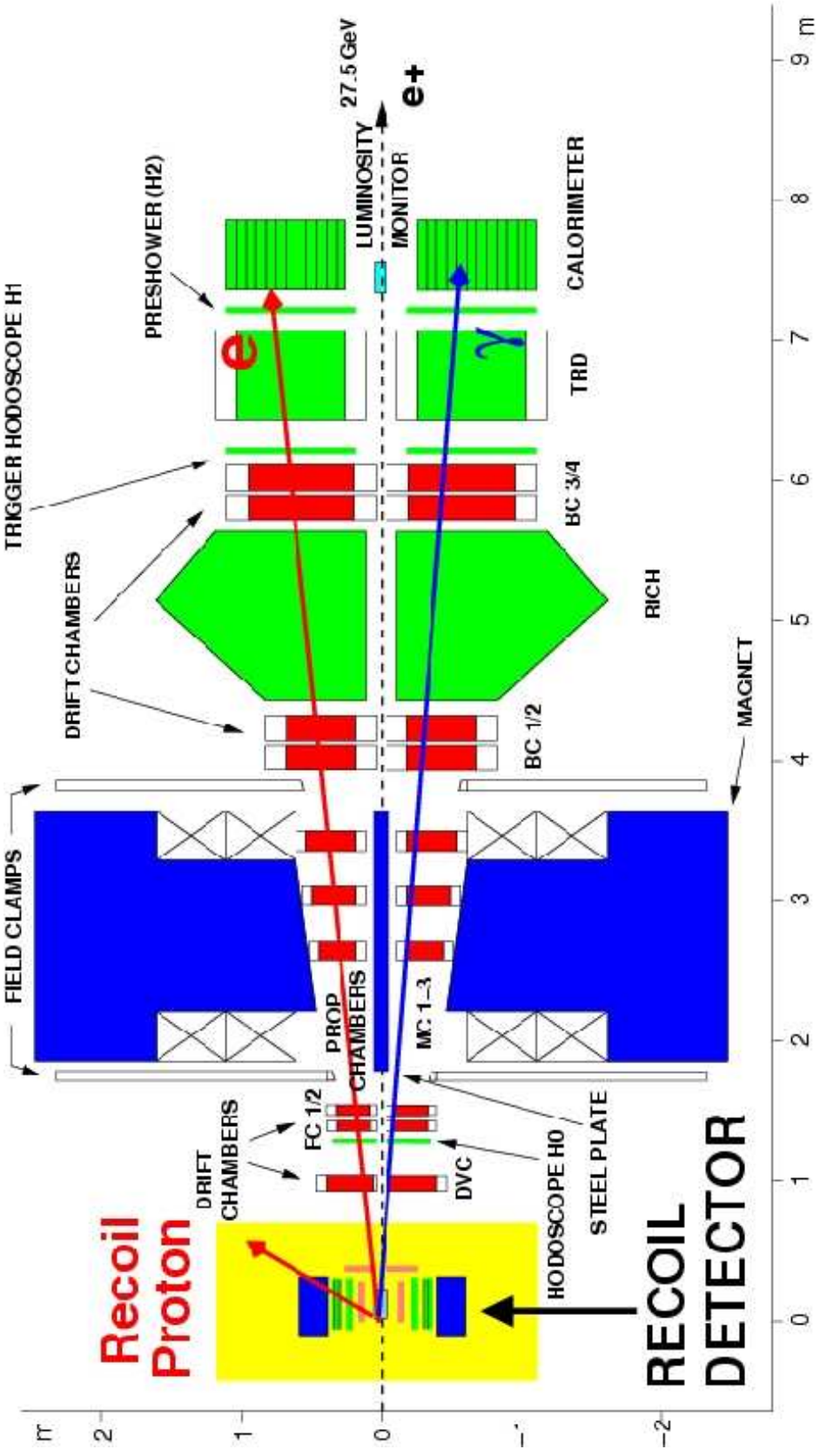

Figure 3.7: The HERMES spectrometer with the addition of the recoil detector around the target cell [21]. The electron and photon from a DVCS interaction are detected in the spectrometer. The proton from the interaction is now detectable with the recoil detector allowing an exclusive DVCS measurement to be made. This spectrometer was used for data taken at HERMES in 2006 and 2007.

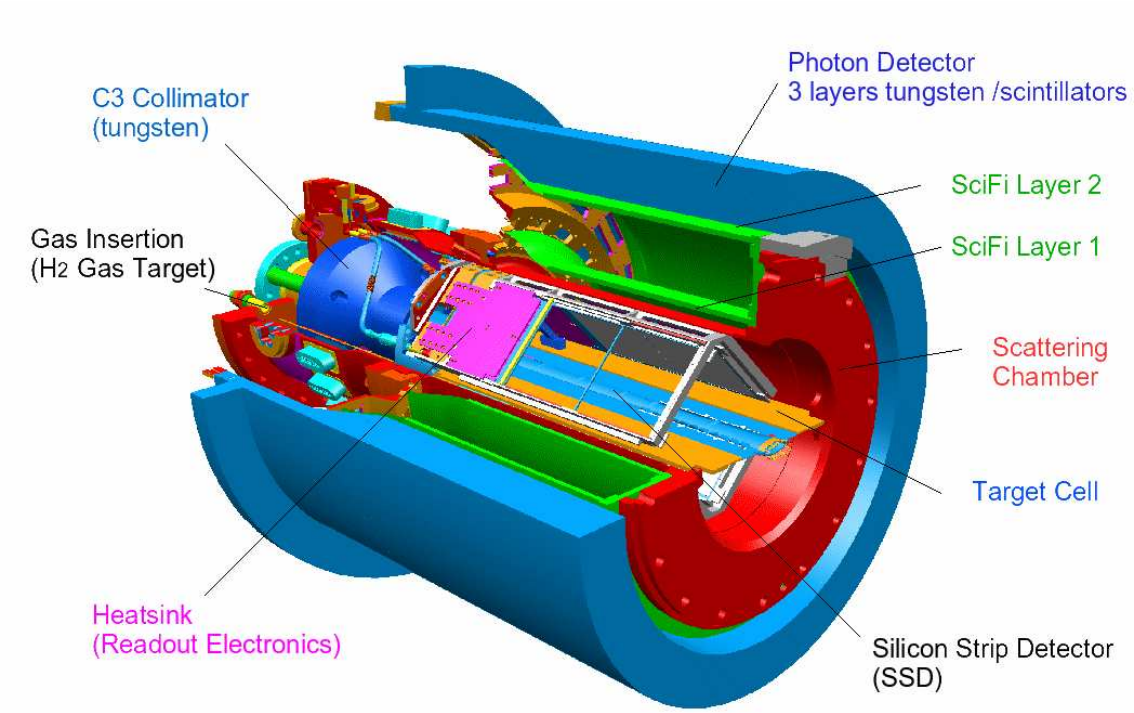

Figure 3.8: The HERMES recoil detector showing the target cell, silicon detector, scintillating fibre tracker and the photon detector, adapted from [68].

momentum component with respect to the momentum of the recoiling proton. This is a violation of the co-planarity with the reaction plane defined by the momentum and real photons.

The Recoil Detector was installed at the HERMES experiment during 2005 and is shown in Fig 3.8. The design of the detector allowed for it to be installed around the target cell. The HERMES experiment took data with the the Recoil Detector fully active during 2006 and 2007 [69]. A greater yield of DVCS events was measured during the recoil data taking years than for all the pre-recoil data taking years combined due to continuous running with an unpolarised target which has a greater density than the polarised target. The first data production including recoil information for data analysis was made available within the collaboration during 2009.

The HERMES Recoil Detector consisted of three active detectors; a Silicon Strip Detector (SSD) surrounding the target cell inside the beam vacuum, a Scintillating Fibre Tracker (SFT), in an inhomogeneous magnetic field of about 1 T, and a Photon Detector (PD) consisting of several scintillator layers [68]. The PD uses an extra layer of lead, the cryostat and the return yoke of the magnet as shower material.

The SSD provided momentum information for recoil particles with momenta below 0.45 GeV/c. As the SSD is located inside the beam vacuum it is possible to detect momenta as low as 0.135 GeV/c, corresponding to kinetic energies as low as 9 MeV. The SFT detector measured the momentum of recoil protons between 0.25 and 1.40 GeV/c. It also detected pions and provided particle identification (PID) for the separation of pions and protons. The photon detector was used to identify neutral pions by detecting photons produced in the $\pi^0 \rightarrow \gamma\gamma$ reaction. It also improved the particle identification in the Recoil Detector acceptance and provided the possibility of a cosmics trigger for alignment purposes. The exclusivity of a given event is established in the recoil detector through the positive identification of the recoil proton, the absence of additional pions and cuts utilising mainly the transverse-momentum balance that can be established due to the measurement of the recoiling proton momentum.

3.5.1 The Target Cell for Recoil Detector Operation

A new target cell was installed at the HERMES experiment as part of the Recoil Detector installation. This target cell differs from the older cell detailed in Fig 3.2. The cell walls were 75 μm thick and had a length of 150 mm, the same length as the SSD. The target cell was centred at +125 mm in the Z direction of the HERMES coordinate system, while the previous cell was centred at the 0 mm position in Z. The cell was elliptical in cross section, with a major (minor) axis of 21 (9) mm. With knowledge of the density of aluminium (2.17g/cm^3), the lowest kinetic energy of protons that could pass through the target cell walls was $\sim$ 3 MeV. During the recoil data taking period the target gas was unpolarised and was injected into the centre of the cell, after which it dissipated to the outer edges of the cell before being pumped away. As the target gas was unpolarised, it was no longer necessary to cool

the gas target with liquid helium to increase the density, therefore a new system that used water at 8^{o}C was developed. This cooling reduced mechanical stress caused by temperature gradients and in second order it kept the cell temperature as constant as possible in order to have a controllable target gas density.

3.5.2 Silicon Strip Detector

The SSD [70] was located inside the scattering chamber within the beam vacuum in order to detect low momentum recoiling protons that would otherwise be stopped within the chamber. Momentum determination for low momentum particles is performed using the energy deposition in the silicon layers can measure the momentum of recoiling protons in the range 135 - 400 MeV/c. This detector also provided two space points used to plot the direction of the tracked particle. It consisted of 16 double sided silicon sensors designed by Micron Semiconductors, with 128 strips per side and a strip width of 758 μm. The sensors measure 99 mm x 99 mm with a thickness of 300 μm and were arranged around the cell in a diamond shape configuration. Each of the four faces comprised of two layers and each contained two sensors. The design of the SSD with the kapton flex foils and electronics is shown in Fig 3.9.

The SSD was sensitive to small energy depositions from minimum ionising particles, which pass through the SSD, and large energy depositions from protons stopping in either silicon layer. To cover the large dynamic range of the expected signals each sensor strip was connected to a high and low gain readout channel. This allowed a clear readout of a large range of energy values.

3.5.3 Scintillating Fibre Tracker

The Scintillating Fibre Tracker (SFT), shown in Fig 3.10, was located outside the scattering chamber and detected charged pions and protons with momenta in the range of 0.3 to 1.4 GeV/c [71]. The SFT served two primary functions within the overall operation of the Recoil Detector: to reconstruct the momentum of the charged particle by bending in the magnetic field and to provide particle identification (PID) to discriminate between the particles by analysing the amount of

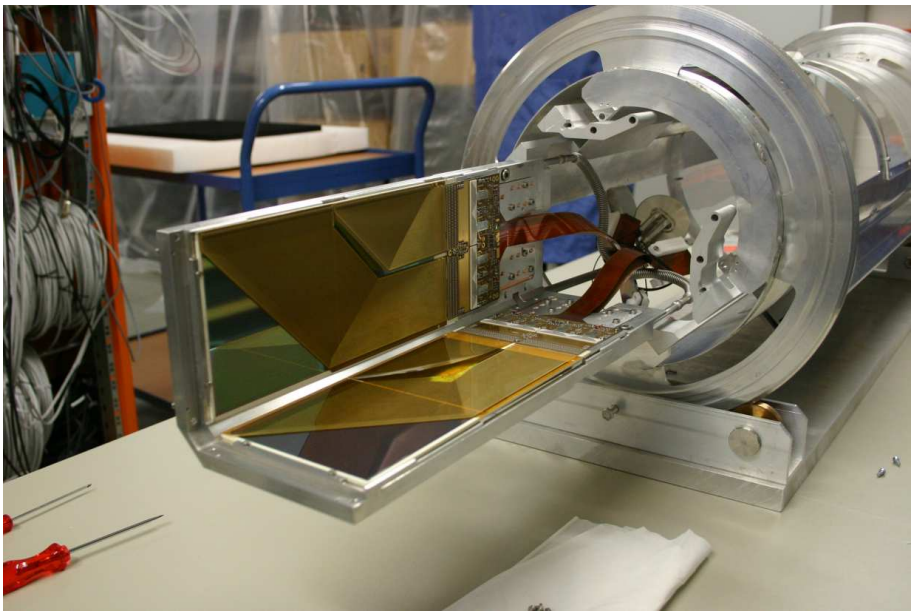

Figure 3.9: A picture of the silicon strip detector inserted into the vacuum pipe. Half of the silicon strip detector structure is shown inside the vacuum chamber. The flex foil readout electronics can be seen on top of the silicon material, as are the leads that connect to the readout system.

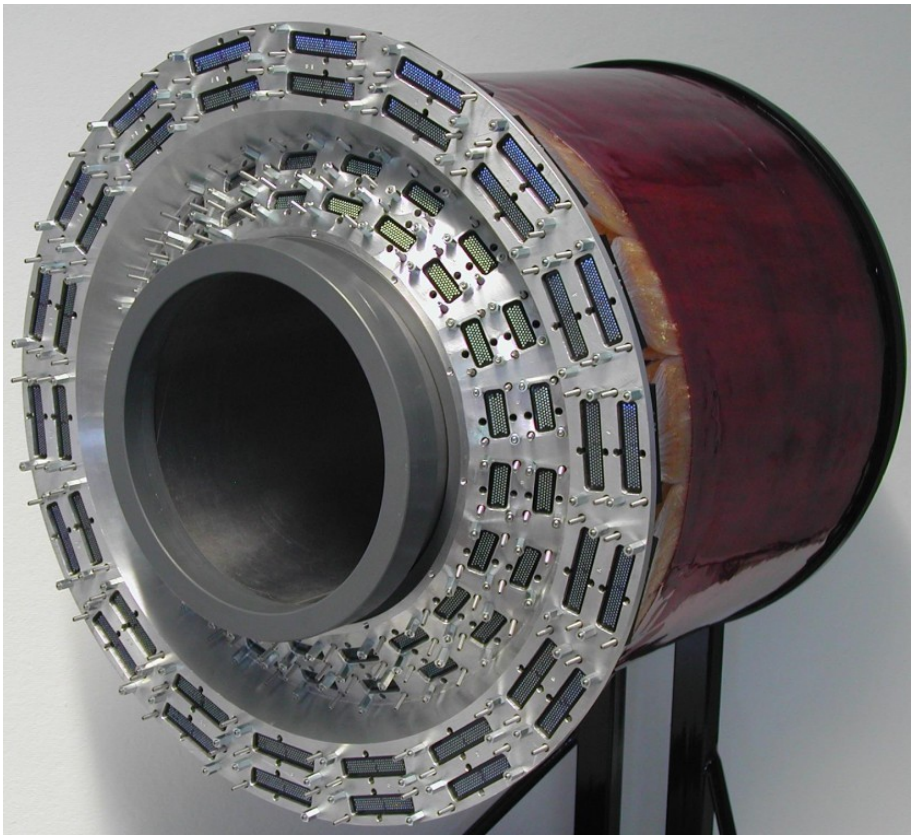

Figure 3.10: A picture of the scintillating fibre tracker detector barrels [71]. The output connections to the readout electronics are shown around the edge of the barrel

scintillation light produced.

The SFT consisted of two concentric barrels of scintillating fibres with an inner radius of 108 mm and 183 mm respectively and a thickness of 4 mm. Each barrel contained two sub-barrels, the inner sub barrel with four layers of fibres and outer sub barrels with two fibre layers. The inner sub-barrel was oriented parallel to the beam axis, the outer sub-barrel was inclined by 10^0 in a stereo configuration. This configuration allowed the determination of a space point of a particle track for each barrel. The track information from the SFT and the SSD were combined in such a manner that the path of a particle through the detector can be reconstructed via the space point information as shown in Fig 3.11. Fibre diameters of 0.5 mm were chosen for the inner and 1 m for the outer layers to ensure that the resolution of the

detector matches the smearing of the tracks by multiple scattering.

The azimuthal angle ϕ and the transverse momentum of a track was resolved from the two SFT barrels alone. This required the assumption that the track comes from a primary vertex at the beam position. Tracks from secondary vertices can only be reconstructed if an additional space point is provided by the SSD. The two stereo layers allowed the reconstruction of the vertex along the z-axis, track space, and the determination of the longitudinal component of momentum and the polar angle θ, the angle between the track and z-axis. The acceptance in θ ranged from 90 degrees down to the acceptance region of the Lambda Wheels installed behind the Recoil Detector. The small stereo angle of 10 degrees was chosen to minimise the track ambiguities.

The active length of the detector modules is 280 mm. The modules were glued together to form a self supporting fibre structure which on both ends is attached to a supporting ring. The downstream end of the fibre was polished and coated with a reflecting surface to minimise light losses. To further ensure that light losses are minimised the SFT barrels were sealed against the scattering chamber and the Photon Detector. At the upstream end the fibres were bundled over a length of 72 mm upstream of the active area in roads and bent into connectors which attach the scintillating fibres to clear light guide fibres. The scintillating fibres were read out by 64-channel multi-anode photomultiplier tubes (PMTs). The 4992 channels of the SFT were read out by 78 PMTs in total.

3.5.4 Photon Detector

The Photon Detector (PD), shown in 3.12, was designed to eliminate the background Δ^+ decays which could not be detected by the SFT and the SSD alone as DVCS events. The two decay channels of the Δ^+ are $\Delta^+ \longrightarrow p\pi^0$ and $\Delta^+ \longrightarrow n\pi^+$. The π^+ can be identified by the SFT and eliminated from the DVCS event sample but the π^0 is not and the detected photon can be identified wrongly as a DVCS candidate. The PD eliminated this source of contamination in the DVCS event sample by detecting the photons of the decay channel of the π^0 which can be of the form $\pi^0 \longrightarrow \gamma\gamma$ or $\pi^0 \longrightarrow \gamma e^+e^-$. In order to complete this task the PD was designed to surround the

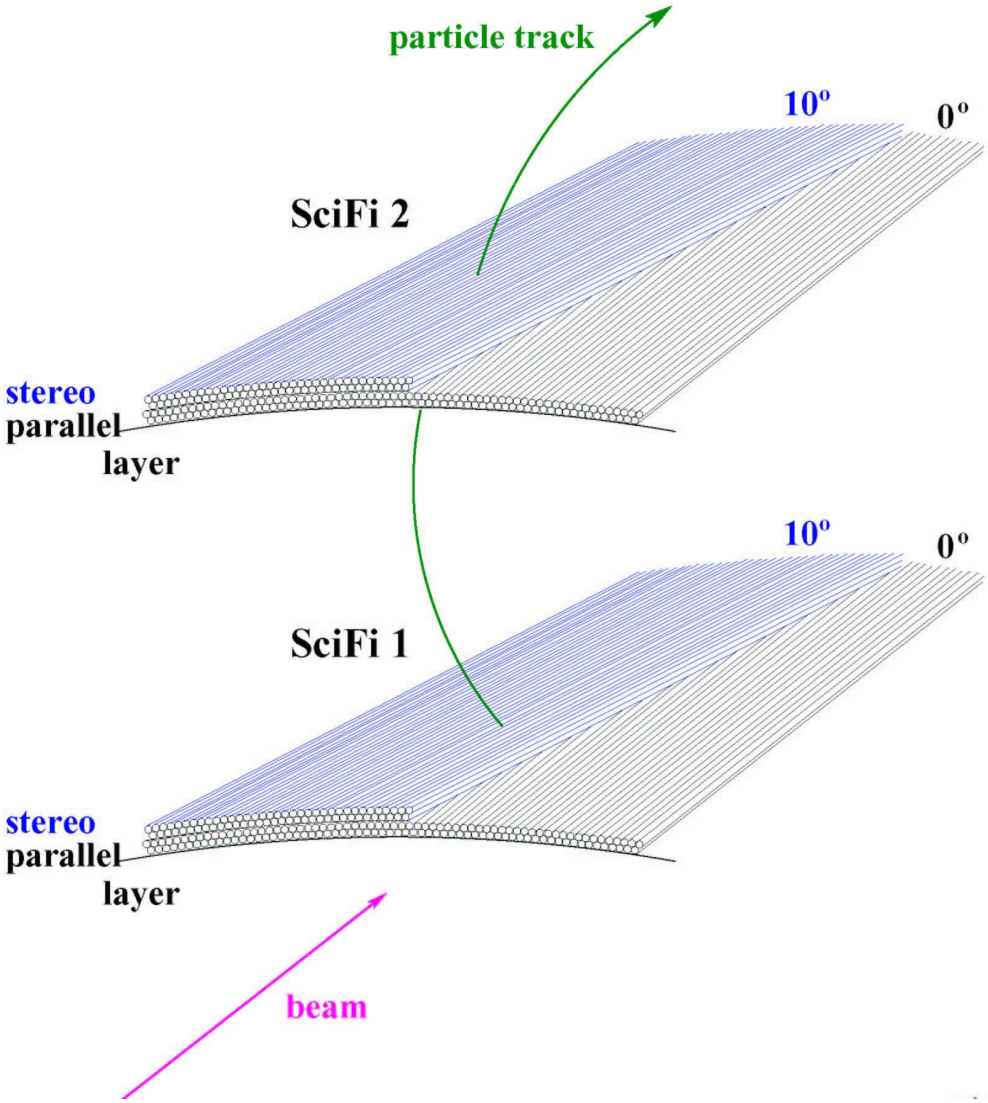

Figure 3.11: A particle track passing through both of the scintillating fibre barrels [71]. The two inner parallel layers and the two outer stereo layers are shown with respect to the HERMES beam. The outer stereo layers are at an angle of 10^0 to the parallel layers.

Figure 3.12: A picture of the photon detector [71]. The scintillating fibres are shown, as are the connection fibres to the readout electronics.

SFT and was located just behind the second SFT barrel and in front of the detector magnet. The PD was based on a segmented shower detector design. Three layers of tungsten were used as converters for the photons. These alternate with three layers of plastic scintillator used as active detector material. The first tungsten converter layer had a thickness of 6 mm corresponding to two radiation lengths whereas the other two layers of converter material corresponded to one radiation length. The scintillating layers were segmented to allow the reconstruction in the case of two detected photons. The innermost layer is oriented parallel to the beam axis and consisted of 60 scintillator strips of 2 cm width and 1 cm thickness. The two outer scintillating layers were inclined by $\pm$ 45^0 with respect to the beam axis thus enabling a coarse spatial resolution of the point of impact of an impinging particle. Each stereo layer consisted of 44 scintillator strips of the same cross section as the innermost layer. A π^0 decays into two photons. The neutral pion can, therefore, be rejected as a DVCS event if one or more of these photons is detected in the PD along with a proton. Each scintillator was read out via two wavelength shifting fibres, which were connected to multi-anode PMTs outside the magnetic field of the recoil magnet.

3.5.5 Superconducting Magnet

A super conducting magnet surrounded the detectors of the Recoil Detector assembly and was of solenoidal configuration. The magnet itself performed some key functions, firstly it provided a tracking method for particles in the SSD and SFT via deflection in the magnetic field and it removed Mϕller electrons by letting them spiral forward protecting the SSD from these background electrons. The magnet consisted of two superconducting Helmholtz coils immersed in liquid Helium bath. The magnetic field strength was 1 T with the homogeneity of the field greater than 20%. An iron yoke supported the magnet mechanically and attenuated the field on the outside to a strength of less than 0.002 T at a distance 2 m from the bore.

Chapter 4

Track Reconstruction Using the Silicon Strip Detector

The Recoil Detector was installed at HERMES during the HERA shut down period of 2005. The detector was primarily designed to provide information on recoiling target protons from the DVCS/BH interaction, see Chapter 2. The three principle main detectors that comprise the Recoil Detector, the Silicon Strip Detector (SSD), the Scintillating Fibre Tracker (SFT) and the Photon Detector (PD), and their functionality are outlined in the previous chapter. In order to obtain useful information from the Recoil Detector a number of software packages were developed that processed the readout of the individual detectors in order that the properties of the recoiling proton can be determined. The software packages for the new detector had to be integrated with the existing software so that information from both the spectrometer and the Recoil Detector could be used to identify the resultant particles of an observed physics event in the most efficient manner. The development of the software packages began before installation of the Recoil Detector using Monte Carlo simulations of the detector as test data. These simulations were used to test the performance of the detector and predict the resolutions that would be achievable with experimental data. Software development continued at HERMES in tandem with construction of the detector and continued after data taking ended in July 2007.

The principle aim of the software developed for the Recoil Detector was to recon-

struct particles. The particle type, momentum and direction of each recoil particle are determined using the track reconstruction software. The particle momentum allows the energy of the particle to be calculated and this can be used with the energy conservation of the reaction process to reject DVCS/BH events if the reconstructed proton energy breaks energy conservation. Identification of pions and photons in the Recoil Detector allowed pion events to be rejected as contaminants of the DVCS/BH event sample.

A number of different methods for tracking in the Recoil Detector were developed separately. This practice used at HERMES, and indeed at many collaborations, allowed a number of different approaches to be analysed for their efficiency and accuracy. The final track reconstruction software contains the optimum algorithms from each of these different tracking methods in order to reconstruct the complete particle track through all the individual detectors and over the entire momentum range of recoil particles. The work presented in this thesis details the method developed for tracking particles using the SSD only, without using the information from the SFT or PD. The development of this tracking method is crucial for low energy protons which deposit large amounts of energy in the SSD, many of which are stopped completely and therefore do not reach the SFT.

4.1 HERMES Reconstruction software

The HERMES Reconstruction software [72] translates signals from the various detectors at HERMES into meaningful information. A Monte Carlo simulation of the experiment was also developed in order to predict detector response to physical events. The software has been developed over the entire lifetime of HERMES and has been expanded to include the Recoil Detector and Lambda Wheels.

4.1.1 ADAMO Database Structure

The HERMES software suite was written using the ADAMO database concept developed at CERN [73]. ADAMO allowed the data to be stored and managed effectively. The structure of an ADAMO database is defined in a language called Data Definition

Language (DDL). The structural definitions, objects, attributes and their relationships for any given database are contained in the DDL file. An extension package was written for the HERMES software called Distributed ADAMO Database (DAD) [74]. This allowed the server and client programs to exchange information in the ADAMO table format, thus allowing the collaboration to use the software in online machines both in the HERMES experimental hall, the DESY site and at satellite institutions around the world. The client-server model is used frequently at HERMES in which a large central computer holds a database centrally and can be accessed remotely by low-level client programs, providing updated and new information to the database.

4.1.2 DAQ and Slow Control

The Data AcQuisition (DAQ) software processes the direct output of the individual detectors of the HERMES experiment. The DAQ is based around an event builder. The program responds to a trigger, see Section 5.2.1, in which the electronic readout of the detector modules produces a signal, indicating that an "interesting" event has been registered in the experimental set-up. The readout signals from the individual modules are combined to produce an event from the raw information. The event information is stored in two separate locations: the tape which is located in the East Hall and the tape robot located at the DESY main site.

The event data as well as other important information is stored in the DAQ database. A number of measurements, known as scaler events, are recorded once during every ten second period of data taking at HERMES. This ten second time period is defined at HERMES as a "burst". An important example of these scaler quantities is the LUMI monitor, recording Bhabba and Mϕller scattering events. The luminosity monitor counts the number of these events in a burst and is then reset. A second prominent example of a scaler event is the DAQ trigger dead time. One set of scalers counts the generated triggers and another set counts the accepted number of triggers. The DAQ has to build events at the rate generated by the triggers, which can as high as 500 Hz. As the DAQ cannot always keep up with the rate of data production due to the processing limits of the hardware, some events are not recorded. The dead time, the ratio of generated and accepted trigger scalers,

can be corrected for and is used as a restriction on the data sample.

The data stream generated by the DAQ is finally organised into "runs". A run is simply a convenient way in which to store one file of data. The DAQ stores 560 MB of data before ending the run and beginning a new one. The HERMES data stream is analysed on the event, run and burst level. During the analysis process restrictions on the data sample are applied on each of these three levels to remove undesired events. The DAQ is one of the few parts of the HERMES software that does not work with the ADAMO format, the output of the DAQ is in the EPIO format.

"Slow control" refers to information from the experimental hardware which only needs to be recorded every few minutes. Factors such as pressure gauge measurements, high voltage settings and measurements of the photomultiplier tube gains by the Gain Monitoring System do not change within the short time scale of the DAQ and, therefore, it was unnecessary to record this information at such a high frequency. The slow control consists of a suite of many programs, interconnected via the client-server model, that read, write and display information about the status of the hardware. The most important of these is the taping client to which the client programs of each individual device feed into. The taping client records the information from each client program in the form of ADAMO tables. One file is created for each fill at HERMES, while information can also be recorded for when there is no beam.

The DAQ and the slow control have different timings recorded by two different clocks. The information from both of these timings had to be synchronised. This is important so that the correct information from both the slow control and the DAQ is analysed together.

4.1.3 HDC, HRC and XTC

The EPIO files are processed using the main software production chain outlined in Fig 4.1. The main software production chain consists of two programs, HDC and HRC. XTC was introduced as additional software to the main production and allowed the detector information from the Recoil Detector and the Lambda Wheels

to be analysed. HDC, HERMES Decoder, decodes the online information and applies detector calibrations. HRC, HERMES Reconstruction Code reconstructs all the wire chamber hits into particle tracks and associates information from the PID detectors with each track. Finally the data is run through ACE, which computes the wire chamber efficiencies. Each stage is discussed in more detail in the following.

HDC [63] processes the raw hit information into DAD files. The HDC achieves this in three important steps. HDC first maps each detector and relates each hardware channel to a software channel, allowing each physical piece of hardware in the electronics trailer to be identified. The next step is calibration: this relates detector signals to physical quantities such as deposited energy. Finally HDC implements the geometry file in order to determine the location of each detector signal in the HERMES coordinate system. The output of the HDC process, the HDC files, are a series of ADAMO tables containing the calibrated response of each detector.

The HERMES detector consisted of front and back sections that were separated by the spectrometer magnet, the field of which caused the charged tracks to bend. HRC reconstructed partial tracks in the front and back sections of the detector separately, due to the absence of the magnetic field in these sections the tracks were straight. The track was reconstructed by projecting both partial tracks back towards the centre. If these tracks matched a full track was recorded and the momentum and charge of this track calculated. Low energy particles, in which the particle bends in the magnetic field such that it does not reach the back section of the detector, were also tracked. In this case the momentum was determined by the bending radius in the magnetic field. HRC takes almost all of its input information from HDC with one notable exception: the alignment file. The alignment file is a precise location of each wire chamber in real space, accurate to $< 0.01\,\text{cm}$. The alignment file was generated using alignment runs taken every year or after installation or reinstallation of detector components. HRC also provided PID information, however, the PID calculations have been superseded by those in the μDST writer. HRC also performs calculations for the calorimeter. A particle that came into contact with the heavy lead doped glass of the calorimeter began a shower, resulting in a cascade of particles. The shower could spread from one calorimeter block to its

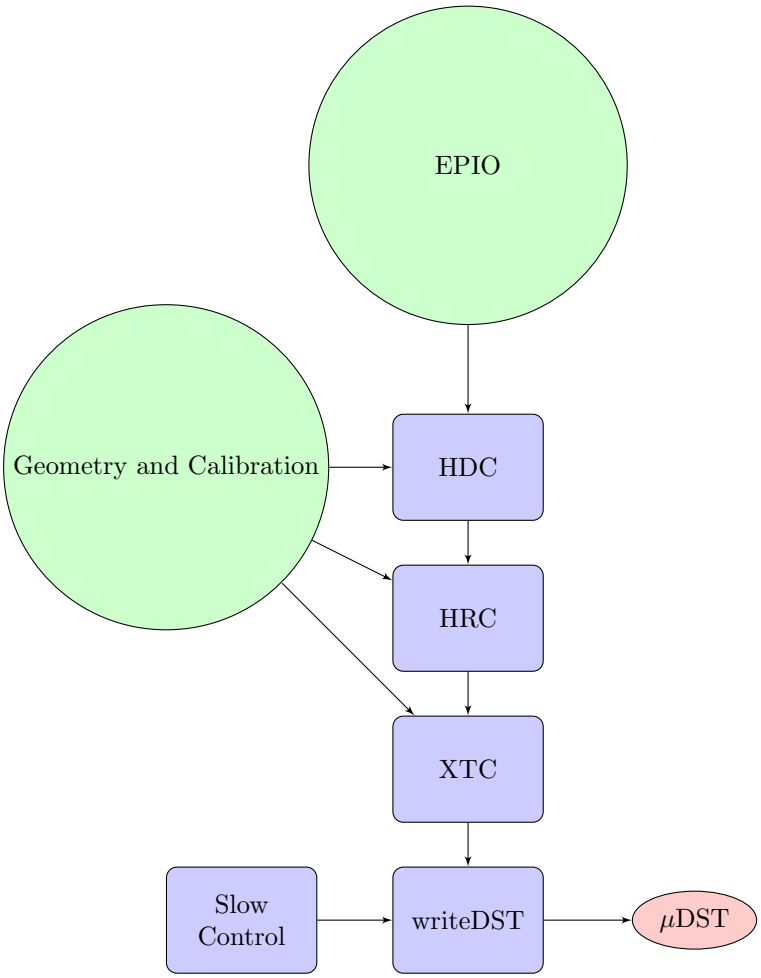

Figure 4.1: An overview of the main software production chain at HERMES. The raw output from the DAQ is processed during the main production using the HDC, HRC and XTC programs. The software relates the raw information to the physical detector using the geometry and calibration files. The output ADAMO tables are created using the output of the detectors and information about the state of the experimental hardware. The final output is a DAD file known as a μDST table which holds all the particle information obtained from the experiment and can be directly analysed.

neighbours. HRC used a clustering algorithm to reconstruct a single calorimeter hit, determining the centre of the hit and the total energy deposited from the 3 × 3 block segments. The output of HRC files is a series of ADAMO tables containing information arranged by particle track.

XTC, eXternal Tracking Code [75], provides reconstruction routines for upgrades to the main spectrometer eg. reconstructing tracks in the Lambda Wheels and the Recoil Detector which are outside the standard HERMES spectrometer acceptance. The Lambda Wheels and the Recoil Detector are treated independently in XTC and are written to separate ADAMO tables. There are a number of different methods within XTC for tracking recoil protons that traverse the different detectors of the Recoil Detector. Each of these methods was constructed as individual routines to ensure that the optimum tracking method can be constructed using all or parts of each individual tracking algorithm. The overall structure of XTC is outlined in Fig 4.2. The tracking methods for the recoil detector are listed and described briefly in Table 4.1.

The Recoil Detector was designed to detect protons and pions with momenta typically less than 1 GeV/c. The momentum of a particle is calculated from the curvature of the particle in the magnetic field of the detector and the energy loss of the particle in the SSD and SFT. The path of a particle can be reconstructed using the spacepoint information, i.e. the coordinate in three-dimensional space where the particle comes into contact with the detector material. The particles detected by the Recoil Detector lose energy as they pass through subsequent materials and therefore the bending in the magnetic field is not a perfect circle. This is taken into account in method 7. The magnetic field used in tracking method 7 is assumed to be homogeneous, when in reality it is not. The inhomogeneity of the magnetic field is taken into account in method 1 which improved the calculation of the particle momentum. As the track reconstruction software was further developed additional refinements were found to negate the necessity of using the inhomogeneous magnetic field map. The final version of this software, "common" tracking, uses subroutines from a number of the different methods and assumes a homogeneous magnetic field. The lookup table and passive material corrections presented in this thesis are in-

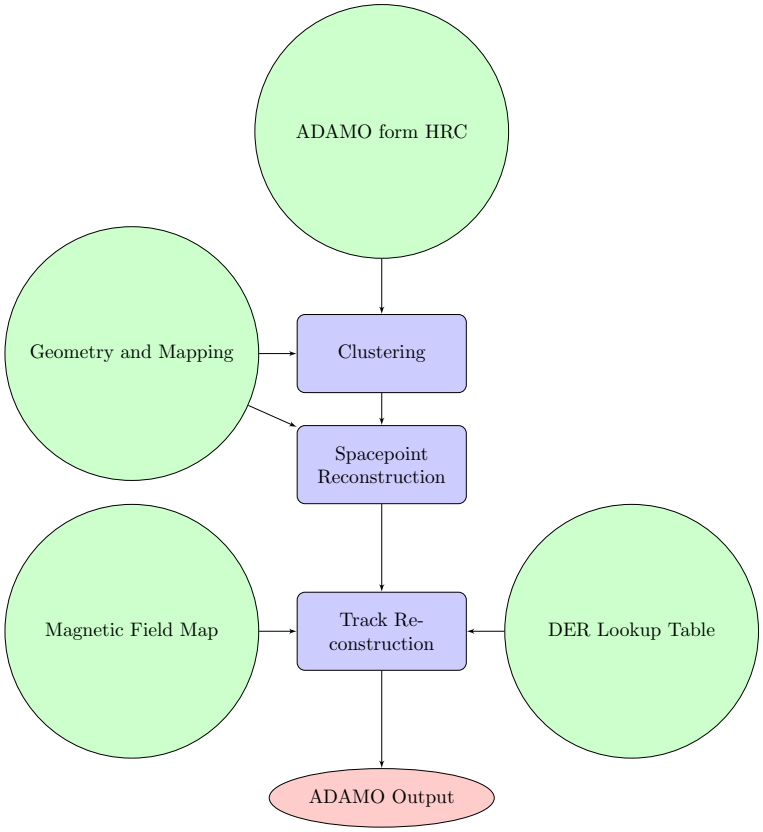

Figure 4.2: An overview of the XTC software package with respect to the Recoil Detector. The ADAMO output from HRC is further processed to include the clustering information from the Recoil Detector. The spacepoint information is taken from the hit in each individual detector and is used to reconstruct the "recoil particle" track. This uses the Recoil Detector geometry, the magnetic field map and a "lookup" table for the SSD.

Method	Description
1	Tracking using spacepoints from the SSD and SFT. Each possible combination of 2, 3 and 4 spacepoints tracks considered. Uses inhomogeneous magnetic field.
2	Full Tracking using clusters in the SSD and SFT.
3	SFT only tracking using two spacepoints and inhomogeneous magnetic field.
7	Tracking using spacepoints from the SSD and SFT. Each possible combination of 4 spacepoints tracks considered. Track fit approach including beam position.
15	Tracking using energy loss and spacepoint in SSD only.
16	Used for protons stopped in SSD, summing energy losses. Included in method 15.
701	Hybrid of the methods 1 and 7.
Common	Utilising subroutines from methods 1, 7, 2 and 15.

Table 4.1: Table summarising the individual tracking methods developed for tracking particles in the Recoil Detector at HERMES. Particle momentum is calculated from the curvature in the magnetic field of the recoil magnet and from energy loss in the individual detectors.

cluded in common tracking. The track is not identified as being of a particular particle type during the reconstruction phase therefore a number of different particle hypotheses are reconstructed, ie. supposing the particle was a pion, kaon, proton or deuteron. There is also an additional hypothesis reconstructed for the "stopped" proton and deuteron, where these particles do not reach the SFT. The pion hypothesis is given for a three space point track in which the momentum is determined by deflection in the magnetic field for both positive and negative charges, the proton hypothesis is given in the positive case. PID methods are applied during the analysis stage to select the correct hypothesis for a given track and disregard the others.

4.1.4 Monte Carlo Production

The Monte Carlo production is a simulation of the perfect experimental detector setup and uses a model of the detector assembly to simulate detector responses to generated physics processes. Simulating the detector in such a manner allowed the design of the detector to be tested before it was constructed. Before construction of the Recoil Detector began the detector components were simulated and tested to find the optimum design for the available space within the existing HERMES spectrometer. Monte Carlo is used at the next stage to track the "recoil particles" through the detector and compare the simulated response in each detector for a particle of known type and momentum with the actual response in the Recoil Detector. Using comparisons of both these sets of information tracking methods and particle identification methods were developed. This method is used to design the look up tables for the SSD only tracking detailed in Section 4.4. Background corrections can also be made at this point in which unwanted events and processes are removed or accounted for. The Monte Carlo also serves a major purpose during the analysis processes as it allows physics processes to be simulated and provides a necessary cross-check of the results. Monte Carlo data is generated using two programs; GMC and HMC. The procedure is summarised in Fig 4.3.

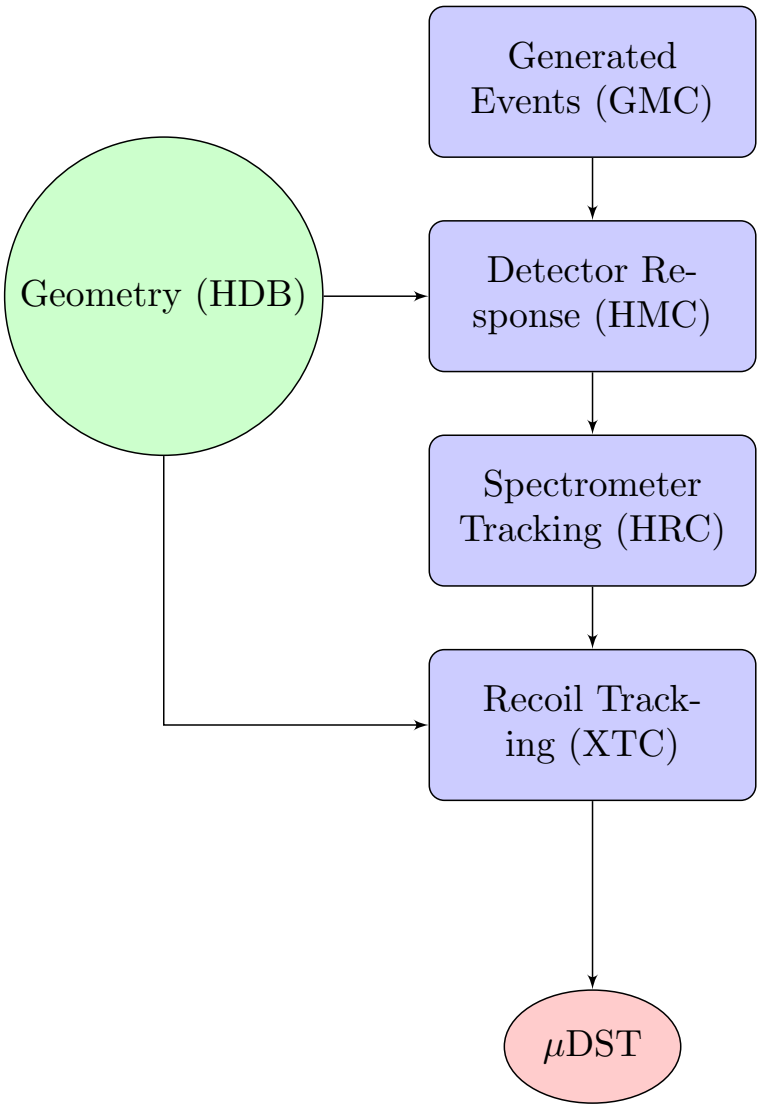

Figure 4.3: An overview of the Monte Carlo μDST production at HERMES. The GMC package simulates the physics processes that take place at HERMES before HMC simulates the detector response. The HRC and XTC tracking packages are applied similarly to both Monte Carlo and Experimental Data.

GMC

Generated Monte Carlo (GMC) consists of a number of different Monte Carlo generators developed to simulate the physics processes that take place in the HERMES experiment, combined into a common user interface. GMC differs to its equivalent for experimental data in that one event per record can have numerous different tracks. The events reconstructed GMC were direct simulations of physical process and not from a simulation of the HERMES spectrometer, this is simulated in HMC. By simulating the physical event the decay processes could of the experimentally recorded event could be studied, therefore, GMC provided more information about each event than HRC. Tracks in GMC are related to each other by parent links so the entire event process can be linked.

HMC

HMC (HERMES Monte Carlo) is the detector simulation package. HMC takes the output of GMC and simulates the response of the physics process in each part of the detector, based on a geometry file that contains information on each part of the hardware. The interaction of a particle to a particular material through processes such as ionisation, multiple scattering, energy loss, bremsstrahlung and hadronic interactions are modelled using GEANT3, a simulation package developed at CERN. HMC models the sensitive and passive parts of each individual detector in the HERMES experiment. In a sensitive material the physical charge induced by an interacting particle is translated into a detector output. In passive material the physical response of an interacting particle is not recorded or accounted for. A "hit", an interaction of a particle with one of the detectors, is recorded in the sensitive parts of the detector with additional information such as energy loss and hit position. The hits are processed into information describing the detector response of the incident particle. Based on the amount of energy deposited in each detector, calculations are performed to simulate the actual (calibrated) signal the detector would have produced. The output at this stage resembles that of HDC and the HDC tables are filled by HMC as well as additional information detailing particle types. HRC can be used to reconstruct the simulated data produced by GMC/HMC. For the

purposes of track reconstruction the physics process information is not necessary, therefore a separate event generator called BACK was developed which randomly passes particles of a known type through the detector without the use of GMC. The track reconstruction using the SSD is based on a lookup table created using the BACK generator.

4.2 Silicon Strip Detector

Semiconductor detectors are now used widely in particle physics and several have been installed in high energy particle experiments around the world [76,77,78]. They have many important applications and functions within larger scale experiments such as high resolution vertex and tracking detectors and as photon detectors in scintillation calorimeters. The semiconductor material most commonly used for detector purposes is silicon or germanium. Silicon is predominantly used for p-n junction detectors as it has a larger band gap than germanium. Integrated circuit technology allows the formation of high density micron-scale electronics on larger silicon wafers. Due to this high density only a small thickness of material, typically around 100-300 μm, is required for ionisation processes to occur and signals to be observed. Semiconductor detectors have the advantage that they feature high spatial and energy resolution, making them ideal for use in the HERMES experiment for tracking protons.

A p-n junction is created in a semiconductor material by doping it with impurities, either n-type or p-type. The n-type material is created with pentavalent impurities giving positive ions which produce donor levels immediately below the conduction band. For p-type materials trivalent impurities are added giving an excess of negative ions which have accepted electrons from the conduction band. These acceptors produce a general surplus of positive carriers. At a junction between p and n-type material electrons cancel the positive holes leaving a depletion layer in which there are no charges. Silicon detectors operate in reverse bias forming a depletion layer without charge carriers. This creates an electric field that sweeps charge carriers liberated by the interacting particle to the electrodes. Detectors are

typically asymmetric in structure, a highly doped p electrode, denoted p^+, and a lightly doped n region, such that the depletion layer extends predominantly into the lightly doped volume. The n-type material is the active material in the p^+n junction and allows the creation of electron/positron pairs while the p side is used only to deplete free charge carriers. The thickness of the depleted region is

$$W = \sqrt{2\epsilon(V + V_{bi})/Ne\sqrt{2\rho\mu\epsilon(V + V_{bi})}} \tag{4.1}$$

where V is the external bias voltage, V_{bi} is "the built in" voltage, N is the doping concentration, e is the electronic charge, ϵ is the dielectric constant = 11.9, $\epsilon_0 \approx 1\,\mathrm{pF/cm}$, ρ is the resistivity (typically 1-10 $\mathrm{k\Omega\,cm}$) and μ is the charge carrier mobility, $1350\,\mathrm{cm^2\,V^{-1}\,s^{-1}}$ for electrons and $450\,\mathrm{cm^2\,V^{-1}\,s^{-1}}$ for holes. This equation becomes

$$W = 0.5[1/\sqrt{R} - V] \times \sqrt{\rho(V + V_{bi})} \tag{4.2}$$

for n-type material and

$$W = 0.3[1/\sqrt{R} - V] \times \sqrt{\rho(V + V_{bi})} \tag{4.3}$$

for p-type material. The conductive p and n regions together with the depleted volume forms a capacitor with the capacitance per unit area

$$C = \epsilon/W. \tag{4.4}$$

When an ionising particle such as a proton comes into contact with the semiconductor material it loses energy by producing electron / hole pairs within the material. The particle is detected by creating mobile charge carriers within the depletion region. The presence of the charge carriers allows the semiconductor material to conduct an electrical signal that can be detected by the readout electronics. The more energy that is lost within the material, the more charge carriers are created within the depletion region and hence the greater the signal conducted by the detector material.

The position information from the ionising particles that interact with the detector is determined by splitting the detector itself into several small sections. This can be achieved by two different approaches. In the first of these methods the semiconductor is constructed as a number of small pads. In this configuration it is difficult

to attach the electronics to each of these pads. To resolve this issue a hybrid device that includes both the silicon and the electronics is used. The second approach is to split the detector into a number of narrow and parallel strips. This type of detector is relatively simple to manufacture by embedding p-doped strips into p-type silicon. Strip widths as low as 20 μm have been achieved. A two sided silicon detector is slightly more difficult to construct as the n^+ strips on the n-side need to be separated electrically from each other. This problem is solved by introducing p^+ electrodes in between these n-type regions. The silicon strip design was used for the silicon detector at HERMES.

4.2.1 The Silicon Modules

The SSD modules were mounted in a diamond configuration, around the HERMES target cell and within the beam vacuum, as shown in Fig 4.4.

The SSD is comprised of eight individual silicon modules. Two silicon modules are positioned on each side of the SSD. The particle tracked in one quadrant of the SSD can be identified by two independent silicon detectors. The silicon detectors were connected to an aluminium heat sink on which the readout hybrids were connected. The modules consisted of a number of n-type strips with p-type strips perpendicular to them. HELIX chips were located on both sides of these modules, which connected to the readout electronics via a series of conducting kapton flex foils.

Due to time restrictions it was decided by the collaboration to use an existing design for the SSD. After considering a number of different designs, the chosen detector that best conformed to the requirements of detecting recoil protons was that of the TTT design of Micron Semiconductors Ltd, Sussex. The design was originally designed for the TIGRE Gamma Ray Telescope [79].

The sensors were square shaped with a side length of 9.9 cm, providing an active area of 97.3 mm$\times$ 97.3 mm^3, with a thickness of 300 μm. Both sides of each of these modules comprised of 128 strips, of width 758 μm. Some minor changes were made to the original design: the bias resistors and the thickness's of the oxide layer were altered. These alterations allowed the silicon detector to operate despite the high

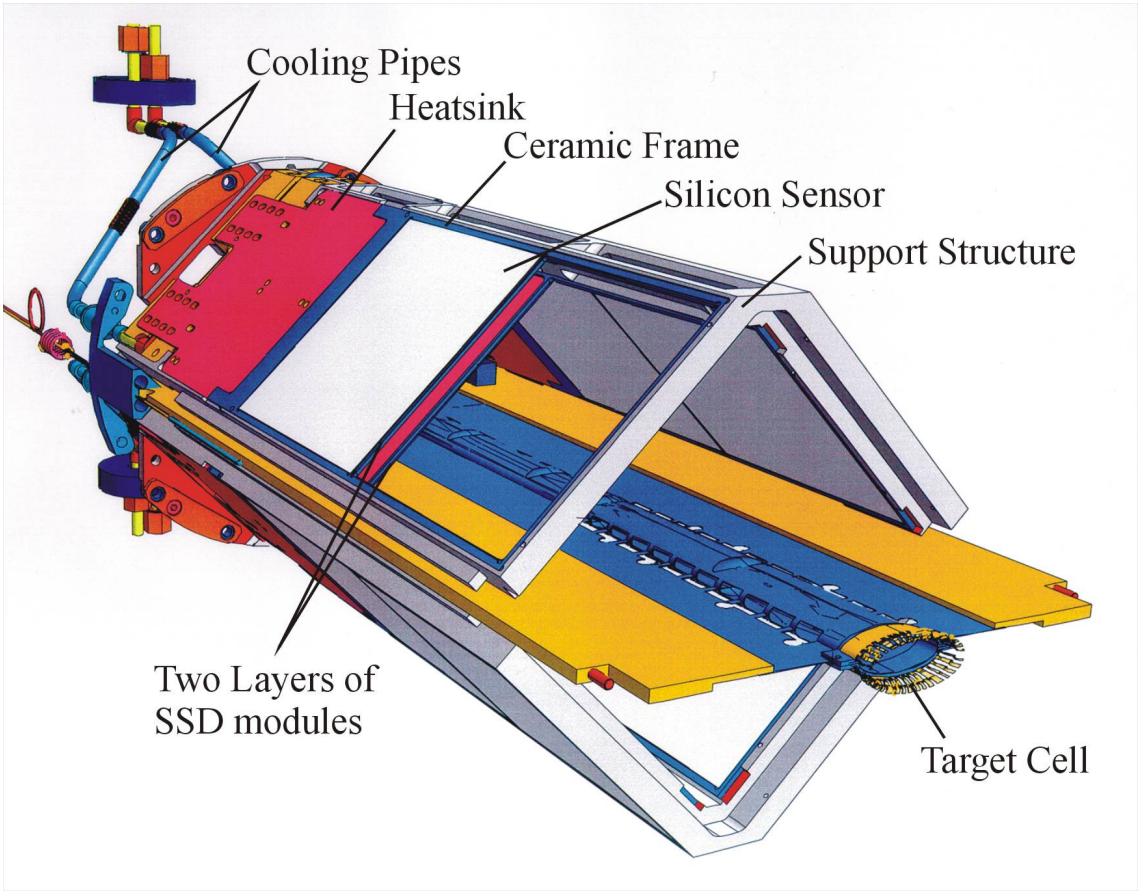

Figure 4.4: The structure of the SSD [64]. The two layers of silicon modules are shown along with the target cell, support structure and cooling mechanism.

background radiation due to the proximity to the beam. The p-side strips were created using boron doping, with an ion implantation density of $2.0 \cdot 10^{15}\,\mathrm{cm}^{-2}$. The n-type implants on the p-side were similarly created using phosphorus doping with a density of $5.0 \cdot 10^{14}\,\mathrm{cm}^{-2}$. The n-side strips were of a complementary design with a nominal ion beam density of $5.0 \cdot 10^{15}\,\mathrm{cm}^{-2}$ and a p-implant density of $5.0 \cdot 10^{14}\,\mathrm{cm}^{-2}$. A bias guard ring was created in the sensor after doping. Finally an aluminium layer for bond pads and charge collection lines and a thin passivation protection layer were applied to the detector.

4.2.2 Readout System

Semiconductor detectors are thin in nature due to the high density of the manufacturing process. These detectors are well suited to situations where the available space is particularly limited. As the detector is relatively small it was possible to position the SSD at HERMES within the confined volume of the beam pipe, allowing the detection of low momentum particles that would otherwise be absorbed within the pipe. Due to this spatial restriction and the high volume of individual strips that comprise the detector as a whole it is not possible to read out each channel individually with an ADC. Instead the front end chips were directly connected to the sensors that serialised and digitised the signals. The director signals are fed through a pre-amplifier, and stored in a buffer before they are transferred via a multiplexer to an ADC. The chips also feature control devices and supply electronics. All readout chips are custom designed for the HERMES experiment.

Two of the serial read out chips that have been developed at HERA are the APC, developed and used extensively in the H1 experiment, and the HELIX chip, developed for HERA-B and used at both the HERMES and ZEUS experiments. The HELIX chip was selected for the readout of the Recoil Detector as this was the most technically advantageous for the detector and had previously been used for the Lambda Wheels so there was a working knowledge of using this chip within the collaboration.

The readout chip was mounted with some additional electronics onto a circuit board made from kapton foil. This unit is known as a “hybrid”. The kapton flex

foil was also used to connect the hybrid to the read out electronics at the end of the beam pipe. The kapton foil partially covers the sensitive material of the SSD, as a consequence particles tracked using the Recoil Detector interact with this passive material.

Semiconductors produce noise that must be taken into account. The signals are low; a Minimising Ion Particle (MIP) passing through silicon deposits around $2.2 \cdot 10^4$ eV. There is no intrinsic charge multiplication, therefore the noise on the charge amplification can be quite prominent. The electronics have a constant intrinsic noise, inherent to the design, that depends on the capacitance of the strips being read out.

In order to develop a tracking method using the silicon detectors it is necessary to have a precise method for measuring the energy loss within the silicon material. The energy loss measured at HERMES was over a wide energy range, therefore a charge splitting read out was devised so that the system was able to give precise measurements for both low and high energy depositions. This ranges from Minimum Ionising Particles (MIPs) to the large energy lost by protons that can at lower momenta be completely stopped within the two layers of silicon. The input pads of the HELIX chips were connected to a ceramic pitch adapter, connected to the capacitor array used to distribute the charge into a high gain and a low gain channel. Each silicon strip is connected to both a high and a low gain HELIX chip, the latter via a 10 pF capacitor. The split into two individual and distinct HELIX chips facilitates the measurement of a large range of energy loss to be determined. The high gain helix chip is used to read out energy losses from 1 to 10 MIP equivalents. The low gain chips, conversely, reads out higher energy losses, up 70 MIP equivalents. By using the low gain helix chip to determine the high energy losses of particles it is possible to track protons that are stopped within the beam vacuum and that would not be measured by the other detectors that comprise the Recoil Detector.

4.3 Energy Loss

The method of tracking and identifying particles by energy deposition has been an integral part of modern detector operation [80,81]. The inner detector of the ATLAS experiment at the Large Hadron Collider (LHC) consists of multiple-layer silicon detectors that have been designed to take advantage of this technique [82]. The energy lost by a particle over a given distance is dependent on the particle type, the initial momentum of the particle and the material the particle passes through. These properties are used by the SSD both in identifying the recoiling proton from other particles such as pions and determining the momentum of the recoiling particle. The silicon detector was optimally used to measure the momentum of recoiling particles up to $\sim 0.6\,\mathrm{GeV/c}$ with higher momenta protons tracked to a greater accuracy using the SFT.

Charged particles lose energy in the silicon by inelastic collisions with the atomic electrons, resulting in ionisation of the atoms and allowing conduction through the p-n junction depletion layer described in Section 4.2. In this ionisation process more energetic electrons, δ-rays, are emitted resulting in an additional energy loss unless they are captured by another atom. This effect is largely ignored when calculating the energy lost in the SSD as the energy losses of heavy particles such as protons are large, creating a number of ions, hence the δ-rays are captured immediately, rendering this correction insignificant.

The dominant contributions to the energy loss of charged particles in the SSD are the Coulomb Interactions with the atomic electrons. Nuclear interaction length in the 300 μm silicon sensors is 7×10^{-2} g/cm^2, hence, the probability of a nuclear interaction in the sensor is less than 1%. Correlated energy loss effects are also negligible due to their dependence on certain incident angles. The probability of a single charged particle undergoing an interaction with an atomic electron is described by the doubly differential cross section $\sigma(E,k)$ where E is the energy lost in an electron with momentum transfer k. The proton in the SSD will experience a number of collisions (n) with atomic electrons. The total energy lost can be described by

$$\Delta = \sum_{i}^{n} E_i. \tag{4.5}$$

The probability of losing an amount of energy Δ when traversing a detector of thickness d is described by the energy loss straggling function $f(d, \Delta)$.

The straggling function, described by Eq 4.5, is known as the restricted energy loss straggling function. This is different to the energy loss straggling function due to the presence of the δ-rays that are created during energy deposition. To determine the energy deposition straggling function the probability of n number of collisions and the probability of a particular energy loss E_i have to be determined. The number of collisions is given by a Poisson distribution with a mean value $\mu = dM_0$, where M_0 given by

$$M_0 = N_e \int \sigma(E) dE \tag{4.6}$$

and N_e is the number of electrons per unit volume. The collision cross section $\sigma(E)$ is determined separately depending on the energy of the momentum transfer and the longitudinal and transverse excitations. The collision process for the large energy transfer cross section, considered for protons in the silicon detector, is the non-relativistic Rutherford cross section [83]

$$\sigma_{nr}(E) = \frac{2\pi z^2 e^4}{m_e \nu v^2 E^2} \tag{4.7}$$

that describes the collision probability of a heavy charged particle with charge ze, velocity v and rest mass M in collision with a free electron with rest mass m_e. In this non relativistic case, the electron receives all the energy E lost by the particle and the corresponding momentum transfer k is $\sqrt{2m_e E}$. To consider the probability of a collision in the relativistic case, such as those which occur at HERMES, this cross section needs to be modified to include the maximum energy transfer for relativistic particles, given by

$$E_m = \frac{Mc^2\beta^2\gamma^2}{\frac{M}{2M_e} + \frac{m_e}{2M} + \gamma} \tag{4.8}$$

where M and m_e are the rest mass of the incident particle and free electron respectively, β is the ratio of the velocity of the particle to the speed of light and $\gamma = \sqrt{1-\beta^2}$. The relativistic Rutherford cross section [83] is then described by

$$\sigma_{rr}(E) = \sigma_{nr}(E) \left[1 - \beta^2 \frac{E}{E_m}\right]. \tag{4.9}$$

The Rutherford cross section described relativistic charged particles that are incident upon free electrons. In the SSD the electrons are bound to the nucleus, therefore, the binding energy must be taken into account. This process is then described by the empirical cross section [84]

$$\sigma_u(E) = \sigma_{rr}(E)\left[1 - \beta^2\frac{E}{E_m}\right]\sum Z_l\left[1 + \frac{d_1}{E} + \frac{d_2}{E^2}\right] \tag{4.10}$$

where Z_l is the number of electrons in the sub shell l, d_1 and d_2 vary depending on the energy transfer. The empirical cross section is the dominant part of the total cross section σ with smaller quantities due to longitudinal and transverse excitations also contributing to the total. If the total cross section is available it is possible to define the set of moments

$$M_m = N_v \int E^m \sigma E dE \tag{4.11}$$

where N_v is the number of atoms in a unit volume, $4.99 \cdot 10^{22}\,\mathrm{cm}^{-3}$, for silicon. The mean number of collisions per unit length is given by the zeroth moment M_0. The mean energy loss is given by the next moment M_1, this is comparable to that given by the Bethe Bloche equation. The M_2 moment is related to the width of the energy straggling distribution. This distribution is also taken into account by modifying the Bethe Bloche equation.

The stopping power of particles passing through the silicon detector is described by the Bethe Bloche equation [85]. This calculates the mean energy loss of a charged particle that is heavier than an electron as it traverses a particular material, and is shown below

$$\frac{dE}{dx} = 2\pi N_a r_e^2 m_e c^2 \rho \frac{Z}{A}\frac{z^2}{\beta^2}\left[ln(\frac{2m_e\gamma^2 v^2 E_m}{I^2}) - 2\beta^2 - \delta - 2\frac{C}{Z}\right] \tag{4.12}$$

where N_a is Avogadro's number, $6.022{\cdot}10^{23}$ atoms per mole, $r_e = \frac{e^2}{m_e c^2}$ is the radius of an electron, $2.817{\cdot}10^{-15}\,\mathrm{cm}$, $m_e c^2$ is rest mass of the electron, ρ is the density of the stopping material ($2.33\,\mathrm{g/cm}^3$ for silicon), Z is the atomic number of the stopping material (14 for silicon), A is the atomic weight of the stopping material (28.09 for silicon), I is the mean ionisation potential (173 eV for silicon), z is the charge of the particle in units of electron charge, and E_m is given by Eq 4.8.

The shell correction takes into account the reduction in the stopping power that occurs in silicon due to the atomic binding of electrons that is neglected by the other contributions. At low energies, the stopping power dE/dx decreases with the natural logarithm of particle energy. As the particle energy increases its electric field flattens and extends so that the distant-collision contribution increases as $\ln(\beta^2\gamma^2)$. The stopping power of the silicon material decreases as the density correction lowers the $\ln(\beta^2\gamma^2)$ dependence to $\ln(\beta\gamma)$ because the stopping power is polarised by the field of the passing particle, reducing the effect of distant collisions.

The Bethe Bloche equation calculates the mean energy loss accurately and in this form is suitable for particle tracking by energy loss. The equation relates the stopping power, dependent on the energy loss and the path length of the incident particle within silicon, to β, therefore i.e. dE/dx is a function only of β. The ratio β relates the velocity of the incident particle to the speed of light and the momentum of a particle can be calculated from this velocity, $p = \gamma mv$. The Bethe Bloche equation is therefore used as the basis for particle momentum reconstruction by energy loss at HERMES.

4.4 DER Tracking Method

The objective of tracking in the SSD is to determine the momentum and the position of the recoiling particle that interacts with the detector. The method developed for tracking with the SSD is known as DER tracking, ΔE Reconstruction. The momentum of the proton is reconstructed using the energy deposited ΔE and the pathlength L of the particle through each of the silicon sensors.

4.4.1 Track Identification and Energy Loss Regions

Any track reaching the outer sensor in the SSD is identified from two spacepoints in each of the silicon sensors. The track is reconstructed as a straight line between these two points. The incident angle α to the sensors is determined from this straight line approximation which ignores the effects of the magnetic field. The polar θ and azimuthal ϕ angles shown in Fig 4.5 describing the path of a recoiling particle are

corrected for the effect of the magnetic field. The φ angle determined from the spacepoint information is re-calculated using the curvature in the magnetic field is denoted ϕ. The track is identified as a real proton track only if the spacepoints in both the sensors lie within the same quadrant and that the track itself can be traced back to the target cell. All track combinations that satisfy the above criteria are analysed as real tracks with the remainder rejected, as also shown in Fig 4.5.

The recoil protons can be identified in the SSD using the energy loss in both the silicon sensors. There are three different methods for reconstructing the momentum of recoil protons, dependent on whether the particle is stopped in the detector or not, as illustrated in Fig 4.6. The momentum of protons that are stopped within the silicon sensors are reconstructed by adding the energy loss in the sensitive silicon and the passive materials. The second method for reconstructing recoil protons, when they are not stopped within the silicon sensors, is to use the energy loss and pathlength in the silicon sensor to identify the initial momentum of the particle using the lookup table described in the following section. There is a third possibility when it is not possible to determine if the proton has stopped within the SSD or not. In this circumstance the recoil momentum is reconstructed using both the stopped proton and the lookup table methods. Both these values are available to the data analyser and the correct value can be selected by using PID selection, momentum cuts and other tracking methods. In circumstances where, after analysis cuts and selection criteria have been implemented, both results remain plausible, the lookup table method should be used as this has been shown to produce the more accurate resolution, as described in section 4.6.3. The appropriate tracking routine is selected by applying cuts based on the energy loss relationship between stopped and non-stopped protons in both silicon sensors shown in Fig 4.6. Stopped protons can also be selected if a proton is stopped in the inner silicon sensor and no energy loss is identified in the outer layer.

4.4.2 Lookup Table Development

A lookup table method was used to determine the initial kinematic energy T of a recoil proton. Lookup tables relate one or more variables to another quantity which

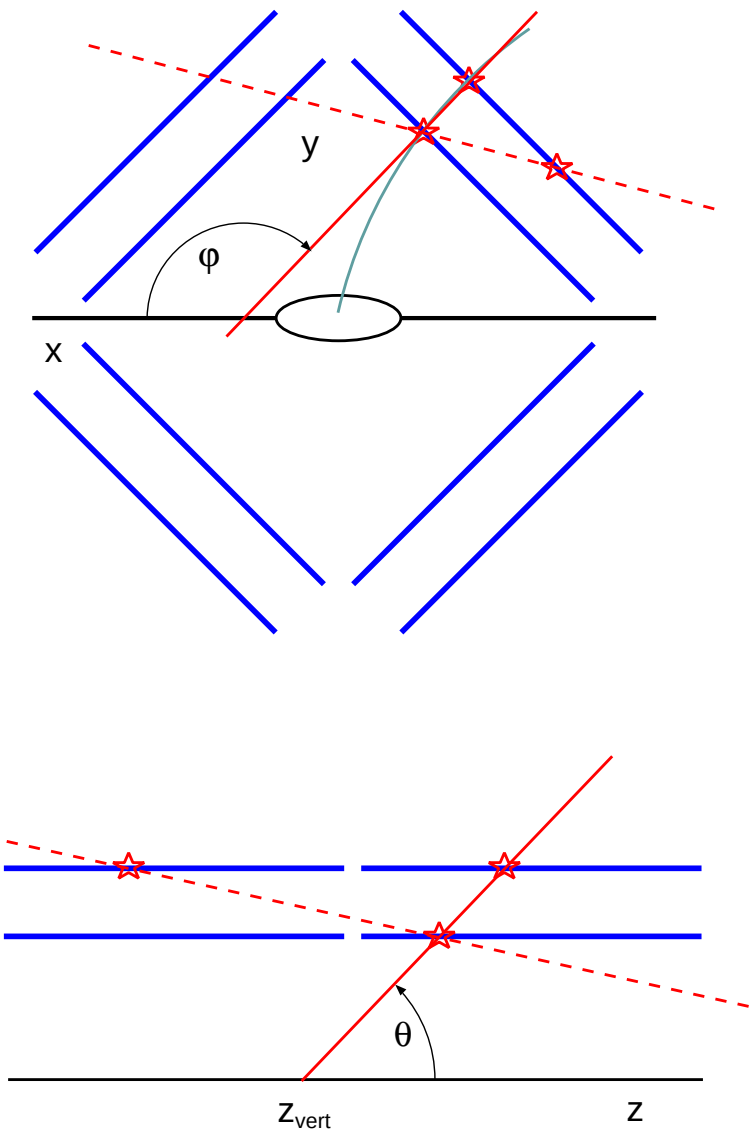

Figure 4.5: An overview of track reconstruction from spacepoints in the SSD [86]. The top figure shows the SSD in x-y coordinate space and the angle between the x-plane and the track φ. The bottom figure shows the z coordinate of the SSD and the angle between the z-plane and the track θ. In both cases a track that is reconstructed as a real track is shown as a continuous red line and a rejected track as a dashed red line. The actual track is shown in grey in the top figure.

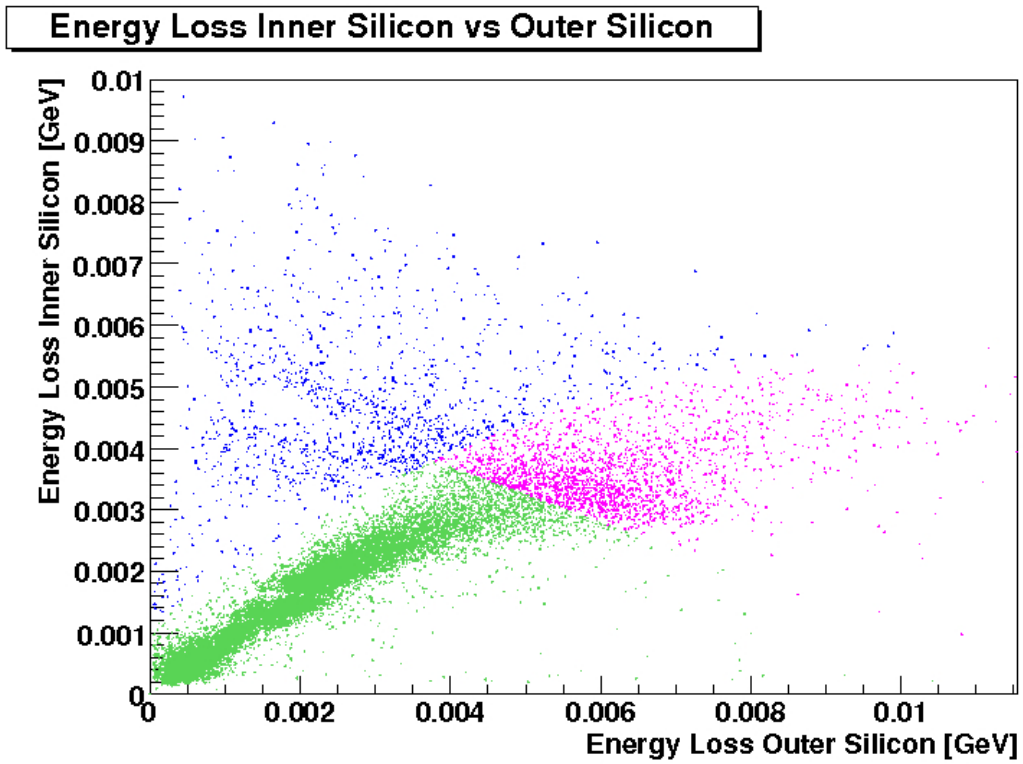

Figure 4.6: The energy loss of a recoil proton in the outer sensor vs the energy loss in the inner sensor. Protons stopped in silicon and not stopped are shown in blue and green respectively. The energy loss region in where it is not possible to distinguish if the proton is stopped or not is shown in magenta.

is dependent on the known input variables, but is not directly calculable from them. In the case of the DER tracking lookup table the known input parameters are the energy loss and pathlengh in the SSD and the desired value is the initial kinematic energy of the recoil proton.

The structure of the SSD allows for the coordinates in three dimensional space of where the particle passes through the detector to be accurately determined. Using the spacepoints from both the outer and inner silicon sensors it is possible to calculate the incident angle of the recoiling particle has on the silicon detector. The incident angle α and the strip width W of each sensor are both used to calculate the pathlength L of the recoil particle

$$L = \frac{W}{cos(\alpha)}. \tag{4.13}$$

The thicknesses of each of the eight silicon sensors can vary from 290 to 310 μm and is taken into account when calculating L. This affects the value of the energy lost in each sensor which is both sensor and angular dependent.

A Monte Carlo simulation is used to determine the relationship between these properties, shown in Fig 4.7. A lookup table that relates the energy loss and the path length, read out and calculable in the silicon, to the kinetic energy of the incident particle just before the sensor was created from this relationship. This information allows each combination of a specific value of path length and energy deposited to yield a unique value for the kinetic energy of the proton. Two individual values of the kinetic energy T can be determined, one for each sensor in the SSD. These two values can then be recombined to give an overall value of the kinetic energy of the recoil proton, which can be used to determine the initial momentum.

The advantage of using the Monte Carlo simulation to construct such a lookup table rather than determining the momentum of the proton from the Bethe Bloch equation, directly, is the inclusion of other effects that are not described by Eq 4.12. Ideally the relation between the kinetic energy path length and energy loss, shown in Fig 4.7, would be a straight line. However, due to energy and angular straggling, modelled in the Monte Carlo, a broad relationship between these quantities is obtained. The lookup table is being used in other tracking methods that use information from the SFT and PD.

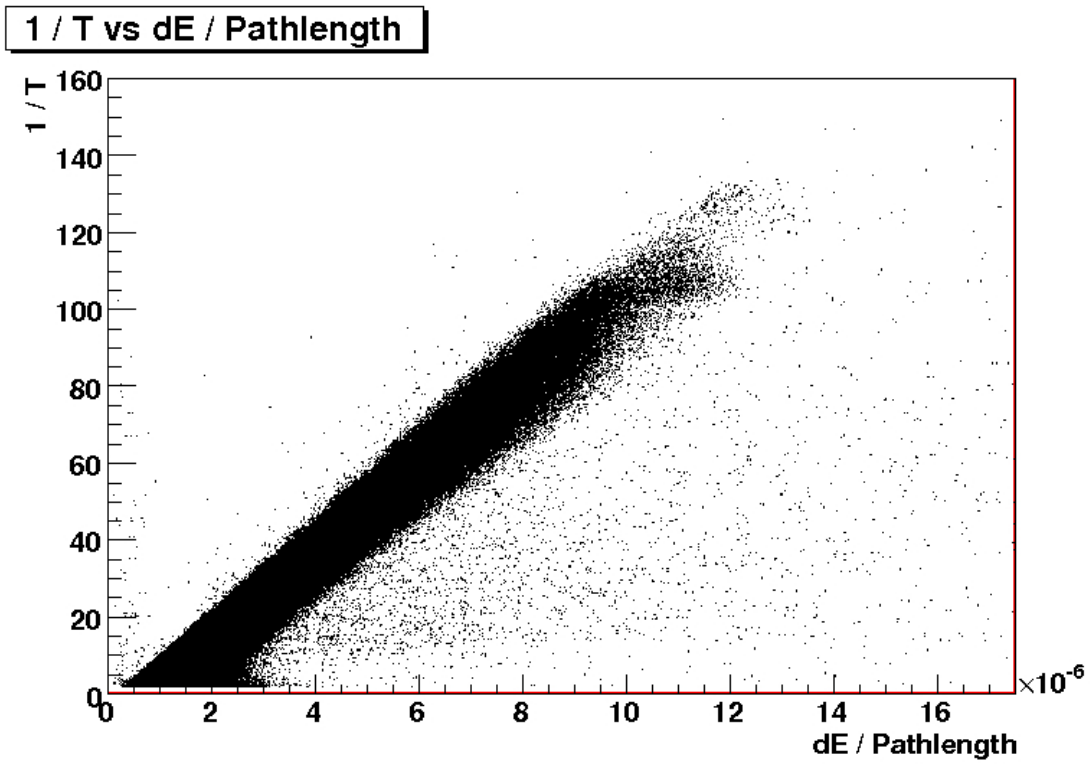

Figure 4.7: Kinetic energy immediately before either of the silicon detectors vs the energy lost divided by the pathlength in the sensor. This linear relationship forms the basis of the lookup table used in the DER method.

A lookup table is constructed with a certain binning, such that a small range of dE/L contains a number of events with a value of the momentum known precisely from the Monte Carlo simulation. Each bin in the lookup table can only return one value of momentum. To determine the momentum of a particular bin the momentum values from each of the events are plotted and a Gaussian fit applied to the distribution, with the mean value of the fit assigned as the momentum value of a particular bin. By using a Gaussian fit to the momentum distribution the contribution from events that have random fluctuations can be minimised. The lookup table at this stage has a number of dE/L bins that span the range in momenta of the recoil protons. The individual bins still fluctuate slightly, therefore it was necessary to introduce a smoothing algorithm, based on a linear fit of the lookup table bins, to remove such fluctuations between individual bins. The smoothed lookup table is then implemented into the DER tracking software such that for each event a kinetic energy of a particular bin can be reconstructed from the energy loss and the path length.

Each bin covers a certain dE/L range, where the same kinetic energy value is returned no matter whether the dE/L value is near the centre or at the edge of a particular bin. In order to improve the precision of this process an additional step was introduced to calculate the fraction of the dE/L values that lie within a certain bin, shown in Fig 4.8. The length of a particular bin is a fixed quantity, but if a dE/L is at the edge of a particular bin it will have a different value to that at the opposite edge. It is more realistic to extend this bin length into the neighbouring bin and calculate the kinetic energy value based on the fractional contribution of two values from separate bins. Introducing this additional step improves the precision and smooths the bin dependence of the tracking method.

4.5 Passive Materials

4.5.1 Description of Passive Materials

The silicon sensors within the SSD were not installed in isolation but rather co-existed with a number of passive materials, including the read out electronics and

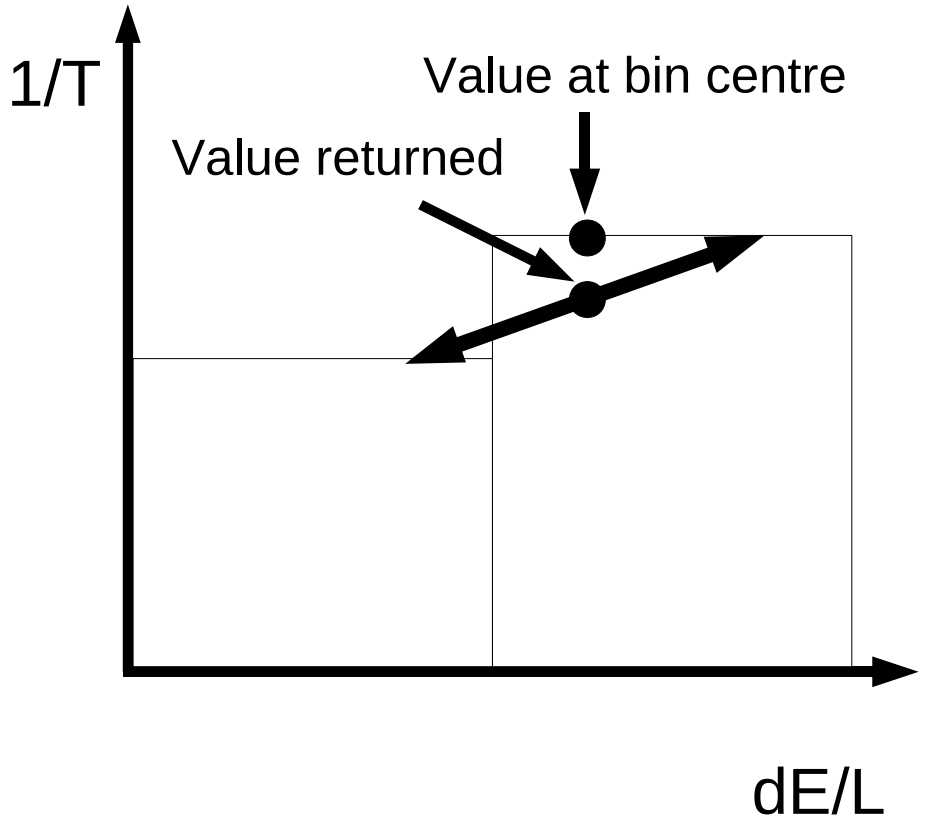

Figure 4.8: An example sketch of two adjoining bins in the lookup table used to determine kinetic energy. In this example the dE/L point is not centred in one particular bin and the bin length is extended from the dE/L point across into the neighbouring bin. In this example the value returned is $T = \frac{1}{3} \times bin1 + \frac{2}{3} \times bin2$.

the walls of the target cell. The particles tracked using the Recoil Detector lose energy as they pass through these inactive materials. This slows the particle and increases the energy lost in the silicon sensors, giving an inaccurate value of the reconstructed momentum that is less than in reality.

The first of the passive materials the recoiling particle encounters before reaching the silicon is the walls of the target cell in which the target gas is held. This is an ellipsoid tube constructed with 75 μm thick aluminium walls. The recoil particles passing through the target cell lose energy in the aluminium material.

Due to the high frequency radiation from the lepton beam used in the HERMES experiment it was necessary to construct a Faraday cage to protect the individual SSD modules from damage. The construction of this RF shield also ensured that there was no interference in the signals of the readout system of the SSD from this background radiation. The RF shield was constructed of 30 μm thick kapton and copper and covered the entire length of both the inner and outer silicon sensors in the SSD, therefore all recoil particles will lose energy in this material in addition to the target cell structure.

The read out system of the SSD allows the information from both silicon sensors to be accessed individually. The information from each of the sensors is read out using kapton flex foils which carry the information to the HELIX readout chips. A particle passing through the silicon will lose energy in this material in addition to the active silicon sensor. Hence it is important to calculate how significant this effect is and to correct for it. The flex foil material was of different shape and surface area on opposite sides of the silicon sensors. The flex foils that were smaller in size and covered less of the sensor, shown in Fig 4.9, were positioned facing each other. Low momentum particles may lose almost all of their energy in the inner silicon sensor of the SSD, therefore, in order to increase the likelihood of the particle reaching the outer sensor it is important to minimise the energy loss between the two sensors. The information from a recoil particle can be more accurately reconstructed from a particle with information from both sensors.

For the inner silicon sensor the flex foil with the larger surface area, shown in Fig 4.10, is positioned facing the target cell and in the outer sensor facing the outer

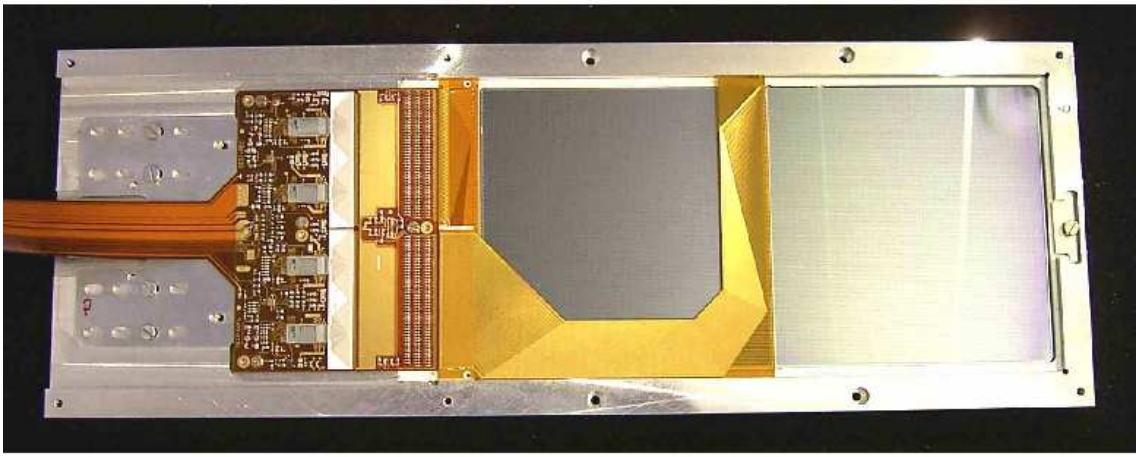

Figure 4.9: A picture of the p-side of the SSD. The intermediate flex foil covers a part of the silicon material [87]. Also shown are the readout electronics.

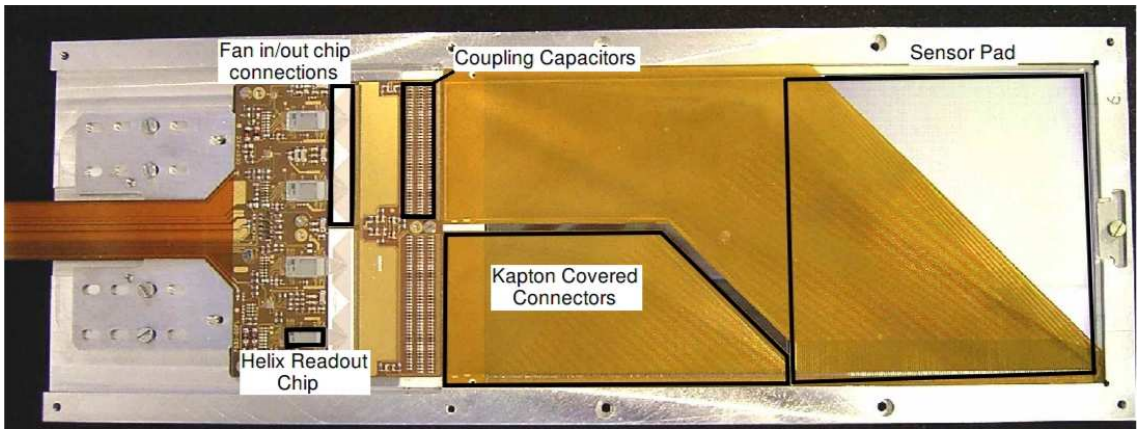

Figure 4.10: A picture of the n-side flex foil [87]. This flex foil was positioned facing the target cell. Also shown is the connection to the readout electronics for data processing.

vacuum. This flex foil is comprised of two different sections; one that has only a small linear gap and the other which covers most of the sensor, apart from a triangular area to the right hand side.

4.5.2 Passive Material Implementation in Monte Carlo

The HERMES Monte Carlo software chain is used to simulate the energy lost in all the passive materials. The target cell is modelled in the $x - y$ coordinate system as an ellipsoid tube with walls 75 μm thick. The RF shield is implemented as a continuous sheet. All particles will pass through the target cell and RF shield.

The flex foil materials which are part of the readout electronics partially cover each of the silicon sensors, therefore, the Monte Carlo simulation is used to determine if a particles pass through the flex foil or not. The track reconstruction software is reliant on the detector output so the passive material information is not available directly. In order to determine if a particle has interacted with the flex foil before the inner sensor the initial energy of the proton is compared with the energy immediately before it interacts with the inner silicon sensor. The energy lost in the target cell walls and the RF shield are also determined using this calculation. If the difference between the initial energy of the proton and the energy after passing through the passive materials before the inner sensor is > 0.5 MeV the proton is identified as passing through the flex foil. A similar method is used to identify the intermediate flex foils between the sensors. In this case the energy of the recoiling proton immediately before the inner sensor is compared with the energy just before the proton interacts with the outer sensor. The results of this method are shown in Figs 4.11 and 4.12 for the intermediate and before inner sensor flex foils respectively. In order to identify if a recoiling proton has passed through either of the flex foils using the track reconstruction software cuts were introduced based on the spacepoint coordinate system. If the spacepoint lies within a flex foil region identified in Figs 4.11 and 4.12 a correction for the flex foils is applied. The slight shifts in the positioning of the sensor in each of the four quadrants are taken into consideration, therefore the cuts are implemented separately for each quadrant, see Fig 4.11.

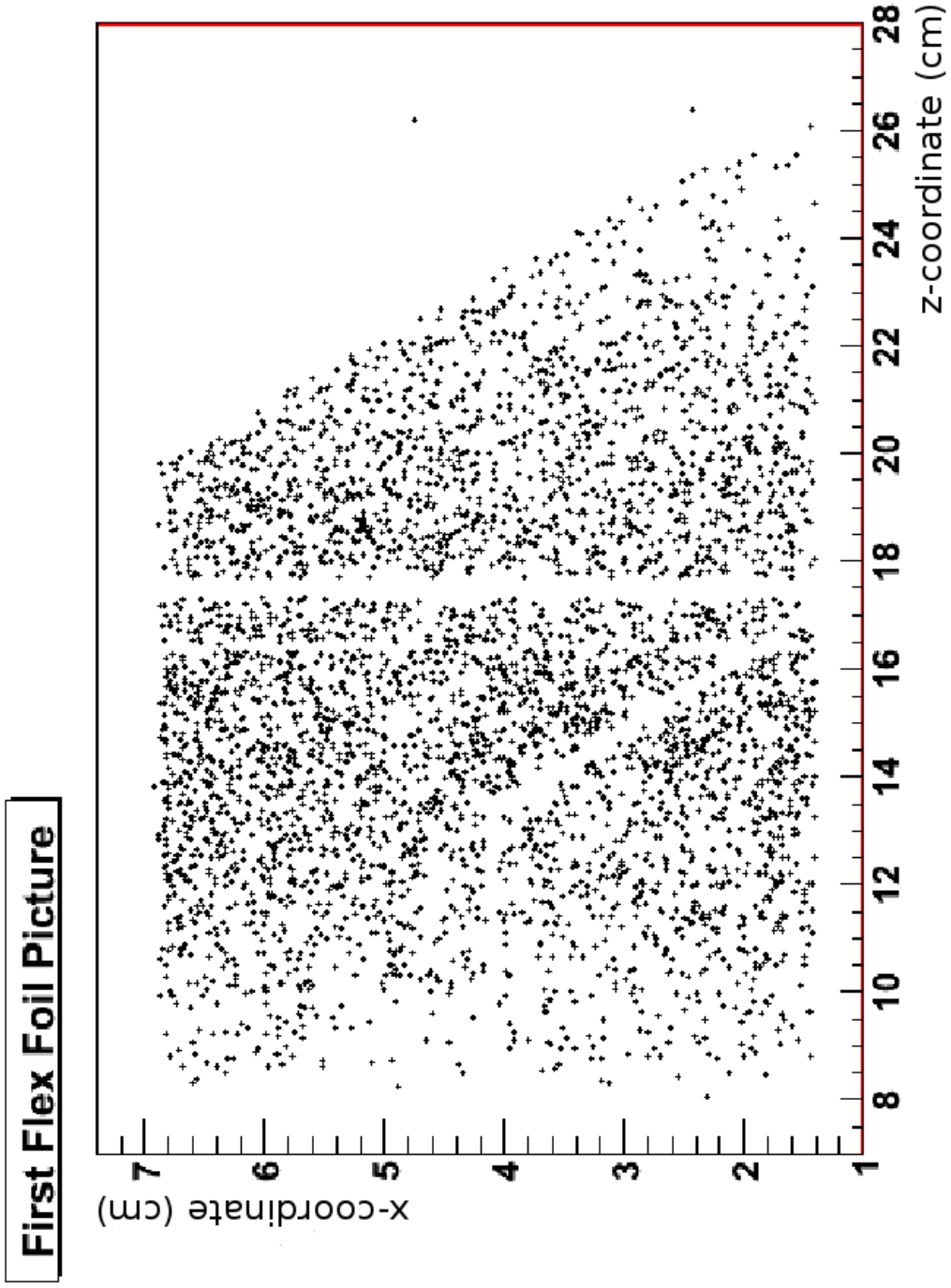

Figure 4.11: The result of the simulation of the flex foil in quadrant 1. The area covered by the material based on x and z spacepoint coordinates is shown.

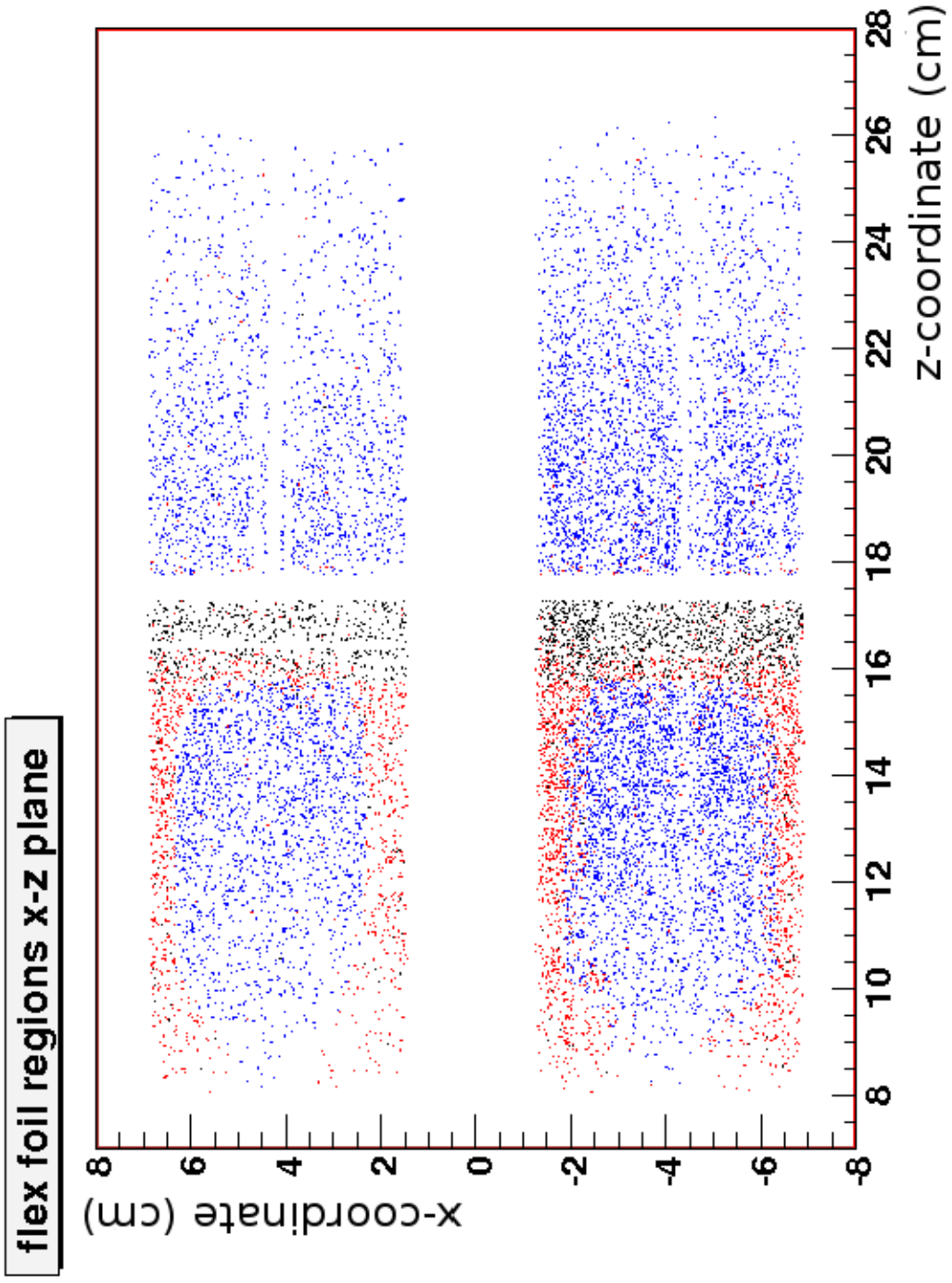

Figure 4.12: The Monte Carlo simulation of recoil protons interacting with an intermediate flex foil. The x and z coordinates of the each hit in one quadrant of the SSD are shown. The protons can encounter one, two or no flex foil layers and this is shown in red, black and blue respectively.

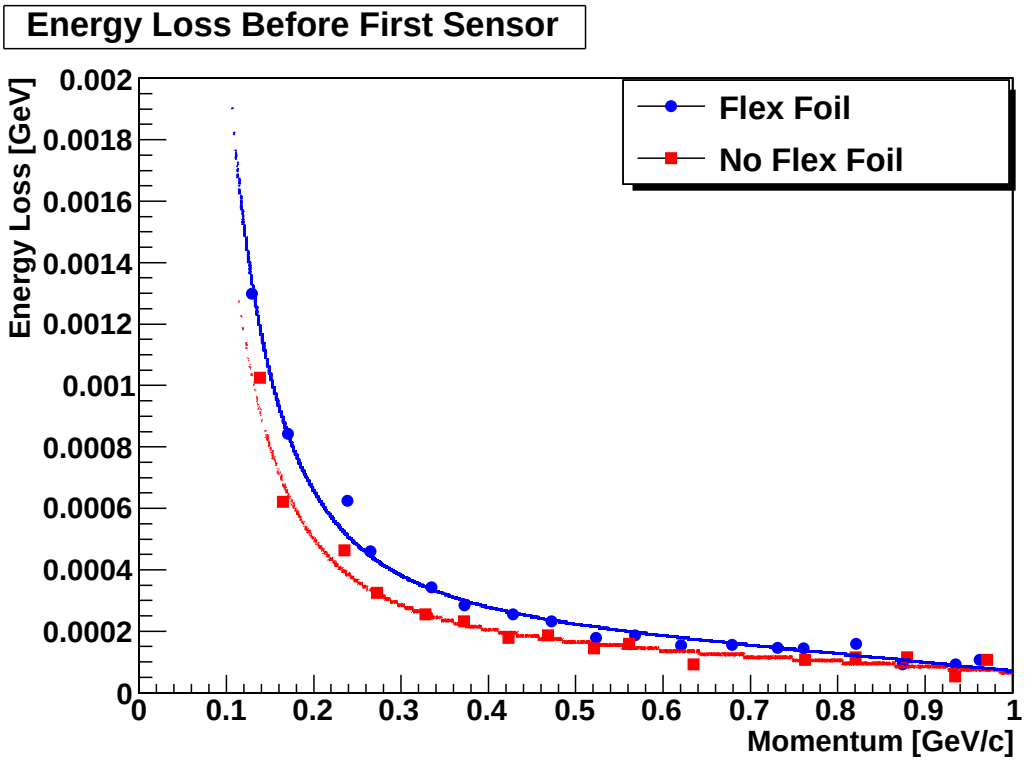

Figure 4.13: Energy lost in the materials before the inner silicon sensor vs momentum of the recoil proton. A momentum dependent Bethe Bloche function is fitted to the data, see Eq 4.15.

4.5.3 Combined Correction for the Passive Materials Before the Inner Silicon Sensor

The recoil proton loses energy as it passes through the target cell, RF shield and flex foil that are positioned before the inner silicon sensor in the SSD. By losing energy in these passive materials a particle loses momentum and in turn loses more energy in the silicon due to the increased possibility of a lower energy particle interacting with the sensor material. By losing more energy in the silicon sensor the reconstruction software will return a lower initial momentum value. The correction function is used in an iterative process after the initial momentum value of the incident proton is determined by the tracking method, and recalculates the momentum including the energy lost in the passive materials.

The correction procedure for the materials in front of the inner silicon sensor implemented in Monte Carlo simulated geometry combines the target cell, RF shield and the outer flex foil. All particles pass through the target cell and RF shield, only the presence or otherwise of flex foil material varies. The passive material correction uses a momentum dependent procedure. The energy loss is calculated in the Monte Carlo using

$$\mathrm{E}_{loss} = \mathrm{E}_{initial} - \mathrm{E}_{before} \tag{4.14}$$

where E_{loss} is the energy lost before the particle reaches the inner sensor, $\mathrm{E}_{initial}$ is the initial energy of the proton immediately after interacting with the electron beam and E_{before} is the energy of such a particle before is comes into contact with the silicon.

The distribution of the energy lost in the passive materials was plotted individually over the entire momentum range in bins of 0.05 GeV. A convolution of a Gaussian and a Landau fit was made to the distribution and the mean value of this function determined for each individual bin. The momentum dependent energy loss curves of the proton interacting with these passive materials, fitted to the mean values of the energy loss in each momentum bin, are shown in Fig 4.13. The function used to fit the energy loss curve is

$$E_{corr} = C_0 + C_1\beta^2 + \frac{C_2}{\beta^2}, \tag{4.15}$$

where C_0, C_1 and C_2 are constants and $\beta = \frac{v}{c}$ and is based on the Bethe Bloche equation 4.12. Protons with the lowest momentum lose the most energy in the passive materials. Using this approach the energy lost in the passive materials is calculated, using Eq 4.15 from the initial momentum given by the track reconstruction software, in the case of DER tracking from the lookup table. The energy lost in the passive materials is then added to this initial momentum value. Using this new value for the initial momentum value the energy lost in each of the SSD sensors is ascertained once again and the initial momentum re-evaluated. The corrections for passive materials are then recalculated using this corrected initial momentum value. The processes continues until the momentum values of the recoiling proton converge. This iterative approach, in which the track reconstruction algorithm is

re-run including the energy loss in passive materials, is particularly important for "silicon only" low momentum track reconstruction methods which are highly sensitive to small changes in energy loss in the silicon sensors. The passive material correction is most significant for silicon only tracking which is used to reconstruct low momentum protons that are not measured in the other detectors.

4.5.4 Correction for the Intermediate Flex Foils

The intermediate flex foils, positioned between the two silicon sensors, are shown in Fig 4.12. The area shown in red has one layer of flex foil material and the black area represents two layers of flex foil material. The blue region is silicon only, where the proton does not pass through any kapton material. The energy loss curves of the proton interacting with the intermediate flex foil are shown in Fig 4.14, and are calculated as described in the previous section. The black region representing twice the thickness, due to the flex foils in the inner and outer sensor overlapping, has a greater energy deposit. The energy loss curves are fitted using the same function as before, see Eq 4.15. Both of these plots are generated using a Monte Carlo simulation of the detector. Using the coordinate system it is possible to determine if the recoil proton has passed through one of these regions and correct for the energy lost.

The energy lost in the intermediate flex foils, $\mathrm{E}_{intermediate}$, is determined by using the incident energy of the proton before it interacts with the silicon detector and subtracting the energy deposited in the inner layer, $\Delta\mathrm{E}_1$, and the energy before it hits the outer layer, E_{outer},

$$\mathrm{E}_{intermediate} = \mathrm{E}_{inner} - \Delta\mathrm{E}_1 - \mathrm{E}_{outer}. \tag{4.16}$$

4.5.5 Determining Kinetic Energy Including Passive Material Corrections

The goal of the DER tracking routine for non-stopped particles is to use both sensors to give two values of the proton momentum calculable from the initial kinetic energy T. The process for determining T from the silicon sensors and the passive materials

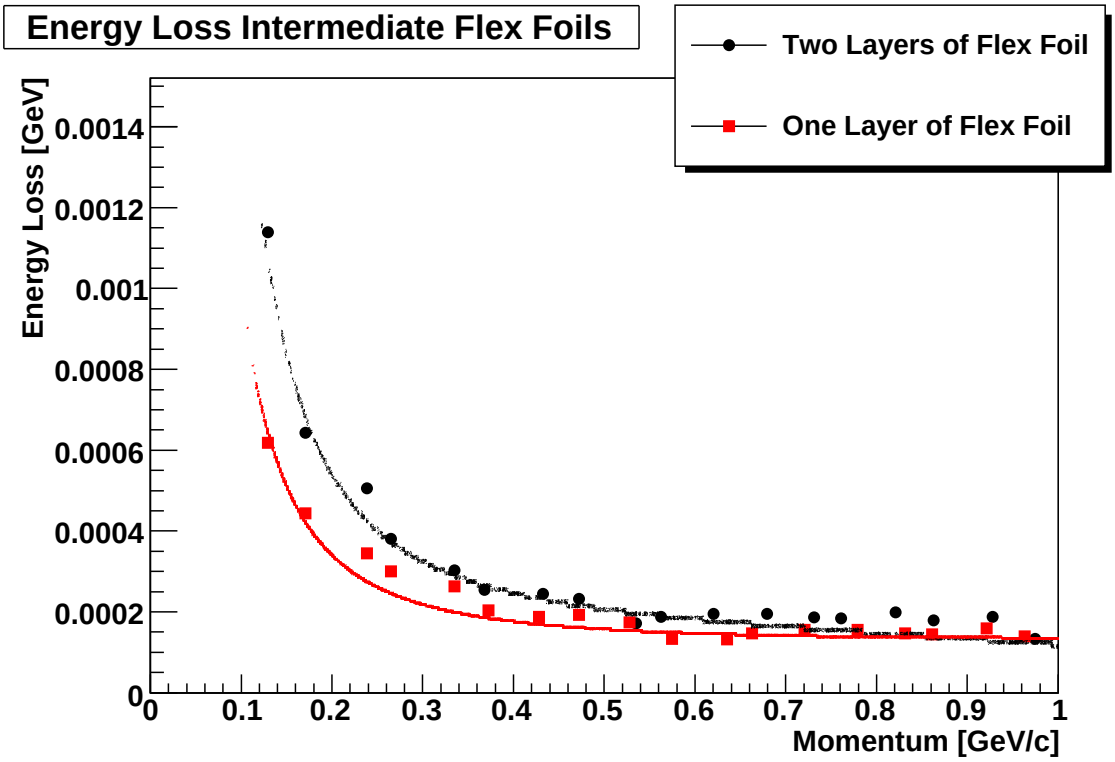

Figure 4.14: Energy loss in the intermediate flex foils vs momentum. The two curves represent the two flex foil areas of different thickness. A momentum dependent function based on the Bethe Bloche equation is fitted to both the energy loss curves, see Eq 4.15.

is iterative, beginning with the sensor information and extrapolating each particle backwards along its track, introducing the passive material corrections. The tracking method is summarised in Fig 4.15. The first step in this process is to determine T immediately before each sensor using the lookup table. The value of the energy deposition and the pathlength from the inner sensor in the SSD are used in the tracking algorithm to generate the value of T_1 of the incident particle from the lookup table

$$T_1 = lookup\left(\Delta E_1, path\right). \tag{4.17}$$

The kinetic energy T_2 before the outer sensor is found using the same direct method, using the same lookup table and tracking procedure. In order to calculate T_2' of the recoiling proton before the inner sensor using information from the outer sensor, the intermediate flex foil correction function to determine the energy lost in these flex foils and the energy lost in the inner silicon sensor are included. These additional energy losses are added to the T_2 value found using the look up table to calculate a second value for the energy lost before the inner sensor.

$$T_2' = T_2 + \Delta E_{flex} + \Delta E_{sensor1}. \tag{4.18}$$

The result of these two steps in the reconstruction chain is two values of T before the inner sensor, which should be equal. These T values from each sensor are then used in the correction function to calculate the energy the particle loses in the passive materials before the inner sensor.

$$T_{1,2}'' = T_{1,2} + \Delta E_{beforefirst} \tag{4.19}$$

The end result is two values for the initial kinetic energy of the recoil proton T_1 and T_2. The momentum of the recoil particle can be determined from the equation

$$p = \sqrt{(T+m)^2 - m^2} \tag{4.20}$$

4.5.6 Stopped Particles

The advantage of the SSD being installed within the beam vacuum is that it is possible to detect recoiling particles with low kinetic energy values that would otherwise

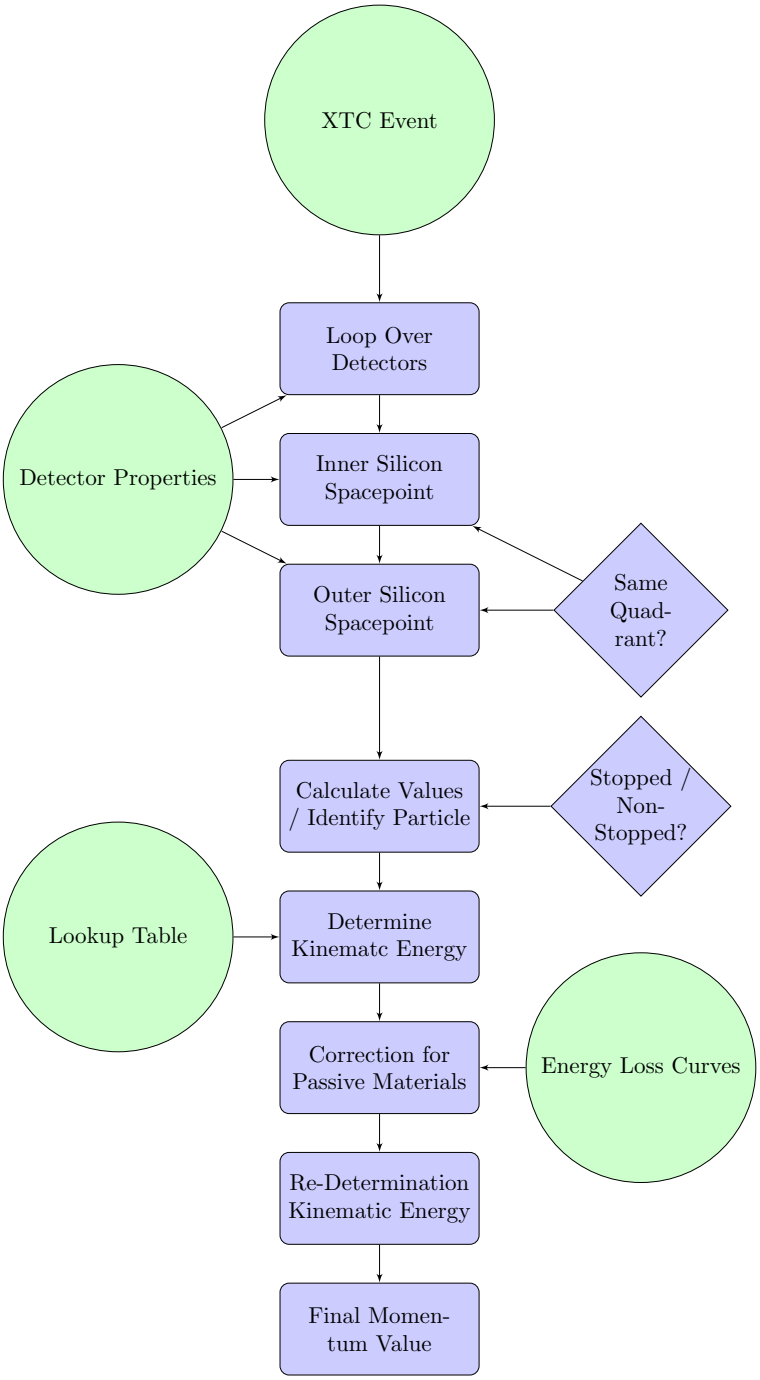

Figure 4.15: A flowchart outlining the different stages of the DER lookup table tracking subroutine. A track is identified in the SSD before the momentum of the track can be determined from the lookup table. After the initial value of momentum has been determined from the detector output a correction is made for the passive materials and the momentum re-calculated.

have been stopped within the beam pipe wall. Some of these particles have such low energy that they are stopped within the silicon sensors. The kinetic energy of these particles can be determined by summing the energy deposited in each of the sensor layers. This calculation also involves the corrections for the passive materials. As a stopped particle loses most of its energy just before it stops, this information is the dominating factor in determining the initial energy of the particle.

Due to the low energy nature of the stopped particles the passive materials are more crucial in determining an accurate value for the initial kinetic energy of the particle. The same iterative method outlined for the non-stopped particles is used in this case. In this instance only one value of kinetic energy is determined. The first step of this iterative process is to use the energy of particles stopped in the outer sensor to determine the intermediate flex foil correction. The values of the energy deposited in both sensors is then added to the flex foil correction value to give the energy immediately before the inner sensor. Using this value and the correction function for passive materials before the inner sensor the initial value of T is determined:

$$T = \Delta E_{sensor1} + \Delta E_{sensor2} + \Delta E_{intermediateflex} + \Delta E_{passive}. \tag{4.21}$$

4.6 Results

The results of the track reconstruction software using Monte Carlo simulated data are compared with the unreconstructed results of a full Monte Carlo detector simulation in order to quantify the accuracy and resolution of the reconstructed values. As the lookup table used in DER tracking is completely based on the Monte Carlo detector simulation it is necessary to ensure that the reconstructed and simulated values are compatible with each other. If this is not the case an incorrect value of momentum would be calculated using this method.

4.6.1 Energy Loss Distribution

The distribution of the energy lost in the inner silicon sensor is shown in Fig 4.16. The energy lost in the silicon is confined to a small range, 0 - 0.0035 GeV, with

the majority of the distribution having an energy loss of less than 0.0005 GeV. This region is where the lookup table most precisely determines the momentum of the recoiling proton. The distribution of the Monte Carlo and reconstructed XTC values are similar. Both are landau distributions, observed due to energy loss straggling, where energy losses are higher than the mean of the peak. The values of the reconstructed energy loss are slightly greater than for the Monte Carlo simulation due to the different way in which this value is determined. The reconstructed energy loss is recorded as one value in each silicon sensor and contains no information on any secondary processes or interactions while the simulated Monte Carlo energy loss records all the energy losses from secondary particles after the incident proton interacts with the silicon sensor individually. The Monte Carlo energy loss value is determined from the sum of all the different processes in the detector which in cases with many hundreds of separate processes being summed to give the overall energy loss within the sensor only the first 100 secondary interactions are included, leading to a smaller approximation of energy loss. The slight fluctuation in the distribution of the reconstructed data is due to two different data files being used to create the distribution one with energy less than than 0.001 GeV and the second with energy loss less than 0.001 GeV.

4.6.2 Angular and Pathlength Distributions

The pathlength of a recoiling proton through each silicon sensor is the second input to the lookup table and is determined from the incident angle to the sensor. As the SSD consists of only outer and inner active silicon layers the incident angle is effectively determined from trigonometric calculations, using the line given between the two hit coordinates in each layer where the proton encounters the detector material with respect to the normal. The distribution of this incident angle is given in Fig 4.17. The distribution of both the reconstructed data and the Monte Carlo data are similar. However, it should be noted that due to the scale of the binning used in Fig 4.17 and the inverse cosine function used to calculate the incident angle from spacepoint information of each silicon strip in the SSD causes the number of events in each bin of the distribution to fluctuate for the reconstructed data. This

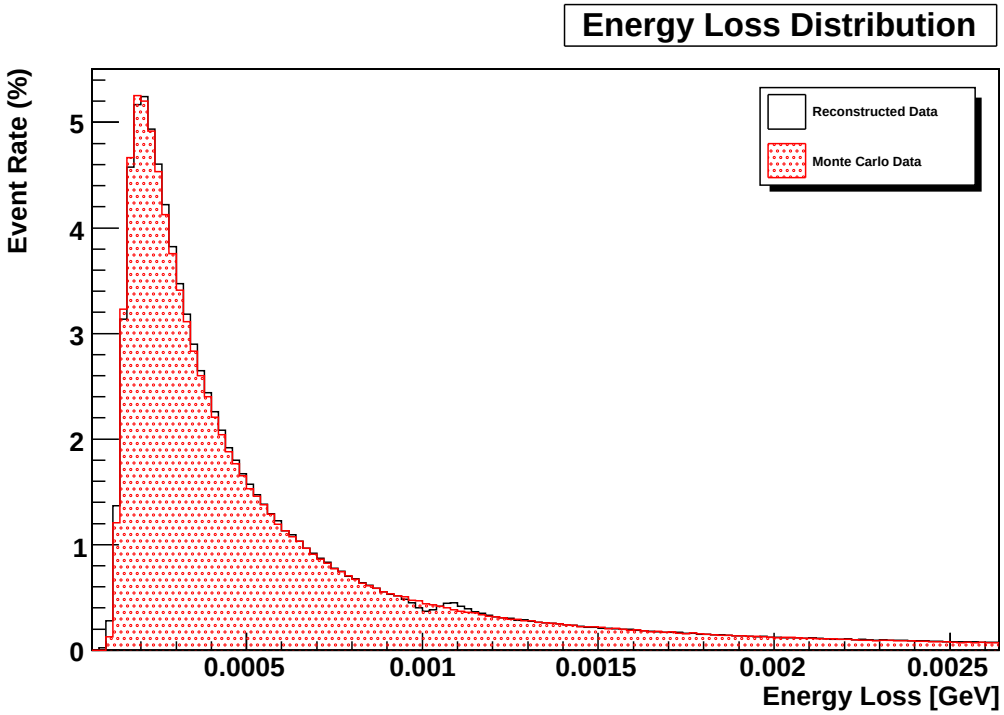

Figure 4.16: The distribution of the energy lost in the silicon sensor expressed as a percentage of the total number of events. The reconstructed data is shown as the black curve and the Monte Carlo simulation in red.

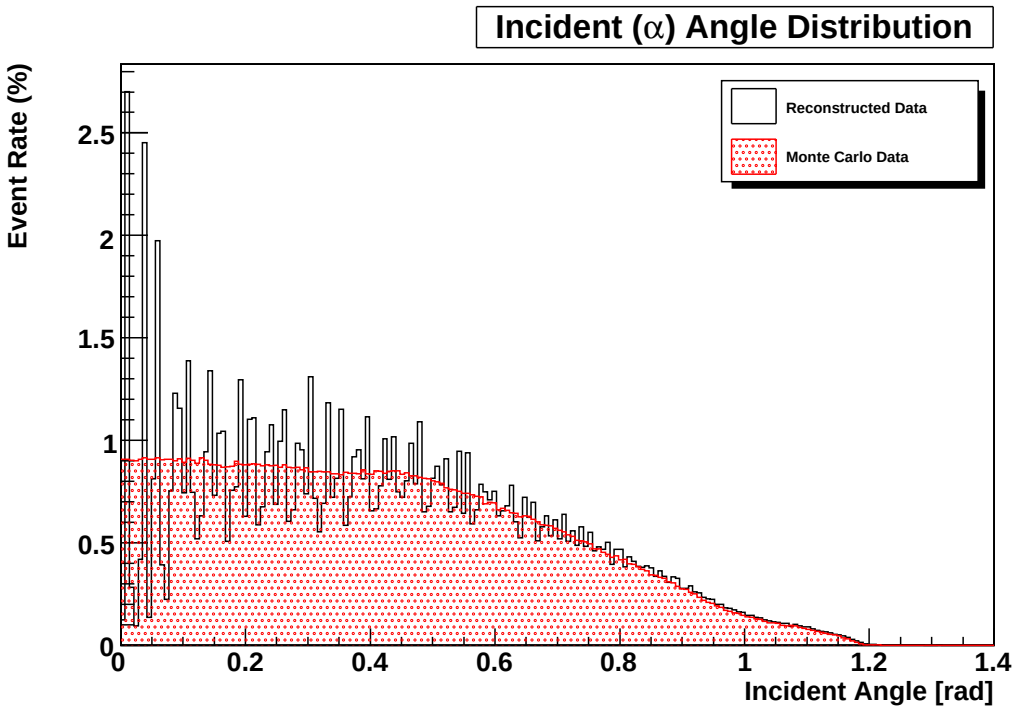

Figure 4.17: The distribution of the incident "alpha" angle to the silicon sensor expressed as a percentage of the total number of events. The reconstructed data is shown as the black curve and the Monte Carlo simulation in red.

is due to the fact that each strip in the SSD returns only one spacepoint, defined as being in the centre of the individual strip. Consequently, each strip in the SSD returns the same value for the incident angle. As the incident angle is determined for each individual strip, rather than from the precise point at which the proton interacts with the SSD sensor, results in the varying number of events with a particular value of incident angle for neighbouring bins in the histogram. The Monte Carlo simulated data does not have this limitation and returns the precise value of the spacepoint hit in each silicon sensor, hence the smooth distribution.

The pathlength is calculated from the incident angle and the thickness of each individual silicon detector; all of which are in the range 300 $\pm$ 10 μm. The distribution of the pathlength for all the silicon layers is shown in Fig 4.18. The Monte

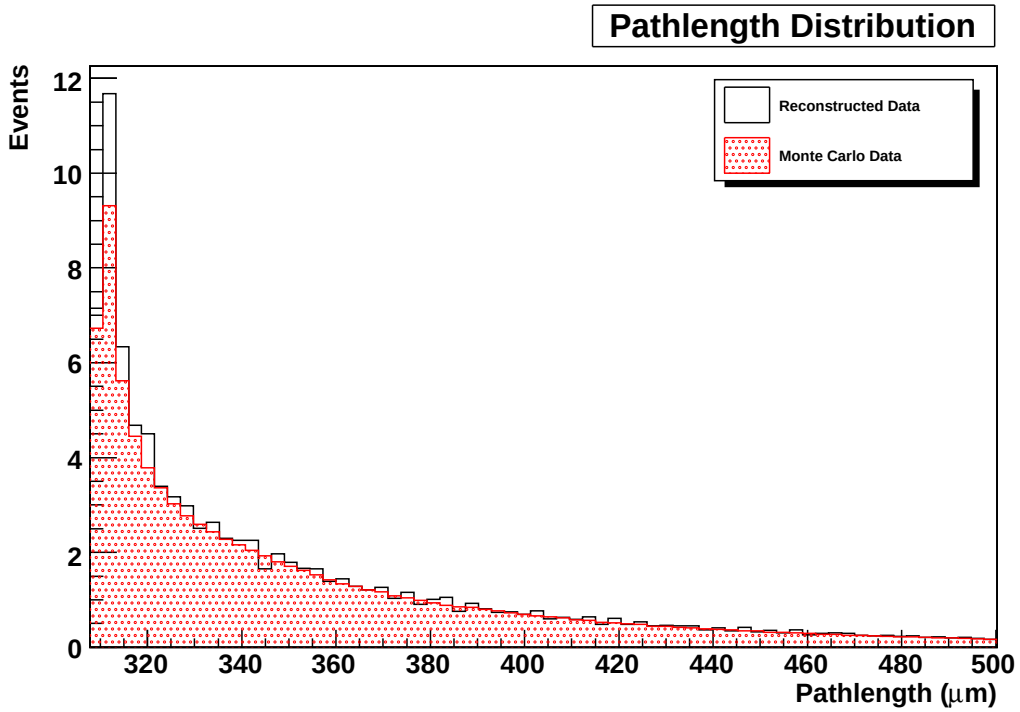

Figure 4.18: The distribution of the pathlength through the silicon sensor traversed by the recoil proton expressed as percentage of the total number of events. The reconstructed data is shown as the black curve and the Monte Carlo simulation in red.

Carlo and reconstructed data agree well with each other and the distributions have the same overall shape. Overall the pathlength calculated from reconstructed data is higher than that for Monte Carlo as seen from the incident angle distribution. This difference arises from the fact that small changes in angle can make significant changes to the cosine values obtained. The small outlying distribution at around 300 nm is due to one of the silicon sensors having a thickness of less than 300 μm.

4.6.3 Momentum Resolution

Both the inner and outer silicon sensors are used to separately determine the momentum of the recoil proton. This allows the most appropriate momentum value to be selected depending on the initial conditions of the recoil proton. For low momen-

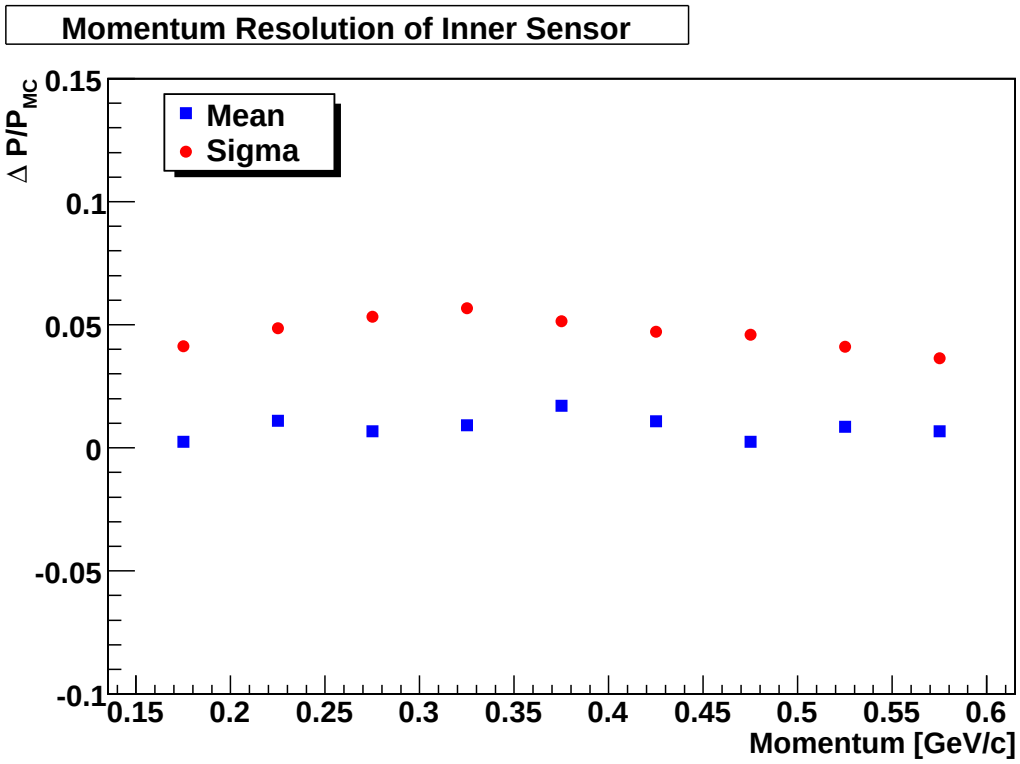

Figure 4.19: The momentum resolution of the inner silicon sensor, the σ value of a Gaussian fit to the normalised distribution of each momentum bin, is shown in red. The mean value of this fit is shown in blue. In general the momentum resolution is constant over the momentum range.

tum protons ie. those with $P < 0.4\,\mathrm{GeV/c}$, the value for the inner silicon sensor is used due to the fact that most of the energy is lost in the inner sensor, giving a more accurate momentum value than the outer sensor. For protons with $P > 0.4\,\mathrm{GeV/c}$ the reconstructed momentum values from both the silicon sensors are equally valid.

The momentum reconstruction performance using the DER tracking methods in the XTC track reconstruction software was tested using HERMES Monte Carlo data. The accuracy of the tracking software was analysed by calculating the normalised difference $(P_{REC} - P_{MC})/P_{MC}$, where P_{REC} is the reconstructed momentum value and P_{MC} the Monte Carlo value. In order to quantify the performance of the DER momentum reconstruction over the entire momentum range the normalised distribution $(P_{REC} - P_{MC})/P_{MC}$ fitted with a Gaussian function is derived for in-

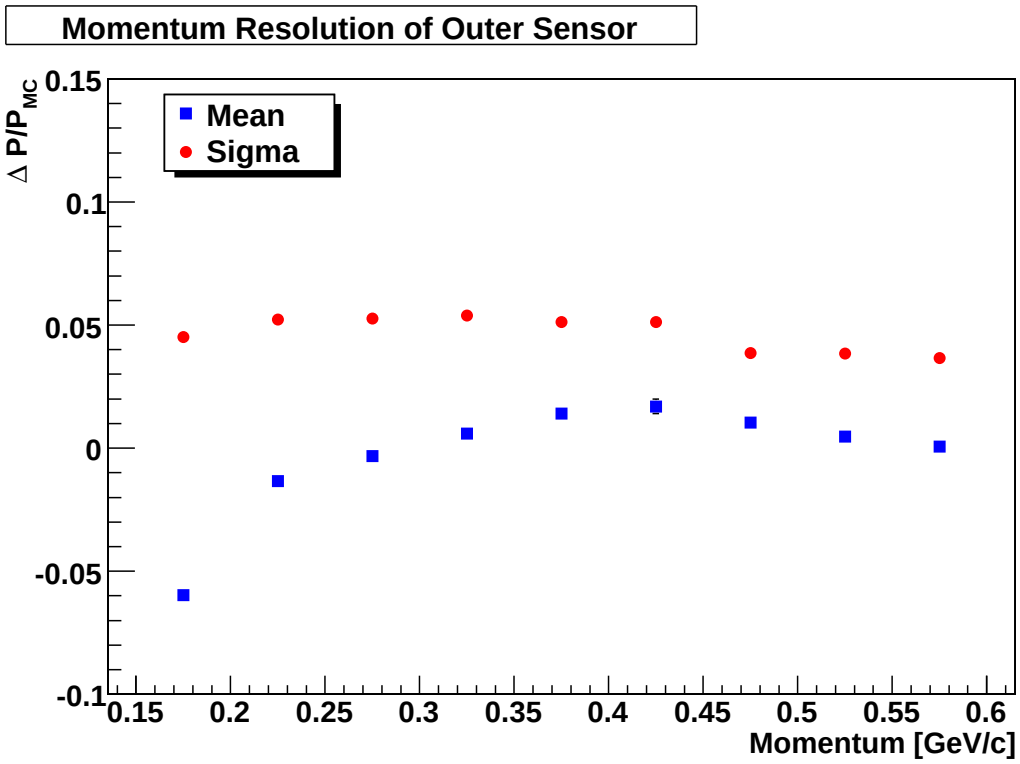

Figure 4.20: The momentum resolution of the outer silicon sensor, the σ value of a Gaussian fit to the normalised distribution of each momentum bin, is shown in red. The mean value of this fit is shown in blue. In general the momentum resolution is constant over the momentum range. The mean of the distribution is shifted at low momentum values. This is due to the fact that protons are stopped in the outer silicon sensors at low momentum values.

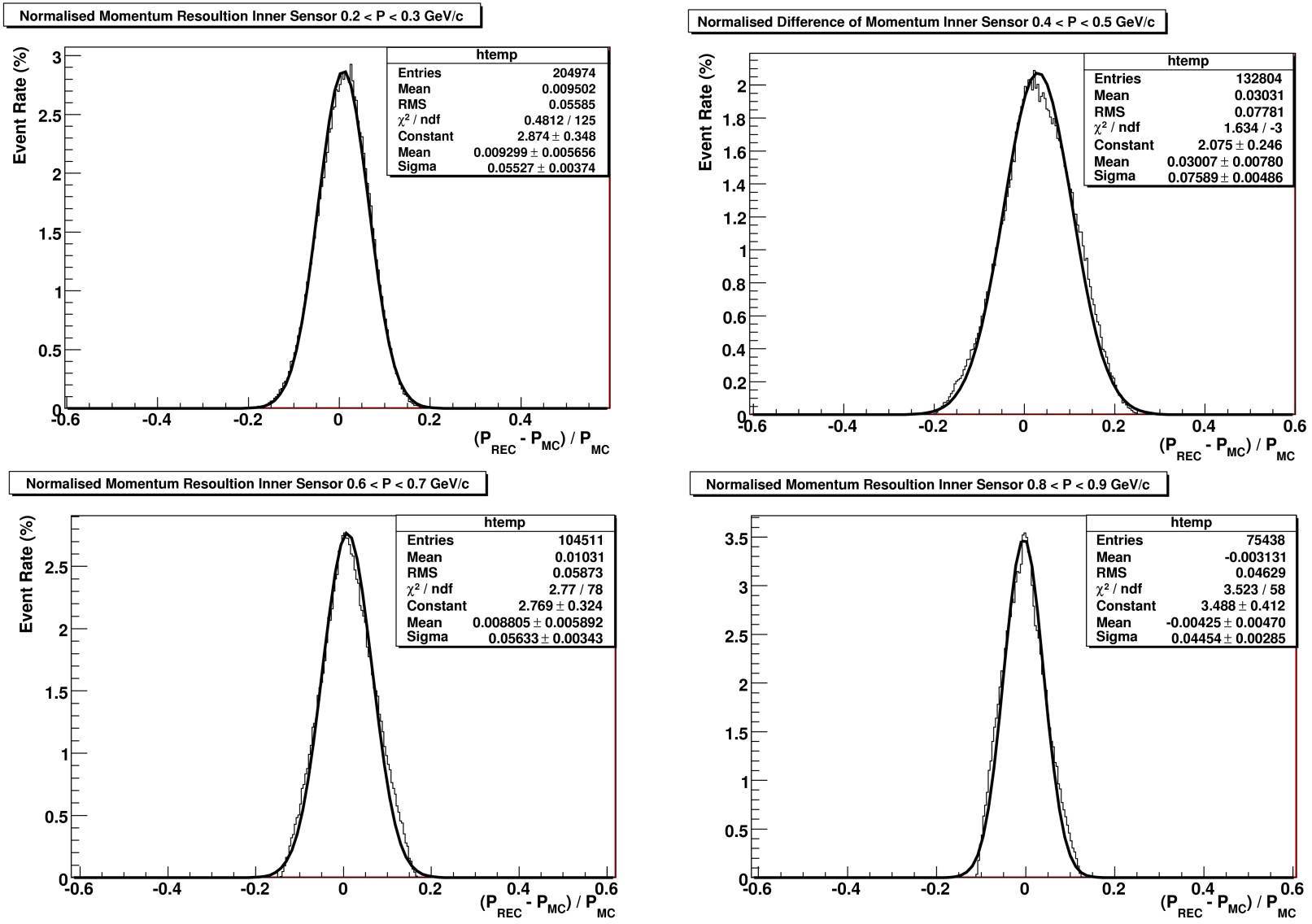

Figure 4.21: The normalised momentum distribution of the inner silicon sensor for a number of different momentum ranges: 0.2 to 0.3 GeV/c, 0.4 to 0.5 GeV/c, 0.6 to 0.7 GeV/c and 0.8 to 0.9 GeV/c. The resolution is obtained from a Gaussian fit to the distribution with the fit parameters shown.

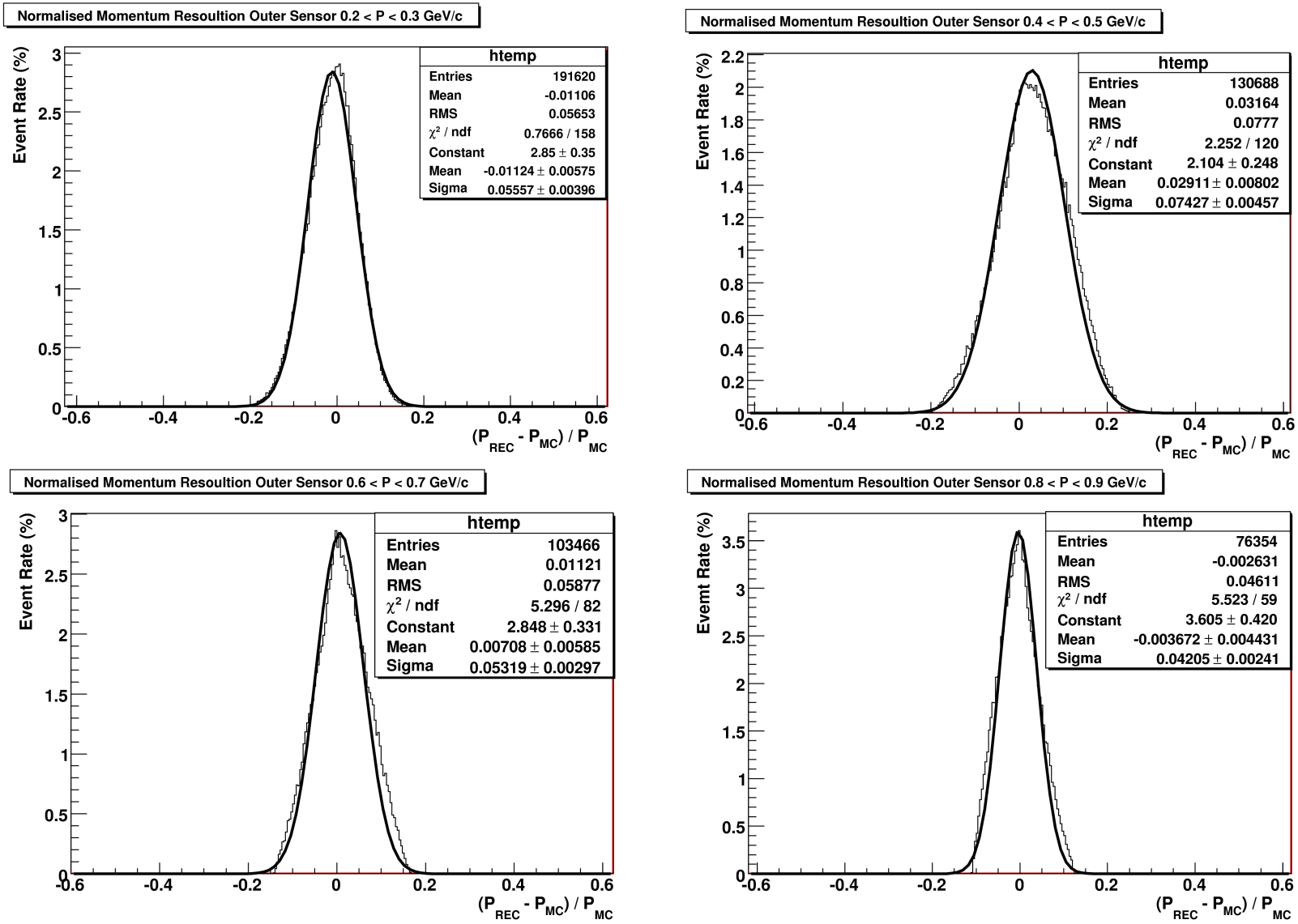

Figure 4.22: The normalised momentum distribution of the outer silicon sensor for a number of different momentum ranges: 0.2 to 0.3 GeV/c, 0.4 to 0.5 GeV/c, 0.6 to 0.7 GeV/c and 0.8 to 0.9 GeV/c. The resolution is obtained from a Gaussian fit to the distribution with the fit parameters shown.

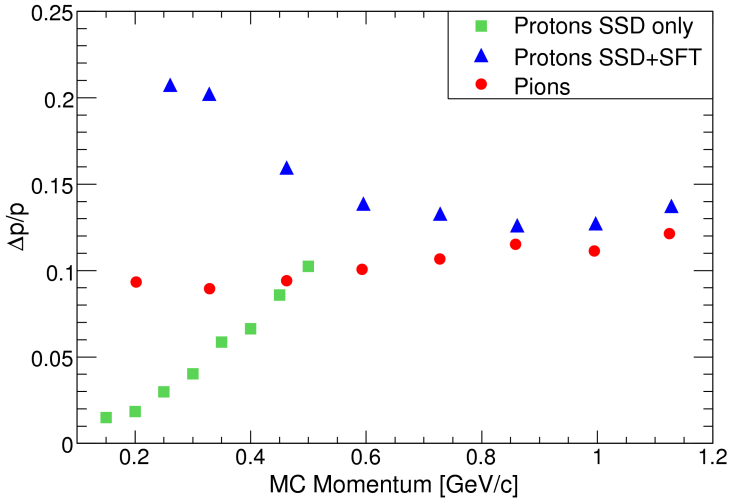

Figure 4.23: The predicted momentum resolution of the SSD and SFT taken from the HERMES Recoil Detector Technical Design Report [21]. The mean values are calculated from a Gaussian fit to the normalised distribution of each bin.

dividual bins 0.1 GeV in size. In total nine such momentum bins ranging from 0.1 to 1 GeV/c are used with the mean and resolution (σ) values from the fit of each bin shown in Figs 4.19 and 4.20 for inner and outer silicon sensors respectively. The expected SSD only resolution, determined using Monte Carlo simulations undertaken during the design of the Recoil Detector, is shown in Fig 4.23. As predicted the DER tracking is the most effective manner in which to reconstruct the momentum of protons less than 0.6 GeV/c and the tracking methods that include the SFT detector are used for values greater than 0.6 GeV/c. Four of the indiviual binned $(P_{REC} - P_{MC})/P_{MC}$ distributions of the inner and outer silicon sensors are shown in Figs 4.21 and 4.22.

The DER tracking method fulfilled all of design requirements for tracking protons with momentum values less than 0.6 GeV/c with the SSD. The tracking software has been adopted by the collaboration and is included both as the stand alone DER tracking and combined in another method which includes the SFT and PD and uses curvature in the magnetic field. The method is compared with the expectations of silicon tracking, first proposed from simulations during the design of the recoil

detector, as published in the Technical Design Report [21], as shown in Fig 4.24. The resolution of the lookup table from both silicon sensors is relatively stable, unlike the original prediction which has an increasing $\frac{\Delta P}{P}$ as the momentum value increases. The stability of the SSD tracking method is due to the line of best fit shown in Fig 4.7 used to construct the lookup table that gives equal weighting to all events in the momentum range 0 to 0.6 GeV/c. The momentum reconstruction of this SSD tracking method is the most precise that has been developed at HERMES. The $\frac{\Delta P}{P}$ value increases with momentum in the original TDR prediction of the SSD performance as it is based on fits to the energy deposit in both SSD sensors, shown in Fig 4.6. The energy deposited in each SSD sensor decreases with increasing momentum, therefore such a fit is less precise as the momentum of the recoiling proton increases. The original predicted resolution did not include other factors, such as the presence of passive materials, which although corrected for decrease the resolution of the momentum obtained, particularly for low momentum protons. Due to the high performance of the lookup table tracking method it is actively used in the HERMES tracking software and will be used for future physics analyses.

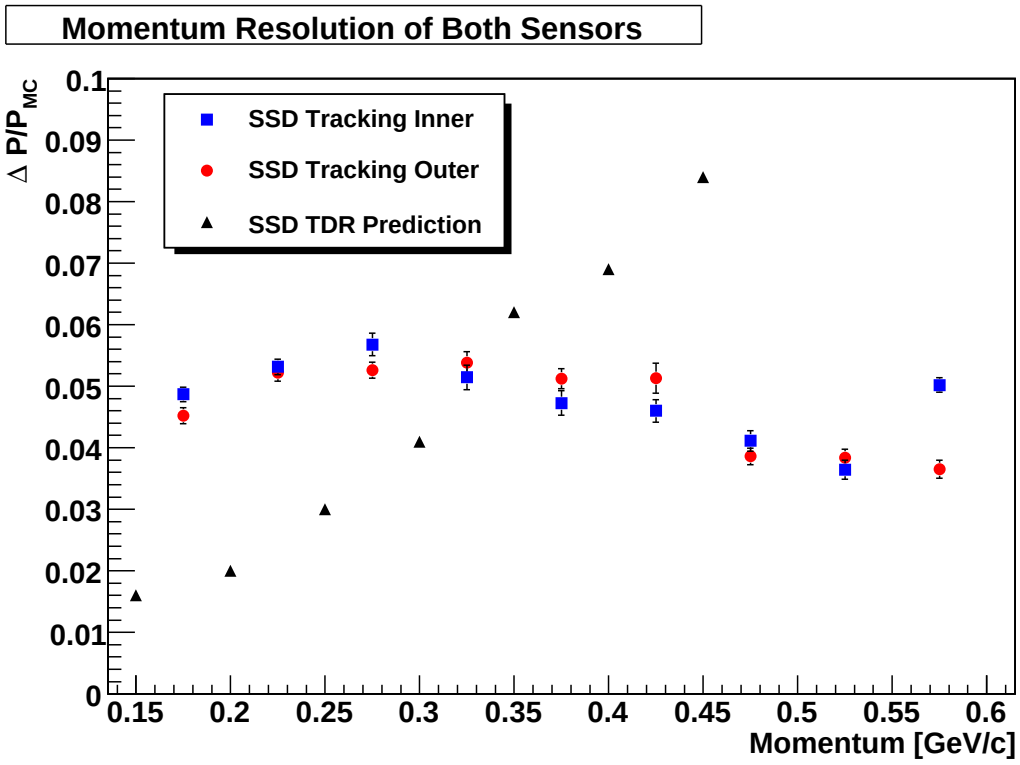

Figure 4.24: The momentum resolution of the inner and outer silicon sensors compared with the expected performance from the Technical Design Report [21].

Chapter 5

Data Analysis

This chapter details the analysis of the hydrogen target data taken during the entire running period of the HERMES experiment, from 1996 until the end of data taking in July 2007. The hydrogen target data taken after the Recoil Detector installation during 2006-2007 is analysed for the first time in this thesis. This new data provided the greatest number of analysable events at HERMES for the DVCS/BH process. The increase in statistics is due to the use of an unpolarised hydrogen target which has a greater density than the polarised target used in previous years of data taking.

5.1 Kinematic Definitions

The DVCS interaction at HERMES is shown in Fig 5.1 in which a positron or electron interacts, via a virtual photon, with a quark inside the target proton. This proton is at rest in the lab frame. The reaction products of this event are a scattered positron/electron, a recoiling proton and a real photon. The proton remains intact throughout the interaction. The reaction process is described

$$e^{\pm}(\mathbf{k}) + P(\mathbf{P}) \rightarrow e^{\pm}(\mathbf{k'}) + P(\mathbf{P'}) + \gamma(\mathbf{q'}), \tag{5.1}$$

where $e^{\pm}$ is the electron/positron beam, P the target proton and γ the real photon. The following kinematic definitions are used to describe the four momentum of the particles involved in this interaction: $\mathbf{k}$ is the four momentum of the beam positron/electron, $\mathbf{P}$ is the four momentum of the target proton at rest, $\mathbf{q}$ is the four

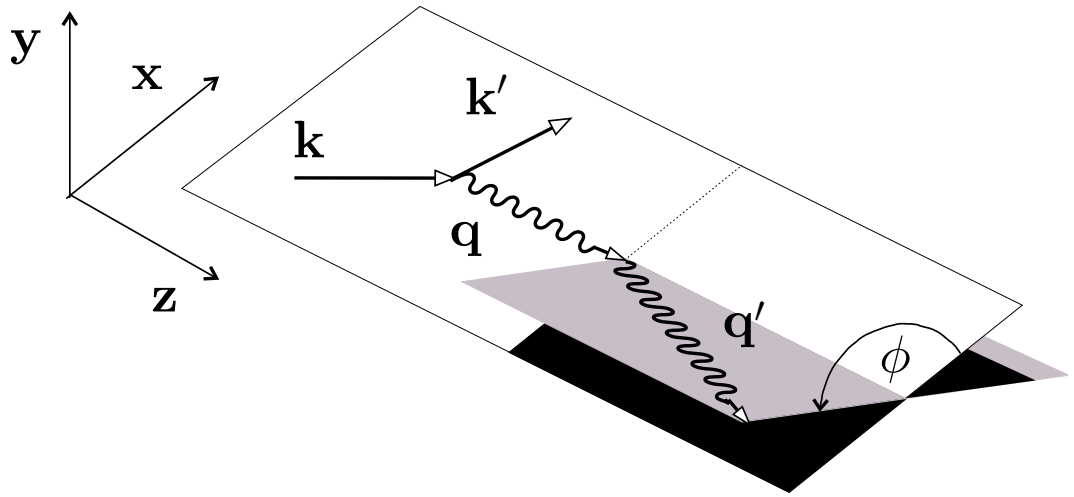

Figure 5.1: The DVCS process on an unpolarised target in the HERMES coordinate system [88]. The angle ϕ is defined as the azimuthal angle between the photo-production and lepton-scattering plane. The incoming lepton with four momenta **k** interacts with the target proton via a virtual photon with four momenta **q** leaving the scattered lepton with four momenta **k'** and a produced photon with four momenta **q'**.

momentum of the virtual photon, **k'** is the four momentum of the scattered lepton detected in the forward spectrometer, **q'** is the four momentum of the real photon detected in the forward spectrometer, **P'** is the four momentum of the scattered proton.

The scattering angle ϕ shown in Fig 5.1 is defined as the azimuthal angle between the lepton-scattering and photo-production planes of the virtual and real photons respectively, i.e.

$$\phi = \frac{\overrightarrow{q} \times \overrightarrow{k} \cdot \overrightarrow{q'}}{|\overrightarrow{q} \times \overrightarrow{k} \cdot \overrightarrow{q'}|} \cdot cos^{-1}\left(\frac{\overrightarrow{q} \times \overrightarrow{k}}{|\overrightarrow{q} \times \overrightarrow{k}|} \cdot \frac{\overrightarrow{q} \times \overrightarrow{q'}}{|\overrightarrow{q} \times \overrightarrow{q'}|}\right). \tag{5.2}$$

The asymmetry results produced at HERMES are binned in three kinematic variables Q^2, x_B and t. The variables Q^2, x_B and the energy loss of the scattered lepton ν have been defined in Section 2.2.2. The photon virtuality Q^2 is calculable directly from the difference between the four-momenta of the initial and scattered leptons. The Mandlestam variable t is calculated as the difference in the four-momenta of the protons or photons in the interaction

$$t = (\mathbf{P} - \mathbf{P'})^2 = (\mathbf{q} - \mathbf{q'})^2 \cong -Q^2 - 2E_\gamma(\nu - \sqrt{\nu^2 + Q^2}cos\theta_{\gamma^*\gamma}), \tag{5.3}$$

where E_γ is the energy of the produced photon and $\theta_{\gamma^*\gamma}$ is the polar angle between the virtual and produced photons, defined as

$$\theta_{\gamma^*\gamma} = cos^{-1}\frac{\overrightarrow{q} \cdot \overrightarrow{q'}}{|\overrightarrow{q}||\overrightarrow{q'}|}. \tag{5.4}$$

If the proton is not detected, as in the analysis presented in this thesis, t is calculated using the reconstructed energy of the real photon. The momentum of the scattered proton in the interaction is identified by calculating the missing mass in the interaction written as

$$M_x^2 = (\mathbf{q} + \mathbf{P} - \mathbf{q'})^2 = M_p^2 + 2M_p(\nu - E_\gamma) + t. \tag{5.5}$$

Assuming that in an elastic process $M_x \equiv M_p$, the mass of the proton, the photon energy can be calculated as

$$E_\gamma = \frac{t}{2M_p} + \nu. \tag{5.6}$$

E_γ can be substituted into Eq 5.3 allowing a constrained t to be calculated.

$$t = \frac{-Q^2 - 2\nu(\nu - \sqrt{\nu^2 + Q^2}cos\theta_{\gamma^*\gamma})}{1 + \frac{1}{M_p}(\nu - \sqrt{\nu^2 + Q^2}cos\theta_{\gamma^*\gamma})}. \tag{5.7}$$

This is independent of the energy measurement of the produced photon, i.e. the only measurement of the photon momentum is provided by the calorimeter with a resolution of approximately 5%. This is an order of magnitude higher than the resolution of the equivalent electron/position momentum measurement. The angle $\theta_{\gamma^*\gamma}$ is calculated from the measurement of the position of the photon in the calorimeter which is a more precise measurement.

The squared invariant mass W of the final hadronic state can be written as

$$W^2 = (\mathbf{P} + \mathbf{q})^2 \cong M_p^2 + 2M_p\nu - Q^2. \tag{5.8}$$

In order to identify exclusive events a cut is placed on the squared missing mass, M_x^2 defined in Eq 5.5. The cut is defined so that the remaining missing mass spectrum is the region in which it could be expected that a proton would be found in the HERMES resolution.

5.2 Data Selection

5.2.1 Data Quality Checks and Criteria

The data at HERMES is recorded at the run, burst and event level as illustrated in Fig 5.2. Different criteria ("cuts") are introduced at each stage of the analysis chain to ensure that the data is of sufficient quality to be analysed. The first of these cuts are applied at the run level. Thirty two individual cuts are applied to each run represented by a hexadecimal number, called a bad bit pattern. The same bad bit pattern is applied to the data from each individual year, including the 2006 and 2007 productions, if the information from the Recoil Detector is not used for event rejection.

The bad bit pattern used is 0x501e03dc, which contains the following criteria:

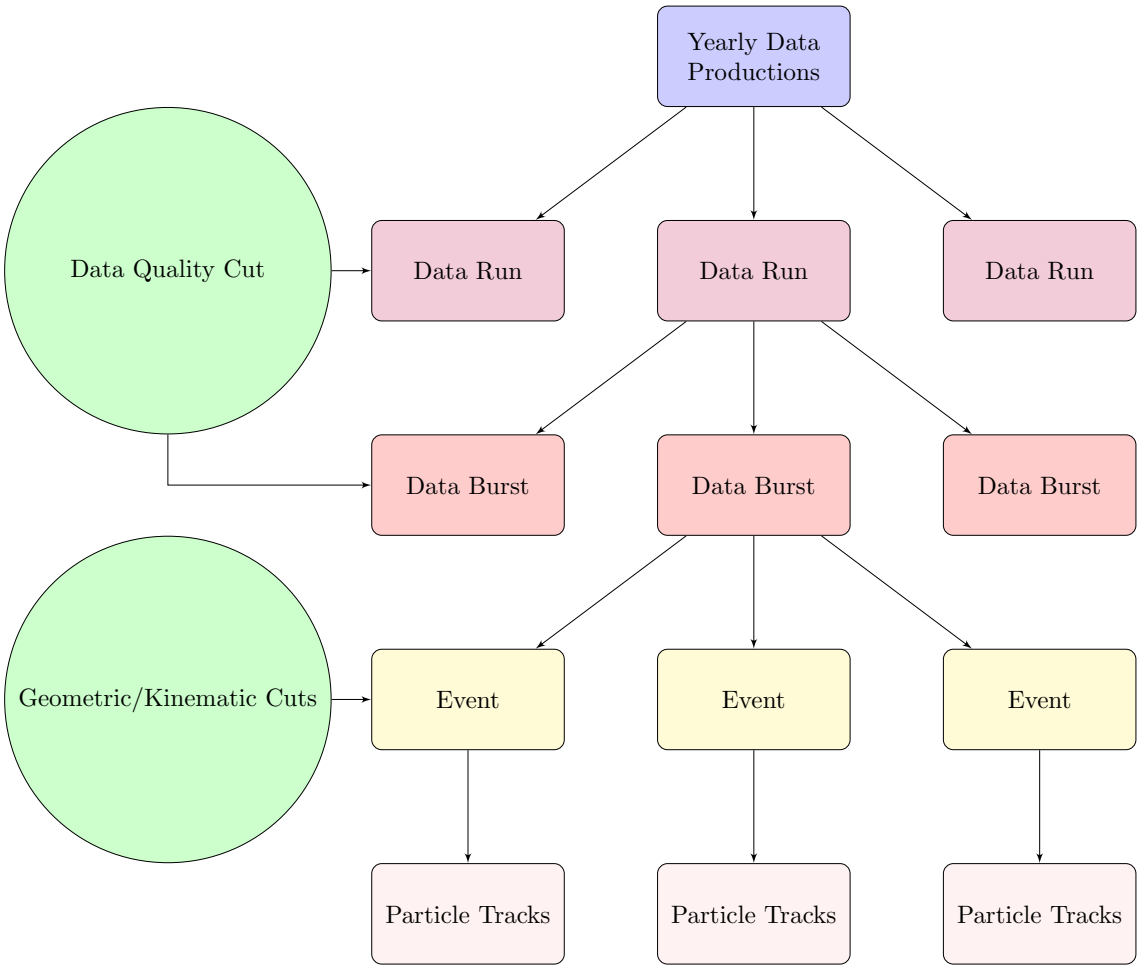

Figure 5.2: A flowchart giving an overview of the data productions at HERMES. A data production is generated for each year individually at HERMES. The data is described on the run, burst and event level as described in chapter 2. Data quality cuts can be made on these individual levels.

- The trigger 21 dead time is not unphysical. This is the main physics event trigger and relates to the energy deposition in the calorimeter and signals in the H0, H1 and H2 hodoscopes.
- The burst length L is within $0 < L \leq 11$ seconds.
- The beam current is between 2 and 50 mA. The lower cut on the beam current discards data with lower count rates. The upper cut discards data with unphysically high currents.
- The burst was not the first in a run. This excludes events recorded during the rise time of the detectors.
- There is no bad μDST record. This cut discards data that are part of the last burst in a fill with reconstructed events. In addition data are discarded which are considered bad due to synchronisation problems, burst or event number jumps or table overflows.
- The PID values were available. This cut discards data with no available PID due to initialisation problems or an unknown Calorimeter threshold.
- The run was marked as analysable. This cut accepts only runs that are marked analysable in the logbook as noted by the shift crew during data taking.
- The latest beam polarisation measurement was made within the last 5 minutes.

The following criteria are detector specific and check that the detector concerned was operational.

- There are no dead blocks in the Calorimeter
- There are no dead blocks in H3 or the Lumi detector
- The Transition Radiation Detector (TRD) was operating
- No High Voltage trips in the FCs or BCs

An additional criteria is applied to the 1996 data production which rejects events where the calorimeter was not performing correctly. Some other data quality cuts applied in addition to the bad bit pattern, are:

- There has been a beam polarisation measurement and events are rejected if the beam polarimeter was not operational. ($g1DAQ.bProdMethod$&0x00800 != 0x00800).
- The beam polarisation measurement is within the range accurately recorded by the beam polarimeter. ($0 < |g1Beam.rPolFit| < 1$).
- TRD was operational in both the top and bottom halves of the spectrometer ($g1Quality.iTrdDQ == 3$).
- The raw luminosity count rate is within the specified limit ($5 < g1Beam.rLumiRate < 3000$).
- The DAQ lifetime is reasonable i.e. the DAQ software was operational for more than 80% of each burst. ($0.8 < g1DAQ.rDeadCorr21 < 1.0$).

Following the application of these data quality criteria, additional restrictions are introduced to select the events that are applicable for this analysis. The first additional step is to remove the events that are detected in, or originate from, unphysical regions of the HERMES experiment due to deflections within the spectrometer. These events are removed by introducing criteria based on the geometry of the spectrometer:

- The vertex position of the interaction originated within the long target cell for data taken between 1996 and 2005 i.e. -18 $\leqslant z_{vx} \leqslant$ 18 cm.
- The vertex position of the interaction originated within the short target cell for data taken in 2006 and 2007 i.e. $0 \leqslant z_{vx} \leqslant 20$ cm.
- The closest transverse distance to the vertex is $0 \leqslant t_{vx} \leqslant 0.75$ cm. This limit ensures that the event originates from the target cell by removing events originating from outside the target cell.

- The energy deposition of the scattered lepton is detected within the fiducial volume of the calorimeter. The struck region of the calorimeter satisfies $|x^{e^{\pm}}_{calo}| < 175\,\text{cm}$ and $30\,\text{cm} < |y^{e^{\pm}}_{calo}| < 108\,\text{cm}$.

- The polar angle between the virtual and real photon is within the limit $5\,\text{mrad} < \theta_{\gamma^*\gamma} < 45\,\text{mrad}$. The azimuthal angle ϕ is not defined below the lower limit due to the finite resolution of the spectrometer. Above the upper limit Monte Carlo studies have shown that an event sample is dominated by background events [89].

- The lepton is not deflected by the septum magnet plates in the spectrometer. This is achieved by placing limits on the measured slopes and spatial offsets of the lepton track. These are:
  $|x_{offset} + 172 * tan\theta_x| < 31\,\text{cm}$,
  $|y_{offset} + 181 * tan\theta_y| < 7\,\text{cm}$,
  $|y_{offset} + 383 * tan\theta_y| < 54\,\text{cm}$,
  $|x_{pos} + 108 * x_{slope}| \leq 100\,\text{cm}$,
  $|y_{pos} + 108 * y_{slope}| \leq 54\,\text{cm}$.

The DVCS/BH event sample is a subset of the DIS sample at HERMES. The DIS sample is determined using the following criteria:

- A scattered lepton is identified using the PID limitation ($2 < g1Track.PID2 + g1Track.PID5 < 100$).

- The scattered lepton has the same charge as the lepton beam.

- Trigger 21 has fired identifying that a physics event has occured in the detector.

- The beam energy is greater than 27 GeV.

- The correct track reconstruction method is used for the scattered lepton i.e. the lepton is tracked by all the tracking detectors in the spectrometer ($(g1Track.iSelect\&0x0100)$ && $(g1Track.iSelect\&0x0200)$).

- $Q^2 > 1\,\text{GeV}^2$ ensures the applicability of factorisation.

- $W^2 > 9\,\mathrm{GeV}^2$ is the kinematic limitation in which the Monte Carlo fragmentation operates correctly. This models allows the background processes to be estimated and removed from the event sample.

- $\nu < 22\,\mathrm{GeV}$ eliminates events in which the efficiency of the photon energy reconstruction is dubious.

In addition to the identification of a charged lepton in the spectrometer it is also necessary to detect one photon in the calorimeter to distinguish a DIS event from the recorded data. The photon is measured using the following limitations on the recorded cluster:

- $E_\gamma > 5\,\mathrm{GeV}$ ensures the photon is of sufficient energy to be accurately reconstructed in the calorimeter and eliminates some background processes that could contaminate the event sample.

- $E_{preshower} > 1\,\mathrm{MeV}$ is the minimum energy required in the preshower detector to ensure that an electromagnetic shower is produced in the calorimeter allowing the energy of the photon to be accurately reconstructed.

- The energy deposition of the real photon is contained within the fiducial volume of the calorimeter. This limitation is different from the criteria used to identify the scattered lepton due to the positional differences of photon and lepton clusters in the calorimeter due to the bending of the lepton allowing a bigger detection range. The photon energy deposit is detected within the limit $|x^\gamma_{calo}| < 125\,\mathrm{cm}$ and $33\,\mathrm{cm} < |y^\gamma_{calo}| < 105\,\mathrm{cm}$.

The DVCS/BH ($ep \to e\gamma p$) events are identified by imposing additional criteria on the DIS event sample. The criteria are:

- Each event contained exactly one photon measured as an untracked cluster in the calorimeter.

- $-t < 0.7\,\mathrm{GeV}^2$ is used to eliminate background events contaminating the analysed sample. Monte Carlo studies have shown that background processes dominate at higher values of $-t$ [89].

$-t$	0.00 - 0.03	0.03 - 0.06	0.06 - 0.10	0.10 - 0.20	0.20 - 0.35	0.35 - 0.70	GeV^2
x_B	0.03 - 0.06	0.06 - 0.08	0.08 - 0.10	0.10 - 0.13	0.13 - 0.20	0.20 - 0.35	
Q^2	1.00 -1.40	1.40 - 1.80 -	1.80 - 2.40	2.40 - 3.20	3.20 - 4.50	4.50 - 10.00	GeV^2

Table 5.1: The $-t$, x_B and Q^2 binning used in this analysis

- $Q^2 < 10\,\text{GeV}^2$ and $0.03 < x_B < 0.35$ define the kinematic region for the binning variables used in this analysis. These limits reject few DVCS candidate events.
- An additional limit is placed on the missing mass of the interaction, consistent with the mass of the proton, in order to identify DVCS/BH events. This is detailed in Section 5.4.3 and is year-independent.

The criteria listed in this section are applied to the entire hydrogen data set over the HERMES experiment's operational lifetime. The Beam Charge (BCA) and Beam Helicity Asymmetries (BHA) are extracted from the resulting DVCS/BH event sample.

5.2.2 Binning of DVCS Asymmetries

The quantity of DVCS/BH events recorded after the installation of the Recoil Detector is very much greater than that of the previous years of data taking, with the 2006 and 2007 data sets containing approximately 32000 and 25000 DVCS/BH events respectively. Asymmetry amplitudes are extracted from the DVCS/BH event sample over a range of $-t$, x_B and Q^2. The data sample is divided into six bins containing approximately equal numbers of DVCS/BH events from which the asymmetry amplitudes are extracted. The kinematic range of each bin is based on the experimental resolution of each variable, as defined by Monte Carlo studies [90]. The size of each bin used to plot asymmetry data is detailed in Table 5.1.

5.3 Extraction Method

As described previously in section 2.5, this thesis contains both a single extraction of the Beam Helicity Asymmetry and the combined extraction of the Beam Charge and the Beam Helicity Interference and DVCS amplitudes. The Maximum Likelihood method for simultaneous extraction of the BHA and BCA and the single charge extraction of the BHA used for current DVCS analyses at HERMES was originally proposed in [91].

5.3.1 Maximum Likelihood Fitting

The first DVCS asymmetry results were produced at HERMES using the Least Squares fitting technique. Using this technique involved fitting the ϕ-binned distribution of the extracted DVCS data. The Maximum Likelihood method was introduced so that the fit could be made to individual data points without introducing potential errors from binning the data in histograms, used in the extraction of amplitudes with the Least Squares method. Maximum Likelihood fitting also allowed the simultaneous extraction of the A_{LU} asymmetry amplitudes induced by the interference and pure DVCS contributions separately at the same time as the A_C amplitudes. The Extended Maximum Likelihood method used in this analysis was selected as it gives the correct values for the asymmetries when constant terms are used in the function that is minimised and this method takes into account that the total number of observed DVCS/BH events is a Poisson Distribution [91]. The fitting function used describes the theoretical dependence of the asymmetries on ϕ. A comparison of the single charge BHA results extracted from 2006 positron, 2006 electron and 2007 positron is detailed in Chapter 6.4.

The likelihood function for a set of N independent data points $\mathbf{x}_i = \{-t, x_B, Q^2, \phi\}$ is determined from the probability density function (p.d.f.) $p(\mathbf{x};\theta)$ depending on a set of m unknown parameters θ is

$$\mathscr{L}(\theta) = \prod_i^N p(\mathbf{x}_i;\theta). \tag{5.9}$$

The values of the parameter set θ are determined by maximising the likelihood func-

tion $\mathscr{L}(\theta)$. The likelihood equations are solved for the logarithm of the likelihood equations i.e.

$$\frac{\partial \ln \mathscr{L}}{\partial \theta_j} = 0, j = 1, ..., m. \tag{5.10}$$

The distribution of events around the angle ϕ are observed to have a Poisson distribution about the expected value θ. To take this distribution into account, the maximum likelihood function is "extended" to include the Poisson p.d.f. $\frac{\mathbb{N}^N e^{-\mathbb{N}}}{N!}$,

$$\mathscr{L}(\theta) = \frac{[\mathbb{N}(\theta)]^N e^{-\mathbb{N}(\theta)}}{N!} \prod_i^N p(\mathbf{x}_i; \theta). \tag{5.11}$$

known as the Extended Maximum Likelihood (EML) function. The N is the expected number of events and $\mathbb{N}(\theta)$ can be interpreted as the normalisation of the extended p.d.f. $\mathscr{P}(\mathbf{x}; \theta) \equiv p(\mathbf{x}; \theta)\mathbb{N}(\theta)$ i.e.

$$\mathbb{N}(\theta) = \int \mathscr{P}(\mathbf{x}; \theta) d\mathbf{x}. \tag{5.12}$$

In practice, maximising the likelihood function leads to a large value due to the large number of DVCS/BH events analysed. A large product of small values may lead to rounding errors during the asymmetry extraction. The negative log-likelihood method is used as a solution to this problem at the same parameters θ as the maximum likelihood. The negative log-likelihood functions to be minimised is,

$$-\ln \mathscr{L}_{EML}(\theta) = -\sum_i^N ln\mathscr{P}(\mathbf{x}_i; \theta) + \mathbb{N}(\theta). \tag{5.13}$$

The number of events available at HERMES are constrained by the data taking period, dictated by the use of the HERA accelerator, and the luminosity. Studies described in [92], have shown that the EML method is the most suitable for use at HERMES as the normalisation is not dependent on a fixed number of events. The EML method is also shown to be more consistent with the Least Squares method. The Standard Maximum Likelihood (SML) is not used as it was found to overestimate the uncertainty of a constant term included in the fit function [91].

5.3.2 Extraction of the Single Charge BHA

The BHA-only extraction is independent of beam charge. The extended probability density function of the total observed exclusive events in x and P reads

$$\mathcal{N}(\mathbf{x}; P; \theta) = \mathcal{L}(P)\epsilon(\mathbf{x}, P)\sigma_{UU}(\mathbf{x})[1 + PA_{LU}(\mathbf{x}; \theta)], \tag{5.14}$$

where $\mathcal{L}$ is the luminosity, A_{LU} the asymmetry around the azimuthal angle ϕ, ϵ the detection efficiency and σ_{UU} the cross section for an unpolarised target. The normalisation reads

$$\mathbb{N}(\theta) = \iint \mathcal{N}(\mathbf{x}, P, \theta) d\mathbf{x} dP, \tag{5.15}$$

and can be approximated in the case that detector efficiency is set to unity as

$$\mathbb{N}(\theta) = \frac{\mathbb{L}}{\overrightarrow{\mathbb{L}}} \frac{\sum_i^{\overrightarrow{N}} [1 + \langle P \rangle A_{LU}(\mathbf{x_i}; \theta)]}{\left[1 - \frac{\langle \overrightarrow{P} \rangle}{\langle \overleftarrow{P} \rangle}\right]} + \frac{\mathbb{L}}{\overleftarrow{\mathbb{L}}} \frac{\sum_i^{\overleftarrow{N}} [1 + \langle P \rangle A_{LU}(\mathbf{x_i}; \theta)]}{\left[1 - \frac{\langle \overleftarrow{P} \rangle}{\langle \overrightarrow{P} \rangle}\right]} \tag{5.16}$$

where N is the observed number of exclusive events, $\mathbb{L}$ is the integrated luminosity $\mathbb{L} = \int \mathcal{L}(P) dP = \int L(t) dt$ and $\langle P \rangle$ is the avarge polarisation with $\rightarrow$ ($\leftarrow$) the positive (negative) polarisation. The standard p.d.f is

$$p(\mathbf{x}; P; \theta) = \frac{\mathcal{N}(\mathbf{x}, P; \theta)}{\mathbb{N}(\theta)}. \tag{5.17}$$

The negative log-likelihood function $-\ln \ell(\theta)$ for the EML method, which is minimised during the extraction procedure, is given as

$$-\ln \mathscr{L}_{EML}(\theta) = -\sum_i^N \ln[1 + P_i A_{LU}(\mathbf{x}_i; \theta)] + \mathbb{N}(\theta), \tag{5.18}$$

The asymmetry amplitudes are dependent on the azimuthal angle ϕ in both the numerator and the denominator. The fit function allows the physical interpretation of the Fourier coefficients decomposing the involved amplitudes. The following decomposition function is used to extract the Beam Helicity Asymmetry

$$A_{LU}(\mathbf{x}; \theta) = A_{LU}^{cos0\phi} + A_{LU}^{sin\phi} sin(\phi) + A_{LU}^{cos\phi} cos(\phi) + A_{LU}^{sin2\phi} sin(2\phi). \tag{5.19}$$

The coefficients used in this function are "asymmetry amplitude's" and should not be identified as Fourier coefficients.

5.3.3 Simultaneous Extraction of BCA and BHA

The simultaneous extraction of the BHA and BCA amplitudes is implemented in a similar manner to the previous section. In order to extract the BCA the beam charge terms are also included in the cross section. The extended p.d.f of the exclusive events in $\mathbf{x}$, P and η reads

$$\mathcal{N}(\mathbf{x}, P, \eta; \theta) = L(P, \eta)\epsilon(\mathbf{x}, P, \eta)\sigma^0_{UU}(\mathbf{x})[1+\eta A_C(\mathbf{x};\theta)+PA^{DVCS}_{LU}(\mathbf{x};\theta)+\eta P A^I_{LU}(\mathbf{x};\theta)] \tag{5.20}$$

where $\mathcal{L}$ is the integrated luminosity, η the detector efficiency, σ^0_{UU} the unpolarised cross section averaged over both beam charges and A_C, A^{DVCS}_{LU} and A^I_{LU} the asymmetries in the azimuthal angle ϕ. The deduction of the normalisation

$$\mathbb{N}(\theta) = \iint_{\eta=1} \mathcal{N}(\mathbf{x}, P, \eta, \theta) d\mathbf{x} dP + \iint_{\eta=-1} \mathcal{N}(\mathbf{x}, P, \eta, \theta) d\mathbf{x} dP, \tag{5.21}$$

in the extraction of the asymmetry amplitudes when the detector efficiency is set to unity. The normalisation can therefore, be approximated as

$$\mathbb{N}(\theta) = \sum_i^N K(P_i, \eta_i)[M_1 + M_2 A_C(\mathbf{x}_i;\theta) + M_3 A^{DVCS}_{LU}(\mathbf{x}_i;\theta) + M_4 A^I_{LU}(\mathbf{x}_i;\theta)], \tag{5.22}$$

with

$$\begin{aligned} K(P,\eta) = &\frac{1}{2}\frac{1}{\overrightarrow{\mathcal{L}}^+}\frac{1}{1-\langle\overrightarrow{P}^+\rangle/\langle\overleftarrow{P}^+\rangle}(P>0,\eta=1),\\ &\frac{1}{2}\frac{1}{\overleftarrow{\mathcal{L}}^+}\frac{1}{1-\langle\overleftarrow{P}^+\rangle/\langle\overrightarrow{P}^+\rangle}(P<0,\eta=1),\\ &\frac{1}{2}\frac{1}{\overrightarrow{\mathcal{L}}^-}\frac{1}{1-\langle\overrightarrow{P}^-\rangle/\langle\overleftarrow{P}^-\rangle}(P>0,\eta=-1),\\ &\frac{1}{2}\frac{1}{\overleftarrow{\mathcal{L}}^-}\frac{1}{1-\langle\overleftarrow{P}^-\rangle/\langle\overrightarrow{P}^-\rangle}(P>0,\eta=-1), \end{aligned} \tag{5.23}$$

and

$$M_1 = \mathbb{L}^+ + \mathbb{L}^-, \tag{5.24}$$

$$M_2 = \mathbb{L}^+ - \mathbb{L}^-, \tag{5.25}$$

$$M_3 = \mathbb{L}^+\langle P^+\rangle + \mathbb{L}^-\langle P^-\rangle, \tag{5.26}$$

$$M_4 = \mathbb{L}^+\langle P^+\rangle - \mathbb{L}^-\langle P^-\rangle, \tag{5.27}$$

where + (−) is the beam charge, → (←) the positive (negative) beam polarisation and $\langle P\rangle$ the average polarisation. The weights are used to account for luminosity imbalances with respect to the beam charge and polarisation. In practice, these quantities were normalised using the number of DIS events listed in Table 5.3. The negative log-likelihood function $-\ln\mathscr{L}(\theta)$ of the EML method, minimised during the asymmetry extraction procedure is given as

$$-\ln\mathscr{L}_{EML}(\theta) = -\sum_i^N \ln[1 + \eta_i A_C(\mathbf{x}_i;\theta) + P_i A_{LU}^{DVCS}(\mathbf{x}_i;\theta) + \eta_i P_i A_{LU}^{I}(\mathbf{x}_i;\theta)] + \mathbb{N}(\theta). \tag{5.28}$$

The asymmetries are extracted from the data using the MINUIT package contained in the ROOT analysis framework developed at CERN [93] for high energy particle physics experiments such as HERMES.

In order to extract the combined BCA and BHA amplitudes the following decomposition is used

$$A_C(\mathbf{x}_i;\theta) = A_C^{cos0\phi} + A_C^{sin\phi}sin(\phi) + A_C^{cos\phi}cos(\phi) + A_C^{cos2\phi}cos(2\phi) + A_C^{cos3\phi}cos(3\phi), \tag{5.29}$$

$$A_{LU,DVCS}(\mathbf{x}_i;\theta) = A_{LU,DVCS}^{cos0\phi} + A_{LU,DVCS}^{sin\phi}sin(\phi) + A_{LU,DVCS}^{cos\phi}cos(\phi) + A_{LU,DVCS}^{sin2\phi}sin(2\phi), \tag{5.30}$$

$$A_{LU,I}(\mathbf{x}_i;\theta) = A_{LU,I}^{cos0\phi} + A_{LU,I}^{sin\phi}sin(\phi) + A_{LU,I}^{cos\phi}cos(\phi) + A_{LU,I}^{sin2\phi}sin(2\phi). \tag{5.31}$$

The minimisation of this function is used to extract the BHA and BCA asymmetry amplitudes. The Fourier coefficients of the BHA and BCA are related to the amplitude of each asymmetry, as detailed in Section 2.6.2

5.4 Systematic Studies

5.4.1 Comparison of the 10 and 13 Parameter Fit Functions

The asymmetry results have been obtained by extracting the parameters of the fits outlined in the previous section. The BHA is dependent on $\sin(n\phi)$ and the BCA on $\cos(n\phi)$ at leading order. In addition to the expected physics motivated harmonics the 13 parameter fit includes non-physical sine and cosine terms in the BCA and BHA amplitudes respectively as a consistency of fit test. The additional terms which are not physical are expected to be zero if the fit has been normalised correctly. In order to show that this is the case and that these extra parameters do not affect the analysis the asymmetry amplitudes were extracted using a fit with (13 parameter) and without (10 parameter) these terms. The 10 parameter fit minimised is:

$$A_C = A_C^{cos0\phi} + A_C^{cos\phi} cos(\phi) + A_C^{cos2\phi} cos(2\phi) + A_C^{cos3\phi} cos(3\phi), \tag{5.32}$$

$$A_{LU,DVCS} = A_{LU,DVCS}^{cos0\phi} + A_{LU,DVCS}^{sin\phi} sin(\phi) + A_{LU,DVCS}^{sin2\phi} sin(2\phi), \tag{5.33}$$

$$A_{LU,I} = A_{LU,I}^{cos0\phi} + A_{LU,I}^{sin\phi} sin(\phi) + A_{LU,I}^{sin2\phi} sin(2\phi). \tag{5.34}$$

The asymmetry amplitudes extracted from 2006 and 2007 unpolarised hydrogen data using both fits are shown in Figs 5.3, 5.4 and 5.5. This is a first check of the fitting function and is not yet corrected for known detector effects.

The presence of the "check" terms causes some slight fluctuations in the amplitude of the extracted asymmetries. The kinematic dependence of the extracted amplitudes over the range of $-t$, x_B and Q^2 values is identical using both fits. Due to the overall compatibility of the amplitudes, the function used to extract the asymmetries is seen to be stable and in all other work presented the 13 parameter fit is used.

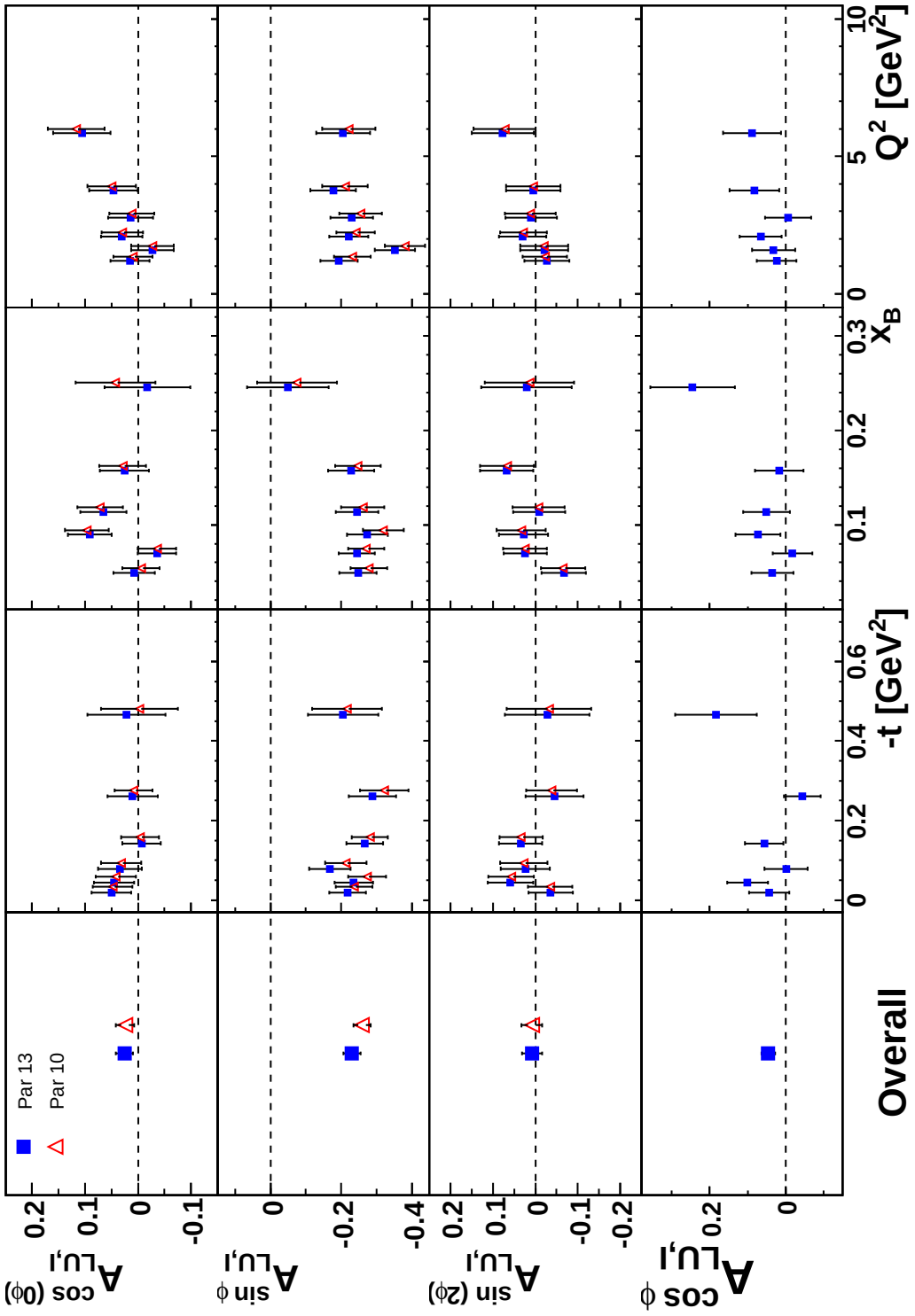

Figure 5.3: The results of the BHA amplitudes from the interference term using the 13 and 10 parameter fitting functions. No significant influence on the physically-motivated asymmetries can be ascribed to the number of parameters in the fit.

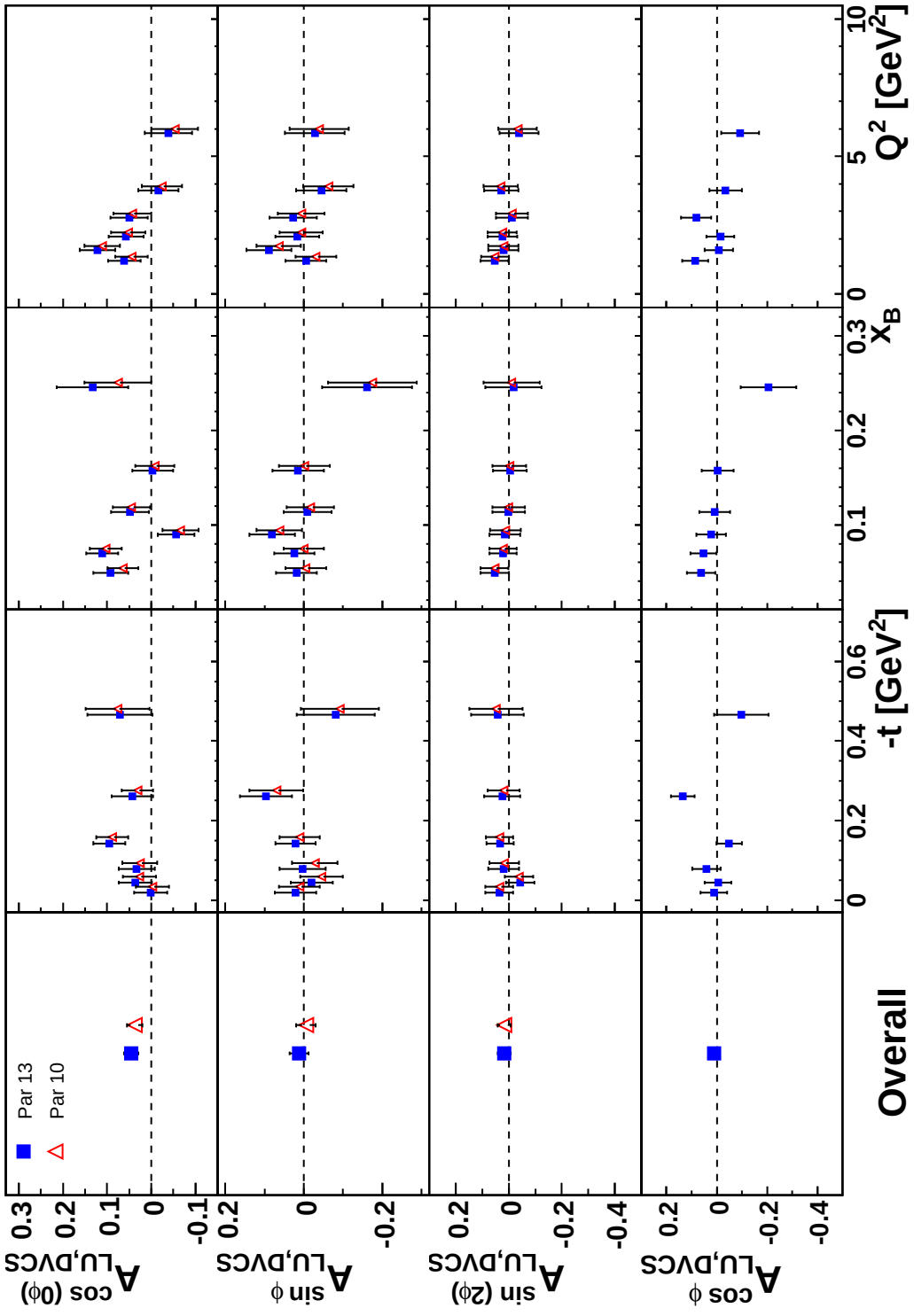

Figure 5.4: The results of the BHA amplitudes from the DVCS squared term using the 13 and 10 parameter fitting functions. No significant influence on the physically-motivated asymmetries can be ascribed to the number of parameters in the fit.

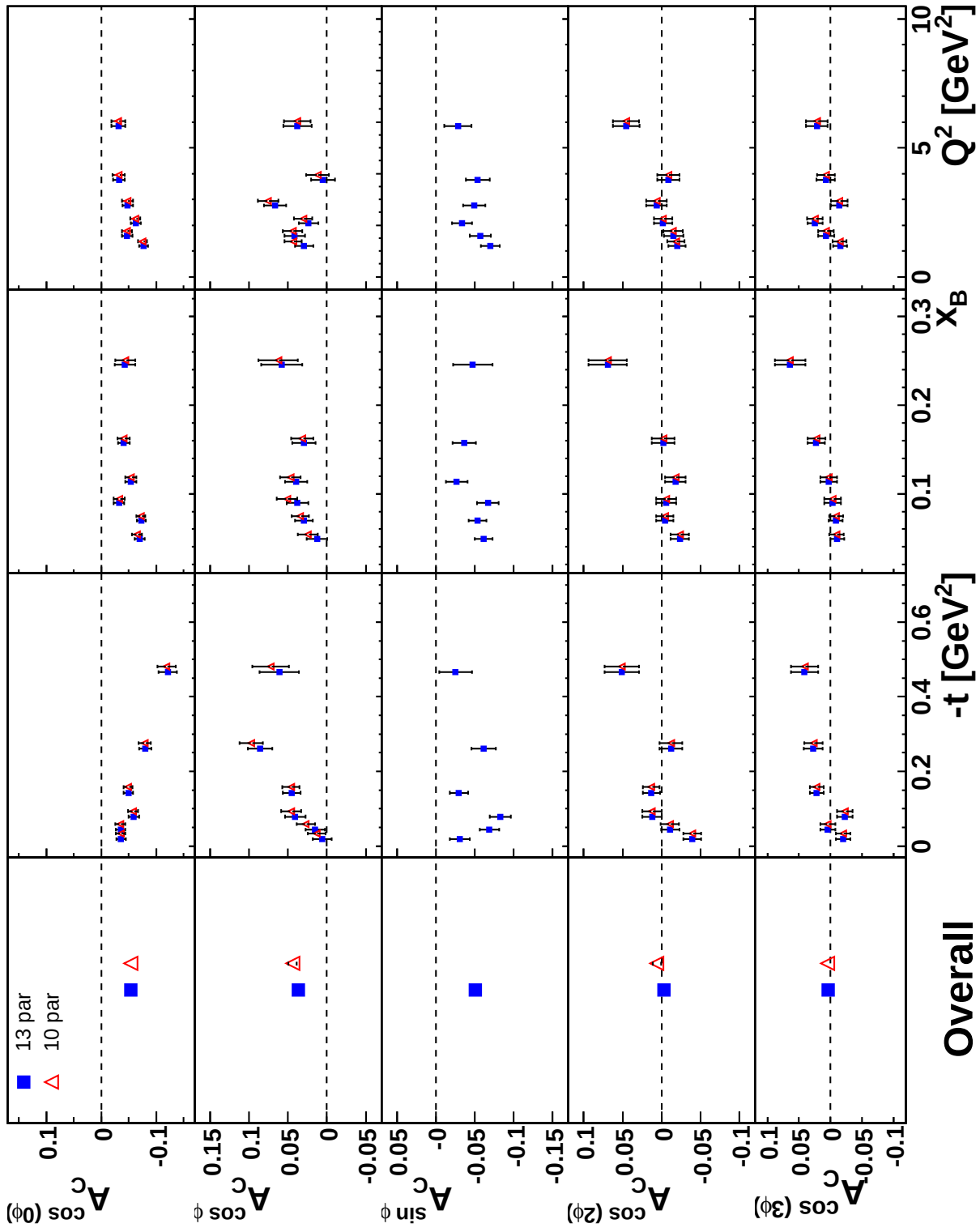

Figure 5.5: The results of the BCA amplitudes using the 13 and 10 parameter fitting functions. No significant influence on the physically-motivated asymmetries can be ascribed to the number of parameters in the fit.

5.4.2 Cross-Check of Data Sample and Results

In order to verify that the identification of DVCS/BH events in each of the data taking years was performed correctly, a cross check was performed with Dietmar Zeiler of Erlangen University. The number of DVCS/BH events identified is identical and the DIS events agree to within 0.05%. The results of this cross-check are presented in Table 5.2.

μDST	Helicity	N_{DVCS}		N_{DIS}		BPol $\langle P \rangle$ [%]	
		D. Zeiler	This Work	D. Zeiler	This Work	D. Zeiler	This Work
96d0	+	1212	1212	829629	829755	50.1466%	50.1466%
96d0	-	0	0	0	0	0%	0%
96d0-p	+	553	553	366465	366538	51.2768%	51.2767%
96d0-p	-	0	0	0	0	0%	0%
97d1	+	0	0	0	0	0%	0%
97d1	-	1652	1652	1168350	1168735	-52.4756%	-52.4756%
97d1-p	+	384	384	3176888	317975	49.6752%	49.6750%
97d1-p	-	1638	1638	1213566	1213840	53.0786%	53.0786%
98d0	+	0	0	0	0	0%	0%
98d0	-	702	702	479389	479469	-30.1470%	-30.1475%
00d2	+	2791	2791	1887579	1887874	53.6930%	53.6930%
00d2	-	4905	4983	3187375	3237320	-55.0303%	-55.0413%
03c0-p	+	396	396	277064	275756	32.1466%	32.1441%
03c0-p	-	0	0	0	0	0%	0%
04c1	+	161	161	109725	109747	33.8550%	33.8554%
04c1	-	0	0	0	0	0%	0%
04c1-p	+	1794	1794	1207353	1207095	32.5564%	32.5566%
04c1-p	-	1433	1433	928162	927962	-40.2725%	-40.2727%
05c1	+	392	392	232497	232532	21.0862%	21.0863%
05c1	-	283	283	181052	181082	-28.3204%	-28.3204%
05c1-p	+	2626	2626	1748896	1748355	33.5334%	33.5339%
05c1-p	-	3817	3817	2466635	2465845	-28.5221%	-28.5220%
06e1	+	29472	29472	17078917	17083751	34.6391%	34.6489%
06e1	-	9238	9238	5148126	5149508	31.8751%	-31.8750%
07c2	+	16205	16205	9355212	9357851	45.9619%	45.9618%
07c2	-	12630	12630	7971616	7973788	-39.6629%	-39.6629%

Table 5.2: The number of DVCS/BH events (N_{DVCS}), DIS events (N_{DIS}) and average beam polarisation $\langle P \rangle$ for each of the data taking years with a hydrogen target. The results from D.Zeiler and the work presented in this thesis are in excellent agreement.

	Total DVCS/BH events	Total DIS events
1996 - 2005 (old)	24817	16649880
2006 - 2007 (new)	67815	39564898
Ratio (new / old)	2.73	2.38

Table 5.3: The number of DIS and DVCS/BH events available from the 1996 - 2005 and the 2006 - 2007 data taking periods. The number of DVCS/BH events is weighted using the beam polarisation. The analysable events is more than double that of the previous analysis as seen in the ratio of the "new" 2006-2007 events and "old" 1996-2005 events

The inclusion of the 2006 and 2007 data has more than doubled the number of DVCS/BH events available compared with data taken from 1996-2005. The overall increase in statistics is summarised in Table 5.3.

The asymmetries from 2006 and 2007 hydrogen data, extracted independently by each analyst, are shown in Figs 5.6, 5.7 and 5.8. The results obtained from the cross-checked DVCS/BH event sample are in agreement and show identical dependence on the kinematic variables $-t$, x_B and Q^2. The statistical uncertainties of the fit in both cases are consistent.

5.4.3 Missing Mass Window Shift

Two independent BHA and BCA results were analysed; the first extracted from the new 2006-2007 data and the second using all the hydrogen data taken from 1996 until 2007. As the experimental configuration itself has changed during the lifetime of HERMES, the data taken from individual years is compared to identify changes that could affect the analysis procedure and experimental results. The average value of the missing mass M_x, i.e. the value of the missing mass consistent with the proton and used to identify DVCS/BH events, has been observed to change over the lifetime of the HERMES experiment. This effect could be due to detector misalignment. The window was altered slightly for different data taking periods to reflect alterations to the experimental setup and different beam charges. The most dramatic change

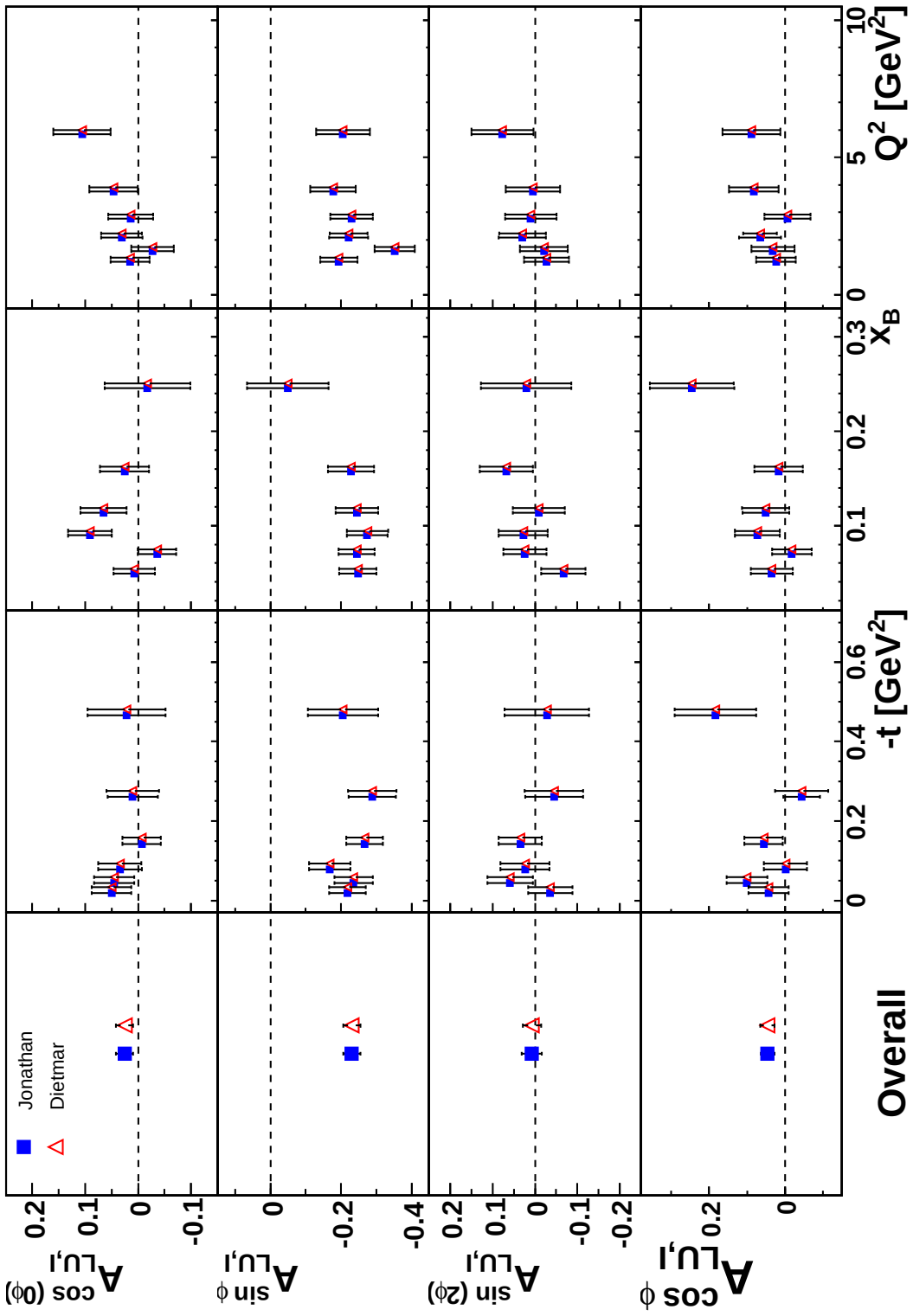

Figure 5.6: The cross-checked results of the BHA amplitudes from the interference term data using the 13 parameter fitting functions. The extracted asymmetry amplitudes are in excellent agreement.

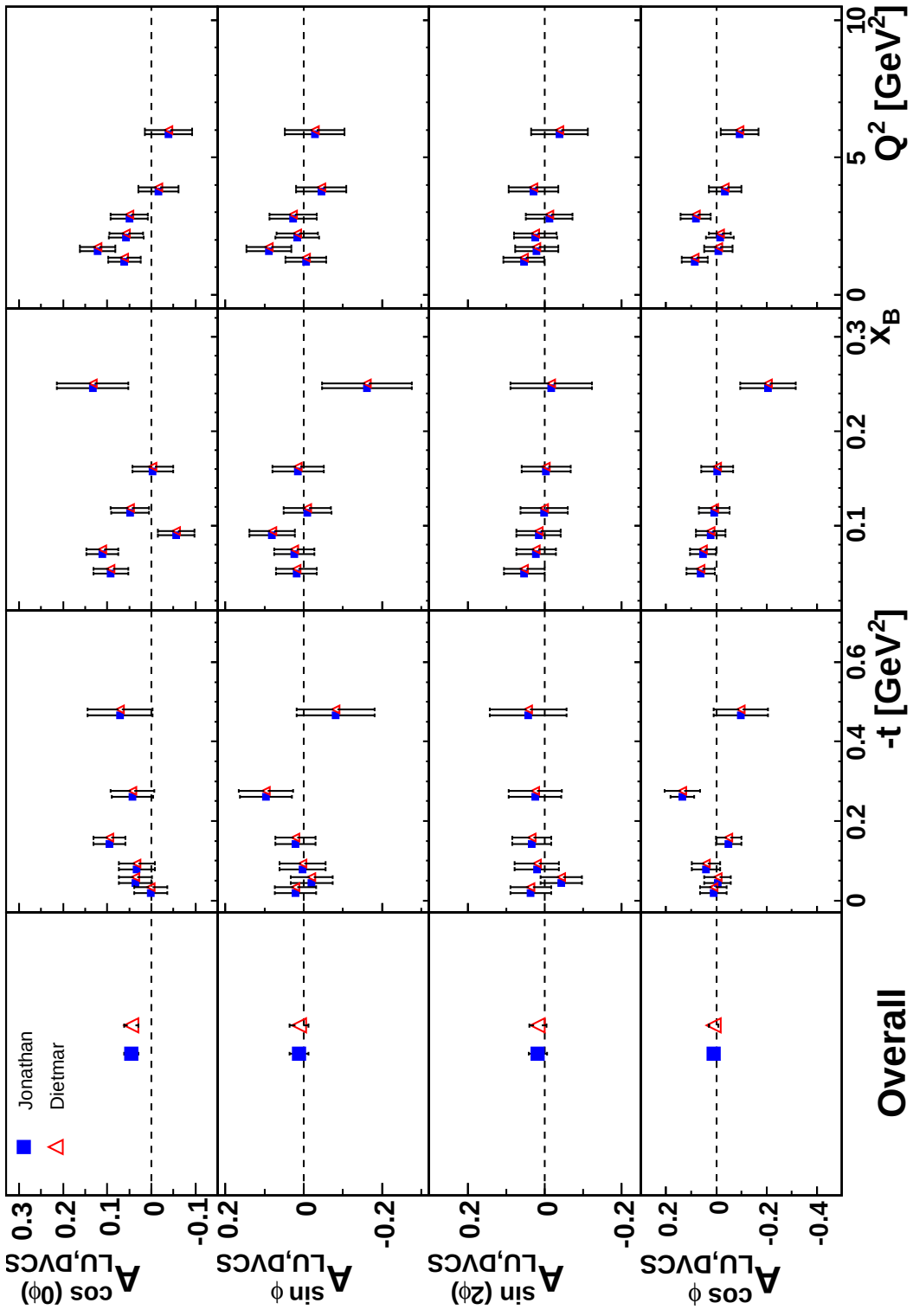

Figure 5.7: The cross-checked results of the BHA amplitudes from the DVCS squared term using the 13 parameter fitting functions. The extracted asymmetry amplitudes are in excellent agreement.

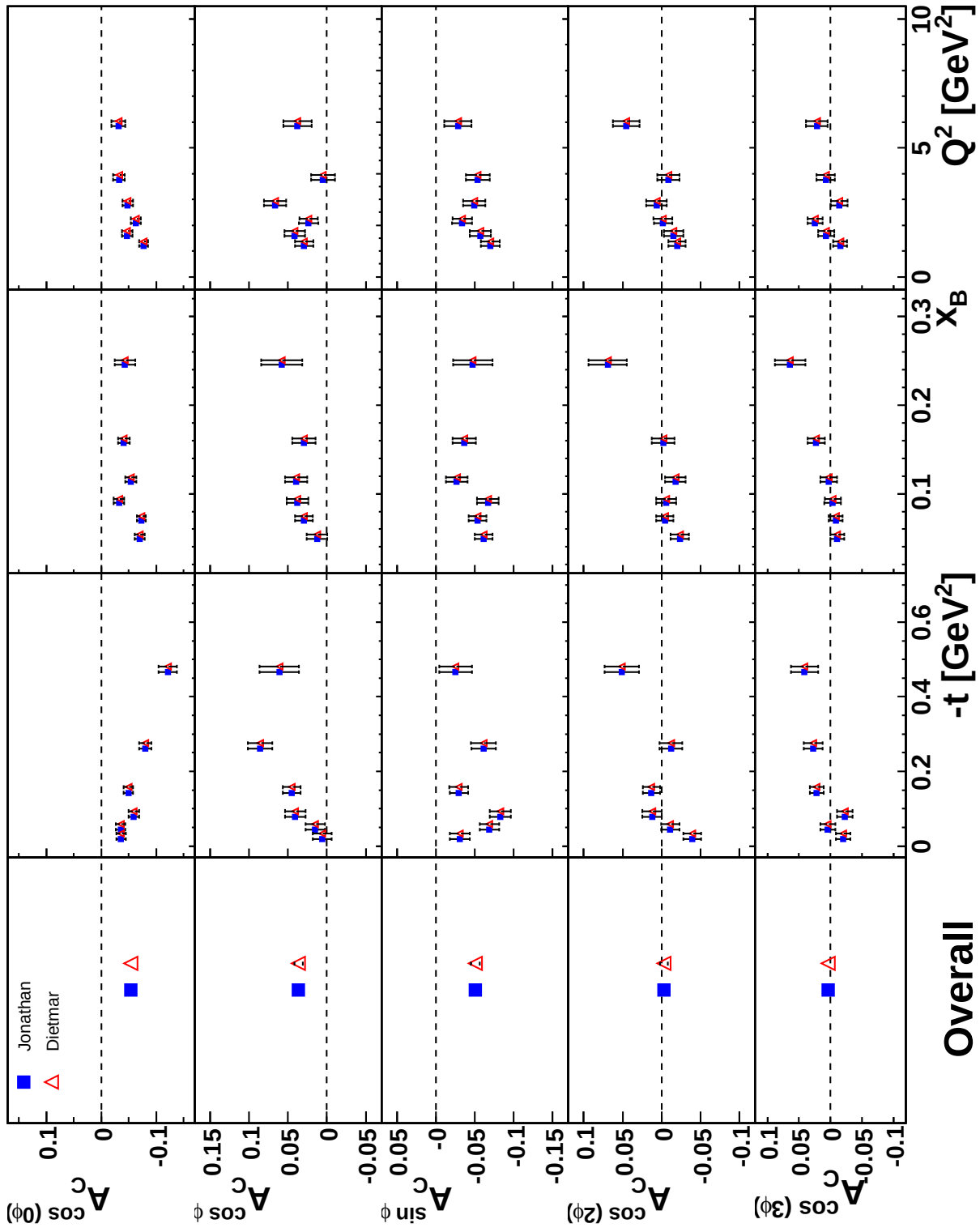

Figure 5.8: The cross-checked results of the BCA amplitudes data using the 13 parameter fitting functions. The extracted asymmetry amplitudes are in excellent agreement.

in the detector setup was in 2005 when the Recoil Detector was installed and the target cell was moved in z by 12.5 cm and shortened to 20 cm [21]. In order to verify that the asymmetry amplitudes were unaffected by spectrometer alterations, the extracted results from data taken before and after installation were compared, in Section 6.2.

In order to identify exclusive events, a cut is placed on the missing mass defined in Eq 5.5. In the analysis presented the recoiling proton from an exclusive event remains undetected as the analysis was performed using only information from the forward spectrometer. The event is identified by using a specific range or "window" defined around the square of the proton mass $(0.938\ \text{GeV})^2$. As the missing mass resolution is restricted by the resolution of the photon energy measurement in the calorimeter the range of the distribution is quite broad, including negative values. The missing mass was calculated as

$$M_x = \sqrt{|M_x^2|}. \tag{5.35}$$

The missing mass window used to determine exclusive events is identified over a range in M_x^2 of $-2.25 < M_x^2 < 2.89\ \text{GeV}^2$. This cut was obtained from a Monte Carlo simulation that resulted in a resolution of $\delta M_x^2 = 1.840\ \text{GeV}^2$ at a peak position of $1.502\ \text{GeV}^2$. This error was propagated as:

$$\delta M_x = \frac{dM_x}{M_x^2} \cdot \delta M_x^2 = \frac{1}{2M_x} \cdot \delta M_x^2 = 0.8\text{GeV}. \tag{5.36}$$

The asymmetric exclusive window chosen is $[M_p^2 - 3\sigma, M_p^2 + 1\sigma]$ around the squared proton mass M_p^2. In practice, this window is shifted for different years of data taking with the change in the peak of the missing mass which was not constant from year to year. The width of the missing mass distribution σ is consistent for all periods of data taking with the exception of 1996-1997. The change in σ after 1997 is attributed to the installation of the RICH detector in 1998.

It has been observed that the missing mass peaks for electron and positron data are shifted with respect to each other [94, 19, 47, 42, 95]. The missing mass window is, therefore, calculated for separate electron and positron periods. The pre-recoil data was split into four time periods, each with a different missing mass window. These periods are summarised in Table 5.4. The two years when data was taken

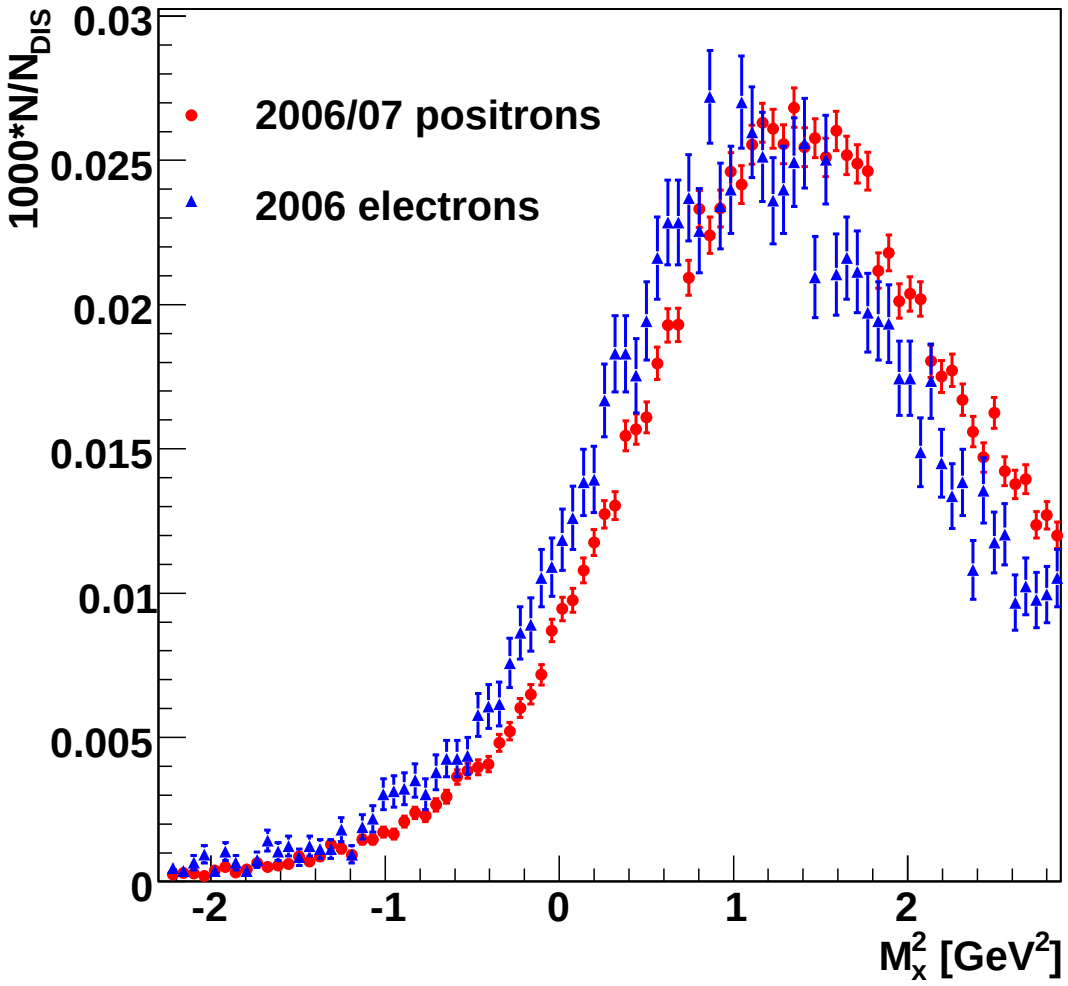

Figure 5.9: The missing mass distribution of the 2006 electron and 2006-2007 positron data within the standard missing mass window -2.25 $< M_x^2 <$ 2.89 GeV^2.

using the electron beam are separated due to the significant time interval between them. For the post-recoil data taking periods three different time periods are used: the 2006 positron data, the 2006 electron data and the 2007 data. The 2006 data is split into two separate periods due to the fact that two beam charges are used. The missing mass distributions for the 2006 electron and 2006 and 2007 positron data are shown in Fig 5.9, which illustrates the shift between the electron and positron data.

The peak of the missing mass window in the 2007 data was found to be time dependent, which was not observed in data taken in other years. One possible

Data Sample	Mean (GeV^2)	Shift (GeV^2)	Window (GeV^2)
96d0, 97d1	1.17	0.02	[-2.08,2.81]
98d0	0.88	-0.27	[-2.52,2.62]
00d2, 03c0, 04c1	1.15	0.00	[-2.25,2.89]
05c1	0.93	-0.22	[-2.47,2.67]
06e1 ele	1.09	-0.06	[-2.31,2.83]
06el pos	1.25	0.1	[-2.15,2.99]

Table 5.4: The mean values for the missing mass distributions in the window between -2.25 $< M_x^2 <$ 2.89 GeV^2 and the resulting shift in the missing mass windows for the different data samples.

explanation for this is the miscallibration of the calorimeter. This effect was found to affect the normalisation of the asymmetry extraction, as shown in Figs 5.3 - 5.13. In order to correct for this, the missing mass window was shifted for each calorimeter calibration period (5000 runs) during the 2007 data, as shown in Fig 5.10. This resulted in a series of different missing mass windows for 2007 data, detailed in Table 5.5. Using these time dependent missing mass shifts improved the overall normalisation of the 2007 extracted asymmetry amplitudes.

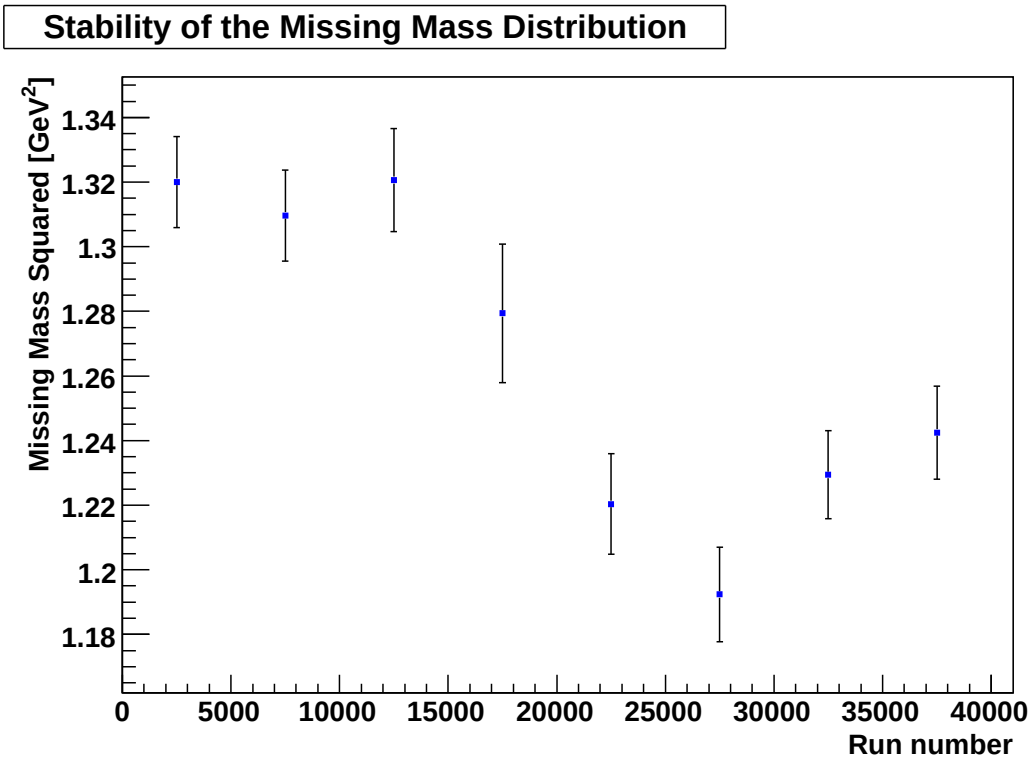

Figure 5.10: The mean of the missing mass window determined from the square of the missing mass value of the DVCS/BH events within a 5000 run time period. The mean of the missing mass is shown for eight individual calorimeter calibration periods over the entire 2007 data set.

Calorimeter Period (run)	Mean (GeV^2)	Shift (GeV^2)	Window (GeV^2)
0 - 5000	1.32	0.17	[-2.08,3.06]
5001 - 10000	1.31	0.16	[-2.09,3.05]
10001 - 15000	1.27	0.12	[-2.13,3.01]
15001 - 20000	1.22	0.07	[-2.18,2.96]
20001 - 25000	1.20	0.05	[-2.20,2.94]
25001 - 30000	1.19	0.04	[-2.21,2.93]
30001 - 35000	1.22	0.07	[-2.18,2.98]
35001 - 40515	1.24	0.09	[-2.16,2.98]

Table 5.5: The mean values for the missing mass distributions in the window between -2.25 $< M_x^2 <$ 2.89 GeV^2 for the 2007 data binned in calorimeter calibration periods.

The asymmetry amplitudes extracted using the shifted missing mass windows are shown in Figs 5.11, 5.12 and 5.13. Using the new missing mass windows reduces the constant $\cos(0\phi)$ term in the BHA extraction, indicating an improvement in the normalisation of the fit to the data. To date, the most significant advance in improving the normalisation of the fit to extract asymmetry amplitudes has been achieved using this approach. The other significant improvement in using the missing mass correction is the suppression of the unphysical $\sin\phi$ term in the BCA which becomes consistent with zero as expected. The kinematic dependences of the asymmetry amplitude values are slightly different after the new missing mass windows are applied. This change in kinematic dependence is most significant in the BCA result. The statistical uncertainties of the asymmetry amplitudes are independent of the correction. Further improvements may be made by identifying the proton directly using the Recoil Detector, therefore not relying on this missing mass approach. The asymmetry amplitudes extracted from the missing mass shifted DVCS event sample are used for the final results. The systematic uncertainty attributed to each asymmetry amplitude is one quarter of the difference between the amplitudes extracted from the DVCS events with the standard and shifted missing mass cuts.

This is due to the effect that this shift is not well understood but the effect does not contribute more than a quarter of the difference to the uncertainty [96].

5.5 Monte Carlo Simulation Studies

A number of systematic studies have been performed to compare the asymmetry results obtained experimentally with asymmetries extracted from Monte Carlo (MC) data. Different Monte Carlo generators are used to simulate the experimental processes and produce theoretical predictions of the asymmetry amplitudes, using models introduced in Section 2.2.2. Monte Carlo simulations can be used to identify the individual reaction processes that are analysed within a selected DVCS/BH event sample. There are three interactions analysed in addition to the Bethe-Heitler and DVCS process that occur at HERMES. These are, in order of significance: associated Bethe-Heitler, Semi-Inclusive Deep Inelastic Scattering (SIDIS) and exclusive π^0 production. Associated Bethe-Heitler events result from interactions with a resonant state of the proton, one of a number of possible resonances most likely at low energies produces a Δ^+ before decaying into a proton or neutron with the emission of a neutral or charged pion respectively. The analysis of experimental data has been performed without using the Recoil Detector to identify protons, hence these background events remain part of the analysed sample.

MC studies have shown that π^0 production and subsequent decay into two photons in the forward spectrometer accounts for 80% of SIDIS background events in the single photon DVCS/BH event sample. In these events, the neutral pion and one of the produced photons is detected while the second is not, either because it lies outside the calorimeter acceptance or that both photons are coincident in the calorimeter and are identified as a single photon event. The remainder of SIDIS background is from η decay. The SIDIS asymmetry amplitudes can be extracted from the experimental data sample and used to correct the BHA and BCA results, later described in Section 5.5.2.

The final contribution is from exclusive π^0 production which accounts for such a small percentage of the total background [97] that the asymmetries cannot be

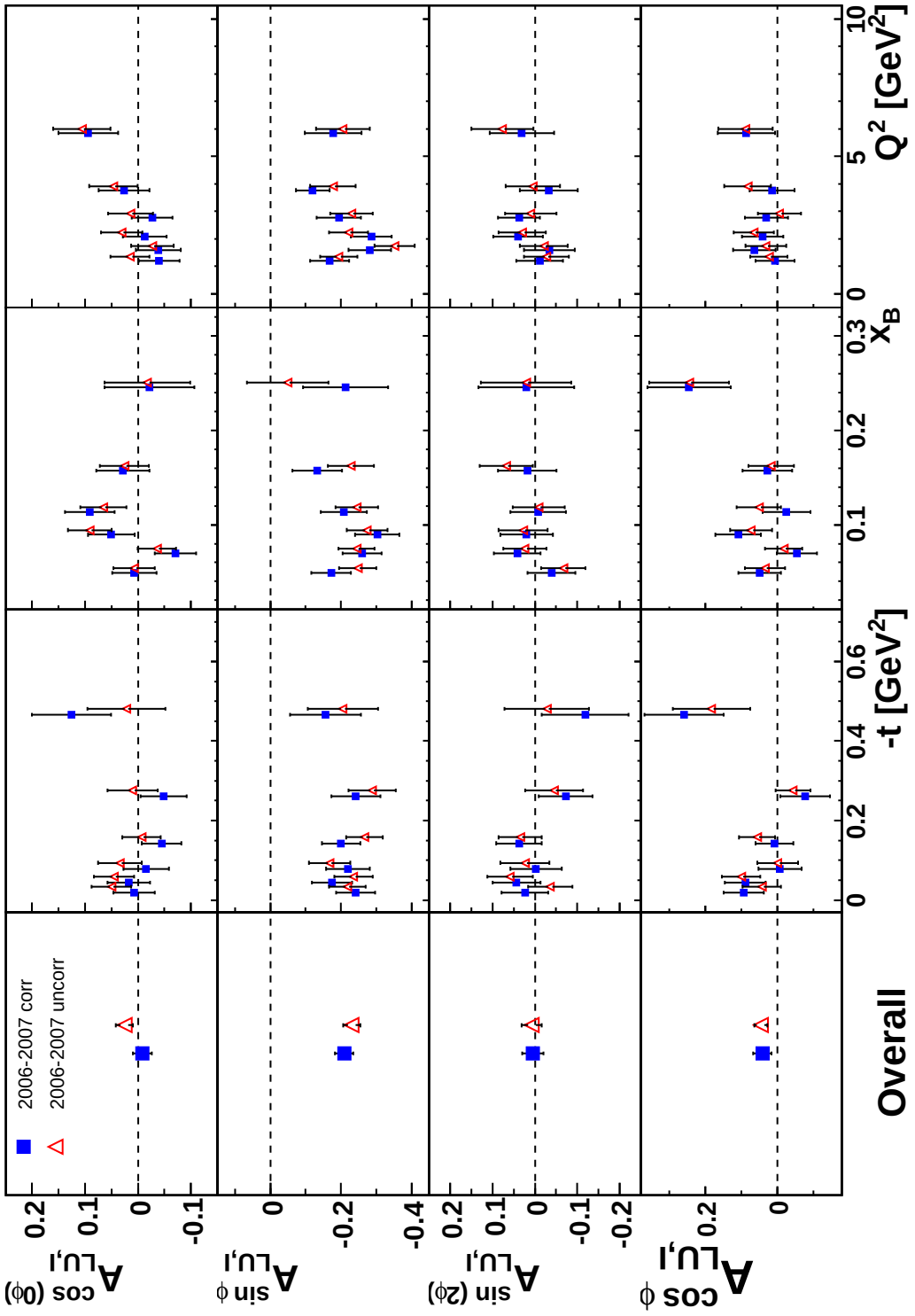

Figure 5.11: The results of the BHA amplitudes from the interference term data using the 13 parameter fitting function on the 2006 and 2007 data with and without the missing mass correction. The constant term $\cos(0\phi)$, which is unphysical, becomes consistent with zero as expected and the value of the $\sin\phi$ term is reduced.

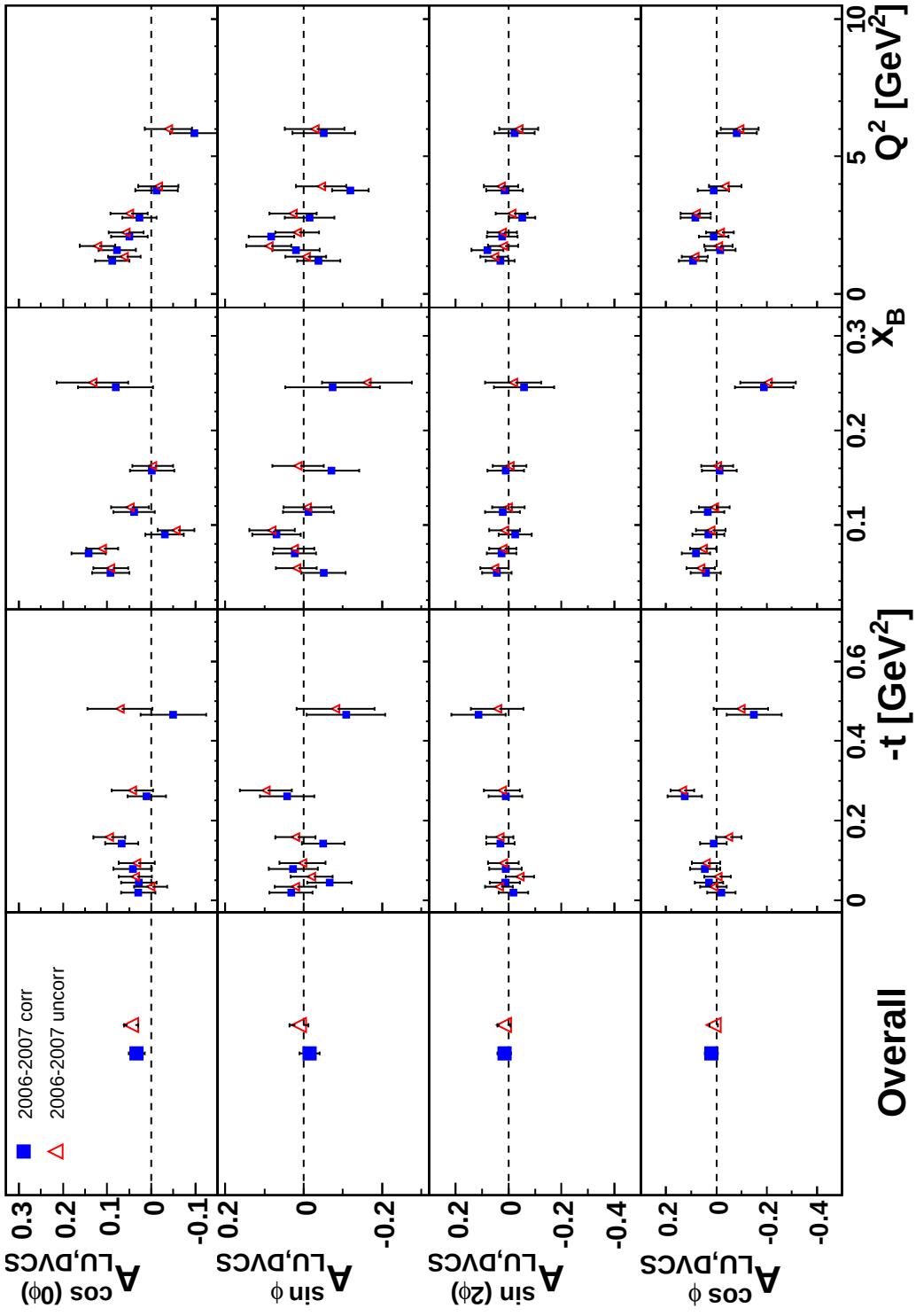

Figure 5.12: The results of the BHA amplitudes from the DVCS squared term using the 13 parameter fitting function on the 2006 and 2007 data with and without the missing mass correction. The constant term $\cos(0\phi)$, which is unphysical, becomes consistent with zero as expected.

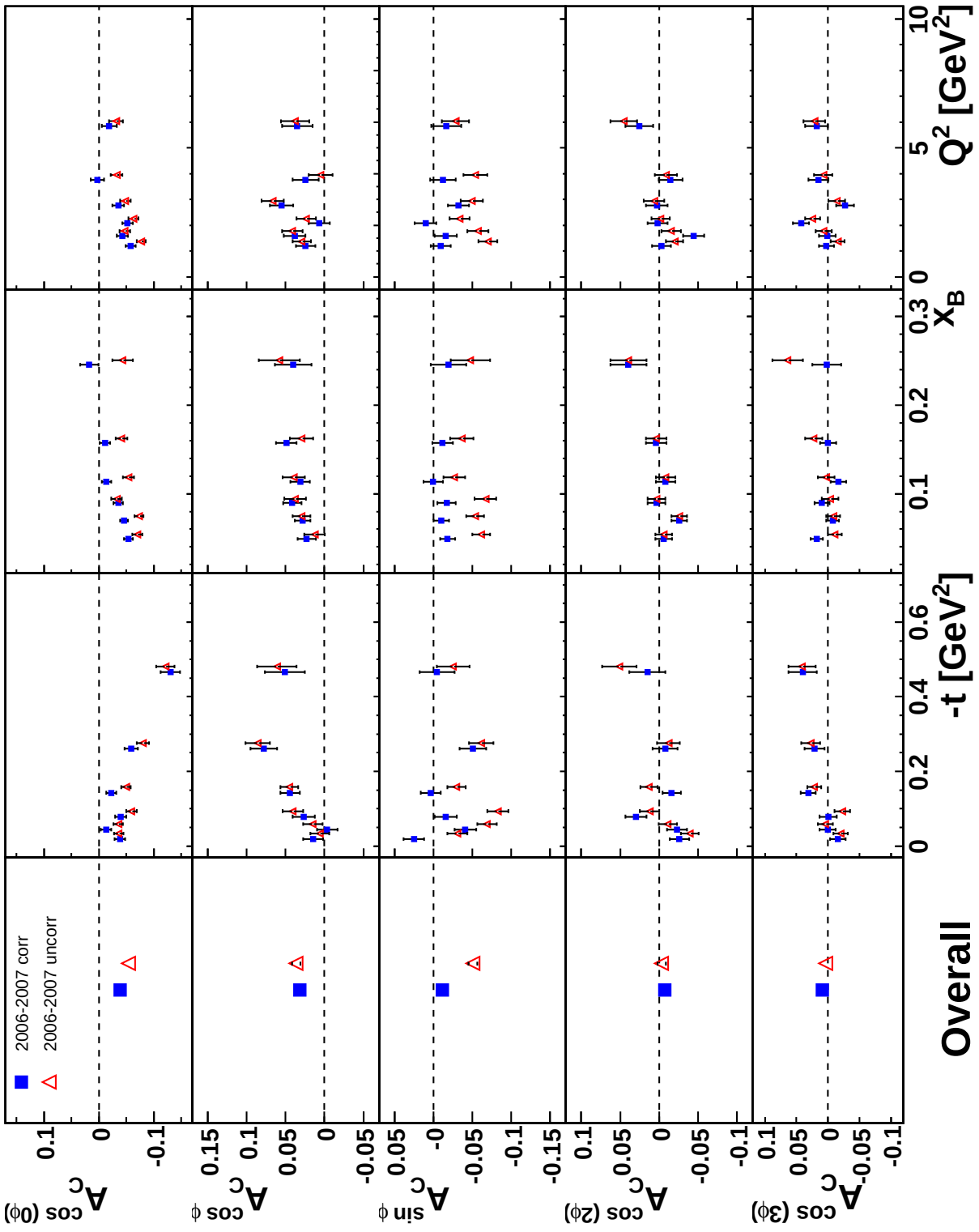

Figure 5.13: The results of the BCA amplitudes data using the 13 parameter fitting function on the 2006 and 2007 data with and without the missing mass correction. The $\sin\phi$ term, which is unphysical, becomes consistent with zero as expected. The overall $\cos\phi$ and $\cos(0\phi)$ amplitudes increase and decrease in value respectively after the correction is applied.

extracted and are assigned a value of $0 \pm \frac{2}{\sqrt{12}}$, equivalent to one standard deviation for a uniform distribution in the range [-1,1].

5.5.1 Using Monte Carlo to Identify the Different Interactions

Monte Carlo simulations of the detector and reaction processes are used to compare the experimental result with expected detector performance and theoretical predictions. Three Monte Carlo generators are used which simulate the different reaction processes. A Monte Carlo generator called GMC_DVCS was used to simulate the elastic Bethe-Heitler and associated Bethe-Heitler processes and a second generator called DISNG was used to simulate the SIDIS process [98]. In order to compare the MC results with data the number of DVCS/BH events produced is normalised using the DIS events from GMC_DVCS. The exclusive π^0 events are obtained from a GMC_EXCL MC simulation by selecting neutral pions. The fractional contribution from each MC generator is recorded in Table 5.6. The experimental and MC data generally agree well at the DVCS/BH event level as shown in Fig 5.14. Once an event has been selected the fractional contribution is calculated using

$$f_{process} = \frac{\sum_i^{N_{process}} w_i}{\sum_i^{N} w_i}, \tag{5.37}$$

where w_i is the MC event weight of a DVCS/BH event, i and $N_{process} \subset N$.

5.5.2 Background Correction

As discussed in the previous section, the fractional contributions of the background processes to the DVCS/BH event sample can be obtained from MC simulation. The SIDIS asymmetry amplitudes are extracted from data by performing a two-photon π^0 dominated event analysis. If one or both of the decay photons of the neutral pion is detected in a SIDIS event, the resulting asymmetry amplitude is the same [96]. Hence, the asymmetry amplitudes extracted from SIDIS events identified using a two-photon analysis can be used to correct for the background SIDIS contamination where only one of the photons is identified. In addition to SIDIS background process,

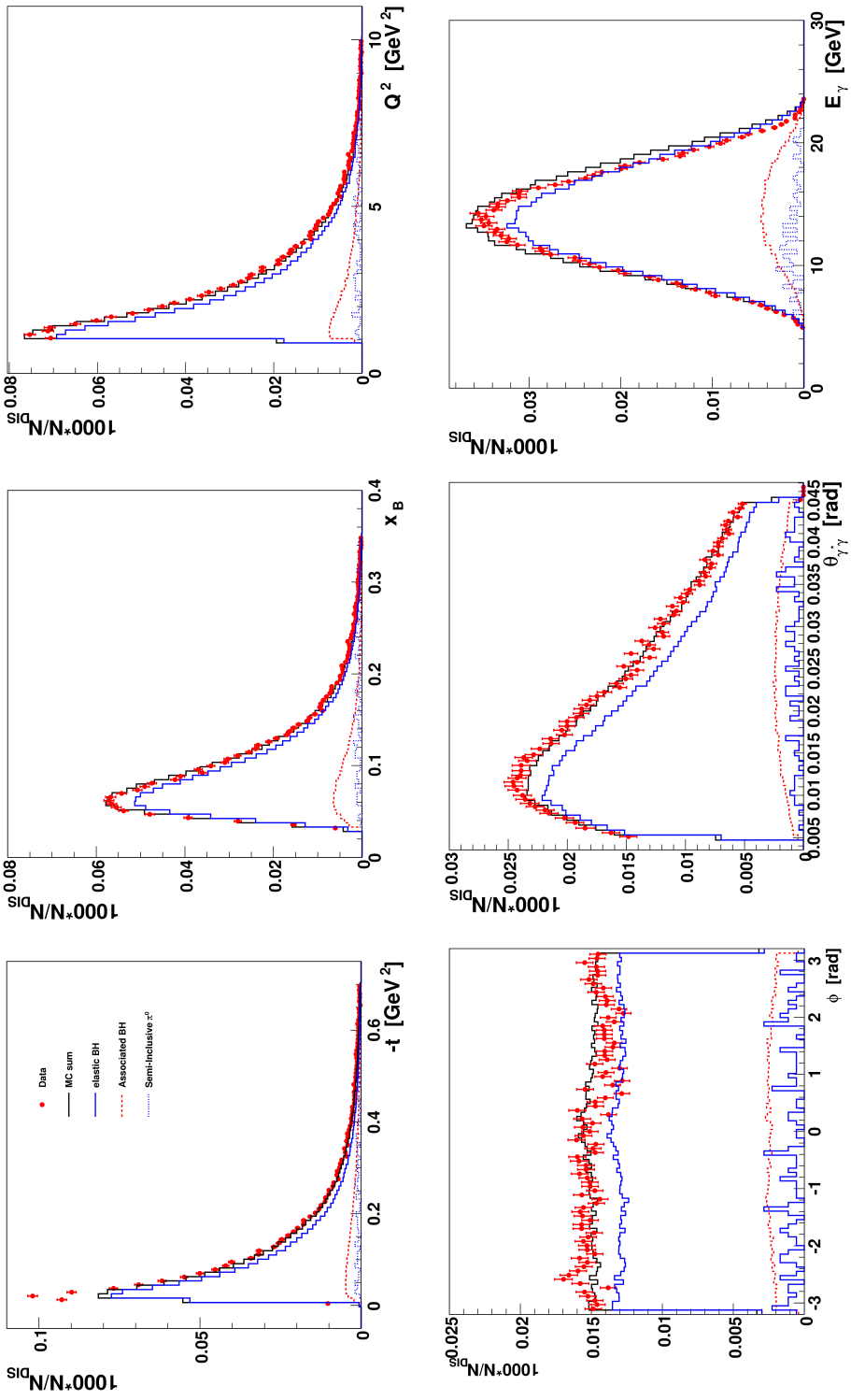

Figure 5.14: Kinematic distributions of $-t$, x_B, Q^2, ϕ, $\theta_{\gamma^*\gamma}$ and E_γ. The distributions are normalised using the number of DIS events and the contribution of each individual reaction process at the exclusive level is shown.

	DVCS/BH	assoc. BH	SIDIS	excl. π^0
overall	84.5 ± 0.1%	11.4 ± 0.1%	3.7 ± 0.3%	0.4 ± 0.5%
$1.0 < Q^2 < 1.4$	85.9 ± 0.2%	8.8 ± 0.1%	4.0 ± 1.2%	0.7 ± 0.7%
$1.4 < Q^2 < 1.8$	86.1 ± 0.3%	10.2 ± 0.1%	3.2 ± 1.1%	0.5 ± 0.7%
$1.8 < Q^2 < 2.4$	86.0 ± 0.3%	10.2 ± 0.1%	1.9 ± 0.7%	0.4 ± 0.6%
$2.4 < Q^2 < 3.2$	83.1 ± 0.3%	12.4 ± 0.1%	4.2 ± 0.9%	0.3 ± 0.5%
$3.2 < Q^2 < 4.5$	83.4 ± 0.3%	13.6 ± 0.1%	2.8 ± 0.6%	0.2 ± 0.5%
$4.5 < Q^2 < 10.0$	79.2 ± 0.4%	15.6 ± 0.2%	5.1 ± 0.8%	0.1 ± 0.5%
$0.03 < x_B < 0.06$	87.7 ± 0.2%	11.3 ± 0.1%	0.8 ± 0.5%	0.2 ± 0.3%
$0.06 < x_B < 0.08$	87.3 ± 0.2%	10.1 ± 0.1%	2.2 ± 0.7%	0.4 ± 0.5%
$0.08 < x_B < 0.10$	86.0 ± 0.3%	11.2 ± 0.1%	2.3 ± 0.7%	0.5 ± 0.7%
$0.10 < x_B < 0.13$	84.5 ± 0.3%	12.3 ± 0.1%	2.7 ± 0.7%	0.5 ± 0.7%
$0.13 < x_B < 0.20$	82.0 ± 0.2%	13.3 ± 0.1%	4.2 ± 0.7%	0.5 ± 0.8%
$0.20 < x_B < 0.35$	76.1 ± 0.5%	13.6 ± 0.2%	9.9 ± 1.5%	0.4 ± 1.2%
$0.00 < -t < 0.03$	94.5 ± 0.3%	4.5 ± 0.1%	0.9 ± 0.5%	0.2 ± 0.4%
$0.03 < -t < 0.06$	89.8 ± 0.3%	6.8 ± 0.1%	3.1 ± 0.8%	0.3 ± 0.5%
$0.06 < -t < 0.10$	86.9 ± 0.3%	9.8 ± 0.1%	2.8 ± 0.8%	0.5 ± 0.7%
$0.10 < -t < 0.20$	81.8 ± 0.2%	13.9 ± 0.1%	3.8 ± 0.7%	0.5 ± 0.6%
$0.20 < -t < 0.35$	74.2 ± 0.3%	20.0 ± 0.2%	5.4 ± 1.0%	0.4 ± 0.8%
$0.35 < -t < 0.70$	66.7 ± 0.4%	27.6 ± 0.3%	5.5 ± 1.2%	0.2 ± 0.9%

Table 5.6: Fractional contributions of the elastic Bethe-Heiter with the contributions of the associated Bethe-Heitler, semi-inclusive pion and exclusive pion background processes to each kinematic bin. The statistical errors of each contribution are also shown. The largest background contribution is from the associated Bethe-Heiter process.

exclusive π^0 production also contaminates the DVCS/BH event sample but the contribution of this process is less than 0.7% in each kinematic bin [23].

The following criteria are used to identify the SIDIS events:

- All previous criteria used to identify DIS events.
- Two trackless clusters pass the fiducial volume cuts of the calorimeter, both of which produce a pulse in the preshower greater than 1 MeV, one of which deposits an energy $E_{\gamma 1} > 5$ GeV, and the second $E_{\gamma 2} > 1$ GeV.
- The reconstructed invariant mass of the π^0 is within the range 0.1 GeV $< m_{\gamma\gamma}$ < 0.17 GeV.
- All exclusive cuts apart from an altered missing mass range described above are applied in this case.
- The fractional energy z of the π^0 is greater than 0.8.

The fractional energy z can be calculated from the two photon events as

$$z = (E_{\gamma 1} + E_{\gamma 2})/\nu = E_{\pi^0}/\nu. \tag{5.38}$$

The missing mass from two photons is calculated by

$$M^2_{\gamma\gamma} = (p_{\gamma 1} + p_{\gamma 2})^2 = 2E_{\gamma 1}E_{\gamma 2}(1 - cos\theta_{\gamma\gamma}), \tag{5.39}$$

where,

$$\theta_{\gamma\gamma} = cos^{-1}\frac{|r_{\gamma 1} \cdot r_{\gamma 2}|}{|r_{\gamma 1}||r_{\gamma 2}|}, \tag{5.40}$$

the polar angle between the two real photons calculated from their positional three-vectors $r_{\gamma 1}$ and $r_{\gamma 2}$. In order to correct for the background processes the following is used:

$$A_{excl} = \frac{1}{1 - f_{SIDIS} - f_{excl.\pi^0}} \cdot [A_{meas.} - f_{SIDIS}A_{SIDIS} - f_{excl.\pi^0}A_{excl.\pi^0}], \tag{5.41}$$

where f_{SIDIS} ($f_{excl.\pi^0}$) is the fraction of SIDIS (exclusive) π^0 events and A_{SIDIS} ($A_{excl.\pi^0}$) is the corresponding asymmetry amplitude. The fractional contribution of the background events to the overall DVCS event sample is determined from the appropriate MC simulation. Propagating the error from the background contribution

(i.e. SIDIS and excl. π^0) together with the measured asymmetry the systematic error can be obtained from

$$\delta_{f_{bg,i}} = \frac{A_{meas.} - A_{bg,i} + A_{bg,j} f_{bg,j} - A_{bg,j} f_{bg,j}}{(1 - f_{bg,i} - f_{bg,j})^2} \cdot \delta f_{bg,i}, \tag{5.42}$$

$$\delta_{A_{bg,i}} = \frac{-f_{bg,i}}{1 - f_{bg,i} - f_{bg,j}} \cdot \delta A_{bg,i}, \tag{5.43}$$

$$\delta = \sum_i \sqrt{(\delta^2_{f_{bg,i}} + \delta^2_{A_{bg,i}})}, \tag{5.44}$$

where bg, i is the background process of interest. The asymmetry $A_{excl.\pi^0}$ cannot be extracted from real data with sufficient statistics to give a realistic result. The background described in the equation, therefore, does not include the effect of the exclusive pion process as $A_{excl.\pi^0} \approx 0$.

The BHA and BCA amplitudes, $A_{LU,I}$ and A_C, dependent on the beam charge are expected to be compatible with zero as an asymmetry extracted from π^0 event can only arise from a two photon exchange mechanism. In the correction the charge related asymmetries are treated as dilutions i.e. the $A_{LU,I}$ and A_C are set to zero. The charge averaged BHA amplitudes arising from the squared DVCS term, $A_{LU,DVCS}$ are expected to have a significant values and are used in the correction. The asymmetry amplitudes extracted from the semi-inclusive π^0 data are shown in Figs 5.15, 5.16 and 5.17. The results show that the $A^{sin\phi}_{LU,DVCS}$ and $A^{sin(2\phi)}_{LU,DVCS}$ amplitudes are significantly non-zero, with values of 0.053 and 0.064, as predicted from previous results [90]. The BCA amplitudes $A_C^{cos\phi}$, $A_C^{cos(2\phi)}$ and $A_C^{cos(3\phi)}$ are all consistent with zero but the other amplitudes expected to be zero, $A^{sin\phi}_{LU,I}$, $A^{sin(2\phi)}_{LU,I}$ and $A_C^{cos(0\phi)}$, have significant values of -0.063, -0.060 and -0.057 respectively. The asymmetry amplitudes are not corrected for these values but they are considered in the systematic error of the results shown in Chapter 6. The amplitude of the constant $A^{cos(0\phi)}_{LU,I}$ term is also larger than expected. A value half the size of the difference between each asymmetry amplitude with and without the semi inclusive background correction contributes to the systematic uncertainty of the final DVCS asymmetry results detailed in chapter 6. This uncertainty takes into account the approximations and assumptions applied during the correction procedure [90].

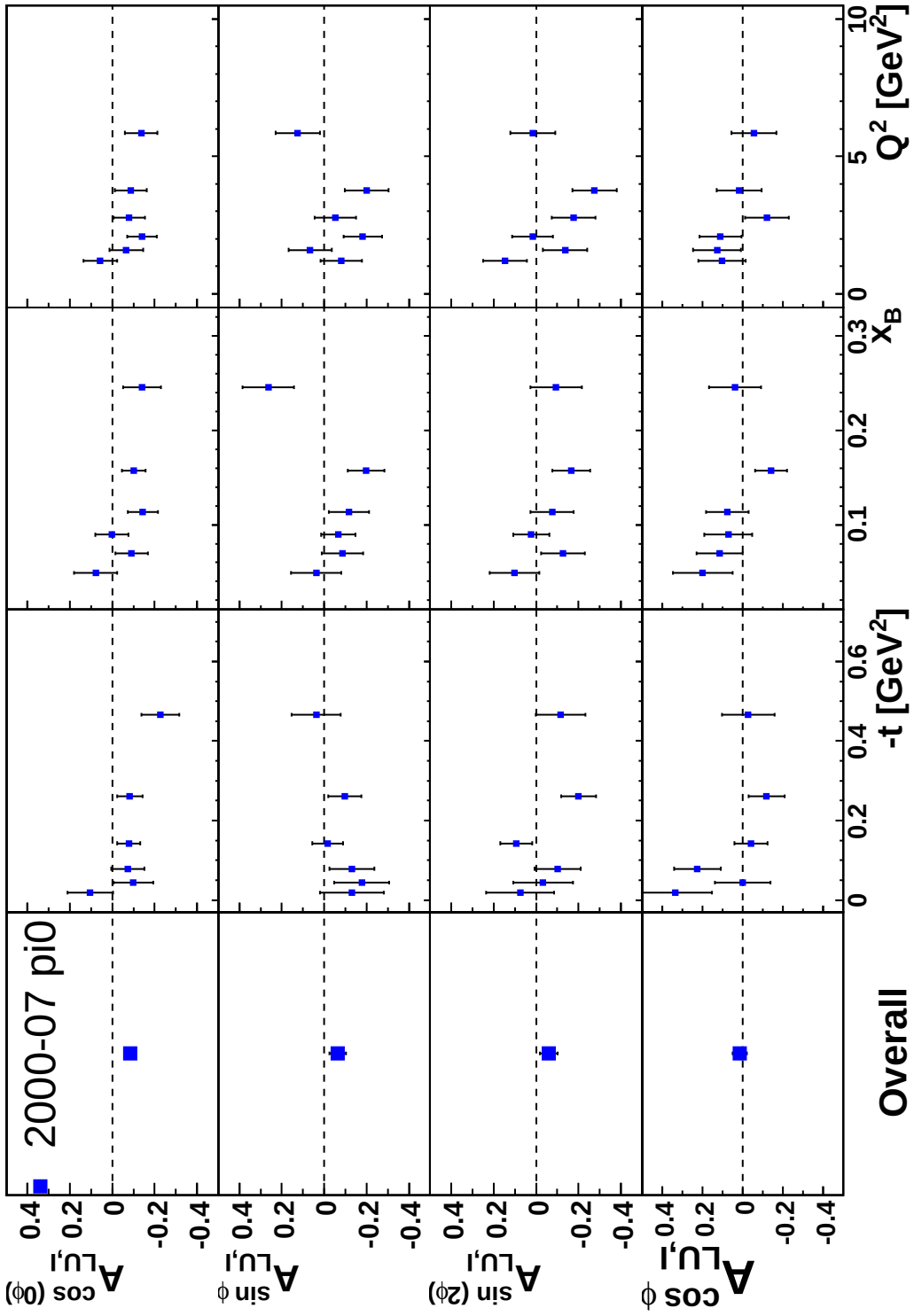

Figure 5.15: BHA amplitudes originating from the interference term extracted from semi-inclusive π^0 events.

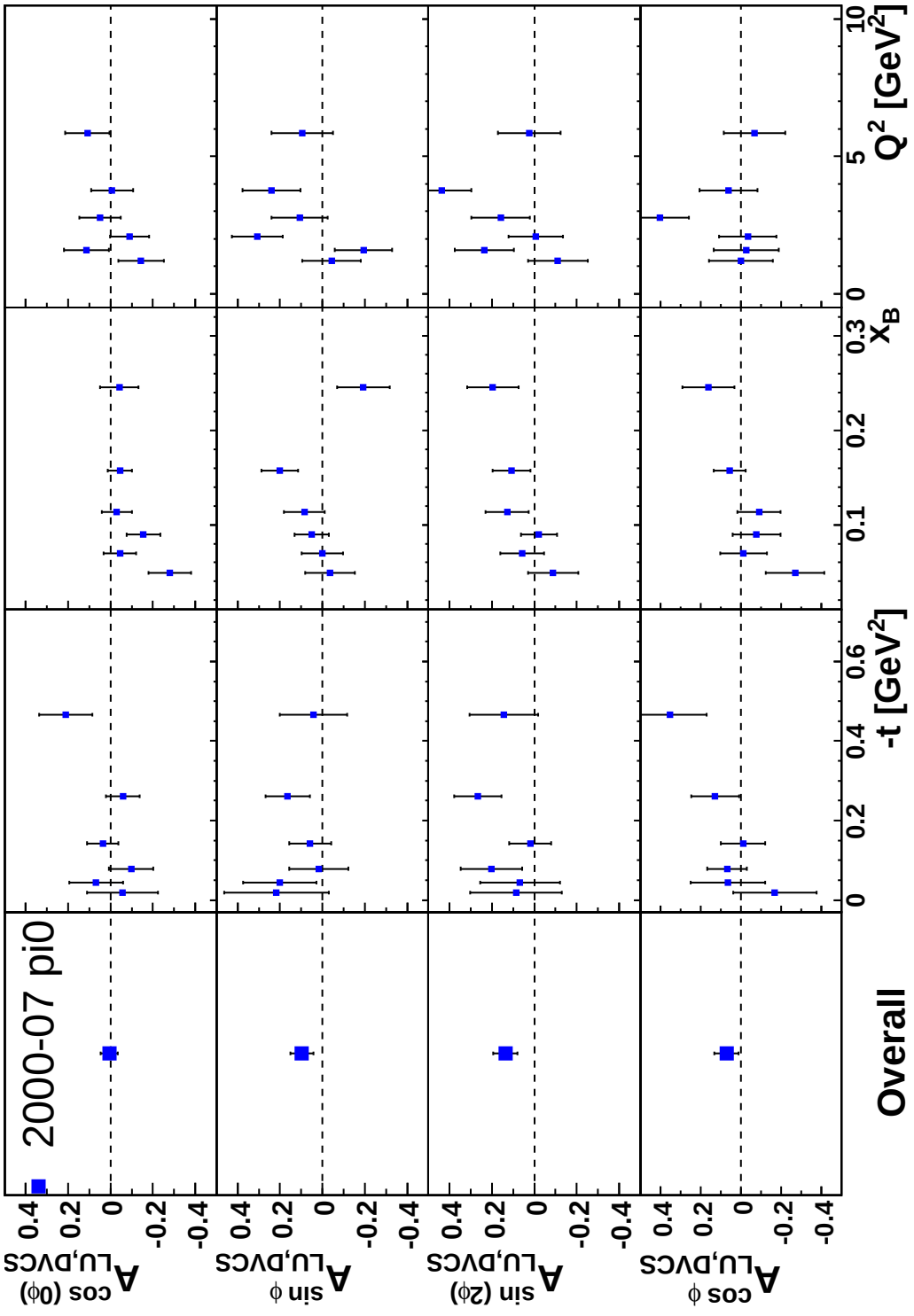

Figure 5.16: The BHA amplitudes originating from the squared DVCS term extracted from semi-inclusive π^0 events.

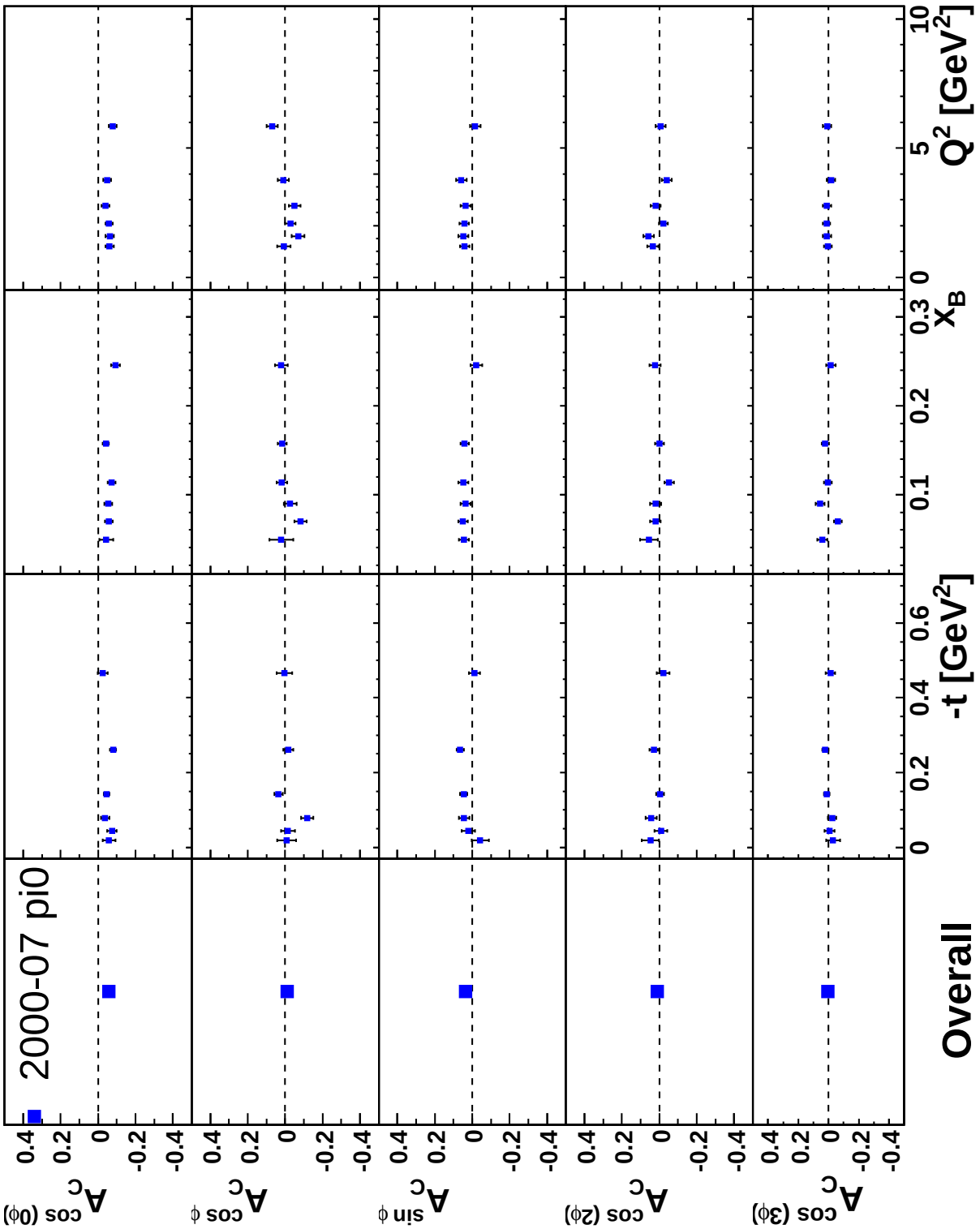

Figure 5.17: The BCA amplitudes originating from the interference term extracted from semi-inclusive π^0 events.

Monte Carlo simulations are also used to correct for radiative effects. The lepton in the DVCS/BH interaction may emit an additional photon before of after it encounters the target proton losing an additional amount of energy. Consequently, the lepton will have lower energy than that detected and the kinematics will be incorrectly reconstructed. If the lepton is emitted out with the electromagnetic field of the target it is known as external bremsstrahlung. External bremsstrahlung events can be eliminated from the event sample as the difference between the energy of the lepton track reconstruction in the front and back parts, of the spectrometer, described in Section 4.1.3, are not compatible. Correcting for the internal bremsstrahlung i.e. the photon is emitted within the electromagnetic field, are known as radiative corrections and are calculable at HERMES using a Monte Carlo simulation called RADGEN. RADGEN takes as input the observed kinematics of an event, potentially generates a radiative photon dependent on the observed kinematics and returns the true kinematics at the interaction vertex. The difference between the observed and true kinematics can be used to develop a migration matrix using the unfolding formalism which can be used to correct the event sample for radiative effects. It should be noted that RADGEN only calculates the lowest order photons and soft photons of energy up to 100 Mev are not simulated. The contribution of soft photons is determined from a data-to-MC comparison using the GEANT detector simulation package. The maximum contribution of soft photons emitted has been found to be 3.2% and 0.8% in the initial and final state respectively [89].

5.5.3 Combined Estimation of Systematic Uncertainty

In addition to the systematic error contributions from the missing mass and background processes, the remaining uncertainty in the extraction of asymmetry amplitudes arises from detector effects and the extraction method. The individual uncertainty contributions are from the spectrometer acceptance, smearing and finite bin width effects. All of these effects are estimated together using an approach known as the "3-in-1" Method. The inclusion of an improved detector alignment for new data productions corrects for the misalignment of detector components [99]. In order to reflect the change in the data productions, the most recent Monte Carlo produc-

tions were created using a perfectly aligned detector. Previous DVCS analyses, using data taken before 2005, have an error that is attributed to the misalignment of the detector, the "4th" contribution to what is then known as the "4-in-1" uncertainty.

In order to determine this systematic uncertainty, the GMC_DVCS MC production is used to generate DVCS/BH events from a proton target using the two different beam charge and polarisation states. This simulation is analysed using exactly the same analysis method as for experimental data, with all the DIS and DVCS/BH event criteria detailed in section 5.2.1. The asymmetry amplitudes are extracted using the Extended Maximum Likelihood technique. A second set of asymmetry amplitudes is generated using a code called QPLOT. In the QPLOT the amplitudes are calculated directly from the Fourier coefficients, detailed in section 2.6.1, and are based on the VGG models of GPDs. The five different VGG models include various combinations of choices of the t-ansatz, skewness, b parameter and D-term, summarised in Table 5.7. The asymmetry amplitudes are calculated using the average value of $-t$, x_B and Q^2 in each kinematic bin from the GMC_DVCS production. QPLOT is model dependent and free from any detector or binning effects. The systematic uncertainty δ_{3in1} is defined as the difference between the generated points from QPLOT, $A_{generated}$, and the reconstructed asymmetry amplitudes from GMC_DVCS MC, $A_{reconstructed}$,

$$\delta_{3in1} = |A_{generated} - A_{reconstructed}|. \tag{5.45}$$

The final systematic error contribution is calculated from the RMS i.e. $\sqrt{\frac{1}{5}\sum_{i=5}^{n}\delta_{i,3in1}^2}$, of the mean value of each of the five VGG QPLOT models. The asymmetry plots showing the first of these VGG type models are shown in Figs 5.18, 5.19 and 5.20.

The BHA amplitudes originating from the interference term $A_{LU,I}^{sin\phi}$ and $A_{LU,I}^{sin2\phi}$ are dependent on $-t$, x_B and Q^2. $A_{LU,I}^{sin\phi}$ and $A_{LU,I}^{sin2\phi}$ decrease in value with increasing t for both the model amplitudes generated from QPLOT and the reconstructed amplitudes from the Monte Carlo DVCS event sample. The model also predicts a dependence on Q^2 and x_B which is not reflected in the reconstructed points. The $A_{LU,I}^{cos0\phi}$ and $A_{LU,I}^{cos\phi}$ terms are both consistent with zero as expected. The reconstructed and calculated BHA arising from the squared DVCS term are all small and compatible with zero. The only result of the BCA not compatible with zero and dependent

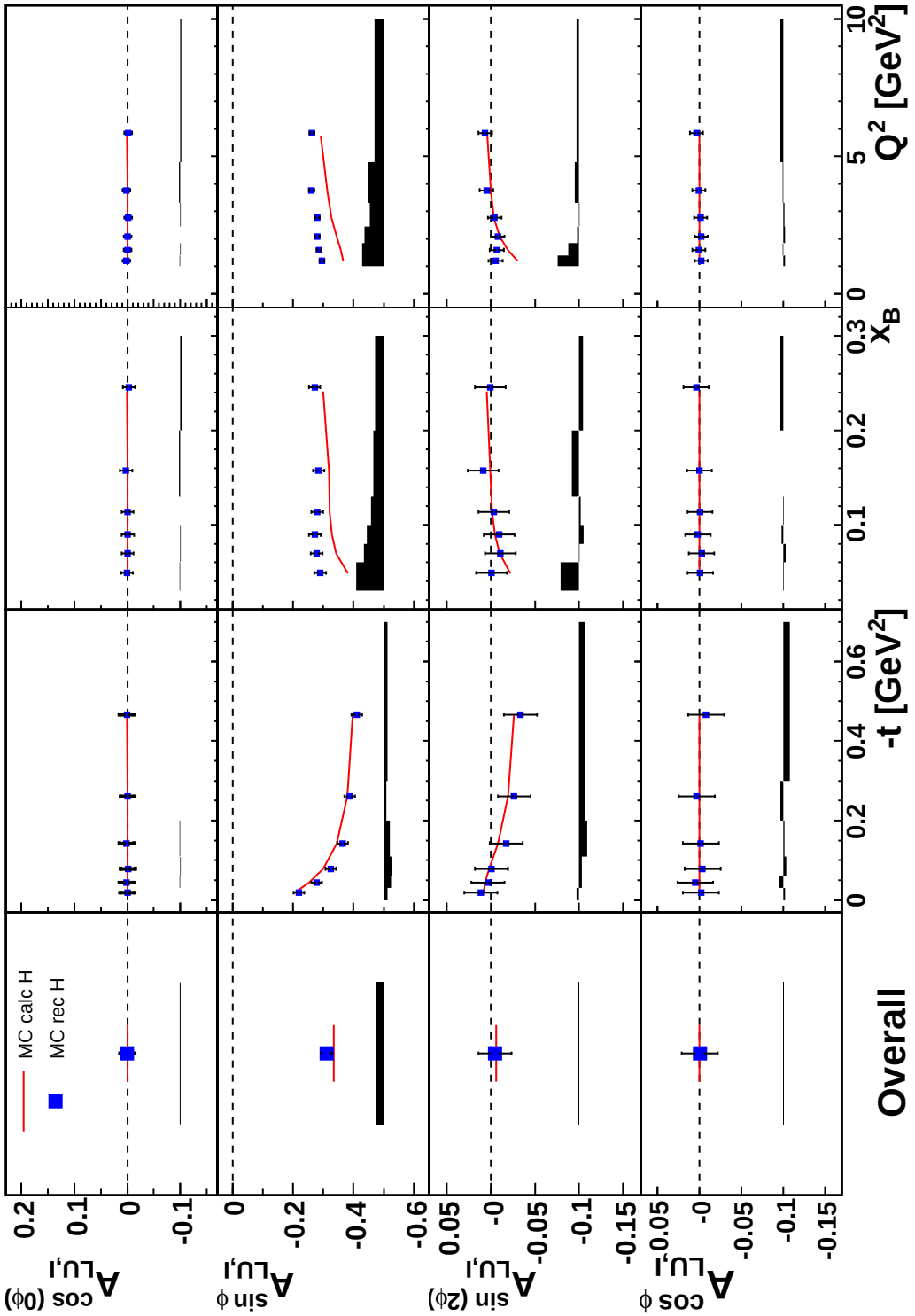

Figure 5.18: BHA amplitudes from the interference term of Monte Carlo VGG Model 1 using the average kinematics from a GMC_DVCS production of DVCS events with the short target cell geometery. Calculated and reconstructed amplitudes are shown. The systematic error (bands) is taken as the difference between these two values.

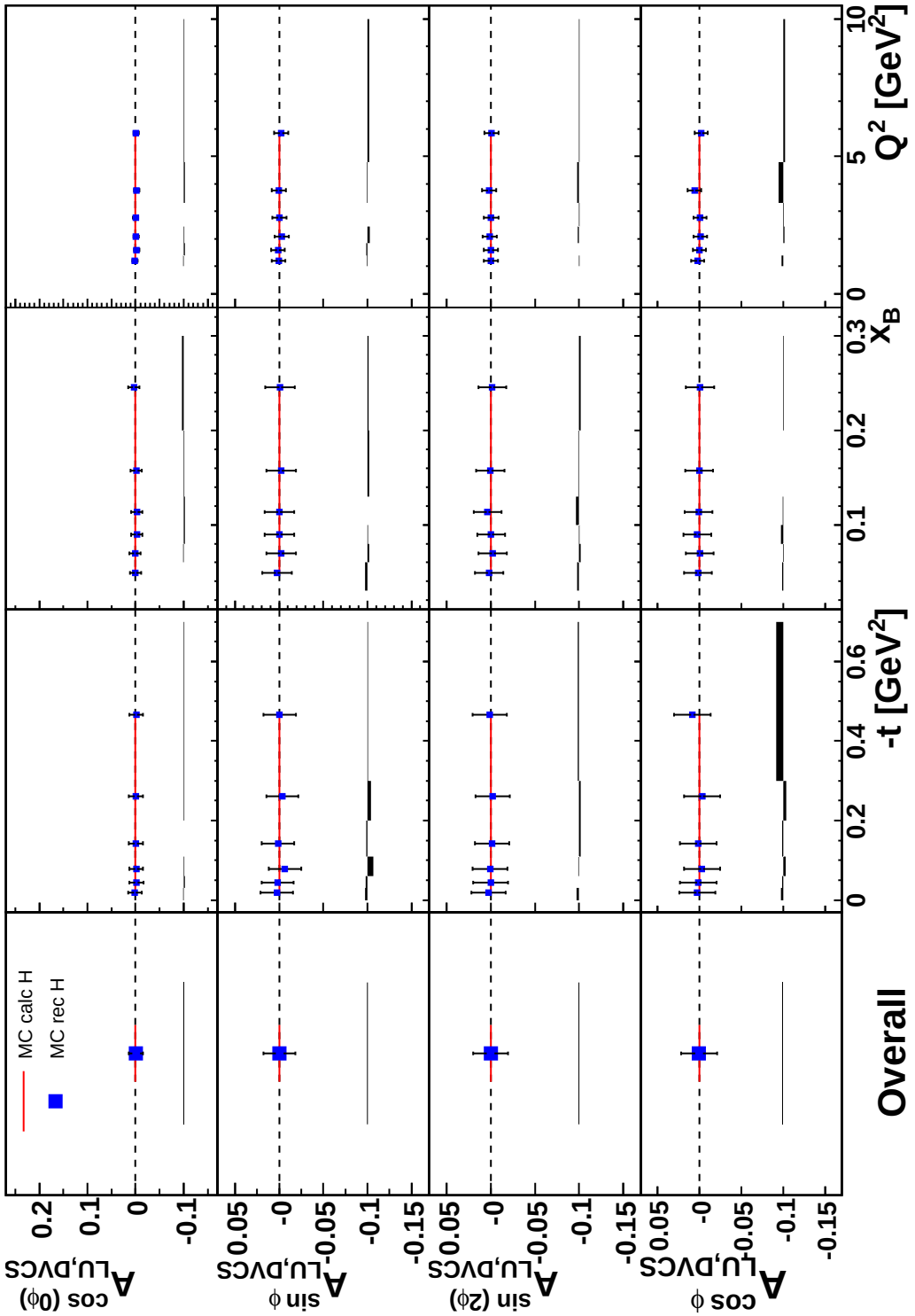

Figure 5.19: BHA amplitudes from the squared DVCS term of Monte Calo VGG Model 1 using the average kinematics from a GMC_DVCS production of DVCS events with the short target cell geometery. Calculated and reconstructed amplitudes are shown. The systematic error (bands) is taken as the difference between these two values.

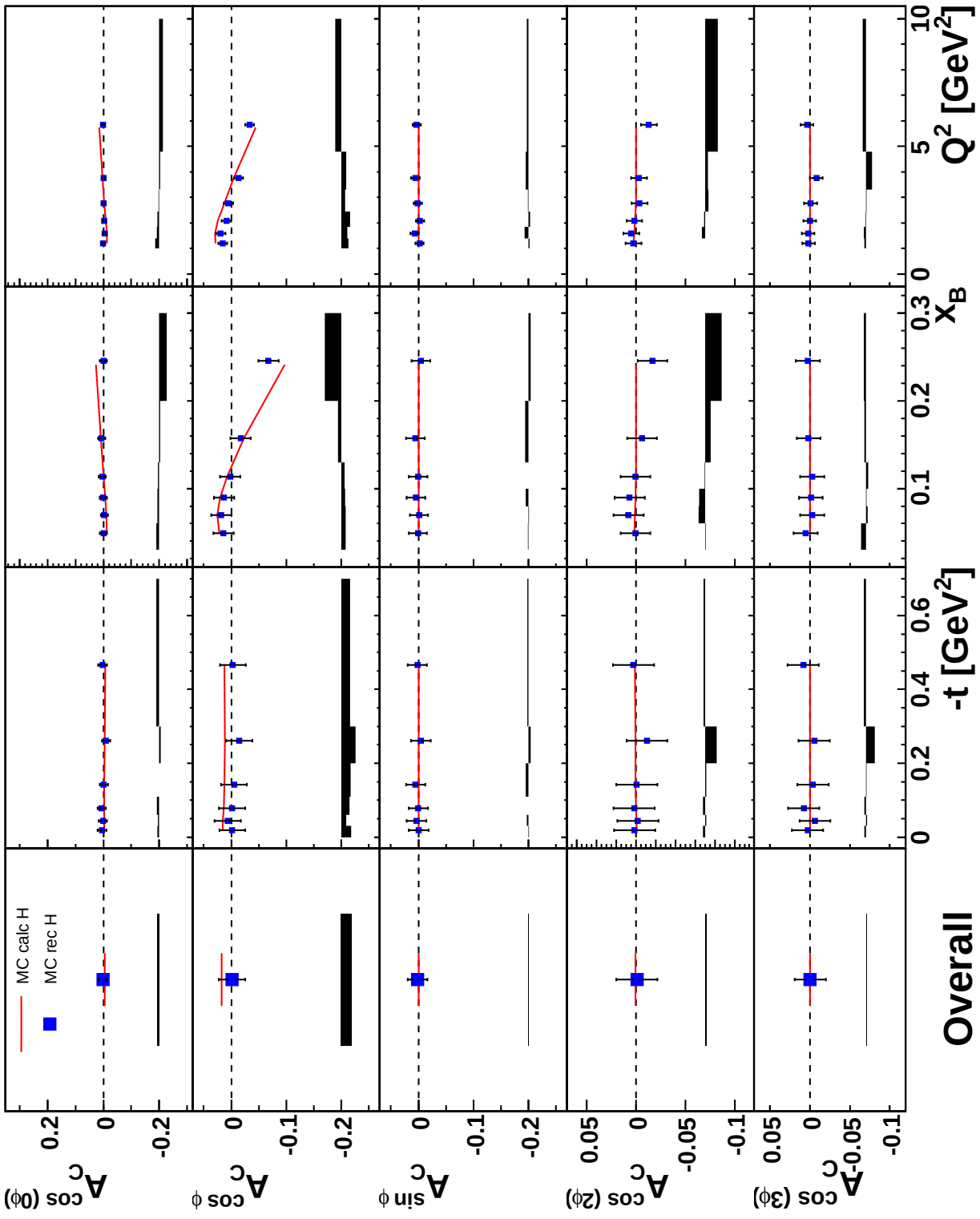

Figure 5.20: BCA amplitudes of Monte Carlo VGG Model 1 using the average kinematics from a GMC_DVCS production of DVCS events with the short target cell geometery. Calculated and reconstructed amplitudes are shown. The systematic error (bands) is taken as the difference between these two values.

Model	Factorised t-ansatz	Skewness	b Parameter	D-term
1	✓	X	9	X
2	✓	✓	1	X
3	✓	✓	3	X
4	✓	✓	1	✓
5	✓	✓	3	✓

Table 5.7: Table summarising the contribution of the factorised t-ansatz, skewness, b parameter and D-term to each VGG model.

on the kinematic binning is $A_C^{cos\phi}$, which decreases in value with increasing Q^2 and x_B. In general, the reconstructed and generated asymmetry amplitudes agree with each other and display a similar dependence on the kinematic binning. The largest differences in the overall asymmetry values are the leading twist $A_{LU,I}^{sin\phi}$ and $A_C^{cos\phi}$ amplitudes.

The "All-in-1" uncertainty is the systematic error contribution of the spectrometer acceptance, smearing, misalignment and finite bin width to the BHA and BCA extracted from the combined 1996-2007 data. The asymmetries are extracted from a DVCS event sample that includes data taken both, with and without, the recoil detector and the correction for the misalignment. In order to measure the systematic uncertainty of this result two Monte Carlo productions were used with the geometry files for both the old and new experimental configuration and alignment files. The uncertainty was determined form the simulated DVCS events in both productions using the 3-in-1 and 4-in-1 methods described previously. The All in 1 systematic uncertainty was calculated by weighting the contribution of both the 3-in-1 and 4-in-1 uncertainty using the number of DVCS events from the 1996-2005 and 2006/07 data taking periods. The All in 1 method, therefore, reflects the systematic uncertainty of the experimental conditions during all years of data taking.

5.5.4 Total Systematic Uncertainty

The total systematic uncertainty δ_{syst} of the BHA and BCA amplitudes has contributions from the Semi Inclusive DIS process δ^2_{BG}, the 3-in 1 / 4-in-1 uncertainty δ^2_{3in1} / δ^2_{4in1} and the missing mass shift $\delta^2_{M_x^2}$. This is calculated using

$$\delta_{syst} = \sqrt{\delta^2_{BG} + \delta^2_{3-in-1} + \delta^2_{M_x^2}} \tag{5.46}$$

for asymmetry results extracted from DVCS events obtained from 2006-2007 and 1996-2005 data.

The results of the individual contributions and the total systematic uncertainty δ_{syst} are summarised in Tables 5.8 and 5.9.

	3-in-1	SIDIS Correction	Missing Mass Shift	δ_{syst}
$A_C^{cos0\phi}$	0.0069	0.0008	0.0038	0.0115
$A_C^{cos\phi}$	0.0017	0.0022	0.0011	0.0050
$A_C^{cos2\phi}$	0.0013	0.0003	0.0010	0.0026
$A_C^{cos3\phi}$	0.0001	0.0003	0.0012	0.0016
$A_{LU,DVCS}^{cos0\phi}$	0.0007	0.0011	0.0029	0.0047
$A_{LU,DVCS}^{sin\phi}$	0.0004	0.0044	0.0068	0.0116
$A_{LU,DVCS}^{sin2\phi}$	0.0003	0.0047	0.0004	0.0054
$A_{LU,I}^{cos0\phi}$	0.0111	0.0025	0.0084	0.0220
$A_{LU,I}^{sin\phi}$	0.0246	0.0045	0.0054	0.0345
$A_{LU,I}^{sin2\phi}$	0.0016	0.0050	0.0006	0.0072

Table 5.8: The individual contributions of the missing mass shift, Semi Inclusive DIS correction and 3-in-1 corrections to the overall systematic uncertainty for the 2006-2007 data.

	All-in-1	SIDIS Correction	Missing Mass Shift	δ_{syst}
$A_C^{cos0\phi}$	0.0066	0.0010	0.0034	0.0110
$A_C^{cos\phi}$	0.0013	0.0021	0.0009	0.0043
$A_C^{cos2\phi}$	0.0014	0.0006	0.0010	0.0030
$A_C^{cos3\phi}$	0.0003	0.0001	0.0006	0.0010
$A_{LU,DVCS}^{cos0\phi}$	0.0007	0.0032	0.0026	0.0065
$A_{LU,DVCS}^{sin\phi}$	0.0006	0.0017	0.0058	0.0081
$A_{LU,DVCS}^{sin2\phi}$	0.0004	0.0017	0.0002	0.0023
$A_{LU,I}^{cos0\phi}$	0.0006	0.0030	0.0054	0.0090
$A_{LU,I}^{sin\phi}$	0.0267	0.00581	0.0031	0.0356
$A_{LU,I}^{sin2\phi}$	0.0031	0.0019	0.0081	0.0131

Table 5.9: The individual contributions of the missing mass shift, Semi Inclusive DIS correction and All in One corrections to the overall systematic uncertainty for the 1996-2007 data.

The asymmetry amplitude with the greatest overall uncertainty is $A_{LU,I}^{sin\phi}$ due to the relatively large 3-in-1 / 4-in-1 contribution. An interesting result is the significant difference between the 3-in-1 and All-in-1 systematic uncertainty of the $A_{LU,I}^{cos0\phi}$ term. This results from the difference between the asymmetry value extracted from Monte Carlo simulation and the VGG model. This difference is explored further in the next chapter. With the exception of $A_{LU,I}^{cos0\phi}$, the other systematic error contributions to 2006-2007 and 1996-2005 BHA and BCA results are similar.

Chapter 6

Final Results

The Deeply Virtual Compton Scattering (DVCS) asymmetry results presented in this thesis are extracted from all hydrogen data available at HERMES for the first time. From this data it is possible to extract both a single charge Beam Helicity Asymmetry (BHA) and the combined BHA and Beam Charge Asymmetry (BCA). These asymmetry amplitudes are presented with their respective uncertainties and VGG model [23] calculations. Two results of the combined analysis of the BHA and BCA are presented in this thesis. The first set of asymmetry results using the combined extraction method with hydrogen data taken in 2006-2007 are shown in Figs 6.1 and 6.2. A comparison of these amplitudes with the published BHA and BCA results [19] from the 1996-2005 data is shown in Figs 6.3 and 6.4. These figures have been released by the HERMES collaboration [88]. The second BHA and BCA result, using the combined extraction method, is extracted from hydrogen data taken during the entire running period of HERMES (1996-2007). These asymmetries are shown in Figs 6.5 and 6.6. Single charge BHA results extracted separately from 2006 positron, 2006 electron and 2007 positron hydrogen data are discussed in Section 6.4.

HERMES has previously published results of BHA and BCA results on an unpolarised hydrogen target. The first BHA result [100] was extracted from 1996-1997 data using the Least Squares fitting method. The first BCA result [44] was extracted using the 1998 electron and 1996-1997 positron data, again using the Least Square Fitting to measure the asymmetry. The second publication of both the BHA

and BCA included all the hydrogen data taken from 1996-2005 [19]. This analysis used the combined extraction technique using the Extended Maximum Likelihood Fitting (EML) method as detailed in the previous chapter. The data used in these publications is a subset of the data used in this analysis, therefore, the published asymmetry results and those presented in this thesis should be comparable. In total 67815 analysable DVCS/BH events were identified in the 2006-2007 unpolarised hydrogen data set. This is more than double the 24817 DVCS/BH events produced during hydrogen data taking from 1996-2005, as summarised in Table 5.3, and is far greater than the 5439 DVCS/BH events available from the 1996-1997 hydrogen data set.

6.1 Combined BHA and BCA Results from 2006-2007 Unpolarised Hydrogen Data

The asymmetry amplitudes extracted from the 2006-2007 and 1996-2007 unpolarised hydrogen DVCS events have been analysed separately. This allows the asymmetry amplitudes extracted from data taken after the installation of the Recoil Detector to be compared with previous results and the compatibility of the two results to be verified as discussed in Section 5.4.

The overall BHA and BCA amplitudes from the combined extraction method are summarised in Table 6.1 and are shown in Figs 6.1 and 6.2. The $A_{LU,I}^{sin\phi}$ and $A_{LU,I}^{sin(2\phi)}$ amplitudes sensitive to the interference term in the scattering amplitude are shown respectively in the first and third row of Fig 6.1. Neither of these amplitudes have a clear dependence on any of the variables $-t$, x_B and Q^2. The significant negative overall value of the leading twist amplitude $A_{LU,I}^{sin\phi}$ is much larger than the value of $A_{LU,I}^{sin(2\phi)}$, which is compatible with zero. The $A_{LU,DVCS}^{sin\phi}$ amplitude shown in the second row of Fig 6.1, dependent on the squared DVCS term in the scattering amplitude, has no particular kinematic dependence and is similarly compatible with zero. $A_{LU,I}^{sin\phi}$ can be used to access the imaginary part of the Compton Form Factor (CFF) $\mathcal{H}$, that can be used to constrain GPD H [101]. The systematic errors calculated as described in 5.5.4 are shown as a band at the bottom of each panel.

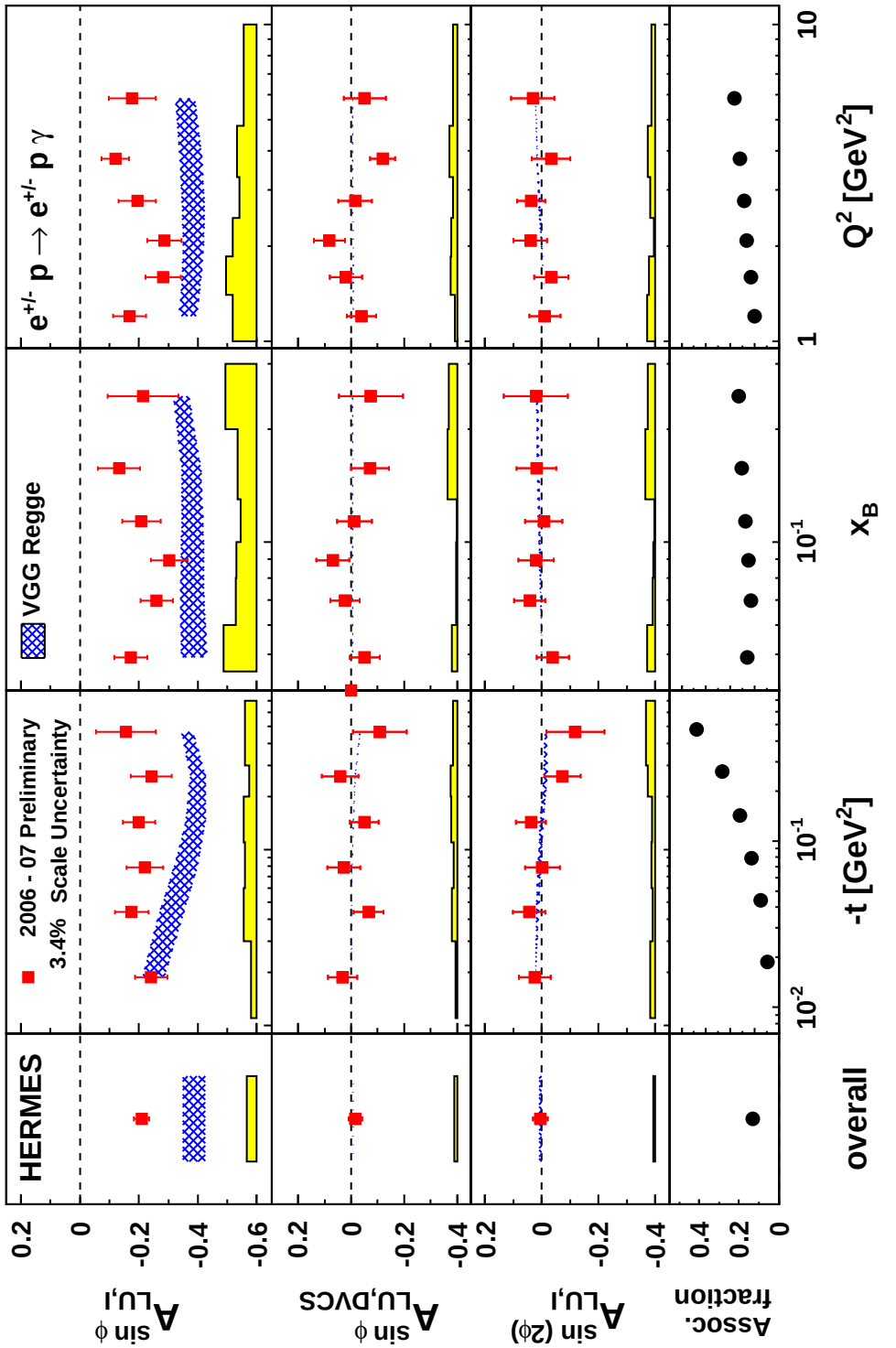

Figure 6.1: Beam Helicity Asymmetry amplitudes extracted from the 2006-2007 unpolarised hydrogen data. The error bars (bands) represent the statistical (systematic) uncertainties. The theory curves are based on the VGG model calculated with kinematic parameters accordant with the data set. The contribution of the Associated Bethe-Heitler to the asymmetry amplitudes is shown in the bottom panel. An additional 3.4% scale uncertainty arises from the precision of the beam polarisation measurement.

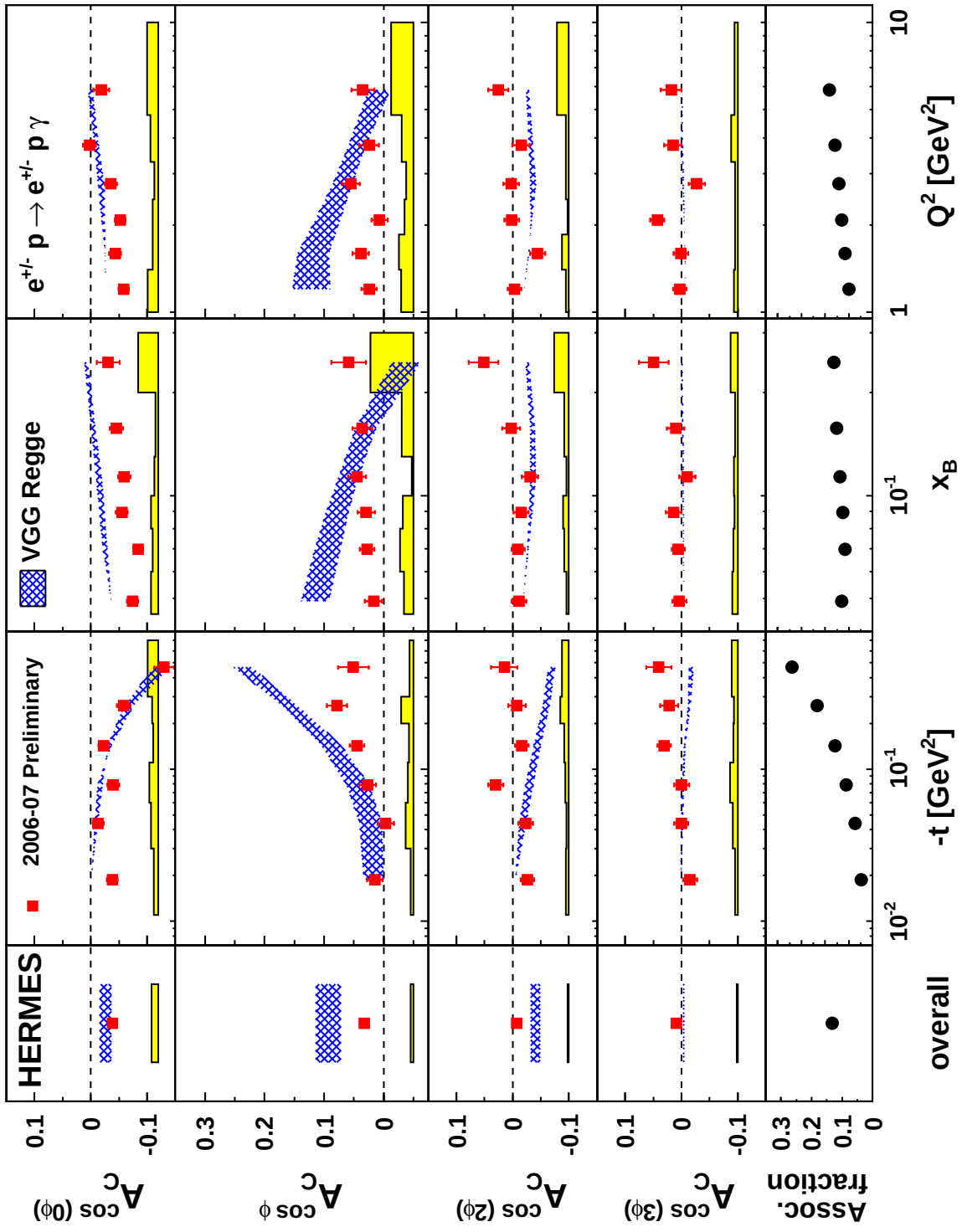

Figure 6.2: Beam Charge Asymmetry amplitudes from the 2006-2007 unpolarised hydrogen data. The error bars (bands) represent the statistical (systematic) uncertainties. The theory curves are based on the VGG model. The contribution of the Associated Bethe-Heitler to the asymmetry amplitudes is shown in the bottom panel.

The VGG model of the asymmetries does not include the Associated Bethe-Heitler contribution.

Asymmetry amplitudes obtained from experimental data are compared with the theoretical calculations from the VGG GPD model [23]. VGG theory bands are shown with a Regge-motivated ansatz to describe the t-dependence. The thickness of the theory bands arises from varying the skewness parameters b_{val} and b_{sea}, free parameters in the VGG model for valence and sea quarks respectively. The values of b_{val} and b_{sea} are varied between one and nine, with the variation of b_{sea} producing the most significant difference in theoretical amplitude value. The theory bands for the $A_{LU,DVCS}^{sin\phi}$ amplitudes are included for completeness, although the VGG model does not include precise twist-3 dependence, rather relating twist-3 to twist-2 via the Wandzura-Wilczek approximation [34]. The absolute value of the broad theory bands for the $A_{LU,I}^{sin\phi}$ amplitude are larger than the amplitude obtained from data and has a dependence on $-t$ that is not evident in the experimental result. The model for $A_{LU,I}^{sin(2\phi)}$is compatible with zero in agreement with the experimental result. The D term can be neglected in the model as it only contributes to the real part of the CFF and does not alter the result of the BHA [33].

The bottom row of Fig 6.1 shows the fractional contribution of the Associated Bethe-Heitler production, which can only be estimated from a Monte Carlo simulation. The overall value of the associated fraction is $\approx$12%. Monte Carlo simulations have shown that the presence of this contamination does not account for the difference between the experimental result and the model calculation [90].

The BCA amplitudes are shown in Fig 6.2. The $A_C^{cos(0\phi)}$ and the $A_C^{cos\phi}$ amplitudes are dependent on the real part of CFF $\mathcal{H}$ and are both significantly non-zero. $A_C^{cos(0\phi)}$ and $A_C^{cos\phi}$ have opposite sign. The absolute value of $A_C^{cos\phi}$ is greater than $A_C^{cos(0\phi)}$. Both of these amplitudes increase as $-t$ increases with the $A_C^{cos\phi}$ amplitude appearing to plateau in the higher $-t$ bins. The BCA amplitudes have no such dependence on either x_B or Q^2. There is a direct relationship between $A_C^{cos\phi}$ and $A_C^{cos(0\phi)}$ as both are related to the quark helicity conserving twist-2 GPDs. Considering only the dominant CFF $\mathcal{H}$ the Fourier coefficient $c_{1,unp}^I$ is directly proportional to $c_{0,unp}^I$, see Section 2.6. The real part of CFF $\mathcal{H}$ can be directly accessed using the $A_C^{cos\phi}$

amplitude. The $A_C^{cos(2\phi)}$ and the $A_C^{cos(3\phi)}$ amplitudes are both compatible with zero and show little variation across the kinematic range of $-t$, x_B and Q^2. $A_C^{cos(2\phi)}$ relates to twist-3 GPDs, and $A_C^{cos(3\phi)}$ relates to gluon helicity flip GPDs.

The VGG theory bands shown in Fig 6.2 are produced by varying both the b_{val} and b_{sea} between the values between 1 and 9 as before. The resulting theory band does not describe the experimental result. The overall value of the $A_C^{cos(0\phi)}$, $A_C^{cos\phi}$ and $A_C^{cos(2\phi)}$ theory bands is double that of the experimentally observed amplitude. The VGG model predicts the kinematic dependence of the $A_C^{cos(0\phi)}$ amplitudes which are offset from those extracted from the HERMES data. The theory bands for the $A_C^{cos\phi}$ amplitudes show dependence on the individual kinematic bins with the $-t$ band continuing to increase in the higher bins instead of levelling off. The x_B and Q^2 bands have a decreasing absolute asymmetry amplitude at higher values while the experimental result has no such dependence. The model also produces an amplitude compatible with zero for the $A_C^{cos(3\phi)}$ in agreement with the expected result. This is because the VGG model does not include the twist-3 or gluon helicity flip GPDs which relate to the amplitudes $A_C^{cos(2\phi)}$ and $A_C^{cos(3\phi)}$ respectively. The Associated Bethe-Heitler contribution is given in the bottom row of the figure.

6.2 Comparison with the Published 1996-2005 Analysis

In order to verify the analysis procedure used in this thesis an independent analysis of the 1996-2005 hydrogen data was undertaken. The asymmetry amplitudes of these two independent analyses of the same data set were found to be consistent as both are extracted using the same target, beams and experimental conditions. The amplitude of the asymmetries are equivalent extracted over the entire kinematic range within experimental error. In order to show the consistency of the asymmetry results extracted before and after the installation of the Recoil Detector the asymmetries extracted from 2006-2007 data are compared with the published 1996-2005 results. The BHA and BCA amplitudes extracted from both data taking periods are shown in Figs 6.3 and 6.4 respectively and the overall amplitudes are summarised in Table

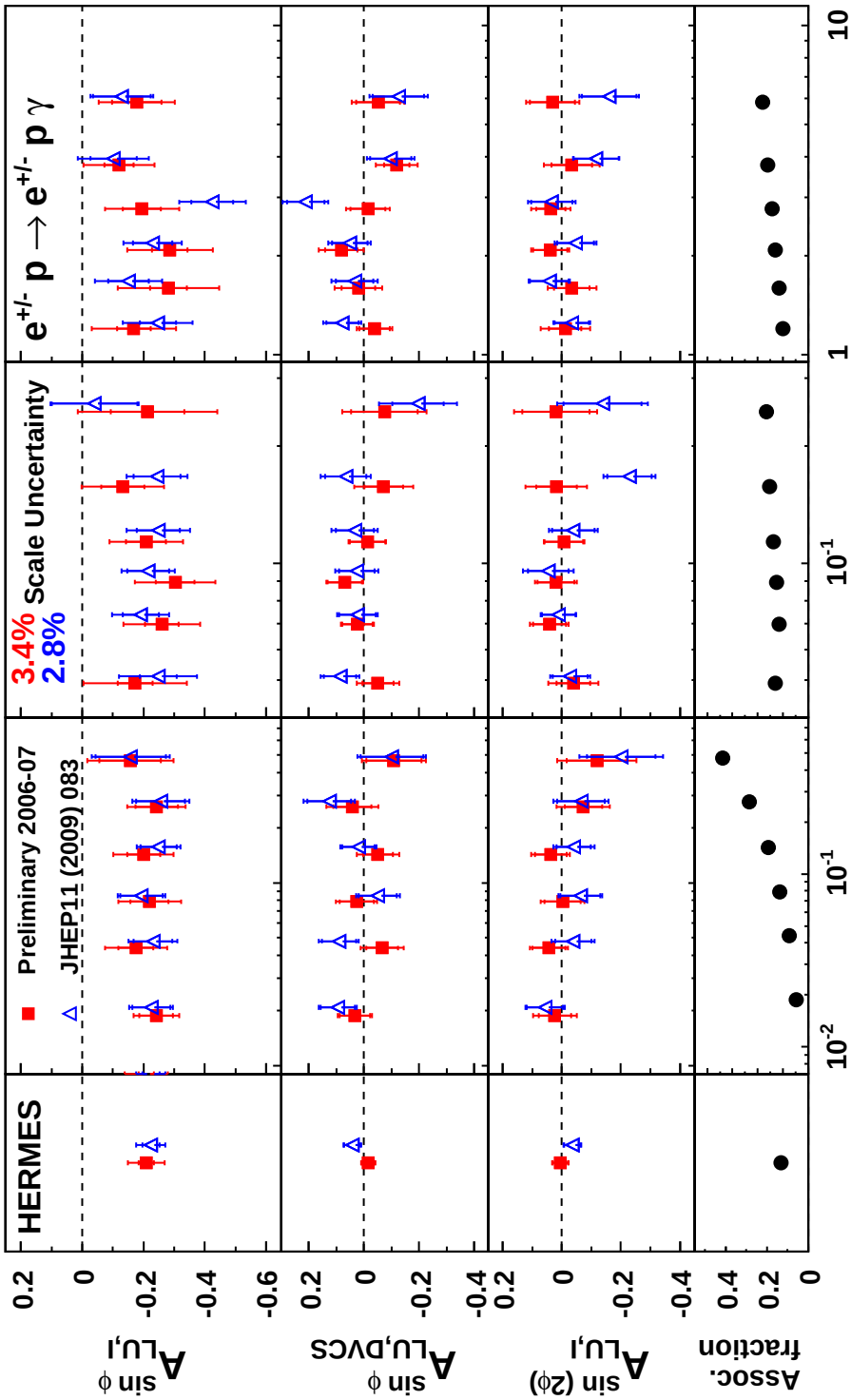

Figure 6.3: Beam Helicity Asymmetry amplitudes from the interference term of the 1996-2005 and the 2006-2007 data. The statistical and systematic error bars are represented by compound error bars. The amplitudes extracted from the DVCS/BH event sample from both data taking periods are compatible. The contribution of the Associated Bethe-Heitler to the asymmetry amplitudes is shown in the bottom panel.

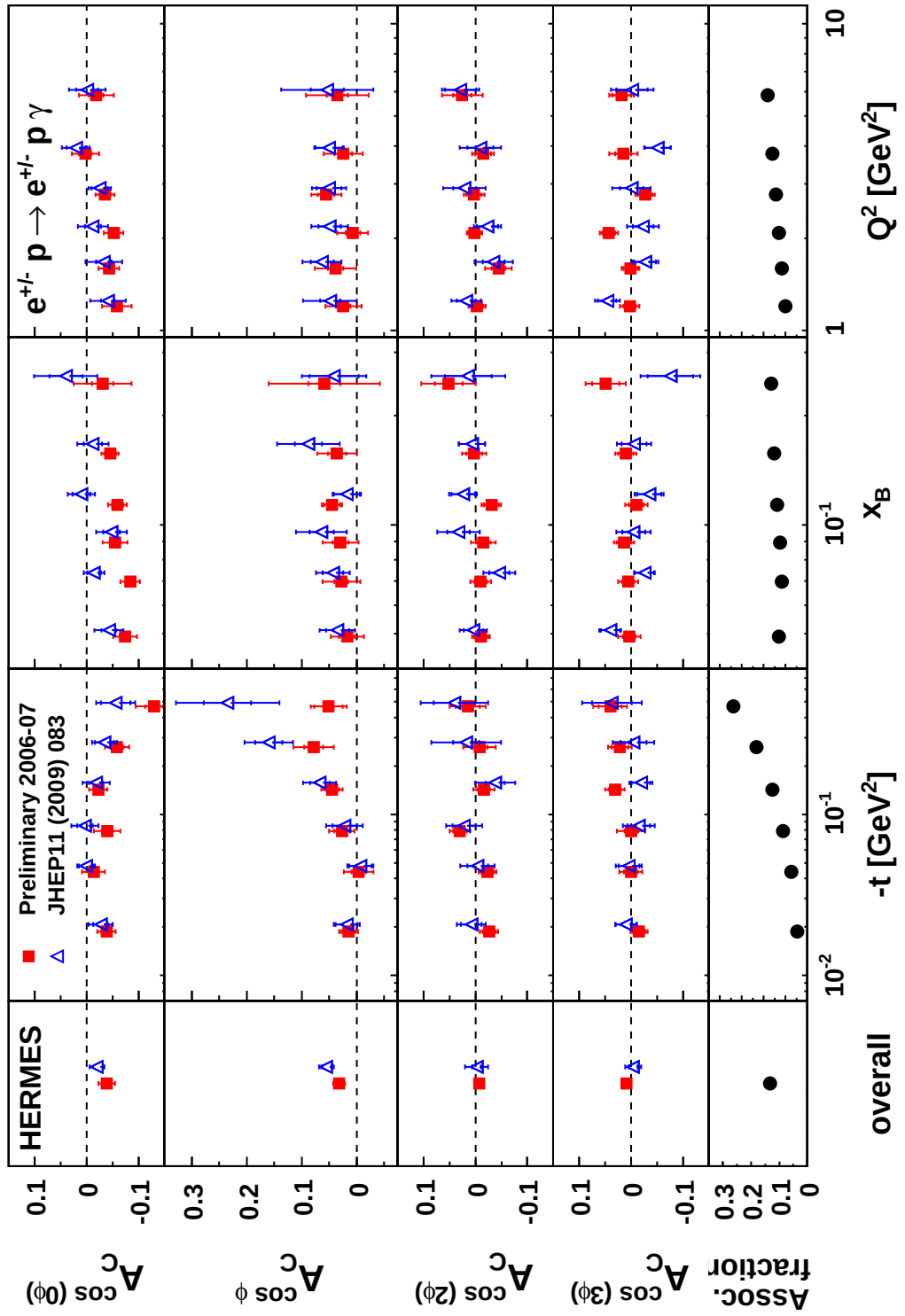

Figure 6.4: Beam Charge Asymmetry amplitudes from the 1996-2005 and the 2006-2007 data. The statistical and systematic error bars are represented by compound error bars. The amplitudes extracted from the DVCS/BH event sample from both data taking periods are compatible. The contribution of the Associated Bethe-Heitler to the asymmetry amplitudes is shown in the bottom panel.

Year	Amplitude	$A \pm \delta(stat.) \pm \delta(syst.)$
$A_C^{cos(0\phi)}$	1996-2005	$-0.020 \pm 0.006 \pm 0.016$
	2006-2007	$-0.038 \pm 0.004 \pm 0.012$
	1996-2007	$-0.031 \pm 0.003 \pm 0.011$
$A_C^{cos\phi}$	1996-2005	$+0.055 \pm 0.009 \pm 0.013$
	2006-2007	$+0.032 \pm 0.006 \pm 0.005$
	1996-2007	$+0.041 \pm 0.005 \pm 0.007$
$A_{LU,I}^{sin\phi}$	1996-2005	$-0.224 \pm 0.028 \pm 0.050$
	2006-2007	$-0.209 \pm 0.026 \pm 0.034$
	1996-2007	$-0.214 \pm 0.018 \pm 0.036$
$A_{LU,DVCS}^{sin\phi}$	1996-2005	$+0.045 \pm 0.028 \pm 0.006$
	2006-2007	$-0.015 \pm 0.026 \pm 0.011$
	1996-2007	$+0.010 \pm 0.019 \pm 0.008$

Table 6.1: Results of the BHA and BCA leading twist amplitudes for the periods 1996-2005, 2006-2007 and 1996-2007. The results are shown together with the statistical and systematic uncertainties. The 1996-2005 amplitudes are taken from [19]

6.1. The overall value of the $A_{LU,I}^{sin\phi}$ amplitude of extracted from both 2006-2007 and 1996-2005 are comparable and have a similar kinematic and the value and shape of the amplitudes are consistent over the kinematic range of $-t$, x_B and Q^2. This is also true for the $A_{LU,I}^{sin(2\phi)}$, $A_{LU,DVCS}^{sin\phi}$, $A_C^{cos(2\phi)}$ and $A_C^{cos(3\phi)}$ asymmetry amplitudes extracted from both data sets which are comparable with zero as expected from model predictions. The overall value of $A_C^{cos\phi}$ extracted from 2006-2007 data is lower in magnitude compared with the value extracted from 1996-2005 data. The $A_C^{cos\phi}$ amplitude for the last two bins of the $-t$ variable are smaller in magnitude for 2006-2007 compared with the previously published amplitudes. The last $-t$ bin has a different kinematic dependence decreasing in value for 2006-2007 data and increasing for 1996-2005 data. Interestingly, the $A_C^{cos\phi}$ amplitudes extracted from 2006-2007 data are similar to recently published BCA result using an unpolarised deuterium target [47]. The overall value of $A_C^{cos(0\phi)}$ from 2006-2007 data is similarly lower than the value extracted from 1996-2005 data. The statistical errors of the asymmetries from 2006-2007 data do not decrease compared with 1996-2005 despite the increase in the available statistics. This is due to the time dependence of the 2007 data and the lower beam polarisation values during the final two years. The beam polarisation at HERMES is not 100% polarised, therefore, it was necessary to scale the polarisation to 100% during the analysis procedure. As a consequence of this scaling the error bars are larger for the Beam Helicity Asymmetry than the Beam Charge and a the beam polarisation was lower during the 2006-2007 data taking period than 1996-2000 the error bars are not dissimilar. Overall the asymmetry results extracted from the 2006-2007 data set are consistent with the two independent analyses of the 1996-2005 data set. The results of the 2006-2007 asymmetry amplitudes are, however, more stable than those extracted from the 1996-2005 data as they do not feature the outlying amplitudes in some of the higher t, Q^2 and X_B bins. These results are also consistent with the deuterium results, shown in Fig 7.1.

6.3 Combined BHA and BCA Results from All Hydrogen Data

The results of the BHA and BCA amplitudes extracted from the 1996-2007 unpolarised hydrogen DVCS event sample are shown in Figs 6.5 and 6.6. The resulting amplitudes are similar to the 2006-2007 amplitudes as expected due to the dominance of the statistics from both of these years. The leading twist $A_{LU,I}^{sin\phi}$ amplitude is the largest BHA result with $A_{LU,I}^{sin(2\phi)}$ and $A_{LU,DVCS}^{sin\phi}$ both being compatible with zero. The BCA amplitudes $A_C^{cos(0\phi)}$ and $A_C^{cos\phi}$ integrated over all kinematics have a non-zero amplitude, while the higher twist amplitudes $A_C^{cos(2\phi)}$ and $A_C^{cos(3\phi)}$ are compatible with zero. Both the $A_C^{cos\phi}$ and $A_C^{cos(0\phi)}$ amplitude distributions have a discernible shape when binned in $-t$. The $-t$ dependence of $A_C^{cos\phi}$ from the 1996-2007 DVCS event sample continues to increase in the high $-t$ bins, as opposed to reaching a plateau as in the 2006-2007 case. The theory bands calculated from the VGG model are also similar to those in Figs 6.1 and 6.2 having been recalculated at the correct kinematics. The systematic error bands were calculated from the weighted average of both the systematic errors from Monte Carlo simulations weighted using the relevant geometry files. The weighting was based on the statistical contribution from each of the independent data sets to the overall result and in each kinematic bin.

6.4 Single-Charge BHA Results from 2006-2007 Unpolarised Hydrogen Data

The HERMES experiment used both an electron and positron beam during different data taking periods. The electron and positron beams were used during 2006 while data taken during 2007 used only the positron beam. The single charge BHA was extracted separately from the 2006 electron, 2006 positron and the 2007 positron data. These asymmetry amplitudes are shown in in Figs 6.7 and 6.8.

The BHA amplitudes are extracted using a four parameter fit, Eq 5.19 that includes the cos(0ϕ), sinϕ, sin(2ϕ) and cosϕ terms. The cos(0ϕ) and cosϕ terms are

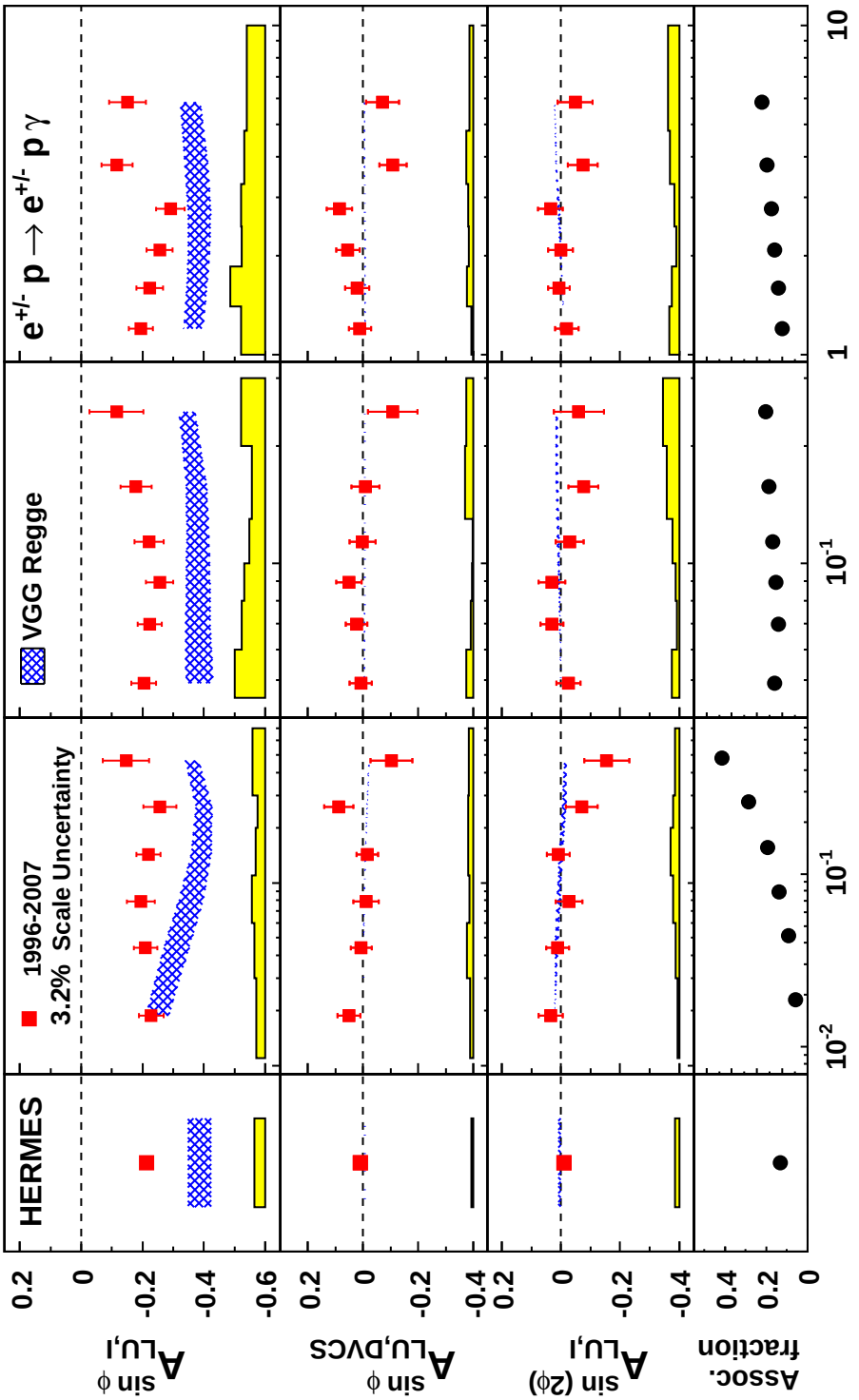

Figure 6.5: Beam Helicity Asymmetry amplitudes extracted from all hydrogen data. The error bars (bands) represent the statistical (systematic) uncertainties. The theory curves are based on the VGG model. The contribution of the Associated Bethe-Heitler to the asymmetry amplitudes is shown in the bottom panel.

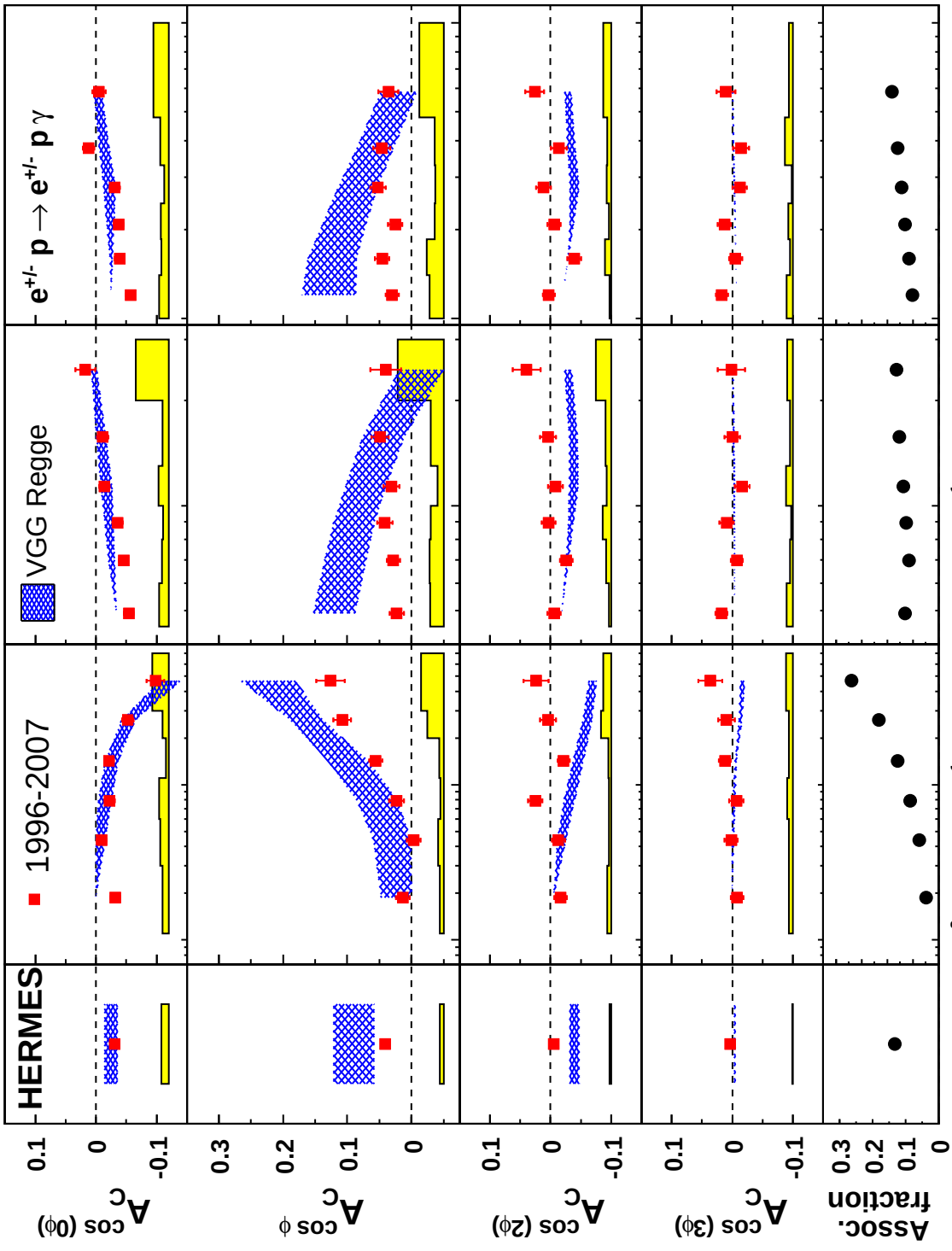

Figure 6.6: Beam Charge Asymmetry amplitudes from all hydrogen data. The error bars (bands) represent the statistical (systematic) uncertainties. The theory curves are based on the VGG model. The contribution of the Associated Bethe-Heitler to the asymmetry amplitudes is shown in the bottom panel.

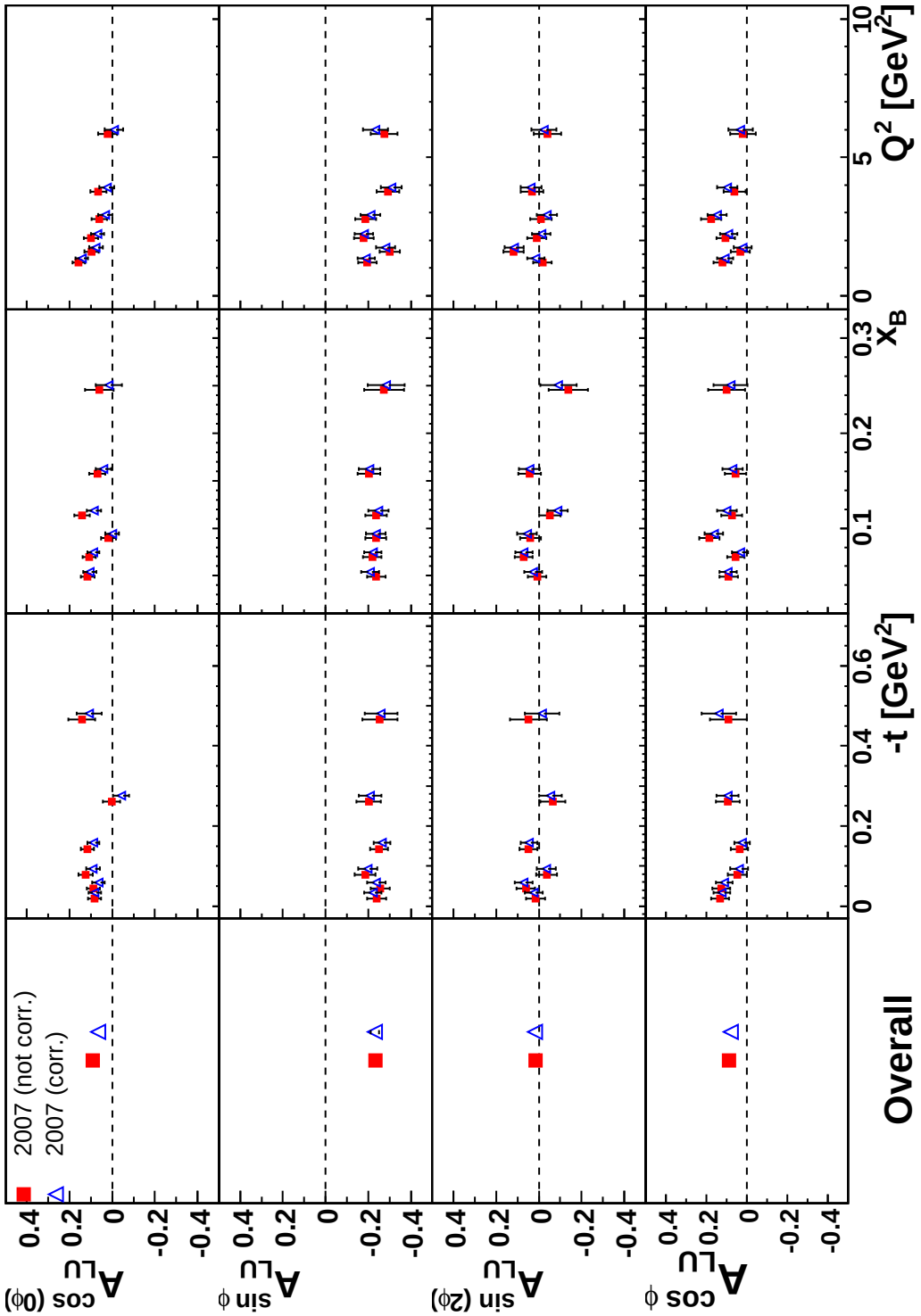

Figure 6.7: The results of the beam helicity asymmetry amplitudes using the 4 parameter fitting function on the 2007 data only. The amplitudes using the standard uncorrected and time dependent corrected missing mass shifts are shown.

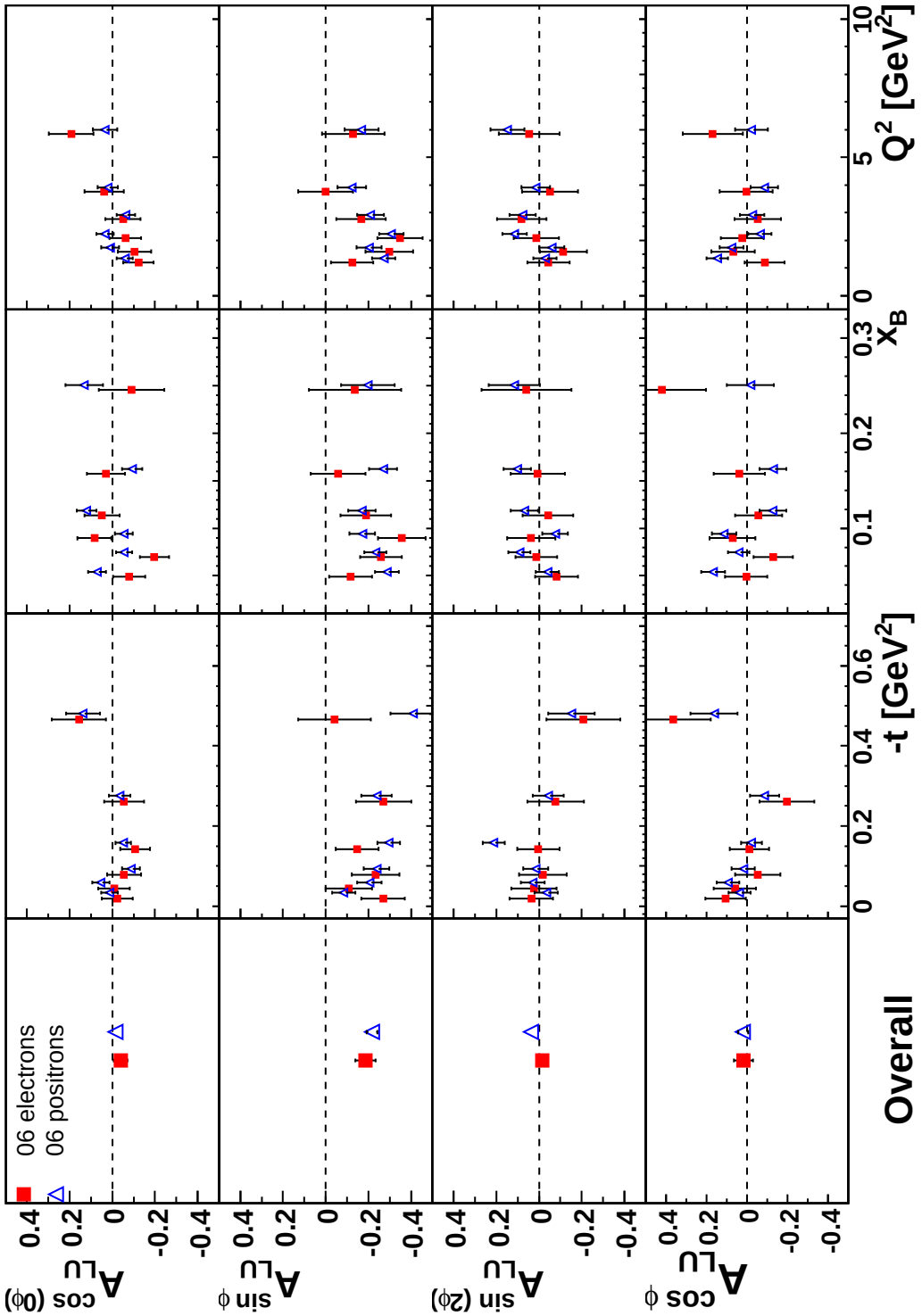

Figure 6.8: The results of the beam helicity asymmetry amplitudes using the 4 parameter fitting function extracted separately from 2006 electron and positron data. The amplitudes extracted from electron data are positive but are shown with negative values for ease of comparison.

included as a check of the stability and normalisation and should have no physical value. The overall amplitudes from the different DVCS event samples remain constant despite the 2007 data having a slightly larger constant $A_{LU}^{cos(0\phi)}$ amplitude. The constant term is reduced by introducing the time dependent missing mass shift as described in Section 5.4.3. The constant $A_{LU}^{cos(0\phi)}$ amplitude from the fit to the 2006 electron and positron data indicates that the fit for both charges has been correctly normalised and does not have the time dependence associated with the 2007 data.

The $A_{LU}^{sin\phi}$ and $A_{LU}^{sin(2\phi)}$ amplitudes include the $A_{LU,I}^{sin\phi}$ and $A_{LU,DVCS}^{sin\phi}$ and $A_{LU,I}^{sin(2\phi)}$ and $A_{LU,DVCS}^{sin(2\phi)}$ amplitudes respectively, but the single-beam charge extraction method does not allow for their disentanglement. The leading twist $A_{LU}^{sin\phi}$ amplitude has the largest overall value while the $A_{LU}^{sin(2\phi)}$ amplitude is compatible with zero. The suppression of the higher order terms is as expected. The value of the $A_{LU}^{sin\phi}$ amplitude is greater for the positron data than for electron data. The amplitudes from electron and positron data have positive and negative values respectively, the values are shown with the same sign in Fig 6.8 for ease of comparison. There appears to be no strong kinematic dependence for any of the amplitudes when projected in $-t$, x_B and Q^2.

The BHA single charge amplitudes are comparable with those extracted from the 1996 and 2005 data and the published BHA result using data taken in 1996 and 1997 shown in Fig 6.9 which has a value of A_{LU,e^+} = -0.23 $\pm$ 0.04(stat.) $\pm$ 0.03(syst.). These BHA single charge results are summarised in Table 6.2. The asymmetries extracted from the positron data are similar in amplitude and are compatible with one another. The BHA extracted from the 1996-2005 and the 2006 data are compatible. The 2007 positron data is most consistent with the first published result.

6.5 Summary

Three separate results have been extracted from HERMES hydrogen data: a combined extraction of the BHA and BCA from both 2006-2007 and 1996-2007 data and a single-charge BHA only extraction of the 2006 positron, 2006 electron and

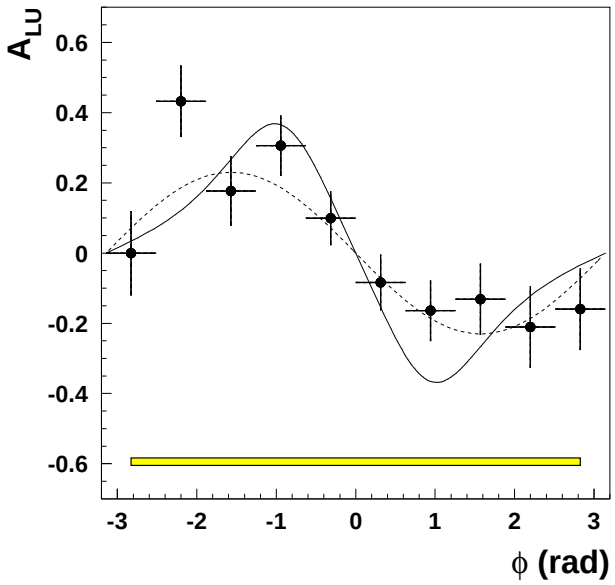

Figure 6.9: The single charge BHA shown as a function of ϕ with a sinϕ function using Least Squares method fitted to the data. Plot taken from [44].

Year	Charge (e^+/e^-)	$A_{LU}^{sin\phi} \pm \delta(stat.)$
1996/1997	e^+	-0.23 ± 0.040
1996-2005	e^+	-0.267 ± 0.065
1996-2005	e^-	$+0.181 \pm 0.046$
2006	e^+	-0.217 ± 0.025
2006	e^-	$+0.182 \pm 0.047$
2007	e^+	-0.232 ± 0.020

Table 6.2: A summary of the results of the single charge BHA $A_{LU}^{sin\phi}$ amplitudes for both positive and negative beam charges including the statistical error. The results were produced using combinations of different data taken over the entire HERMES data taking period. Due to the large statistical sample available for 2006 and 2007 these results are shown separately. The 1996/1997 amplitudes are taken from [89] and 1996-2005 amplitudes from [90].

2007 positron data. The single-charge BHA extraction is included to confirm that these results are consistent with those previously published by the collaboration and that the $A_{LU,I}$ and $A_{LU,DVCS}$ amplitudes, obtained from the combined extraction, sum to give the value of A_{LU}. The results have been described in the previous section and their relation to the underlying GPDs and Compton Form Factors explained. The experimental results have been compared to theoretical values based on the VGG model. The asymmetry results are all compatible with one another and those previously published by the HERMES collaboration using both a hydrogen and deuterium target.

Chapter 7

Conclusions and Outlook

Generalised Parton Distributions (GPDs) can be used to describe the structure of the nucleon and give experimental access to the total angular momentum of quarks in the nucleon, leading to a complete description of the nucleon spin. Deeply Virtual Compton Scattering (DVCS) using an unpolarised hydrogen target is used to access GPD H.

All of the hydrogen data taken during the entire running period of HERMES have been included in the analysis presented in this thesis. The Beam Charge Asymmetry (BCA) and the Beam Helicity Asymmetry (BHA) originating from the interference and the squared DVCS term have been extracted simultaneously from the DVCS/BH event sample. The asymmetry results of the 2006-2007 hydrogen, 1996-2005 hydrogen [19] and 1996-2005 deuterium data including the statistical and systematic uncertainties have been extracted along with their dependence on the kinematic variables $-t$, x_B and Q^2 and are shown in Fig 7.1. The results presented in this thesis are the most precise measurement of DVCS asymmetries at the kinematic conditions of the HERMES experiment. The BHA leading amplitude $A_{LU,I}^{sin\phi}$, sensitive to the DVCS and Bethe-Heitler (BH) interference term, has a negative overall value of -0.209 $\pm$ 0.026 $\pm$ 0.034. The $A_{LU,DVCS}^{sin\phi}$, sensitive to the squared DVCS term, and the higher twist $A_{LU,I}^{sin(2\phi)}$ amplitudes are both suppressed with overall values of -0.015 $\pm$ 0.026 $\pm$ 0.011 and 0.005 $\pm$ 0.025 $\pm$ 0.007 respectively. The leading amplitudes of the BCA, $A_C^{cos(0\phi)}$ and $A_C^{cos\phi}$, are both non-zero, with overall values of -0.039 $\pm$ 0.004 $\pm$ 0.011 and 0.032 $\pm$ 0.006 $\pm$ 0.005, and have opposite sign as predicted from

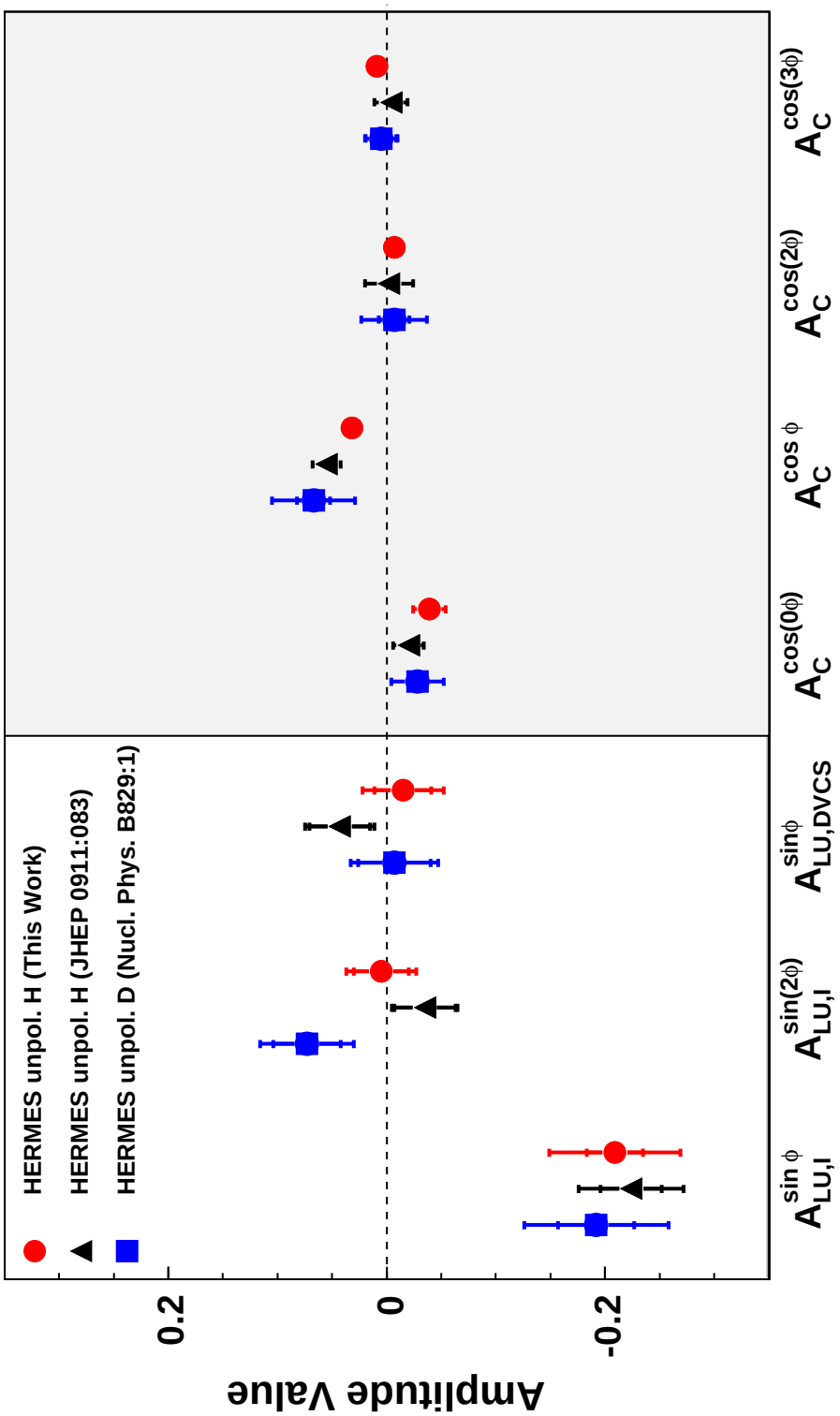

Figure 7.1: Summary of the $A_{LU,I}^{sin(n\phi)}$, $A_{LU,DVCS}^{sin(n\phi)}$ and $A_C^{cos(n\phi)}$ amplitudes extracted from 2006-2007 unpolarised hydrogen data (full red circles). The results from the 1996-2005 hydrogen data [19] (black triangles) and the 1996-2005 deuterium data [47] (blue squares) are also shown. The statistical and systematic uncertainties are shown as compound error bars.

theoretical models. The higher moment amplitudes of both the BHA and BCA are suppressed. As with the BHA amplitudes there is no strong dependence on the kinematics, apart from expecting a possible increase in value with increasing $-t$ in the first part of the kinematic range. The results of the analysis presented in this analysis are in statistical agreement with the results from the 1996-2005 hydrogen and 1996-2005 deuterium data which exhibit larger errors.

All DVCS analyses performed at HERMES from the start of data taking in 1996 until now, including the analysis presented in this thesis, have relied upon calculating the missing mass in the DVCS interaction to identify the proton. The experiment was upgraded in 2005 to include a detector that would allow the proton from a DVCS/BH event to be identified and measured directly. Data using this new detector was taken from 2006 until the end of data taking in July 2007. The analysis of DVCS at HERMES will be improved by including information from the recoiling target proton in the final state, allowing background events to be more precisely removed from the exclusive event sample. To this end software has been developed [64, 102] to track the recoil protons from the raw information provided by the detectors that comprise the recoil detector, namely, the Silicon Strip Detector (SSD), Scintillating Fibre Tracker (SFT) and the Photon Detector (PD). A method that reconstructed the tracks of protons using the energy loss in the SSD has been developed. This method of track reconstruction has been included in the complete recoil tracking package and will be used in future DVCS analyses. The final DVCS results at HERMES will use the Recoil Detector to identify the recoiling proton present in a DVCS event. This will remove background events present in this analysis. Removing the background processes from the exclusive event sample will reduce both the statistical and systematic uncertainty of the asymmetry results. The DVCS/BH event sample obtained using the Recoil Detector will, therefore, be a subset of the DVCS/BH events used to produce the results in this thesis.

The available theoretical models do not describe the experimental data. Instead of using models, recent attempts to constrain the values of GPDs, in particular GPD H, have involved making fits and parametrisations to the globally available DVCS data [103, 104, 101]. Other experiments continuing to measure DVCS information

at different kinematics to that of HERMES include COMPASS at CERN [105] and Hall A and B at Jefferson Lab [106]. These experiments will expand the present knowledge of both DVCS and GPDs, and ultimately, the internal structure of the nucleon.

Bibliography

[1] R.P.Feynman, "Very High-Energy Collisions of Hadrons.," *Phys. Rev. Lett.*, vol. 23, pp. 1415–1417, 1969.

[2] M. Gell-Mann, "A schematic model of baryons and mesons," *Phys. Lett*, vol. 8, pp. 214–215, 1964.

[3] D. M. Dennison, "A Note on the Specific Heat of the Hydrogen Molecule," *Proceedings of the Royal Society of London. Series A, Containing Papers of a Mathematical and Physical Character*, vol. 115, pp. 483–486, 1927.

[4] X. Ji, "Gauge-Invariant Decomposition of Nucleon Spin and Its Spin-Off," *Phys.Rev.Lett.*, vol. 78, pp. 610–613, 1997.

[5] J. Ashman *et al.*, "An investigation of the spin structure of the proton in deep-inelastic scattering of the polarized muons," *Phys Lett B*, vol. 206, p. 234, 1988.

[6] J. Ashman *et al.*, "An investigation of the spin structure of the proton in deep inelastic scattering of polarized muons on polarized protons," *Nucl. Phys*, vol. B328, p. 1, 1989.

[7] E.Leader and M.Anselmino, "A crisis in the parton model: where, oh where is the protons spin?," *Z. Phys*, vol. C41, p. 239, 1988.

[8] M. Alugard et al., "Deep inelastic scattering of polarized electrons by polarized protons," *Phys Lett*, vol. 37, p. 1261, 1976.

[9] The HERMES Collaboration, "HERMES collaboration Technical Design Report," tech. rep., HERMES Internal Report 93-015, July 1993.

[10] The HERMES Collaboration, A. Airapetian et al., "Precise determination of the spin structure function $\mathbf{g_1}$ of the proton, deuteron and neutron," *Phys.Rev*, vol. D75, 2007.

[11] R. Kaiser, "Private Communication.".

[12] A. V. Belitsky and D. Mueller, "Nucleon hologram with exclusive leptoproduction," *Nucl.Phys. A*, vol. 711, pp. 118–126, 2002.

[13] F.M.Dittes, D. Mueller, and D.Robaschik, "The Altarelli-Parisi Kernel as Asymptotic Limit of an Extended Brodsky-Lepage kernel," *Phys. Lett*, vol. B209, pp. 325–329, 1988.

[14] D. Mueller, D. Robaschik, B. Geyer, F. M. Dittes, and J. Hoeji, "Wave Functions, Evolution Equations and Evolution Kernels from Light-Ray Operators of QCD," *Fortsch.Phys.*, vol. 42, p. 101, 1994.

[15] K. Kumericki, D. Mueller, and K. Passek-Kumericki, "Fitting DVCS amplitude in moment-space approach to GPDs," *K.K. at DIS 2008 and D.M. at Diffraction Workshop 2008*, 2008.

[16] A. V. Radyushkin, "Nonforward Parton Distributions," *Phys.Rev. D*, vol. 56, pp. 5524–5557, 1997.

[17] I. I. Balitsky and A. V. Radyushkin, "Light-Ray Evolution Equations and Leading-Twist Parton Helicity-Dependent Nonforward Distributions," *Phys.Lett. B*, vol. 413, pp. 114–121, 1997.

[18] X. Ji, "Deeply Virtual Compton Scattering," *Phys.Rev. D*, vol. 55, pp. 7114–7125, 1997.

[19] The HERMES Collaboration, A. Airapetian et al., "Separation of contributions from deeply virtual Compton scattering and its interference with the Bethe–Heitler process in measurements on a hydrogen target," *JHEP*, vol. 0911, p. 083, Sept. 2009.

[20] The HERMES Collaboration, A. Airapetian et al., "Nuclear-mass dependence of azimuthal beam-helicity and beam-charge asymmetries in deeply virtual Compton scattering," *Phys.Rev.*, vol. C81, p. 035202, Nov. 2010.

[21] The HERMES Collaboration, "The HERMES Recoil Detector Technical Design Report," tech. rep., HERMES Internal Report 02-003, 2002.

[22] M. Burkardt, "Impact Parameter Dependent Parton Distributions and Off-Forward Parton Distributions for $\zeta \to 0$," *Phys.Rev.D*, vol. D66:114005, 2002.

[23] M.Vanderhaeghen, P.A.M.Guichon, and M.Guidal, "Deeply virtual electroproduction of photons and mesons on the nucleon: Leading order amplitudes and power corrections," *Phys. Rev.*, vol. D60:094017, 1999.

[24] A. V. Radyushkin, "Double distributions and evolution equations," *Phys.Rev. D*, vol. 59, p. 014030, 1999.

[25] K. Goeke, M. V.Polyakov, and M. Vanderhaeghen, "Hard Exclusive Reactions and the Structure of Hadrons," *Prog. Part. Nucl. Phys.*, vol. 47, pp. 401–515, 2001.

[26] V. A. Korotkov and W. D. Nowak, "Future Measurements of Deeply Virtual Compton Scattering at HERMES," *Eur.Phys.J. C*, vol. 23, pp. 455–461, 2002.

[27] R. L. Jaffe, "Spin, Twist and Hadron Structure in Deep Inelastic Processes," *MIT-CTP-2506*, 2009.

[28] A. V. Radyushkin, "Generalized Parton Distributions," *JLAB-THY-00-33*, 2007.

[29] A. V. Radyushkin, "Scaling Limit of Deeply Virtual Compton Scattering," *Phys.Lett. B*, vol. 380, pp. 417–425, 1996.

[30] S. Boffi and B. Pasquini, "Generalized parton distributions and the structure of the nucleon," *Riv.NuovoCim.*, vol. 30, p. 387, Nov. 2007.

[31] X. Ji, "Off-Forward Parton Distributions," *J.Phys.G*, vol. 24, pp. 1181–1205, 1998.

[32] P. G. Mankiewicz, L. and T. Weigl, "Hard exclusive meson production and nonforward parton distributions," *Eur. Phys. J. C*, vol. 5, pp. 119–128, 1998.

[33] M. V. Polyakov and C. Weiss, "Skewed and double distributions in pion and nucleon," *Phys.Rev.D.*, vol. 60:114017, 1999.

[34] S. Wandzura and F. Wilczek, "Sum Rules for Spin Dependent Electroproduction: Test of Relativistic Constituent Quarks," *Phys Lett*, vol. B72, p. 195, 1077.

[35] N. Kivel, M. V. Polyakov, and M. Vanderhaeghen, "DVCS on the nucleon : study of the twist-3 effects," *Phys.Rev. D*, vol. 63, p. 114014, 2001.

[36] V. Guzey and T. Teckentrup, "The dual parameterization of the proton generalized parton distribution functions H and E and description of the DVCS cross sections and asymmetries," *Phys.Rev. D*, vol. 74:054027, 2006.

[37] V. Guzey and M. V. Polyakov, "On the mistake in the implementation of the minimal model of the dual parameterization and resulting inability to describe the high-energy DVCS data," *arXiv:0810.3899*.

[38] V. Y. Petrov, P. V. Pobylitsa, M. V. Polyakov, I. Boernig, K. Goeke, and C. Weiss, "Off-forward quark distributions of the nucleon in the large n_c limit," *Phys.Rev. D*, vol. 57, pp. 4325–4333, 1998.

[39] M. Guidal, M. V. Polyakov, A. V. Radyushkin, and M. Vanderhaeghen, "Nucleon Form Factors from Generalized Parton Distributions," *Phys.Rev.D*, vol. 72, 054013, 2005.

[40] A. V. Belitsky, D. Mller, and A. Kirchner, "Theory of deeply virtual Compton scattering on the nucleon," *Nucl.Phys. B*, vol. 629, pp. 323–392, 2002.

[41] M. Diehl, "Generalized Parton Distributions," in *Baryons*, 2002.

[42] D. F. Mahon, *Deeply Virtual Compton Scattering off Longitudinally Polarised Protons at HERMES*. PhD thesis, University of Glasgow, 2010.

[43] M. Diehl, T. Gousset, B. Pire, and J. P. Ralston, "Testing the handbag contribution to exclusive virtual compton scattering," *Phys.Lett.B*, vol. 411, pp. 193–202, 1997.

[44] The HERMES Collaboration, A. Airapetian et al., "The Beam–Charge Azimuthal Asymmetry and Deeply Virtual Compton Scattering," *Phys.Rev.D*, vol. 75:011103, 2007.

[45] The HERMES Collaboration, A. Airapetian et al., "Measurement of Azimuthal Asymmetries With Respect To Both Beam Charge and Transverse Target Polarization in Exclusive Electroproduction of Real Photons," *JHEP*, vol. 06, p. 066, Feb. 2008.

[46] The HERMES Collaboration, A. Airapetian et al., "Exclusive leptoproduction of real photons on a longitudinally polarised hydrogen target," *JHEP 06*, vol. 019, 2010.

[47] The HERMES Collaboration, A. Airapetian et al., "Measurement of azimuthal asymmetries associated with deeply virtual Compton scattering on an unpolarized deuterium target," *Nucl. Phys.*, vol. B 829, pp. 1–27, Nov. 2009.

[48] M.Dueren, "The HERMES Experiment: From Design to the First Results," *University Erlangen-Nuernberg, DESY Grey Report: DESY-HERMES 95-02*, 1995.

[49] M. J. Murray, *DVCS at HERMES: The Recoil Detector & Transverse Target Spin Asymmetries*. PhD thesis, DESY, 2008.

[50] A.A.Sokolov and I.M.Ternov, "On polarization and spin effects in synchrotron radiation theory," *Sov. Phys. Doklady*, vol. 8, p. 1203, 1964.

[51] J.Buon and K.Steffen, "HERA variable-energy "mini" spin rotator and head-on ep collision scheme with choice of electron helicity," *Nucl. Instrum. Meth. A*, vol. 245, pp. 248–261, 1986.

[52] D.P.Barber et al., "The HERA polarimeter and the first observation of electron spin polarization at HERA," *Nucl. Instrum. Meth. A.*, vol. 329, pp. 79–111, 1993.

[53] M. Beckmann, A. Borissov, S. Brauksiepe, F. Burkart, H. Fischer, J. Franz, F. H. Heinsius, K. Konigsmann, W. Lorenzon, F. M. Menden, A. Most, S. Rudnitsky, C. Schill, J. Seibert, and A. Simon, "The Longitudinal Polarimeter at HERA," *Nucl. Instrum. Meth. A*, vol. 479, pp. 334–348, 2002.

[54] The HERMES Collaboration, "The HERMES Polarized Hydrogen and Deuterium Gas Target in the HERA Electron Storage Ring," *Nucl. Instrum. Meth. A*, vol. 540, pp. 68–101, 2005.

[55] A.Nass et al., "The HERMES polarized atomic beam source," *Nucl. Instrum. Meth. A.*, vol. 505, pp. 633–644, 2003.

[56] C. Baumgarten et al., "A gas analyzer for the internal polarized target of the HERMES experiment," *Nucl. Instrum. Meth. A.*, vol. 508, pp. 268–275, 2003.

[57] C. Baumgarten et al., "The storage cell of the polarized H/D internal gas target of the HERMES experiment at HERA," *Nucl. Instrum. Meth. A.*, vol. 496, pp. 277–285, 2003.

[58] R. Kaiser, *Measurement of the spin structure of the neutron using polarised deep inelastic scattering.* PhD thesis, Simon Fraser University, 1997.

[59] K. Ackerstaff, "The HERMES Spectrometer," *Nucl.Instrum.Meth. A*, vol. 417, pp. 230–265, 1998.

[60] D. Rykbash et al., "The HERMES RICH Detector," *Nucl Instrum Meth. A*, vol. 433, p. 98, 1999.

[61] F.Sauli, "Principles of Operation of Multiwire Proportional and Drift Chambers," *CERN-77-09*, 1977.

[62] G.Charpak, "Electronic inmaging of ionizing radiation with limited avalanches in gases," *Rev. Mod. Phys.*, vol. 65, pp. 591–598, 1993.

[63] W.Wander, *Reconstruction of High-Energy Scattering Event in the HERMES Experiment.* PhD thesis, Friedrich-Alexander-Universitaet-Erlangen-Nuernberg, 1997.

[64] G. D. Hill, *Deeply Virtual Compton Scattering off Unpolarised Deuterium at HERMES.* PhD thesis, University of Glasgow, 2008.

[65] M. Tytgat, "Particle identification with the HERMES RICH," *Nucl. Instrum. Meth. A.*, vol. 433, pp. 286–288, 1999.

[66] H. Avakian, "Performance of the Electromagnetic Calorimeter of the HERMES Experiment," *Nucl. Instrum. Meth. A*, vol. 417, pp. 69–78, 1998.

[67] T. Benisch et al., "The luminosity monitor of the HERMES experiment at DESY," *Nucl. Instrum. Meth. A.*, vol. 471, pp. 314–324, 2001.

[68] B. Seitz, "The HERMES recoil detector : a combined silicon strip and scintillating fibre detector for tracking and particle identification," *Nucl. Instrum. Meth. A.*, vol. 535, pp. 538–541, 2004.

[69] N. Pickert, "First data from the HERMES Recoil Detector," *Nucl.Instrum. Meth. A.*, vol. 581, pp. 504–506, 2007.

[70] M.Reinecke et al., "A silicon strip recoil detector for momentum measurement and tracking at HERMES," *Nuclear Science Symposium Conference Record*, vol. 1, pp. 561–565, 2003.

[71] M.Hoek, *Design and Construction of a Scintillating Fibre Tracker for measuring Hard Exclusive Reactions at HERMES.* PhD thesis, Justus-Liebig-Universitaet Giessen, 2006.

[72] N. C. R. Makins, "HERMES Software Bootcamp," 2002.

[73] E. D. CERN PTG, Programming Techniques Group, "ADAMO Users Guide for Version 3.3," tech. rep., CERN, 1993.

[74] W. Wander, "DAD - Distributed ADAMO Database System at HERMES," in *Proceedings of CHEP 95, Rio de Janerio*, 1995.

[75] A. Mussgiller, "Recoil ADAMO Tables," tech. rep., HERMES Internal Documentation, 2009.

[76] V. A. Mitsou for the ATLAS SCT Collaboration, "Readout Electronics Tests and Integration of the ATLAS Semiconductor Tracker," 2007.

[77] CMS Collaboration, "Commissioning and Performance of the CMS Silicon Strip Tracker with Cosmic Ray Muons," *JINST*, vol. 5, p. T03007, Nov. 2009.

[78] D. Beznosko, "Novel Multi-pixel Silicon Photon Detectors and Applications in T2K," *Proceedings of DPF-2009*, Oct. 2009.

[79] D. Bhattacharyaa, T. J. ONeilla, A. Akyzb, J. Samimic, and A. D. Zych, "Prototype TIGRE Compton -ray balloon-borne telescope," *New Astronomy Reviews*, vol. 48, pp. 287–292, 2004.

[80] J. Ponpona, P. Sifferta, and F. Vazeille, "Thin dE/dx detectors of uniform thickness made on epitaxial silicon," *Nucl. Instrum. Meth.*, vol. 112, pp. 465–467, 1973.

[81] R. Bellwied et al., "The STAR Silicon Vertex Tracker: A large area Silicon Drift Detector," *Nucl. Instrum. Meth. A.*, vol. 499, pp. 640–651, 2003.

[82] S. G. for the ATLAS Collaboration, "ATLAS Inner Detector performance," *Nucl. Instrum. Meth. A.*, vol. 462, pp. 285–290, 2001.

[83] E. A. Uehling, "Penetration of Heavy Charged Particles in Matter," *Annual Review of Nuclear Science*, vol. 4, pp. 315–350, 1954.

[84] H. Bichsel, "Straggling in thin silicon detectors," *Rev. Mod. Phys.*, vol. 60, p. 663699, 1988.

[85] W. Leo, *Techniques for Nuclear and Particle Physics Experiments: A How To Approach*. Springer-Verlag, 1994.

[86] J. Burns and I. Lehmann, "Status of DER Momentum Reconstruction," tech. rep., University of Glasgow, 2007.

[87] A. Musgiller, "MC Flex-Foil Material.".

[88] J. Burns, "DVCS on an Unpolarised Hydrogen target (2006-2007 and 1996-2007)," *HERMES Internal Report*, 2010.

[89] F. Ellinghaus, *Beam Charge and Beam Spin Azimuthal Asymmetries in Deeply Virtual Compton Scattering.* PhD thesis, Humboldt-Universität, 2004.

[90] D. Zeiler, *Deeply Virtual Compton Scattering off an Unpolarized Hydrogen Target at the HERMES Experiment.* PhD thesis, University Erlangen-Nuremberg, 2009.

[91] X. Lu. and Z. Ye., "Simultaneous Extraction of the BSAs and the BCA Associated with DVCS with the Extended Maximum Likelihood Method," *HERMES Internal Report*, 2007.

[92] R. Barlow, "Extended Maximum Likelihood," *Nucl. Instrum. Meth. A.*, vol. 297, pp. 496–506, 1990.

[93] R. Brun et al., "ROOT An Object Orientated Data Analysis Framework," tech. rep., CERN, www.root.cern.ch.

[94] The HERMES Collaboration, A. Airapetian et al., "Transverse momentum broadening of hadrons produced in semi-inclusive deep-inelastic scattering on nuclei," *Phys.Lett.B*, vol. 684, pp. 114–118, June 2009.

[95] E. Avetisyan, J. Bowles, J. Burns, C. Riedl, C. V. Hulse, and S. Yaschenko, "Analysis of the 2006/2007 data," *HERMES Internal Report*, 2009.

[96] Z. Ye., *Transverse Target spin asymmetry associated with deeply virtual Compton scattering on the proton and a resulting model-dependent constraint on the total angular momentum of quarks in the nucleon.* PhD thesis, University of Hamburg, 2006.

[97] A. Vandenbroucke, *Exclusive π^0 Production at HERMES: Detection - Simulation - Analysis.* PhD thesis, Universiteit Gent, 2006.

[98] B. Krauss, *Deeply Virtual Compton Scattering and the HERMES-Recoil Detector*. PhD thesis, University Erlangen-Nuremberg, 2004.

[99] E. Aschenauer and Z. Ye, "Misalignment Effects on the Beam-Spin and Beam-Charge Asymmetries in DVCS," *HERMES Internal Report*, 2005.

[100] The HERMES Collaboration, A. Airapetian et al., "Measurement of the Beam-Spin Azimuthal Asymmetry Associated with Deeply-Virtual Compton Scattering," *Phys.Rev.Lett.*, vol. 87, p. 182001, 2001.

[101] M. Guidal and H. Moutarde, "Generalized Parton Distributions from Deeply Virtual Compton Scattering at HERMES," *Eur. Phys. J.*, vol. A42, p. 71, 2002.

[102] A. Osborne, *Exclusive ρ^0 Meson Cross Section Ratios on Deuterium and Hydrogen Targets*. PhD thesis, University of Glasgow, 2006.

[103] K. Kumericki and D.Mueller, "Deeply virtual Compton scattering at small x_B and the access to GPD *H*." arXiv:0904.0458.

[104] H.Moutarde, "Extraction of the Compton form factor $\mathcal{H}$ from deeply virtual Compton scattering measurements at Jefferson Lab," *Phys. Rev.*, vol. D79, p. 094021, 2009.

[105] N. d'Hose, E. Burtin, P. Guichon, and J. Marroncle, "Feasibility study of deeply virtual compton scattering using COMPASS at CERN," *The European Physical Journal A - Hadrons and Nuclei*, vol. 19, pp. 47–53, 2004.

[106] F. X. Girod and R. A. Niyazov et al, "Deeply Virtual Compton Scattering Beam-Spin Asymmetries," *Phys.Rev.Lett.*, vol. 100, p. 162002, Nov. 2008.

List of Figures

List of Tables

Appendix A

Asymmetry Results

Kinematc Bin	$-t$ [GeV^2]	x_B	Q^2 [GeV^2]	$A_{LU,I}^{sin\phi}$ $\pm\delta_{stat.}$ $\pm\delta_{syst.}$	$A_{LU,DVCS}^{sin\phi}$ $\pm\delta_{stat.}$ $\pm\delta_{syst.}$	$A_{LU,I}^{sin(2\phi)}$ $\pm\delta_{stat.}$ $\pm\delta_{syst.}$
Integrated	0.117	0.097	2.521	-0.209 ± 0.026 ± 0.034	-0.015 ± 0.026 ± 0.011	0.005 ± 0.025 ± 0.007
$0.00 \leqslant -t \leqslant 0.03$	0.018	0.068	1.720	-0.242 ± 0.055 ± 0.019	0.032 ± 0.055 ± 0.007	0.023 ± 0.055 ± 0.018
$0.03 < -t \leqslant 0.06$	0.043	0.088	2.259	-0.175 ± 0.057 ± 0.044	0.091 ± 0.062 ± 0.021	0.044 ± 0.056 ± 0.008
$0.06 < -t \leqslant 0.10$	0.078	0.099	2.512	-0.220 ± 0.062 ± 0.039	-0.051 ± 0.069 ± 0.012	-0.003 ± 0.061 ± 0.013
$0.10 < -t \leqslant 0.20$	0.142	0.110	2.785	-0.200 ± 0.054 ± 0.044	0.020 ± 0.058 ± 0.023	0.004 ± 0.054 ± 0.011
$0.20 < -t \leqslant 0.35$	0.260	0.121	3.272	-0.242 ± 0.062 ± 0.026	0.126 ± 0.079 ± 0.024	-0.073 ± 0.064 ± 0.026
$0.35 < -t \leqslant 0.70$	0.460	0.125	3.819	-0.156 ± 0.111 ± 0.039	-0.101 ± 0.114 ± 0.016	-0.119 ± 0.102 ± 0.032
$0.03 \leqslant x_B \leqslant 0.06$	0.095	0.049	1.338	-0.173 ± 0.056 ± 0.112	-0.051 ± 0.056 ± 0.021	-0.039 ± 0.056 ± 0.028
$0.06 < x_B \leqslant 0.08$	0.091	0.069	1.799	-0.260 ± 0.055 ± 0.070	0.023 ± 0.055 ± 0.004	0.042 ± 0.055 ± 0.010
$0.08 < x_B \leqslant 0.10$	0.104	0.089	2.300	-0.303 ± 0.062 ± 0.069	0.069 ± 0.062 ± 0.004	0.020 ± 0.062 ± 0.008
$0.10 < x_B \leqslant 0.13$	0.121	0.113	2.928	-0.209 ± 0.065 ± 0.055	-0.012 ± 0.065 ± 0.002	-0.007 ± 0.065 ± 0.002
$0.13 < x_B \leqslant 0.20$	0.159	0.157	4.058	-0.133 ± 0.071 ± 0.064	-0.071 ± 0.071 ± 0.036	0.018 ± 0.069 ± 0.034
$0.20 < x_B \leqslant 0.35$	0.231	0.244	6.139	-0.214 ± 0.121 ± 0.106	-0.074 ± 0.120 ± 0.032	0.021 ± 0.113 ± 0.027
$1.00 \leqslant Q^2 \leqslant 1.40$	0.076	0.054	1.199	-0.168 ± 0.055 ± 0.082	-0.037 ± 0.055 ± 0.008	-0.011 ± 0.055 ± 0.028
$1.40 < Q^2 \leqslant 1.80$	0.089	0.069	1.590	-0.282 ± 0.061 ± 0.104	0.020 ± 0.061 ± 0.025	-0.035 ± 0.060 ± 0.021
$1.80 < Q^2 \leqslant 2.40$	0.104	0.085	2.079	-0.286 ± 0.058 ± 0.081	0.082 ± 0.058 ± 0.023	0.040 ± 0.058 ± 0.005
$2.40 < Q^2 \leqslant 3.20$	0.126	0.105	2.768	-0.194 ± 0.063 ± 0.058	-0.015 ± 0.063 ± 0.016	0.038 ± 0.049 ± 0.017
$3.20 < Q^2 \leqslant 4.50$	0.151	0.134	3.764	-0.120 ± 0.047 ± 0.068	-0.119 ± 0.047 ± 0.029	-0.033 ± 0.069 ± 0.025
$4.50 < Q^2 \leqslant 10.0$	0.218	0.200	5.819	-0.178 ± 0.080 ± 0.044	-0.052 ± 0.080 ± 0.016	0.031 ± 0.076± 0.014

Table A.1: Results of the $A_{LU}^{sin\phi}$ amplitudes with statistical and systematic uncertainties and avarge kinematics from unpolarised hydorgen taken during the 2006-2007 experimental data taking period at HERMES for each $-t$, x_B and Q^2 bin.

Kinematc Bin	$-t$ [GeV^2]	x_B	Q^2 [GeV^2]	$A_C^{cos(0\phi)} \pm\delta_{stat.} \pm\delta_{syst.}$	$A_C^{cos\phi} \pm\delta_{stat.} \pm\delta_{syst.}$	$A_C^{cos(2\phi)} \pm\delta_{stat.} \pm\delta_{syst.}$	$A_C^{cos(3\phi)} \pm\delta_{stat.} \pm\delta_{syst.}$
Integrated	0.117	0.097	2.521	-0.039 ± 0.004 ± 0.011	0.032 ± 0.006 ± 0.005	-0.007 ± 0.006 ± 0.003	0.009 ± 0.006 ± 0.001
$0.00 \leqslant -t \leqslant 0.03$	0.018	0.068	1.720	-0.038 ± 0.009 ± 0.008	0.015 ± 0.013 ± 0.004	-0.026 ± 0.012 ± 0.005	-0.015 ± 0.012 ± 0.004
$0.03 < -t \leqslant 0.06$	0.043	0.088	2.259	-0.013 ± 0.010 ± 0.013	-0.004 ± 0.013 ± 0.013	-0.023 ± 0.013 ± 0.004	0.000 ± 0.012 ± 0.009
$0.06 < -t \leqslant 0.10$	0.078	0.099	2.512	-0.040 ± 0.010 ± 0.015	0.027 ± 0.014 ± 0.009	0.030 ± 0.013 ± 0.006	-0.001 ± 0.013 ± 0.013
$0.10 < -t \leqslant 0.20$	0.142	0.110	2.785	-0.023 ± 0.009 ± 0.008	0.044 ± 0.012 ± 0.007	-0.016 ± 0.012 ± 0.008	0.031 ± 0.012 ± 0.007
$0.20 < -t \leqslant 0.35$	0.260	0.121	3.272	-0.058 ± 0.012 ± 0.011	0.078 ± 0.017 ± 0.020	0.008 ± 0.016 ± 0.015	0.021 ± 0.016 ± 0.006
$0.35 < -t \leqslant 0.70$	0.460	0.125	3.819	-0.130 ± 0.017 ± 0.018	0.051 ± 0.025 ± 0.006	0.015 ± 0.023 ± 0.011	0.040 ± 0.022 ± 0.010
$0.03 \leqslant x_B \leqslant 0.06$	0.095	0.049	1.338	-0.074 ± 0.010 ± 0.012	0.017 ± 0.015 ± 0.015	-0.011 ± 0.013 ± 0.004	0.003 ± 0.012 ± 0.009
$0.06 < x_B \leqslant 0.08$	0.091	0.069	1.799	-0.084 ± 0.009 ± 0.010	0.028 ± 0.012 ± 0.022	-0.010 ± 0.012 ± 0.008	0.005 ± 0.012 ± 0.007
$0.08 < x_B \leqslant 0.10$	0.104	0.089	2.300	-0.055 ± 0.010 ± 0.013	0.029 ± 0.015 ± 0.017	-0.015 ± 0.014 ± 0.010	0.014 ± 0.014 ± 0.005
$0.10 < x_B \leqslant 0.13$	0.121	0.113	2.928	-0.060 ± 0.011 ± 0.007	0.045 ± 0.015 ± 0.003	-0.031 ± 0.014 ± 0.004	-0.010 ± 0.014 ± 0.007
$0.13 < x_B \leqslant 0.20$	0.159	0.157	4.058	-0.045 ± 0.012 ± 0.004	0.036 ± 0.017 ± 0.019	0.003 ± 0.015 ± 0.008	0.010 ± 0.015 ± 0.005
$0.20 < x_B \leqslant 0.35$	0.231	0.244	6.139	0.031 ± 0.020 ± 0.035	0.059 ± 0.029 ± 0.072	0.052 ± 0.027 ± 0.026	0.050 ± 0.026 ± 0.012
$1.00 \leqslant Q^2 \leqslant 1.40$	0.076	0.054	1.199	-0.058 ± 0.009 ± 0.019	0.024 ± 0.012 ± 0.020	-0.026 ± 0.012 ± 0.004	0.0027 ± 0.012 ± 0.006
$1.40 < Q^2 \leqslant 1.80$	0.089	0.069	1.590	-0.043 ± 0.010 ± 0.010	0.038 ± 0.014 ± 0.023	-0.023 ± 0.013 ± 0.012	0.001 ± 0.013 ± 0.004
$1.80 < Q^2 \leqslant 2.40$	0.104	0.085	2.079	-0.052 ± 0.010 ± 0.009	0.007 ± 0.014 ± 0.014	0.030 ± 0.013 ± 0.001	0.043 ± 0.013 ± 0.005
$2.40 < Q^2 \leqslant 3.20$	0.126	0.105	2.768	-0.035 ± 0.011 ± 0.007	0.055 ± 0.015 ± 0.012	-0.016 ± 0.012 ± 0.005	-0.027 ± 0.014 ± 0.004
$3.20 < Q^2 \leqslant 4.50$	0.151	0.134	3.764	0.003 ± 0.012 ± 0.014	0.024 ± 0.017 ± 0.019	-0.008 ± 0.016 ± 0.005	0.015 ± 0.01 ± 0.011
$4.50 < Q^2 \leqslant 10.0$	0.218	0.200	5.819	-0.019 ± 0.014 ± 0.019	0.035 ± 0.019 ± 0.037	0.015 ± 0.023 ± 0.021	0.018 ± 0.018 ± 0.005

Table A.2: Results of the $A_C^{cos\phi}$ amplitudes with statistical and systematic uncertainties and avarge kinematics from unpolarised hydorgen taken during the 2006-2007 experimental data taking period at HERMES for each $-t$, x_B and Q^2 bin.

Appendix B

BHA and BCA Monte Carlo Results Using Pre and Post-Recoil Geometry

Two individual Monte Carlo data productions simulating the HERMES experiment with and without the Recoil Detector were created in order to determine the effect the new configuration would have on the DVCS results. As with experimental data both the BHA and BCA were extracted from the simulated DVCS/BH events. The amplitudes obtained from both simulations were compared to verify that the BHA and BCA amplitudes extracted from hydorgen data recorded at the HERMES experiment with the Recoil Detector from 2006-2007 and without the Recoil Detector from 1996-2005 should be equivalent. The asymmetry amplitudes obtained from Monte Carlo data with and without the Recoil Detector are equivalent and have identical dependence on $-t$, x_B and Q^2, as shown in Figs B.1, B.2 and B.3. The new experimental geometry used to simulate the presence of the Recoil Detector also includes a new implementation of the detector alignment, improving upon the previous measurement of the alignment of the detectors and reducing the systematic error. This improvement, however, does not appear to influence significantly the value of the asymmetry amplitudes.

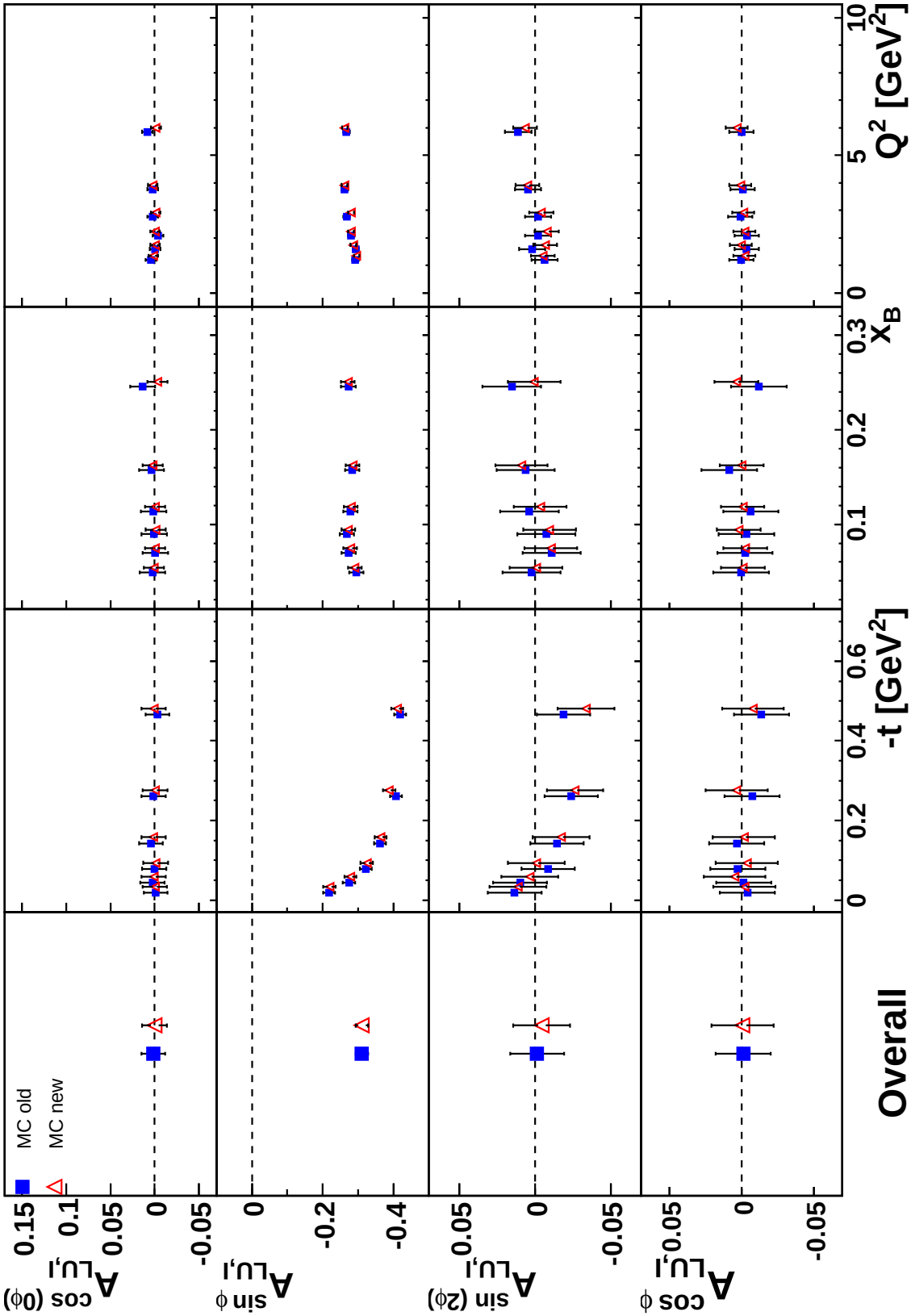

Figure B.1: Beam Helicity Asymmetry amplitudes from the interference term of Monte Carlo Model 1 using the average kinematics from a GMC_DVCS production of DVCS events with the "new" and "old" geometry files simulating the experiment with and without the recoil detector respectively.

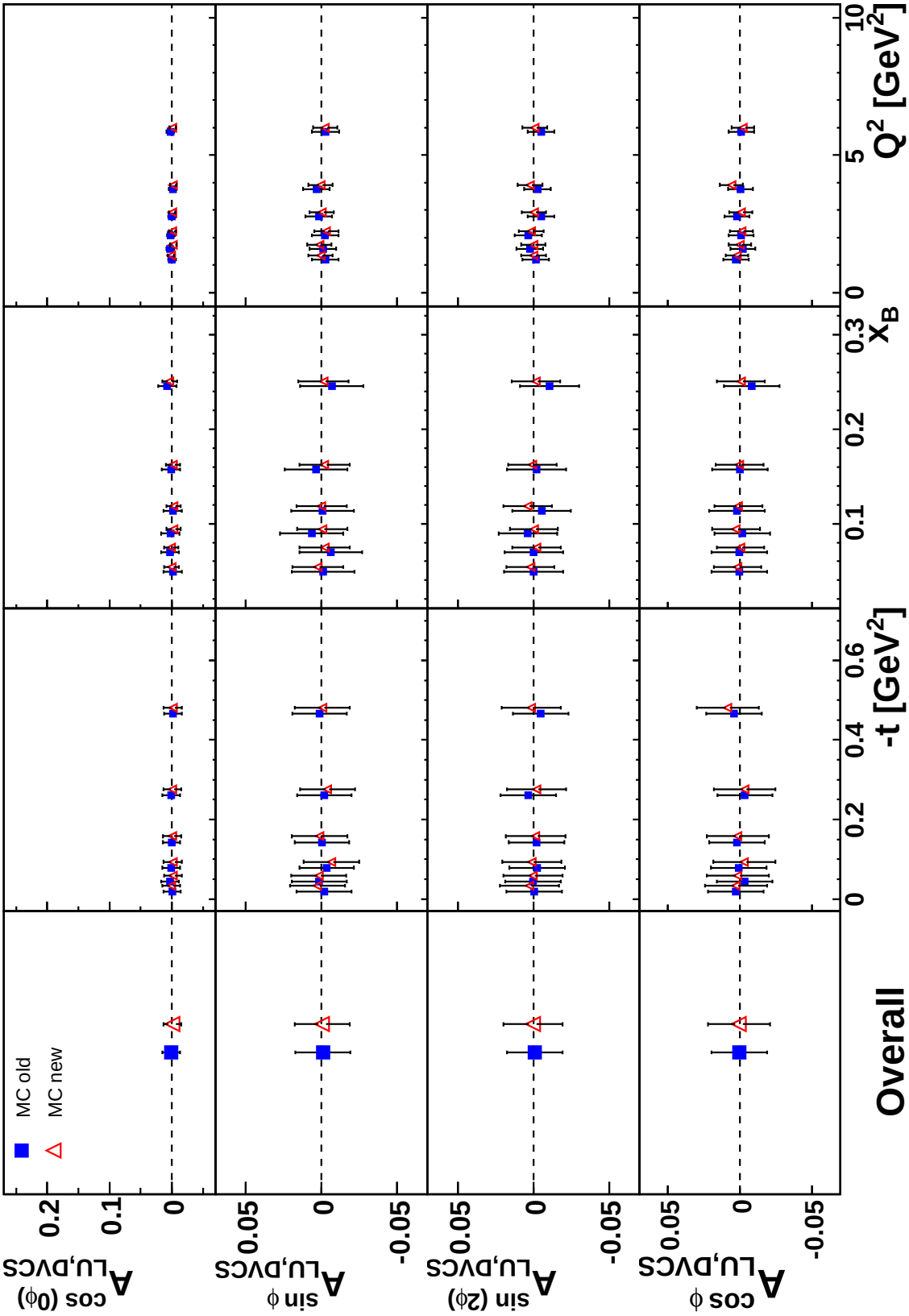

Figure B.2: Beam Helicity Asymmetry amplitudes from the squared DVCS term of Monte Calo Model 1 using the average kinematics from a GMC_DVCS production of DVCS events with the "new" and "old" geometry files simulating the experiment with and without the recoil detector respectively.

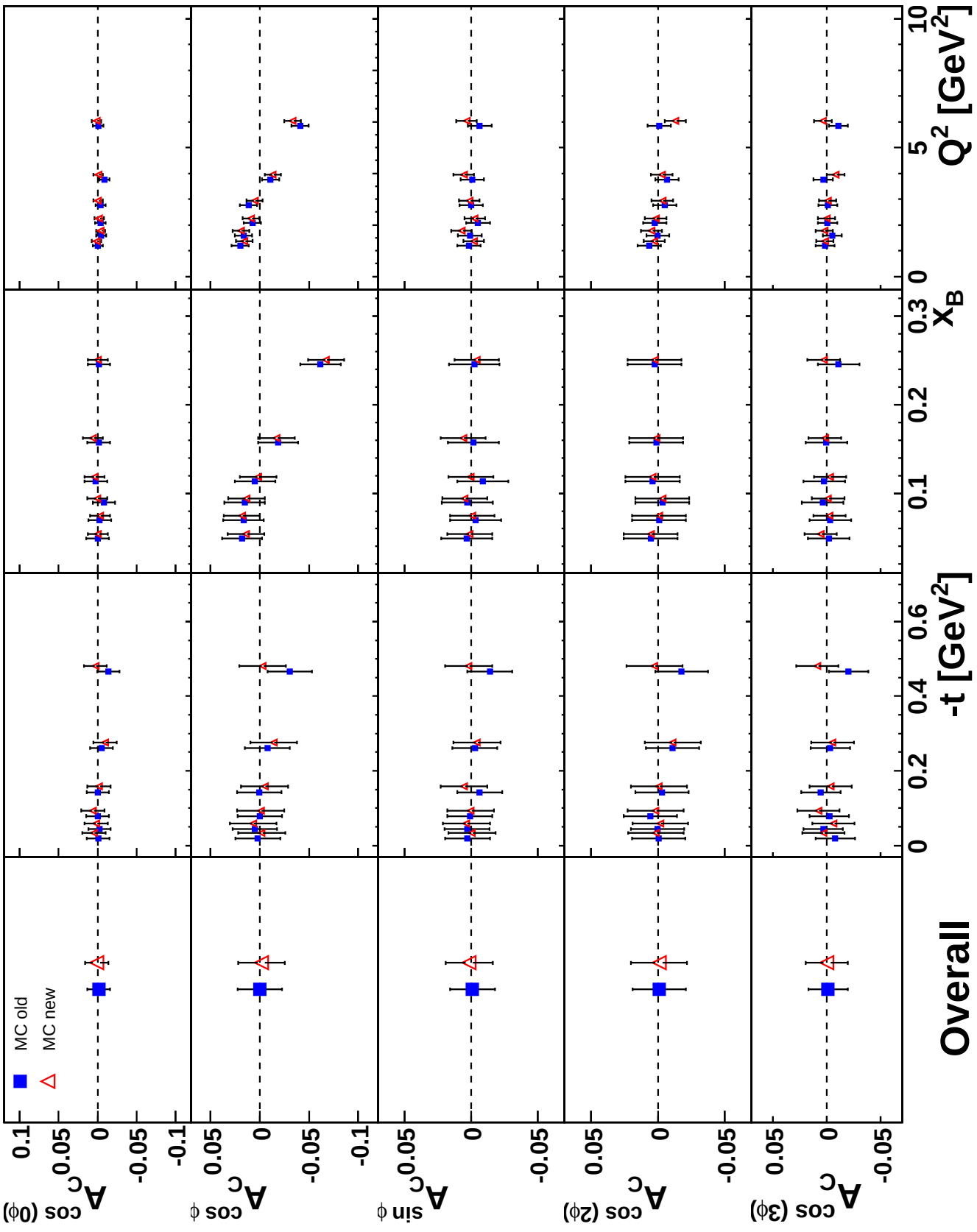

Figure B.3: Beam Charge Asymmetry amplitudes of Monte Carlo Model 1 using the average kinematics from a GMC_DVCS production of DVCS events with the "new" and "old" geometry files simulating the experiment with and without the recoil detector respectively.

Appendix C

Input to the VGG Code

The following details the input to the VGG code obtained from Guidal.

- 4 : 2-body DOUBLY POLARIZED cross sections for (D)DVCS polarized electron, polarized target
- 3 : Bethe-Heitler + DVCS contribution
- 1 : proton target
- 25 : ξ dependent parametrization with MRST02 NNLO distribution
- 2 : evolution with scale sqr = Q sqr
- Give the value for the power b in the profile function for the valence contribution to H : 1 or 9
- Give the value for the power b in the profile function for the sea contribution to H : 1 or 9
- 2 : Regge inspired ansatz for the t-dependence
- Enter slope alphap (GeV^{-2}) : 0.8
- Do you want to evaluate the D-term contribution to the GPD H? : 2 = No
- Do you want to evaluate the GPD E? : 2 = double distribution contribution + D-term contribution

- Give the model for the double distribution part of the GPD E : 2 = valence quark + VM contribution
- Give the value of Ju (e.g. 0.3) : 0.3
- Give the value of Jd (e.g. 0.1) : 0.1
- Do you want to evaluate the pi0 pole contribution (i.e. SPD Etilde)? : 1 = Yes
- Do you want to include twist-3 corrections ? : 2 = Include twist-3 corrections for L photon in Wandzura-Wilczek approximation
- With (1) or without (2) Htilde ? : 2
- Give the polarization of the target proton : 1 = proton polarized along x-axis
- Calculation for what LEPTON charge ? : 2 or 1 positively and negatively charged lepton.
- Give the value of beam energy in GeV (e.g. 27.) : 27.56
- Give the value of Q^2 in GeV2 (e.g. 5.0) : 2.46
- Give the value of x_B (e.g. 0.3) : 0.095
- Give the value of Q'^2in GeV^2 (e.g. 2.0) : 0.00
- Give the value of $-t$ (in GeV^2) : 0.118
- Give the first value for the angle phi (in deg) to calculate : 0
- Give the step in the angle phi (in deg) (e.g. 10.) :10
- Give the last value in the angle phi (in deg) (e.g. 180.) : 180